Towards Light Induced Apoptosis

Investigating the Application of a Red-Shifted Photoswitch to Induce Cell Death

A thesis submitted to Cardiff University for

the degree of Doctor of Philosophy by

Martin Heinrich Übler

Supervisor: Rudolf K. Allemann

Cardiff University
School of Chemistry
January 2021

Acknowledgments

I would like to thank Prof. Rudolf K. Allemann for giving me the opportunity to carry out the PhD in his group, for his supervision, for his financial support and for all the resources in the laboratory that made this project possible.

Furthermore, I'd like to thank some people who directly or indirectly contributed to this work – this PhD wouldn't have been the same without them. Firstly, I'd like to thank Dr. Louis Luk for teaching me peptide synthesis, for always having an open ear and open door for me and for the countless scientific conversations we had. Special thanks to Dr. Robert Mart for his priceless knowledge, scientific expertise and his suggestions during the entire PhD and the writing of this thesis. I also would like to thank Dr. Luke Johnson for his help in the biolab and the scientific conversations. Massive thanks to the Photobiochem-PhD-students, Dr. Raquel Cruz Samperio and Dr. Mindaugas Kalvaitis, who took me under their wings when I started my PhD, showing me around in Cardiff, their endless moral support and help in the lab. Many thanks to Raquel for her enormous patience training me in the cell culture lab. I would like to thank the Analytical Services in the School of Chemistry for their great and competent work, particularly my friend Tom Williams, whose help was invaluable.

I want to thank everyone in the Allemann and Luk group for their help and support during this time. Specially, I want to thank the girls in the Allemann-office (Gwawr, Jenny, Sara, Irene) for all the banter and conversations. Many thanks to Florence for being the perfect fumehood-buddy. I also would like to thank Dr. Victor Gonzalez Requena for all the banter we had in the lab during late hours. Big thanks to Dr. Christopher Jones who introduced me to the pub culture in Cardiff, for his moral support throughout and for always being there for me. I want to thank Dr. Alexander Nödling, Dr. Nicolo Santi and Davide Cardella from the Luk-group, for all the great gym- and coffee-sessions. I also would like to thank Alexandre Canet for our many, many coffee walks around Roath Park and for the interesting and inspiring discussions we had.

Most importantly, I would like to thank my family for all their moral and financial support throughout this time.

Abstract

Manipulating protein-protein interactions of the tightly regulated Bcl-2 network with peptides can restore the apoptotic process in immortal cancerous cells. Chemical staples on BH3-peptides have previously been used to enforce α-helical structures to disrupt protein-protein interactions of the Bcl-2 family. However, these staples are either permanently active or require UV-light to control apoptotic events in a spatiotemporal manner. A tetra-*ortho*-chloro substituted azobenzene staple has recently been reported to reversibly stabilise α-helical peptide structures upon irradiation with red light (light state) and was expected to improve existing BH3-stapled peptide systems.

The reported photochromic staple and a number of apoptosis-inducing peptides were synthesised. Solid-phase peptide synthesis (SPPS) was used to generate the pro-apoptotic and cell-penetrating peptides and an enzymatic ligation of the peptides was explored. A solid phase stapling approach was investigated to attach the linker to the peptide prior to cleavage from the resin. Successfully stapled peptide constructs were tested and characterised using biophysical assays *in vitro* including fluorescence polarization (FP) and protein-NMR binding assays. Furthermore, cell death induction was tested on live mammalian cells *in vivo*.

Characterisation of the majority of constructs *in vitro* proved challenging due to poor solubility of the azobenzene moieties under assay conditions. Modification of the peptides with hydrophilic sequences did not improve the solubility. In FP assays, all tested peptides showed specific binding to the anti-apoptotic protein Bcl-x_L to some degree, although with large margins of error. Peptides containing water-soluble linker or solubilizing sequences showed significantly lower margins of error suggesting that these were a product of the limited solubility. However, no significant difference between dark (*trans*) and light (*cis*) state could be observed for any of the stapled constructs. Binding of the constructs with the target protein was further investigated using protein-NMR techniques but no specific binding was observed for the stapled peptides. The dark state of the constructs showed higher cytotoxicity against mammalian cells than the light state, this was hypothesised to be a result of the physical properties of the linker.

This work has demonstrated the use of solid phase peptide synthesis for the generation of pro-apoptotic-CPP constructs and chemical modification of such constructs prior to cleavage from the solid support. In addition, specific binding of the constructs to the anti-apoptotic protein Bcl-x_L has been demonstrated. Challenges in solubility and control by light have been highlighted and it is hoped that these findings will lead to improved designs in the future.

Table of Contents

List of Figures

List of Tables

List of Schemes

List of Abbreviations

AA	Amino acid	Da	Dalton
AP	Atmospheric pressure	DBP	Dynamic BH3 profiling
Abs	Absorbance	DBU	Diazabicycloundecene
AIF	Apoptosis inducing factor	DCM	Dichloromethane
Ant	Antennapedia protein	DIC	*N*,*N*'-Diisopropylcarbodiimide
APAF-1	Assembly factor 1	DISC	Death-inducing-signaling-complex
Bad	Bcl-2 associated agonist of cell death	DIPEA	*N*,*N*-Diisopropylethylamine
Bak	Bcl-2 homologous antagonist killer	DMF	Dimethylformamide
Bax	Bcl-2-associated X protein	DMEM	Dulbecco's Modified Eagle Media
Bcl-2	B-cell lymphoma 2	DMSO	Dimethyl sulfoxide
Bcl-w	Bcl-2-like protein 2	DNA	Deoxyribonucleic acid
Bcl-x_L	B-cell lymphoma-extra large	dNTP	Deoxyribose nucleotide triphosphate
Bfl-1	Bcl-2-related protein A1	DTT	Dithiothreitol
Bid	BH3 interacting domain death agonist	*E.*	*Escherichia*
Bik	Bcl-2 interacting killer	EDTA	Ethylenediaminetetraacetic acid
Bim	Bcl-2 like protein 11	e.g.	*Exempli gratia;* for example
BLA	Biologic license applications	eq	Equivalent
Bmf	Bcl-2 modifying factor	ES	Electrospray
Boc	*tert*-butyloxycarbonyl	EtOH	Ethanol
Bok	Bcl-2 related ovarian killer	FACS	Fluorescence-assisted cell-sorting
bp	Base pair	FAM	Carboxyfluorescein
°C	Degrees Celsius	FBS	Fetal bovine serum
CD	Circular dichroism	FDA	Food and drug administration
CI	Confidence Interval	FITC	Fluorescein isothiocyanate
CPP	Cell-penetrating peptide	Fmoc	Fluorenylmethoxycarbonyl PG
CuAAc	Copper(I)-catalyzed azide-alkyne cycloaddition	FRET	Förster-resonance energy transfer
CV	Column volume	FSC	Forward scattering

FT	Flow through	mg	Milligram
FWD	Forward	µg	Microgram
g	Gram	min	Minute
GG	Golden Gate assembly	ml	Millilitre
h	Hour	µl	Microlitre
HeLa	Human cervical cancer cell line	Mmt	Methoxytrityl PG
Hrk	Activator of apoptosis hara-kiri	MOM	Mitochondrial outer membrane
HPLC	High-performance liquid chromatography	MOMP	Mitochondrial outer membrane permeabilization
Hz	Hertz	MS	Mass spectrometry
i.e.	*Id est;* that is	ng	Nanogram
IPTG	Isopropyl β-D-1-thiogalactopyranoside	Ni-NTA	Nickel-nitrilotriacetic acid
IR	Infrared	nm	Nanometre
kbp	Kilobase pair	NME	New molecular entities
kDa	Kilodalton	NMP	*N*-Methyl-2-pyrrolidone
L	Litre	NMR	Nuclear magnetic resonance
λ	Wavelength	Noxa	Phorbol-12-myristate-13-acetate-induced protein 1
LB	Lysogeny broth	NS	Non-specific
LC	Liquid chromatography	OD	Optical density
LED	Light-emitting diode	PAGE	Polyacrylamide gel electrophoresis
LiCl	Lithium chloride	Pas	Penetration accelerating sequence
M	Molar	PCD	Programmed cell death
MALDI	Matrix-assisted laser desorption/ionization	PCR	Polymerase chain reaction
Mcl-1	Induced myeloid leukemia cell differentiation protein Mcl-1	PEG	Polyethylene glycol
MHz	Megahertz	PG	Protecting group
mM	Millimolar	PLI	Protein-ligand interactions
µM	Micromolar	TAE	Tris-acetate EDTA
PPI	Protein-protein interactions	ppm	Parts per million

PSS	Photostationary state	TAT	Transcription-transactivating protein
Puma	p53 upregulated modulator of apoptosis	TB	Terrific broth
RCM	Ring-closing metathesis	TCEP	Tris(2-carboxyethyl)phosphine hydrochloride
REV	Reverse	TEV	Tobacco Etch Virus
s	Second	TFA	Trifluoroacetic acid
SAHB	Stabilized α-helix of Bcl-2 domains	TM	Transmembrane
SPPS	Solid-phase peptide synthesis	TNF	Tumor-necrosis-family
δ	Chemical shift	TOF	Time-of-flight
t	Time	Trt	Trityl PG
tBid	Truncated Bid	UV-Vis	Ultraviolet-visible
T	Temperature	w/v	Weight per volume

Amino Acids

Alanine	Ala	A	Asparagine	Asn	N
Cysteine	Cys	C	Proline	Pro	P
Aspartic acid	Asp	D	Glutamine	Gln	Q
Glutamic acid	Glu	E	Arginine	Arg	R
Phenylalanine	Phe	F	Serine	Ser	S
Glycine	Gly	G	Threonine	Thr	T
Histidine	His	H	Valine	Val	V
Isoleucine	Ile	I	Tryptophan	Trp	W
Lysine	Lys	K	Tyrosine	Tyr	Y
Leucine	Leu	L			
Methionine	Met	M			

I. Introduction

1. Targeting Protein-Protein Interactions

a. Small Molecules and Peptides

Protein-protein interactions (PPI) are crucial for living systems as they are integral to the majority of biological functions. Protein function depends on the interaction with partners, whether it be another protein or other biomolecules such as nucleic acids, lipids or co-factors.[1–3] Protein-protein interactions alone underpin a range of vital biological events, from enzyme substrate interactions through receptor-ligand binding to immunological functions, such as antibody-antigen interactions.[1,4,5] Protein-protein interactions govern biomolecular pathways resulting in many physiological and also pathological events and are therefore of major significance to medicine as well as research. The interaction surface between two proteins, their interface, is crucial for molecular recognition by a combination of chemical and physical characteristics.[6–8] The surface area of PPI-interfaces was found to cover an average area of roughly 1000–3000 $Å^2$.[9] Analyses of the amino acid composition of PPI interfaces revealed an increase in amino acids with hydrophobic side-chains at interfaces, often clustered into patches.[4,6,10] PPI interfaces are usually flat, lacking distinct cavities so that recognition between the proteins occurs *via* a multitude of weaker electronic interactions across a large interface including van der Waals forces, hydrogen bonding or cation-π interactions.[4,11,12]

Dysregulation of pathways involving PPIs or changes in specificity and affinity of PPIs can lead to many conditions, including cancer, asthma and inflammatory diseases.[3,13–15] As a consequence, PPI interfaces are potential drug targets as specifically blocking such interfaces could restore function. Targeting disease-related PPIs not only expands the number of potential drug targets, but may also produce drug candidates with increased specificity leading to fewer adverse effects.[3,16] To give an idea of the potential importance of this field, there are estimated to be up to 10,000 disease-modifying proteins giving rise to between 130,000 and 650,000 of potentially addressable PPI interfaces of which only a relatively small number (about 400 proteins) have been explored as targets for therapeutic development so far.[17,18]

Due to the rather large, flat and featureless area of the interface, the inhibition of protein-protein interactions was considered *undruggable* for a number of years.[3,13,17,19] Thus, a common approach was to tackle proteins by blocking their binding sites for their cofactors or other substrates (protein-ligand interactions, PLI) in order to modulate the activity of a target protein.[17,19,20]

PPIs have traditionally been targeted by small molecules (< 500 Da.), which still provide the majority of drugs. Analyses of the PPI-interfaces have revealed that hydrophobic residues tend to clusters into patches, so called *hot spots*. Alanine scanning mutagenesis has shown that maximising the hydrophobic interactions between amino acid sidechains at the interface is the driving force for PPI formation.[18,21] These hot spots tend to cluster in sizes comparable to small molecules (200-400 $Å^2$), are conformationally flexible enough to bind to suitable drug-like molecules,[3,6,16,18] and binding a molecule to these patches is sufficient to inhibit some PPIs.[12,22]

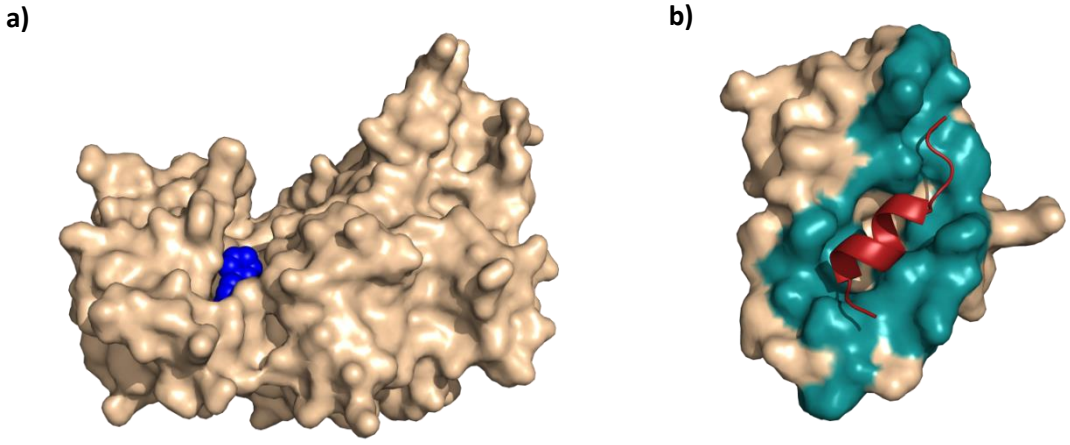

Figure I.1 *a) Example of a small molecule-inhibitor: SRPIN340 covering a 'hot spot' in serine-arginine protein kinase 1 (PDB: 4WUA) by binding in a nearby cavity b) A p53-peptide bound to MDM2, the teal surface indicates the interface surface covered by the peptide-residues (cut-off distance: 4.5 Å, PDB: 1YCR).*

However, despite methods being known to tailor their cellular uptake, oral availability, stability and solubility, small molecules frequently suffer from non-specific or off-target side-effects. The average cost of developing a new prescription drug has been estimated as US $1.3 billion when failures during the developing process, thought to represent approximately up to 70% of the total costs, are included.[23] Lack of efficacy, toxicology and clinical safety concerns are the predominant causes of failure during the development of new drug candidates and recent numbers suggest that the rate of failure as high as 90% until approval.[24] A common consensus demanding lower healthcare costs through reduced drug pricing and a higher drug safety, quality and efficacy, and the resulting increase in R&D costs has put the pharmaceutical industry under increasing economic pressure.[25] In 2018, 59 drugs were approved by the FDA, a record number of new molecular entities (NME). However, only 14 of them were assigned the breakthrough therapy designation, where NMEs are intended to promise substantial

improvement over existing therapies. Only two of those approved are expected to achieve annual sales of US $2 billion or more by 2024, a significant fall over previous years. Out of all newly approved drugs, 17 fall into the class of biologic license applications (BLAs), the highest number since 1993, which shows the importance of novel approaches to drugs beyond small molecules.[26]

Among the milieu of bioactive natural products are more than 7000 naturally occurring peptides, known to play crucial roles in human physiology as hormones, neurotransmitters, growth factors or ion channel ligands.[27] In marked contrast to small molecules, these peptides display high selectivity to their target proteins. Furthermore, peptides are metabolised into non-toxic amino acids, avoiding the problem of metabolite accumulation in organs noted for many small molecule drugs.[3] Considering their attractive pharmacological profile, naturally occurring peptides are an excellent starting point for the design of novel pharmaceuticals. Currently, around 80 peptide-drugs are marketed in the U.S., Europe and Japan and there are more than 400 peptide-based drugs under global clinical development.[28,29] In 2018, global sales for peptide-drugs were estimated to be worth around US $25 billion.[30] Peptide therapeutic candidates have traditionally suffered from major drawbacks, but new synthetic and tailoring strategies offer solutions to many of them and have fostered a revival of interest in novel peptide-based drug candidates.

The methodology for peptide synthesis on a solid support was first introduced by Merrifield and involved the repeated application of *tert*-butyloxycarbonyl (Boc) protected amino acid building blocks. Harsh conditions (hydrogen fluoride) are required to liberate the peptide from the solid support, which somewhat limited the large scale application of this technique but the concept of step-wise synthesis of peptides anchored to a solid-support has revolutionised the field of peptide synthesis. Today, the fluorenylmethoxycarbonyl (Fmoc) protecting group has replaced Boc for all but some specialist applications. Fmoc-chemistry allows the use of much milder and safer conditions and has made the synthesis of peptides highly accessible for less specialised laboratories. Several companies now offer automated peptide-synthesis solutions, capable of the convenient, reproducible synthesis of generic peptides in a reasonably short time. A wide range of solid supports are also now commercially available making it possible to choose the most suitable resin for the target peptide depending on its chemical and physical properties (e.g. the length of the peptide, its solubility, desired cleaving conditions, C-terminal functionality etc.). Various natural and unnatural amino acid building blocks are now readily available from commodity chemical suppliers, containing a broad range of different protecting groups. This enables a number of different approaches for chemical manipulations beyond

simple deprotection/chain extension cycles and expands the range of functionalities that peptides can display. Techniques have been reported that allow direct modification of the resin-anchored peptide by selective reaction of functionalities bearing protecting groups orthogonal to those used for peptide synthesis, including internal cyclisation. To date, the majority of peptide-drugs target PPIs in the extracellular space, but next generation peptide-based drugs are widely anticipated to address intracellular PPIs.[3,28] Compared to recombinantly produced protein drugs, peptides have lower manufacturing costs, improved tissue penetration due to their smaller size and are more stable at room temperature.

With modern computer modelling approaches peptide conformations can be predicted with increasing accuracy. Combined with improvements in structure-activity relationship calculations, the ease of rapidly synthesising sequences to test hypotheses may give peptide-based drugs a serious advantage over small molecule screening in future.[3,25,27]

b. Modifying the Limitations of Peptide Drugs

The relatively large, flat and mostly featureless interface of most PPIs is a key issue as contemporary drug discovery slowly exhausts the number of targets amenable to small molecule approaches. Peptides are highly specific due to their interaction with a large area of interface hot spots and show only very limited off-target effects. However, peptides also exhibit several limitations that have hitherto hindered their successful application as widespread drug-candidates.[3,31] Numerous research groups have been trying to overcome those limitations over the last decades using different approaches. The increasing number of peptide based drugs on the market and in clinical trials shows that their efforts are paying off with PPIs previously considered undruggable now being successfully addressed.

A key-limitation of peptides as drug-candidates is the physiological degradation through the action of endopeptidases in tissue or cellular organelles and by the less specific exopeptidases in circulation and peripheral organs. These peptidases are important for the organism to endogenous signalling peptides after performing their function, but can also efficiently clear peptide therapeutics.[25,32] Administration of therapeutics often occurs far from their site of action, which requires the penetration of several biological barriers before therapeutics can reach their targets. Some peptide sequences also suffer from inherently poor bioavailability and biodistribution due to physiochemical properties including aqueous solubility, liphophilicity, and chemical as well as metabolic stability. Generally, unmodified peptides can be considered poor drug candidates due to a low oral availability, short half-lives in circulation

time due to metabolic degradation, rapid removal from the blood stream through renal and hepatic clearance; unmodified peptides usually survive only few minutes in the blood stream before enzymatic degradation takes place.[25,32] Peptides are also generally poor at crossing physiological barriers due to being too large and too polar to passively diffuse through membranes.[25,33]

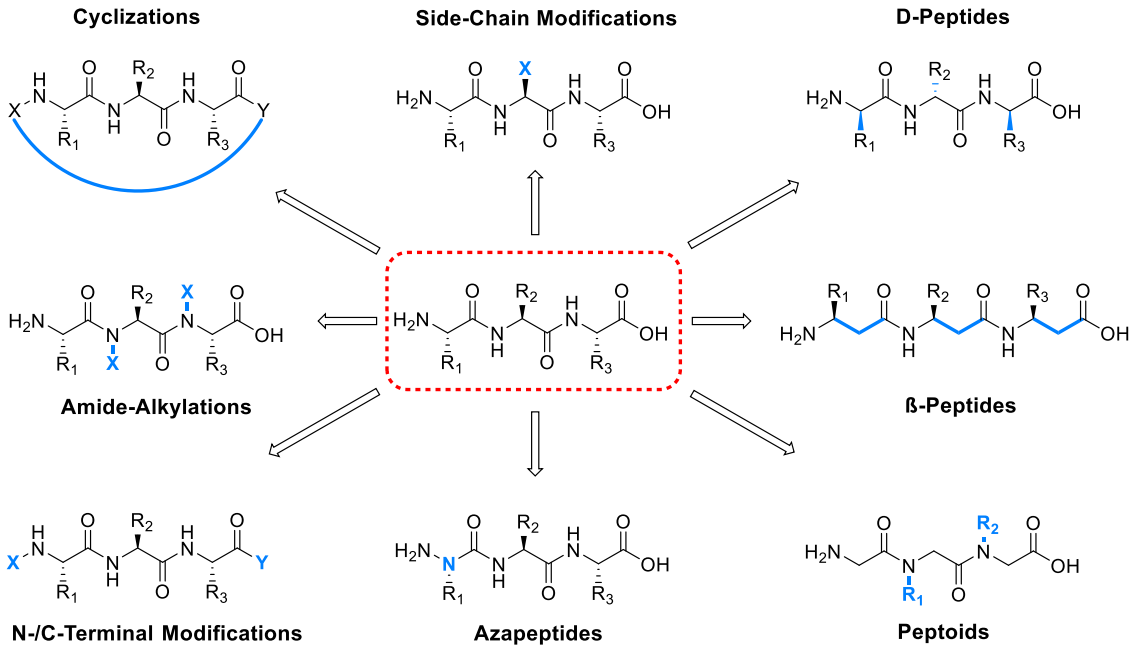

Figure I.2 *Different types of modifications on peptides used to overcome their physical limitations as drug-candidates.*

Fortunately, chemical modifications to peptides have helped to overcome most of these issues as shown by the increasing number of peptide-drugs entering the market. Generally, peptide derivatives and potential peptide-drug candidates can be classified into three main groups depending on the degree of their chemical modification on their peptide bond compared to its native form. 1) *Modified peptides* (Figure I.2) exhibit only small modifications without any change to the peptide bond. Modifications include alterations at the C- or N-termini, introduction of unnatural amino acids/D-amino acids, backbone alkylation or cyclisation. 2) *Pseudopeptides* only show a partial peptide bond character due to their modifications, examples of this group include amide bond surrogates, azapeptides or peptoids. 3) *Peptide mimetics* don't contain any peptide bonds, but instead mimic the spatial positioning of peptide sidechains, usually to improve the pharmacological and pharmacokinetic profiles of a lead peptide sequence. In the literature, these terms are often used interchangeably and *peptide*

mimetics may refer to any type of chemical modification of the native peptide including *pseudopeptides* or even *modified peptides*.[32]

i. N- and C- Terminal Modifications

Peptides consisting of *L*-amino acids with free N- or C-terminii are rapidly degraded in the circulation by exopeptidases. Naturally occurring peptides and proteins therefore often have their termini protected by N-terminal acetylation or C-terminal amidation or circulate as pro-drugs and to be unmasked by specific endopeptidases inside the appropriate cellular compartments.[34–36] Many peptide drug candidates utilize similar terminal capping to prevent premature degradation, but the longer half life time comes at the cost of modifying the properties of the peptide. For example, acetylation of the N-terminus has been reported to increase the liphophilicity and the α-helical character of certain peptides, which had the effect of reducing bioavailability due to enhanced uptake by non-target cells reducing specificity.[32,37]

ii. Alkylation of Amide Nitrogen

Alkylation of peptides is a versatile strategy applied in order to prevent proteolytic degradation of the peptide backbone. Peptides bearing methylated amide nitrogens have often been shown to have improved stability against endopeptidase-degradation while maintaining their activity. However, these peptoids are more conformationally restrained than their parent and their ability to form secondary structures or interact with their targets through hydrogen bonding is compromised. Peptides that are already conformationally restricted, such as cyclic peptides, might benefit from this enhanced backbone rigidity as shown by a number of natural products that possess alkylated amide backbones for increased stability.[38,39]

iii. Side-Chain Modifications

A higher metabolic stability can also be achieved by altering amino acids in regions of peptides sequence recognised by endoproteases to either alternative natural amino acids, by applying side-chain modifications or by incorporating unnatural amino acids. In order to maintain target selectivity, chemically similar amino acids to the original ones are usually of preferred choice. This approach is particularly useful when the mode of degradation and the proteases involved are known.[40,41]

Unnatural amino acids can be an elegant way not only to circumvent *in vivo* enzymatic degradation,[42] but also offer the opportunity for further chemical modification of the resulting peptide *via* their side chains. Unnatural amino acids in peptide chains have been used for ligations,[43,44] cyclisations,[45,46] to photo-cage reactive groups in side-chains[47,48] or to enhance passage through the blood-brain barrier (BBB).[49]

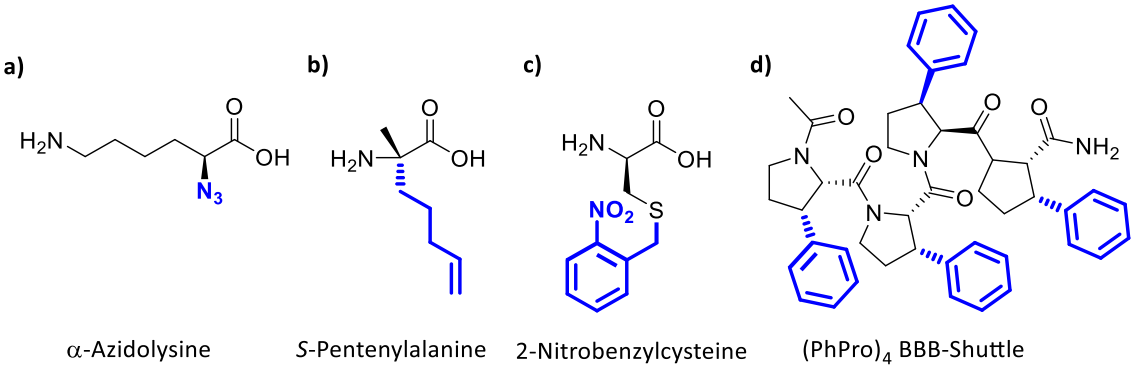

Figure I.3 *a)-c) Different types of side-chain modifications that can be exploited further after incorporation into a peptide-chain with synthetic chemistry, such as azide-alkyne addition, metathesis reaction or photo-reaction. d) Side-chain modifications can also alter the uptake properties of a peptide.*

Introducing unnatural amino acids into peptide chains can modify the secondary and tertiary structure of peptides, which may result in an enhanced stability or activity. Increased backbone rigidity at certain positions of a peptide can stabilize local secondary structures. This can be achieved using conformationally-constrained α,α-dialkylated glycine residues such as α-aminoisobutyric acid[50] or pseudo-prolines derived from serine or threonine residues, condensated with an aldehyde or a ketone to form an oxazolidine ring. Cysteine-derived pseudo-prolines likewise form thiazolidines (Figure I.4). Replacement of naturally occurring prolines with pseudo-prolines has shown to enhance the properties of peptides through the stabilization of the *cis*-peptide bond and can increase water solubility due to improved solvation of the more polar oxazolidine/thiazolidine ring. Pseudo-prolines are commonly used during SPPS to prevent aggregation by disrupting the formation of undesired β-sheet aggregate structures forming during the synthesis. Treatment with acid then removes the protecting group and releases the side-chain of serine/threonine/cysteine.[32,51]

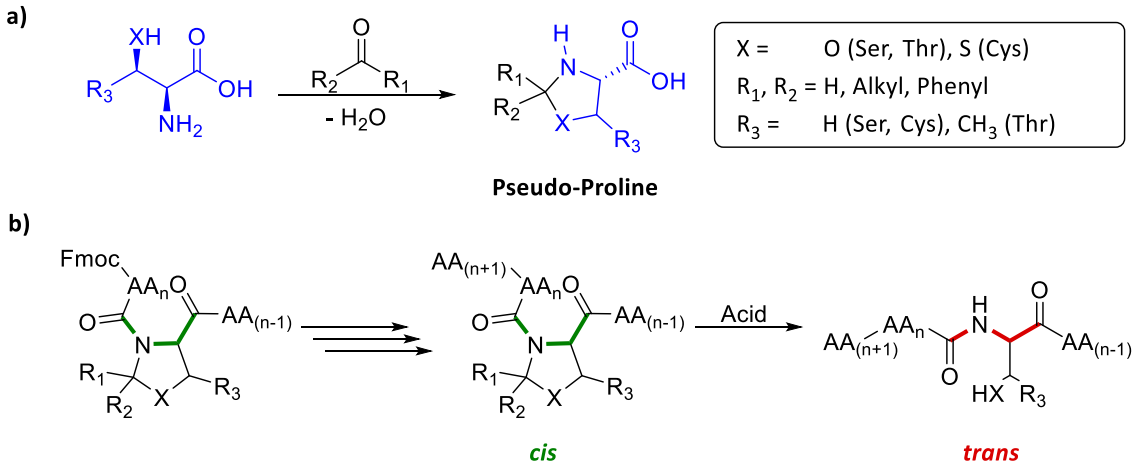

Figure I.4 *a) Synthesis of pseudo-prolines from serine, threonine or cysteine using ketones or aldehydes. b) Incorporation of pseudo-prolines during peptide-synthesis can help to avoid aggregation through the stabilisation of a (temporary) cis-peptide bond.*

iv. Chirality Changes

With only very few exceptions, naturally occurring proteins contain only *L*-amino acids. Proteins containing *D*-amino acids are mostly found in bioactive peptides from molluscs, arachnids, crustaceans and vertebrates. However, over the last decades, *D*-amino acids, predominantly *D*-aspartate and *D*-serine, have also been found in both their free form and incorporated into human proteins. They are mostly found in elderly people with specific diseases and are thought to form by spontaneous racemization over time, hence their presence is often related to a molecular index of aging.[52,53]

Replacing some of the *L*-amino acids in a peptide chain with *D*-amino acids may prevent proteolytic degradation by enzymes, but may also result in loss of activity due to conformational changes. However, peptide drug analogues containing *D*-amino acids have been found to provoke significantly weaker immune responses and thoughtful application of *D*-amino acids might strike the right balance between proteolytic resistance and activity. A promising approach using *D*-amino acids is the synthesis of *retro-inverso* peptides. In those peptides, only *D*-amino acids are used and the sequence is inverted. This results in a peptide structurally similar to the original despite the amino acid stereochemistry *D*-peptide analogue.[51,54,55]

v. Cyclisations

Historically, the discovery of the cyclic peptide gramicidin S with antibiotic properties in 1944, led to an increased interest in cyclic peptides. Thousands of naturally occurring cyclic peptides are now known to date and many of them have been used as therapeutic agents, such as colistin, oxytocin and cyclosporin A.[32,46]

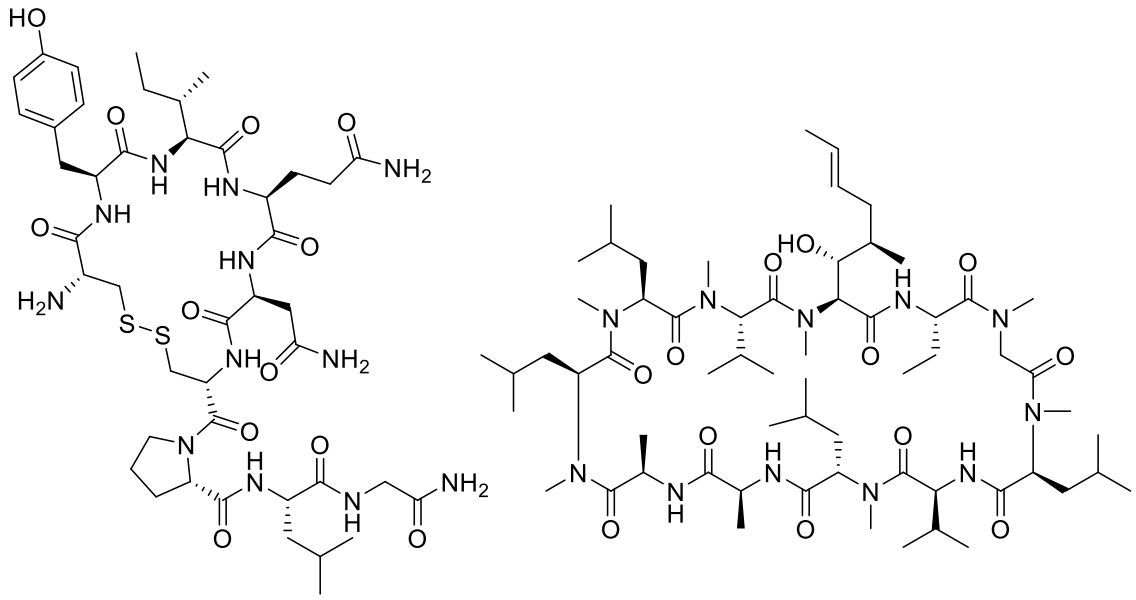

Oxytocin Cyclosporin A

Figure I.5 *Oxytocin and cyclosporin are naturally occurring peptides that have been used for therapeutic purposes. Oxytocin (pitocin) is applied to induce labour and causes contraction of the uterus. Cyclosporin A has been utilized for a number of applications, such as organ transplants to prevent rejection or for rheumatoid arthritis.*

Cyclisation of peptides has become a common strategy to achieve improved stability against proteolytic degradation and reduced conformational flexibility, enhanced potency, selectivity, membrane permeability and even oral bioavailability.[31] Peptides are cyclised from *N*- to *C*-terminus lack any cleavable termini and therefore exhibit an improved metabolic stability, but more commonly cyclisation is performed on a specific, bioactive part of the sequence through amino acid side-chains. Generally, there are four possible ways to cyclise a peptide: *1) Side chain-to-side chain*, *2) Side chain-to-tail*, *3) Head-to-side chain* and *4) Head-to-tail* (Figure I.6).[46] When the cyclisation supports the stabilization of a secondary structural element, the element forming the cycle is often referred to as a *staple*. For example, α-helices formed by peptides can be stabilized when sidechains of residues lying on the same face of the helix are macrocyclised (*Side chain-to-side chain*). One of the most common approaches is the

introduction of two cysteine residues into a peptide chain and their subsequent oxidation to form a disulfide bond between them.[3,56]

Whether carried out in solution or on solid phase, selective cyclisation of peptides generally require the application of orthogonal protecting groups. One of the key-advantages of solid-supported cyclisation reactions is the simplicity of purification by simple washing and filtration. Macrocyclisation reactions in solution often have to be carried out under high dilution in order to minimize unwanted intermolecular side-reactions. Slow, equimolar addition of the reagents to the reaction mixture is often best using one or more syringe pumps.[46]

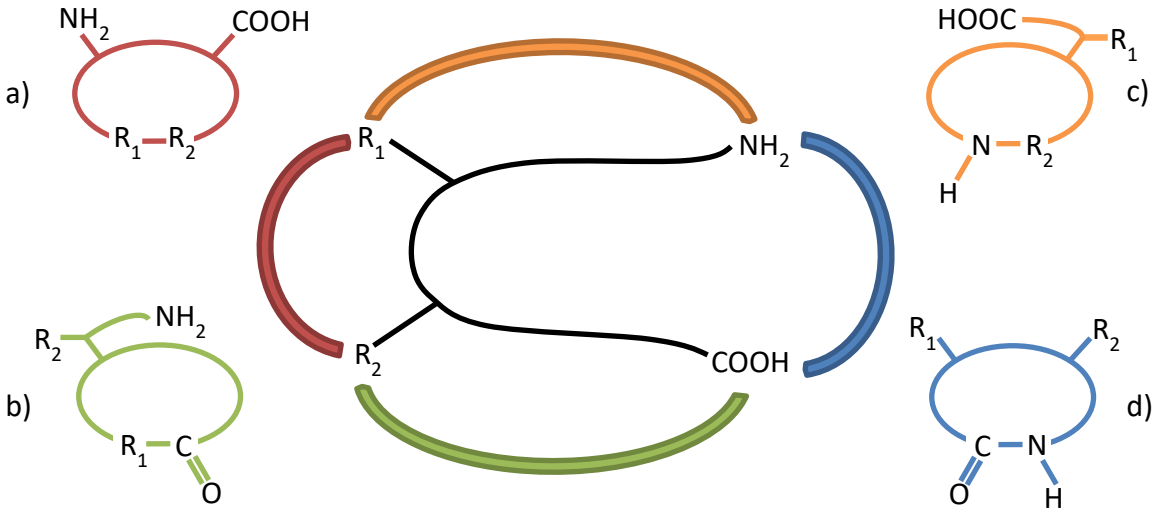

Figure I.6 *Four different types of macrocyclisations in peptides. a) Side chain-to-side chain b) Head-to-side chain c) Side chain-to-tail d) Head-to-tail.*

Biomimetic macrocyclisation approaches use activated thioesters to react with free amine groups to form an amide bond or with a thiol group of cysteine side-chains in a trans-thioesterification reaction, with the latter usually followed by an *S*-to-*N* acyl migration to form a more stable amide bond. Peptides containing C-terminal thioesters and N-terminal cysteine residues can be cyclised in a head-to-tail fashion under mild conditions in a intramolecular *native chemical ligation* reaction.[57–60]

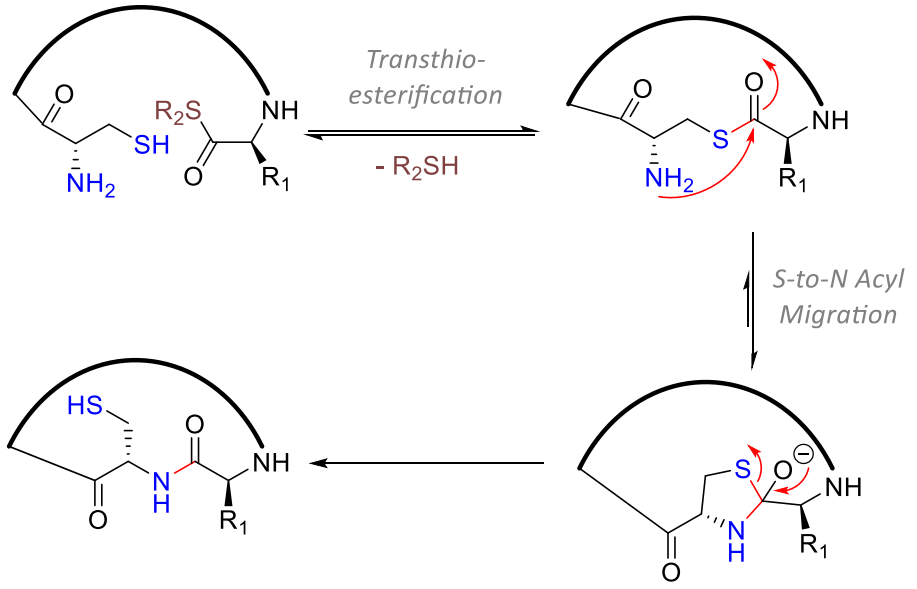

Figure I.7 *Intramolecular native chemical ligation (NCL) can be used to cyclise peptides.*

Introduction of unnatural amino acids into a peptide chain during SPPS can vastly expand the scope of on-resin modification. Cysteine-mediated ring-closing reactions have been carried out with alkene residues as photo-initiated thiol-ene/thiol-yne reactions in order to conduct *side-chain-to-tail* [61] or *side-chain-to-side chain* stapling reactions [62]. There are several reported examples of 1,3-dipolar cycloadditions between azides and alkynes in peptides ('click-chemistry') for ring-closing reactions.[63,64] This strategy leaves a 1,2,3-triazole in the peptide chain, an amide isostere of growing interest due to its thermodynamic and physiological stability. Introducing two non-natural amino acids bearing alkene groups gives the opportunity to use ring-closing metathesis (RCM) reactions to form peptide macrocycles. A common approach first introduced by Grubbs and further developed by Verdine and co-workers is to use RCM reactions to stabilize α-helices with *all-hydrocarbon-staples*. [65,66]

An even milder contemporary approach takes advantage of advances in microbiology by using heterologously expressed peptide ligases to cyclise linear peptides. These enzymes catalyze the formation of peptide bonds and are highly substrate and site specific. Depending on the enzyme, a particular sequence of amino acids is recognised and one or more peptide bonds are cleaved. A specific combination of amino acids from the opposite terminus of the peptide can then be recognized by the enzyme and ligated to the initial recognition sequence. This technique is not traceless as the remainder of the residues of the enzyme recognition sequence remain after the cyclisation. The inherent reversibility of most enzymatic are another drawback, requiring further chemistry to trap the product formed or cleaved recognition site

fragment in order to drive the reaction to completion. Yields can therefore be a problem and the formation of cyclic peptides on a preparative scale may prove challenging. Enzymatic reactions are also restricted to peptides soluble in the relatively tight range of conditions (solvent, cofactors, pH) required for the enzyme to work at an optimal rate. This may cause problems with particularly hydrophobic peptides, which might not be soluble under purely aqueous conditions. However, enzymatic ligation of amenable substrates has now been successfully applied in a number of cases.[67–69]

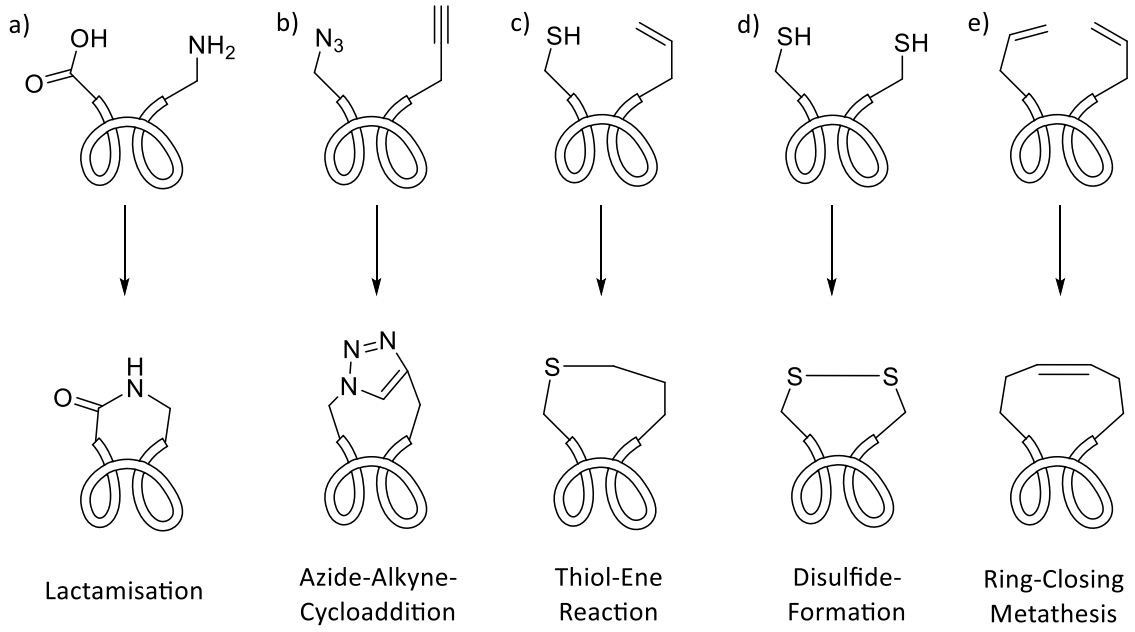

Figure I.8 *Different peptide-cyclisation techniques shown as head-to-tail cyclisations.*

vi. Pseudopeptides and Peptide Mimetics

Altering amide bond or the α-carbon of the peptide backbone leads to molecules with only a partial peptide character, collectively referred to as pseudopeptides. Introducing changes in the peptide bond completely prevents proteolytic degradation, but also may significantly modify the biochemical properties of the compound including the flexibility, hydrophobicity and overall conformation. Modification of the backbone bond may prove particularly useful in compounds already conformationally restricted, such as cyclic peptides. Amide bond surrogates replace the amide bond between two amino acids in a peptide chain with other chemical groups of similar sizes and bond angles. Hydrogen bond surrogates stabilize secondary structures in peptides by mimicking a hydrogen-bond acceptor-donor relationship

with a covalent linkage (Figure I.9). An important consideration when selecting the most appropriate surrogate is to match the desired stereochemistry and electronic properties of the parent peptide; typical examples are ethyl-, ethylene-groups or 1,2,3-triazoles moieties.[70] Another approach to create pseudopeptides is the use of peptoids. Peptoids are peptide-like structures where the side-chain is located on the nitrogen of the amide bond, as a tertiary amide. The main-disadvantage of this approach lies in the increased structural flexibility due to the lack of hydrogen bonding, which may impair their biological activity if particular conformations are required for binding.[32] When one or more α-carbons are replaced by a nitrogen atom, the resulting molecules are termed azapeptides. Azapeptides have been reported to show improved biological properties compared to their natural analogues, such as longer duration of action and improved metabolic stability, particularly when used as enzyme inhibitors.[71]

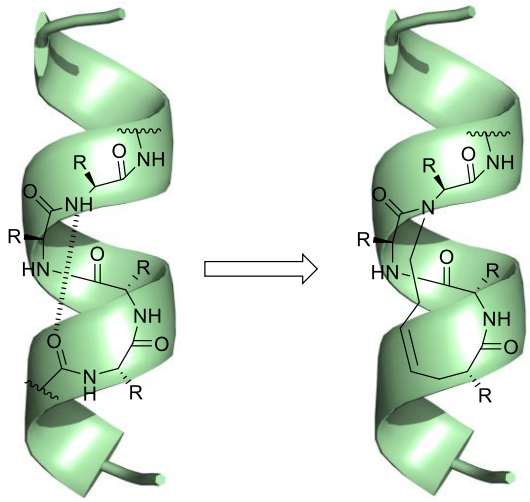

Figure I.9 *Hydrogen-bond surrogates mimic hydrogen bonds in α-helices through covalent bonds.*

Peptide mimetics are small molecules that resemble native peptides but contain no peptide or peptide-like bonds. They attempt to combine the benefits of small molecule drug candidates, such as the superior oral availability, with the advantages of peptide-drugs, such as the improved specificity and reduced off-target effects. However, as they compromise between the two groups, they do suffer from lower specificity and higher toxicity compared to native peptides. Correctly mimicking the spatial distribution of interaction amino acid sidechains requires detailed structural data on the interaction between the native peptide and the PPI interface to design an effective mimic, which is often considered as the limiting factor.[32]

Most successful peptide drugs have been subjected to an extensive optimization process and usually contain one or more of the features mentioned above. Typically, optimization begins by searching for the minimal active sequences of a lead peptide, leading to a truncated analogue that can still interact with the target protein. Alanine scanning is then commonly used to determine the contribution of different residue to the overall binding affinity and D-amino acid scanning can determine potential cleavage sites. Selected amino acids can then be replaced by pseudopeptides to prevent proteolytic degradation and/or cyclisation can be applied to decrease conformational flexibility to limit negative entropic effects on binding. N- and/or C-terminal modification can then further increase the stability towards exopeptidases, and reduce immunogenicity. Finally, addition of transporter groups may enhance membrane penetration and reduce clearance.[25]

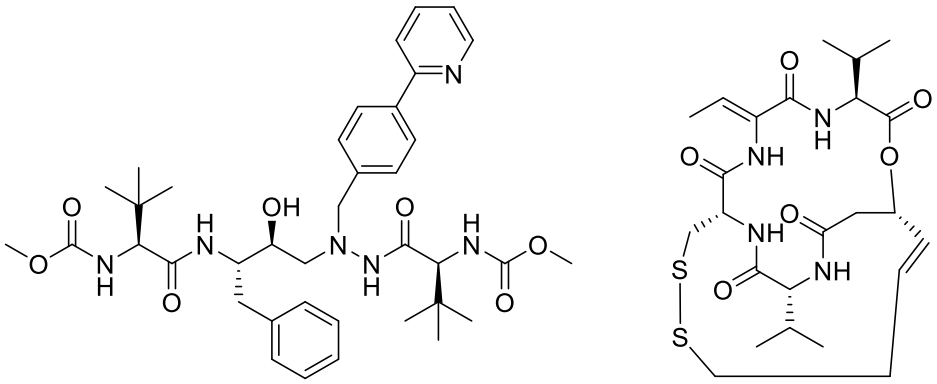

Figure I.10 *Atazanvir (Reyataz®), an orally available peptide-drug that treats and prevents HIV/AIDS. Romidepsin (Istodax®), a cyclic peptide used as an anti-cancer drug in T-cell lymphoma.*

c. Future Prospects for Peptide and Peptoid Drugs

Peptide-based drugs have only recently become a practical approach to target PPIs, having previously been neglected due to the intrinsic disadvantages described above. Advances in solid phase chemistry, especially the advent of Fmoc-chemistry and the ready availability of reagents for it, have lowered the technical barrier to entry to peptide synthesis and it is now possible to synthesize peptides rapidly and reproducibly in good yields. Microwave-assisted automated peptide synthesizers now allow the synthesis longer peptide chains in less than a day. The result of these advances are illustrated by an analysis by Lau *et al.* of a database containing of all peptide therapeutics entering clinical trials from the years 1980-2017.[28]

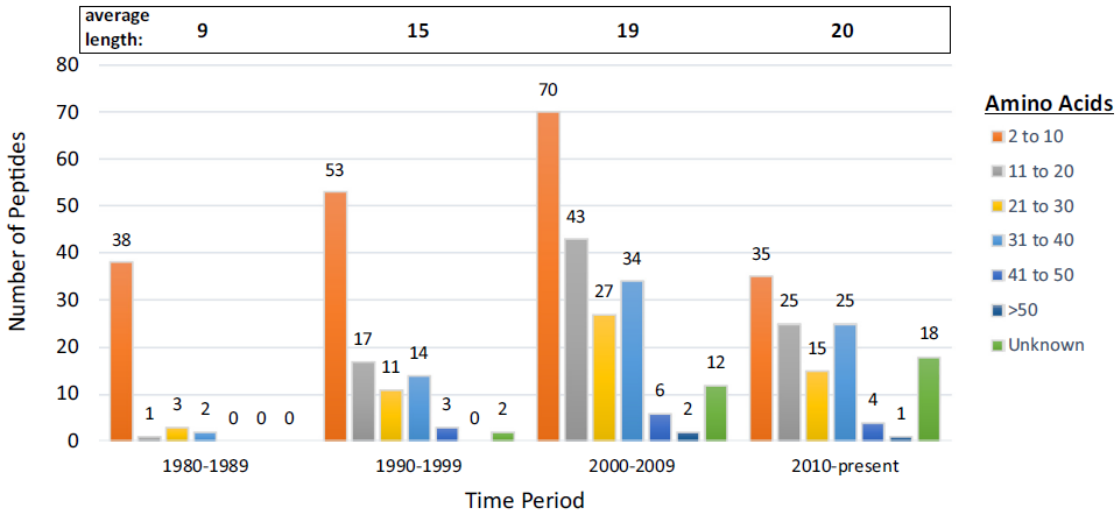

Figure I.11 *Peptides entering clinical trials from 1980-2017 by their average length in amino-acids. A clear trend towards more and longer peptides entering clinical trials can be seen over the time (Figure adapted from [28]).*

The numbers of peptides entering clinical development gradually increased between 1980 and 2010, with a five-year-average at over 22 peptides per year in 2011. The average length of peptides entering clinical development also changed significantly during this time; 86% of peptides entering development between 1980 and 1989 contained fewer than 11 amino acids, whereas in 2010-2017 only 28% of the peptides contained fewer than 11 amino acids and 20% contained between 31 and 40 amino acids. The same study noted a steady increase in drugs containing peptides conjugated to other macromolecules, such as lipids, different proteins or polyethylene glycol chains, from 5% from 1980-1989 to 30% from 2010-2017. Furthermore, significant recent progress in the field of multifunctional peptides, cell penetrating peptides and peptide sequences that can direct cargoes to specific cellular compartments will extend the applicability of future peptide drugs to even more targets.[72–7475]

2. Apoptosis and the Bcl-2-Network

a. Programmed Cell Death – An Overview

Programmed cell death (PCD) is crucial to the development in various species as the deliberate elimination of cells can be necessary for four main reasons: sculpting and deleting structures, regulation of cell numbers, and elimination of defective cells. There are three main routes for intracellularly-triggered PCD in mammalian cells: apoptosis, autophagy[76–78] and (programmed)

necrosis, sometimes also referred to as necroptosis.[76,78,79] These pathways play distinct roles; where apoptosis involves the orderly destruction of cell contents, necrotic tissues release intracellular material into the extracellular milieu leading to inflammatory response. On the other hand, autophagy does not always lead to cell death, but can play pro-survival or pro-death roles depending on the circumstances.[76–78]

PCD is vital for the formation of tissue, organogenesis, and remodelling[80,8182] and for fitness-based selection of overproduced nervous, immune and reproductive cells[83,84] by removal of abnormal or potentially dangerous cells.[76,78] For example, apoptosis is the known mechanism for the removal of the interdigital web during the development of digits in higher vertebrates.[76,80] However, the inactivation of pro-apoptotic genes in mice models resulted in partial removal of interdigital tissue, indicating that several back-up mechanisms for PCD exist.[85]

Mammalian cells that undergo apoptosis show characteristic morphological changes, such as cell shrinkage, nuclear condensation, membrane blebbing and loss of adhesion. This is the result of a number of biochemical changes inside the cell including DNA being cleaved into fragments, flipping of phosphatidylserine to the external leaflet of the membrane, activation of a number of specific proteases leading to intracellular protein cleavage.[77,78] Caspases are a family of cysteine proteases that cleave after aspartate residues which are present in cells as proenzymes that once activated can initiate a cascade by activation of other pro-caspases leading to degradation of crucial nuclear and cytoskeletal proteins.[86] Apoptosis can be induced extrinsically by a death receptor mediated pathway, a T-cell mediated perforin/granzyme pathway, or by an intrinsic mitochondrial pathway.

The extrinsic apoptosis pathway is initiated through the transmembrane receptors of the tumor-necrosis-family (TNF) which share a cysteine rich extracellular domain of about 80 amino acids, which is referred to as the *death domain*.[87] The receptor oligomerizes upon binding with a *death ligand*, such as Fas, and subsequently recruits cytoplasmic proteins, such as FADD, and procaspase-8 leading to the formation of a death-inducing-signaling-complex (DISC). This complex subsequently auto-activates pro-caspase-8 initiating the caspase cascade, the self-destruction of the cell. Caspase-8 can also truncate the BH3-only protein Bid, linking the extrinsic with the intrinsic signaling pathway.[77,78,86]

Mammals defend themselves against the adverse effects of virus- or cancer-affected cells by the action of cytotoxic CD8+ cells, a subgroup of T-cells that recognises such target cells and kill them either by activating extrinsic apoptosis pathways through the activation of death

receptors, or the intrinsic pathway by introducing granzyme A and granzyme B to the cytoplasm of the target cell *via* perforin pores. While granzyme A mediates caspase-independent DNA degradation,[86,88] granzyme B can trigger the intrinsic PCD pathways at several points including direct activation of pro-caspases 3[88,89] and 10[86] and the subsequent activation of other caspases or cleavage of the pro-apoptotic BH3-only protein Bid leading to mitochondrial-mediated cell-death.

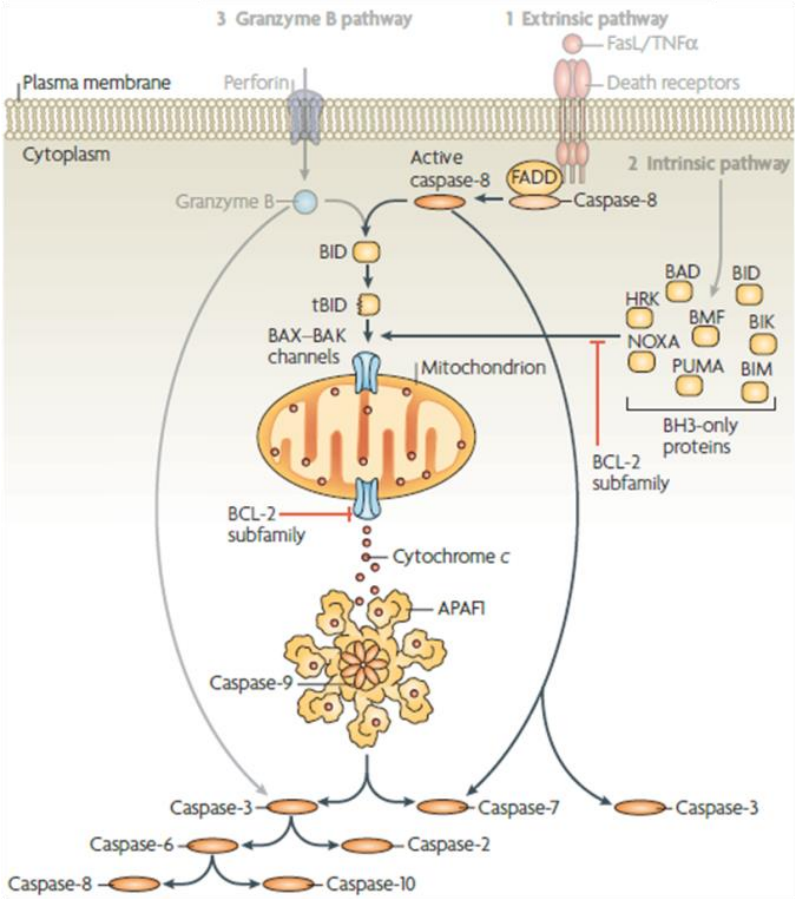

Figure I.12 *Different pathways leading to apoptosis through the activation of the cascade of caspases. The extrinsic pathway involves the binding of a death ligand, such as FasL or tumour necrosis factor-α (TNFα) to the death receptor leading to the recruitment of adaptor proteins, such as the Fas-associated death domain protein (FADD). This then leads to the recruitment and aggregation of caspase-8 promoting its auto-activation. The active caspase-8 further activates caspase-3 and -7. Caspase-8 mediated proteolysis of the BH3-only protein Bid to give truncated Bid (tBid) is a cross-point between the intrinsic and extrinsic pathways. tBid can lead to the release of mitochondrial cytochrome c. The apoptotic protease-activating factor-1 (APAF1) and caspase-9 form an apoptosome leading to the activation of further caspases upon the release of cytochrome c. Granzyme B can be delivered through pore-forming proteins, such as perforin, and can process caspase-3 and -7 as well as Bid to initiate apoptosis. The intrinsic pathway (highlighted) is activated through certain stimuli related to cellular stress or damage, which in turn lead to the activation of specific BH3-only proteins that act as sensors. The activation of BH3-only proteins above a certain threshold removes the inhibitory effect of the anti-apoptotic proteins and leads to pore-formation through Bax/Bak-oligomers and the release of cytochrome c. (Figure adapted from [90]).*

The intrinsic apoptosis pathway is characterised by permeabilization of the mitochondrial outer membrane (MOMP) and the subsequent release of cytochrome c into the cytosol. This step is widely considered to be a point of no return and marks the inevitable initiation of the controlled cell death. Cytosolic cytochrome c assembles with assembly factor-1 (Apaf-1) of into a complex known as the apoptosome which activates pro-caspase-9, leading to activation of the caspase cascade.[77,90,91] Other mitochondrial proteins released during MOMP include apoptosis-inducing factor (AIF) and endonuclease G, which both can promote cell death in a caspase independent manner. The tightly-regulated proteins of the B-cell-lymphoma 2 (Bcl-2) family are key-regulators of the intrinsic pathway. Family members can be categorized into three main groups: multi-domain anti-apoptotic, multi-domain pro-apoptotic and pro-apoptotic BH3-only domain proteins. The intrinsic pathway is activated in response to intracellular stress signals caused by oxidative stress, heat shock, UV light, ionizing radiation or lack of growth factors. These stimuli lead to upregulation of the production of BH3-only proteins or activation of latent BH3-only proteins, which subsequently interact and activate the pro-apoptotic multi-region Bcl-2 family members leading to MOMP. For example, severe damage of the DNA can lead to the activation of the intrinsic apoptosis pathway by the tumor suppressor p53 protein *via* production of the BH3-only proteins PUMA and NOXA eventually leading to MOMP and apoptosis.[86,92] Dysregulation of this carefully balanced equilibrium of proteins is often observed in cancerous cells, rendering the protective intrinsic apoptosis pathway inactive. Regulation of this pathway is therefore an excellent starting point for anti-cancer agents.[78,92–94]

b. The Bcl-2 Family

The Bcl-2 family is divided into three subgroups: multi-domain anti-apoptotic, multi-domain pro-apoptotic and pro-apoptotic BH3-only domain proteins (Table I.1) which may form various homo- as well as hetero-dimers. The proteins consist of up to four conserved Bcl-2 homology regions, which are named BH1-BH4 accordingly. The main-members of the group of multi-region anti-apoptotic proteins (Bcl-x_L, Bcl-2, Bcl-w) possess all four domains, the main-multi-regional pro-apoptotic proteins (Bak, Bax) BH1-3.[95] Both of these groups contain C-terminal transmembrane region (TM) that enable them to locate and insert into the outer mitochondrial membrane. Strategic mutations have confirmed that the amphipathic α-helical BH3 domain is critical for the binding of pro-apoptotic to anti-apoptotic family members. These findings are supported by the action of BH3-only proteins, which stimulate the cell death.[92,94,96]

Table I.1 *Overview of the most important members of the Bcl-2 family and their Bcl-2 homology domains (BH1-4). TM: Transmembrane region.*[97–100]

Class	Protein	Domains
Anti-apoptotic	Bcl-2	BH1 BH2 BH3 BH4 TM
	Bcl-x_L	BH1 BH2 BH3 BH4 TM
	Bcl-w	BH1 BH2 BH3 BH4 TM
	Mcl-1	BH1 BH2 BH3 TM
	Bfl-1	BH1 BH2 BH3 TM
Pro-apoptotic	Bax	BH1 BH2 BH3 TM
	Bak	BH1 BH2 BH3 TM
	Bok	BH1 BH2 BH3 TM
Pro-apoptotic BH3	Bad	BH3
	Bid	BH3
	Bik	BH3 TM
	Bim	BH3 TM
	Hrk	BH3 TM
	Noxa	BH3
	Puma	BH3

The role of these proteins can be generally described as following: Production of BH3-only proteins is either upregulated or they are activated from a latent form and act either directly or indirectly to activate the pro-apoptotic multi-domain proteins Bax or Bak. The latter pair is often referred to as executioner proteins, as they can form oligomeric pores on the outer mitochondrial membrane. Anti-apoptotic proteins, such as Bcl-2 or Bcl-x_L, can inhibit apoptosis by sequestering either the multidomain executioner proteins or the BH3-only proteins. The BH1, BH2 and BH3 regions of the anti-apoptotic proteins fold in such a way as to create a shallow hydrophobic groove on the surface that can bind a α-helical BH3 region from either type of pro-apoptotic protein.[101,102] These interactions are very dynamic, involving conformational changes and alternating binding partners depending on their affinities. Hence, BH3-only proteins can be further sub-categorized into *activators*, members with high affinity for binding and directly activating the Bax and Bak, and *sensitizers*, members that bind

principally to the anti-apoptotic proteins. Several models have been proposed to describe the various interactions of these proteins leading to apoptosis,[96,103] however determining the exact interactions between different partners including conformational and localization changes is a challenging task and experiments often do not represent the actual situation inside the cell where several decisive steps may occur with proteins bound to the mitochondrial membrane.
The complexity of the speciation of Bcl-2 family proteins is demonstrated by the anti-apoptotic protein Bcl-x_L which has been suggested to exist as a homodimer in the cytosol,[94,104] but just like pro-apoptotic Bax,[93,105] Bcl-x_L can also undergo reversible conformational changes leading to an equilibrium between the cytosol and insertion into the outer mitochondrial membrane.[94]

Bcl-x_L consists of eight α-helices and a trans-membrane domain, which are connected through loops of different lengths. Helix α5 and α6 form the core of the protein and are mostly hydrophobic. They are flanked by α3 and α4 on one side and α1 and α2 on the other side. The BH1, BH2 and BH3 regions are close to each other and form the top of the long hydrophobic groove whose base is defined by α3 and α4 (Figure I.13). Studies showed that the trans-membrane region can adopt an α-helical structure (sometimes referred to as helix α9) that docks into the hydrophobic groove.[106]

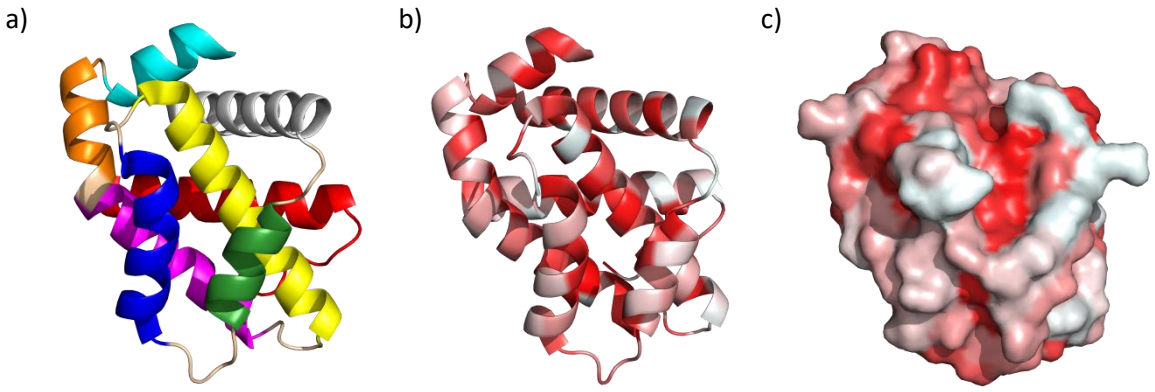

Figure I.13 *The structure of Bcl-x_L (PDB: 1R2D) with the TM-region and loop between α1 and α2 omitted for clarity. a) Helices*: *α1 (red), α2 (grey), α3 (green), α4 (blue), α5 (yellow), α6 (magenta), α7 (orange), α8 (cyan). b) Cartoon coloured to indicate hydrophobic residues (red). c) Surface-representation of Bcl-x_L showing the exposed hydrophobic groove.*

The structure of Bcl-2 is very similar to Bcl-x_L, but the hydrophobic groove is partly formed by α3 resulting in a slightly longer binding groove (Figure I.14). This change along with significant changes in residues along the edge of the groove at positions 104 (Ala in Bcl-x_L, Asp in Bcl-2), 108 (Leu in Bcl-x_L, Met in Bcl-2), and 122 (Ser in Bcl-x_L, Arg in Bcl-2) account for the divergent binding affinities of BH3 peptides to these two proteins.[93,107]

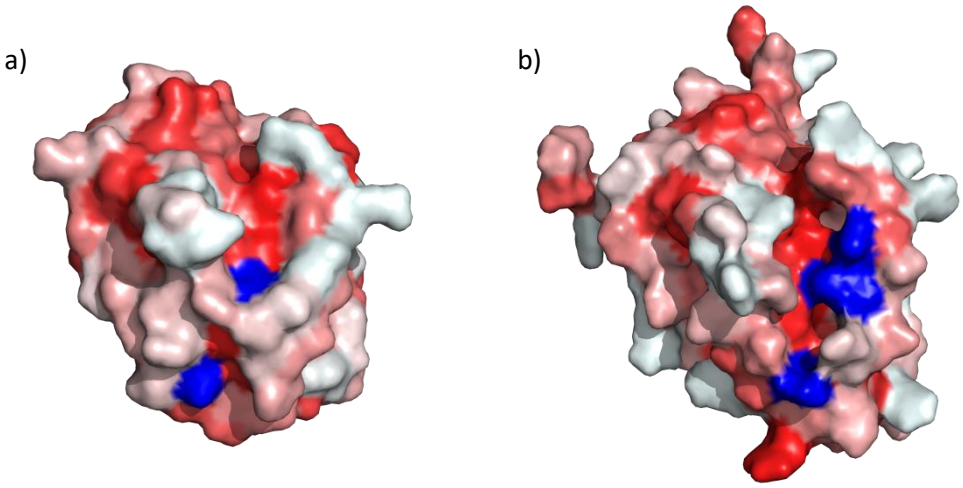

Figure I.14 *Surface-representation of Bcl-x_L (a) showing Leu108 and Ser122 (blue) and Bcl-2 (b) with the residues Asp104, Met108 and Arg122 (blue). Residue Ala104 in Bcl-x_L points to the bottom side of the graphic representation and therefore cannot be seen. These three residues distinguish the hydrophobic grooves of Bcl-2 and Bcl-x_L. (PDBs: 1R2D [Bcl-x_L], 1G5M [Bcl-2]).*

The altered binding groove may also contribute to the altered localisation of the two proteins; Bcl-2 is typically anchored to the outer mitochondrial membrane through its trans-membrane region,[108] whereas Bcl-x_L predominantly exists in the cytosol prior activation (Form 1). It is further suggested that both can adopt two different membrane bound forms, interacting either solely through their transmembrane regions (Form 2) or with insertions of α5 (Form 3) (Figure I.15).[94]

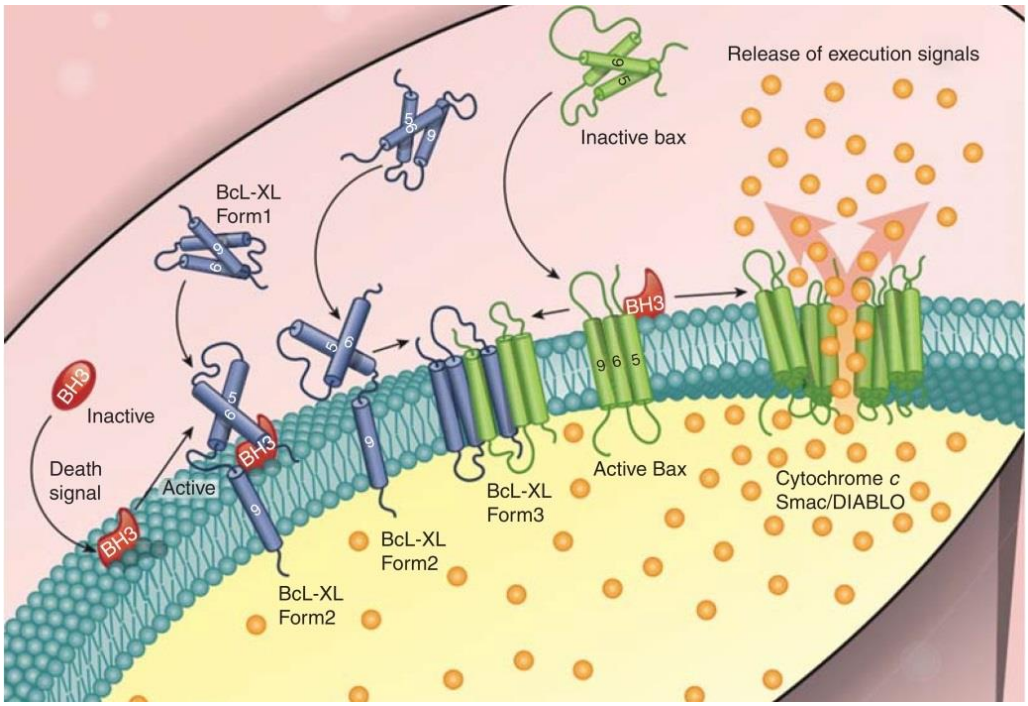

Figure I.15 *Different conformations of the protein Bcl-x_L during various stages of the induction of apoptosis. Form1: cytoplasmic/loosely attached to the MOM. Form2: helix 9 is inserted into MOM, this is thought to bind BH3-only proteins and to recruit more Bcl-x_L to the MOM. Form3: Binding of the pro-apoptotic proteins Bax/Bak. Inactive Bax undergoes a conformational change at the membrane when activated by BH3 proteins. (Figure adapted from [94]).*

Similarly to anti-apoptotic Bcl-2 family members, Bak can undergo several conformational changes, including the insertion of several helices into mitochondrial outer membranes prior to oligomerization leading to the eventual pore-formation.[109] Experiments have shown that full length Bax targets mitochondria only following conformational changes upon exposure to a death signal *in vitro*. Amino-terminal truncated Bax was observed to target mitochondria directly with no prior activation necessary.[110] The precise sequence of events leading to oligomerization and subsequent pore formation have not yet been fully resolved, however experiments using a stapled version of the BH3-protein Bim and Bax revealed a second hydrophobic pocket on Bax, opposite the canonical BH3-binding pocket. This rear-pocket is covered by the unstructured loop between helix 1 and 2. Cleaving the equivalent loop from Bcl-2 had previously been shown to convert it to a pro-apoptotic protein[107], suggesting another conserved familial trait. In the cytoplasmic form of Bax, the front-BH3-pocket is masked by α9 and Bax is monomeric and inactive. Upon activation, Bax inserts several helices including α9 into the outer mitochondrial membrane, liberating both the front and rear BH3 binding pockets.[111,112] In this state, α9 may be the displaced by transient binding of activators to the

rear pocket, which exposes the Bax BH3 region so that large pore-forming oligomers may form *via* front to front/back to back or front to back interactions of the (Figure I.16).[105,112,113]

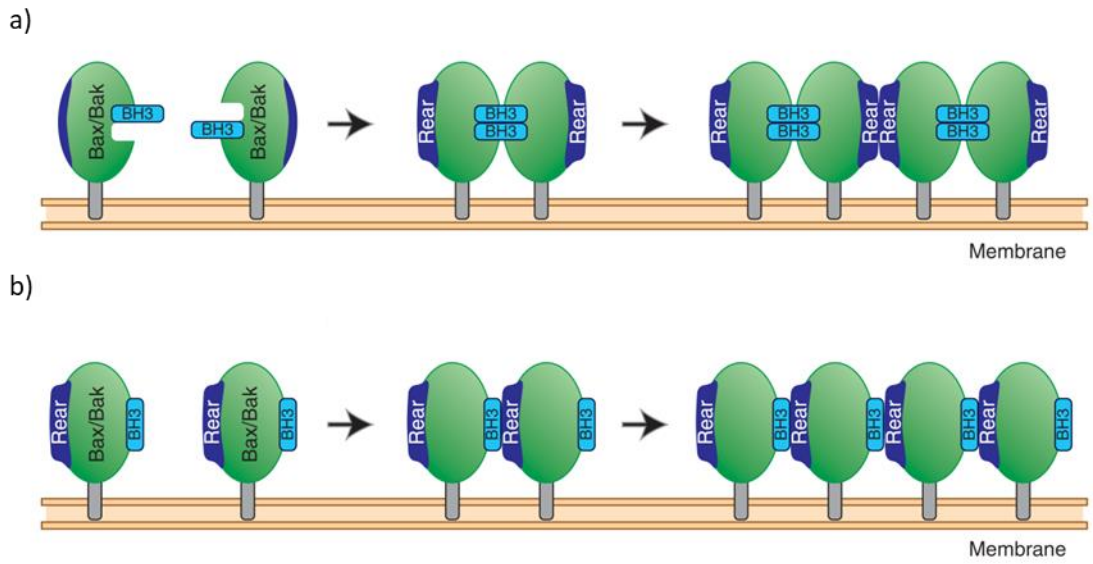

Figure I.16 *Two different models for the oligomerization of the pro-apoptotic proteins leading to pore formation. Active Bax/Bak proteins have helices embedded within the MOM leading to the exposure of their BH3-region. a) Symmetrical oligomerization: The exposed BH3-region binds into the front pocket of another Bax/Bak protein consisting of the BH1-3 groove. This in turn leads to a conformational change exposing the rear pocket enabling the propagation. b) Asymmetrical oligomerization: The exposed BH3 region of active Bax/Bak interacts with the rear pocket of an adjacent monomer. Consequent rear pocket-to-front pocket interactions lead to the formation of oligomers. (Figure adapted from [*[94]*]).*

The activation mechanism is slightly clearer for Bak, which contains a small helix instead of the more flexible unstructured loop between the α1 and α2 helix in Bax obstructing the rear-pocket position.[96] Bak is normally found in a membrane bound form, where it can form homodimers with a subsequent conformational change releasing the *N*-terminus and uncovering α6 which leads to the formation of oligomeric pores.[103,109,114,115]

With the exception of Bid, NMR experiments and calculations suggest that the BH3-only proteins are generally unstructured in the absence of a binding partner, only forming α-helices upon binding to the hydrophobic groove of anti-apoptotic proteins.[102] Additional methods such as posttranslational modifications can also be used to control BH3 binding. The BH3-only protein Bad contains two normally phosphorylated serine residues which must be dephosphorylated to allow exposure of its BH3-domain to interact with anti-apoptotic proteins Bcl-x_L and Bcl-2.[116] Bid is activated by cleavage of a long loop to a truncated (tBid), active form

which exposes >200 Å^2 previously buried hydrophobic surface, including the hydrophobic face of its BH3 region, which allows it to insert into the outer mitochondrial membrane to interact with executioner proteins.[92,93,117,118]

c. Bcl-2 Family Interaction Models

The interactions of the various members of the Bcl2-network were described in different models that have been proposed (Figure II.17).

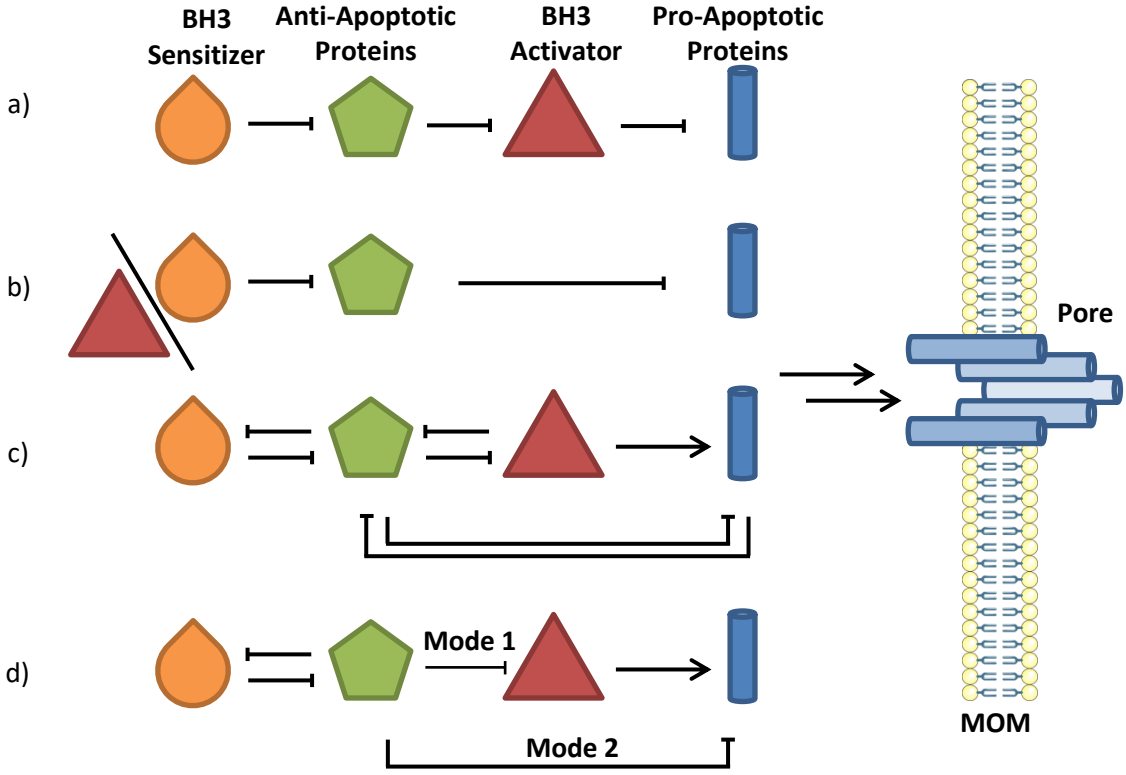

Figure I.17 *Different proposed modes of action between the Bcl-2-proteins leading to the formation of pores in the mitochondrial outer membrane (MOM). a) Direct activation model b) Displacement model c) Embedded-together model d) Unified model.*

i. Direct Activation Model

In this model, the BH3-only proteins are divided into *activators* and *sensitizers* depending on their affinity for their anti-apoptotic partner proteins. The BH3-*activator* proteins directly activate multi-region pro-apoptotic proteins, and the anti-apoptotic proteins only sequester the BH3-only proteins (and not the pro-apoptotic multi-domain proteins). The *sensitizer*-proteins liberate sequestered *activator*-proteins from the anti-apoptotic proteins and making

them available to activate the multi-domain pro-apoptotic proteins Bax and Bak. As a consequence, sensitizer proteins promote cell death only indirectly in this model. Thus, upon an apoptosis signal, the BH3-only activators are either activated through different mechanisms (transcriptional, post-transcriptional or post-translational) or released from the anti-apoptotic proteins by sensitizer BH3-only proteins. This model does not involve any direct inhibition of Bax and Bak by anti-apoptotic proteins. In this model tBid, Bim and Puma are designated *activator* proteins (although Puma has been described as sensitizer too) with Bad and Bmf acting as sensitisers for Bcl-2, Bcl-x_L and Bcl-w, with Bik and Hrk sensitisers for Bcl-x_L, Bcl-w and A1 and Noxa sensitisers for Mcl-1 and A1 only.[94,96,103,119]

ii. Displacement Model

This model postulates that the pro-apoptotic proteins Bak and Bax are constantly active and therefore have to be sequestered by the anti-apoptotic proteins to ensure cell survival. In order to induce apoptosis, the pro-apoptotic multi-domain proteins have to be released from these complexes by BH3-only proteins. As the BH3-only proteins function solely as liberators of Bax and Bak from the anti-apoptotic proteins, no further classification of the BH3-only proteins into *activators* and/or *sensitizers* is necessary. This model is sometimes also referred to as the *indirect activation* model. As the different BH3-only proteins have different binding affinities to the various anti-apoptotic proteins,[96,120] the correct combination of BH3-proteins is required for optimal release of Bak and Bax and for MOMP to occur. BH3 peptides derived from Bak and Bax have shown to form complexes with anti-apoptotic proteins, underlining their likely ability to form complexes with anti-apoptotic proteins.[121] Tentative evidence for a latent active form of Bak and Bax were obtained from cells lacking Bim or Bid undergoing apoptosis, hinting that the displacement model might not be enough to describe all actions that take place leading to apoptosis. However, other methods of triggering the apoptosis pathway cannot be ruled out.[122]

iii. Embedded Together Model

While the *direct-activation* and *displacement* models only consider solution phase affinities of the various participants, the *embedded together* model attempts to account for how sequestration of various species into membranes might influence their interactions. As previously discussed, proximity to a membrane is believed to allow access to additional

conformations, further complicating the situation. In this description, activator and sensitizer BH3-only proteins can recruit and activate anti-apoptotic proteins on the outer mitochondrial membrane (i.e., Bcl-x_L Form 2, Figure I.15). In turn, anti-apoptotic proteins can sequester both the BH3-only proteins and the pro-apoptotic multi-domain proteins Bax and Bak in the membrane. Similar to the *displacement model*, this model involves sensitizer BH3 proteins displacing both the activator BH3-only proteins and Bax or Bak from complexes with membrane-bound anti-apoptotic proteins. As only the activated forms of the pro-apoptotic proteins are in complex with the anti-apoptotic proteins, the BH3 sensitizer proteins release Bax and Bak conformers that are able to oligomerize and pore-formation. Activator BH3 proteins can activate the pro-apoptotic proteins leading to their insertion into the membrane and subsequent oligomerization.

As a consequence, the *embedded together model* can be seen as a combination of both previous models, which also takes the interactions of the proteins on the membrane into account. For example, it has been found that the first step of the Bax activation is the binding of tBid onto the membrane whereupon it causes cytosolic recruitment of Bax and its several conformational changes leading to the eventual oligomerization and pore formation (*direct activation*).[96,108,123] The anti-apoptotic protein Bcl-x_L can sequester both membrane bound tBid, preventing it from recruiting Bax from the cytosol, and membrane-bound, activated Bax but both these interacting complexes are prone to disruption by BH3-sensitizers (*displacement model*).[104,124]

iv. Unified Model

The *unified model* builds on the *embedded together* model, but makes a distinction between the inhibition of the activator BH3-proteins by anti-apoptotic Bcl-2 members (Mode 1) and the inhibition of activated Bax and Bak (Mode 2). This model considers the inhibition of Bax and Bak by anti-apoptotic Bcl-2 members to be the more effective, so that e.g., tBid, is more easily displaced by a sensitizer molecule leading to eventual MOMP. The consequence of these interactions are that cells with a high, but inactive activator BH3-protein load where these molecules are held in check by an elevated level of anti-apoptotic proteins, a situation previously described in the literature as cells being *primed for death*, are actually less susceptible to apoptotic stimuli than less stressed cells. This occurs because upon the elevated levels of anti-apoptotic proteins initially engaged in Mode 1 inhibition provide a buffer to continue more effective Mode 2 inhibition even against greatly elevated levels of competing

activator BH3-proteins as they form lower-affinity complexes.[125] This mechanism allows anti-apoptotic protein expression levels to be tailored to the level of stress a cell should receive, whilst maintaining apoptotic competence to combination of stimuli to a sufficient level. The *unified model* uses this distinction to explain changes in mitochondrial morphology, with mitochondrial fusion and fission, usually positively regulated by Bax and Bak, affected by the presence of Mode 2 complexes whereas Mode 1 complexes are suggested to have little effect on the mitochondrial morphology.

d. BH3 Protein Domain Inhibitors

i. General Considerations

In cancer cells, deregulation of apoptosis mostly affects the signalling pathways upstream of Bax/Bak activation,[126] with half of all cancers protected against death signals due to aberrant overexpression of anti-apoptotic proteins.[127,128] However, since the downstream apoptotic machinery widely remains unaffected, much effort has been focussed on restoring the function of this latter stage of the apoptotic machinery. Restoration of apoptotic function might be achieved either by direct activation or up-regulation of pro-apoptotic Bcl-2 proteins or by decreasing the effective level of anti-apoptotic proteins through inhibition or displacement to achieve indirect activation. As previously described, the BH3 regions play a key role in defining the PPI networks, so a common approach is to use BH3-mimics that bind to the hydrophobic groove of the anti-apoptotic proteins with high affinities.[129] However, the variety of affinities of specific members to each other within the Bcl-2 family and the individual nature of tumours makes it difficult to predict the response of a cancer cell to a given BH3 mimetic. Peptides corresponding to the BH3 region of several key proteins are therefore used to profile the dependency of a tumour on individual anti-apoptotic proteins (*BH3 profiling*). By observing the MOMP and apoptosis initiation these experiments can be used to identify how responsive the tumour is to a specific BH3 peptide. BH3 peptides derived from Bim and Bid interact strongly with all anti-apoptotic proteins and can also activate the pro-apoptotic effectors Bak and Bax, allowing them to be used as a reference. In contrast, sensitizer BH3 peptides bind strongly only to specific anti-apoptotic proteins and not to effectors, with Noxa being selective for Mcl-1 and Bad binding only Bcl-2 and Bcl-x_L. BH3 profiling has shown that while some tumours are highly dependent on specific anti-apoptotic proteins, such as the chronic lymphocytic leukemia (CLL) and Bcl-2 protein[130] or T-cell acute lymphoblastic leukemia and Bcl-x_L,[131] most display a heterogeneous anti-apoptotic dependence. By using a fluorophore

capable of detecting MOMP, *dynamic BH3 profiling* (DBP) aims to detect the earliest indications of apoptosis. This technique can be applied directly to patient samples, which are split and treated first with candidate chemotherapeutics, then panels of pro-apoptotic BH3-derived.[132] Changes in response to BH3 peptides to cells that have received particular drugs uncover additional *apoptotic priming*, which would indicate a suitable treatment and inform clinical decisions.

ii. Small Molecule Inhibitors

Targeting PPIs with small molecules is often very challenging due to the flat and rather featureless interface of the proteins. Solution structures of a Bak-derived peptide bound to Bcl-x_L revealed the peptide bound in a deep hydrophobic groove, potentially druggable by small molecules.[133] HA 14-1 (**1**, Figure I.18) was the first small molecule identified to inhibit Bcl-2 and discovered using computational modelling. Compound **1** disrupts mitochondrial functions and leads to cytochrome c release at micromolar concentrations by displacing Bax from Bcl-2.[134] It induced apoptosis in a number of tumours and enhanced apoptotic response to common anti-cancer agents and γ-irradiation.[129] Several other series of small molecules suggested to disrupt the interface of the anti-apoptotic proteins have been found to actually induce apoptosis in a Bax/Bak independent fashion, suggesting that the cell death occurs through an unidentified other mechanism and not *via* the mitochondrial pathway.[135]

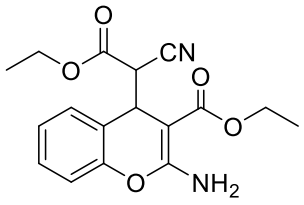

1

HA 14-1

Figure I.18 *Structure of the first small molecule found to inhibit Bcl-2.*

ABT-737 (**2**, Figure I.19) is a very specific inhibitor of Bcl-2 and Bcl-x_L that was developed by Abbott Laboratories in 2005. The hydrophobic binding groove of Bcl-x_L was divided into two smaller halves and molecules were synthesized targeting each one of them (*fragment based drug discovery*). The resulting lead compounds were chemically linked, then further chemically optimized in order to achieve higher affinities for the anti-apoptotic proteins. This approach

yielded one of the most potent and specific inhibitors, with nanomolar affinities for Bcl-2, Bcl-x_L and Bcl-w, but poor binding to Mcl-1 and A1. Mechanistically, ABT-737 shows similarities to the BH3 domain of sensitizer Bad, is able to disrupt the complex of Bax and Bcl-2 but does not bind directly Bax.[136] The apoptotic effects of this compound are completely abrogated in Bax and Bak deficient cells, indicating that ABT-737 acts as a true BH3 mimic and apoptosis occurs *via* mitochondrial pathways.[135] However, ABT-737 was found not to be bioavailable after oral administration, which led to the development of the orally available analogue ABT-263 (**3**).[137] ABT-263 entered phase 1 and 2 clinical trials for solid tumors and CLL and was found to inhibit the action of Bcl-2, Bcl-w and Bcl-x_L. However, a decrease in platelet count (thrombocytopenia) was observed when **3** was tested *in vivo*, a side effect linked to the Bcl-x_L inhibition which limited its general clinical usefulness.[133] As thrombocytopenia-related issues can be mitigated with appropriate dosing, several studies have been carried out and more are ongoing to evaluate the safety of **3** for use in combination with other anti-cancer agents.[138,139]

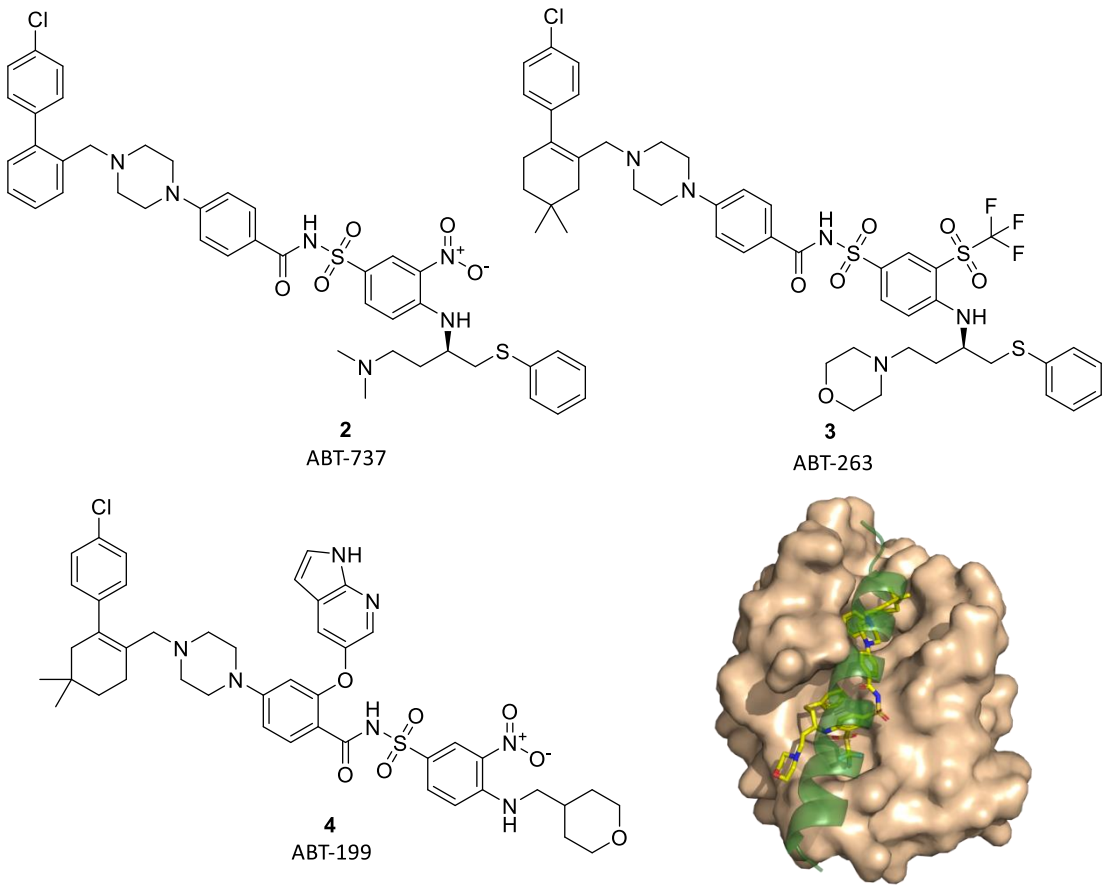

Figure I.19 *The ABT-series and Bcl-x_L. The BH3-domain of Bax is shown together with ABT-263 in the hydrophobic groove of Bcl-x_L in order to illustrate the binding location. (PDB: 4LVT (ABT-263 in Bcl-x_L), 2XA0 (BAX-peptide in Bcl-x_L)).*

ABT-199 (**4**) is a different analogue based on the same lead-compound designed to selectively target Bcl-2 to avoid thrombocytopenia. It binds to Bcl-2 10-fold more tightly than ABT-263 and has 5000-fold selectivity for Bcl-2 over Bcl-x_L as it makes additional contacts outside the major binding groove (Figure I.19). In clinical trials **4** was occasionally so effective that it caused tumor lysis syndrome, where a large number of cancer cells were killed at once, in some CLL patients. Response rates were more than 80% and secondary effects were deemed controllable[133] leading to **4** being the first FDA BH3-mimic approved for cancer treatment (CLL patients with 17p chromosomal deletion) in 2016. It is now available under the name *venetoclax* and there are many ongoing studies for its application in combination with other cancer drug treatments although results in solid tumors have not been promising so far.[132,140] Further selective BH3-mimetic drugs can be expected soon, particularly as pre-clinical experiments showed an increased expression of anti-apoptotic Mcl-1 when drugs target Bcl-2/Bcl-x_L meaning additional selective inhibitors could be required.[132,140]

iii. Peptide Based Inhibitors

Any BH3-domain peptide sequence should theoretically be able to mimic BH3-only proteins and *in vitro* assays have shown that short BH3-peptides can disrupt the interaction between the pro-apoptotic and anti-apoptotic proteins of the Bcl-2 family and to induce Bax/Bak oligomerization leading to subsequent cell death through apoptosis.[103] However, to date, no BH3-peptide drug has been approved by the FDA. Despite their affinity and specificity advantages, peptides derived from the full length proteins suffer from significant drawbacks, such as a low bioavailability, metabolic stability and unfavourable pharmacological characteristics (see chapter I.1.b.).

As for most peptides, unmodified BH3 peptides are not readily taken up by cells, but uptake can be improved by linking the peptide sequence to a cell-penetrating-peptide sequences (CPP). CPPs are short peptide sequences (up to ~30 amino acids) that are able to penetrate cell membranes and can be used to translocate cargoes inside the cell. The majority contain a high density of residues with positively charged side-chains, though amphipathic CPPs also exist. The mechanism by which CPPs facilitate uptake is not yet fully understood, appearing to vary depending on the cargo, cell line, mode of linkage between CPP and cargo (covalently bound or an electrostatic admixture) and the concentration of the CPP-cargo complex. Most likely, cellular uptake of CPP-cargo complexes involves a combination of several endocytosis

mediated pathways (e.g. clathrin mediated, caveolae mediated, macropinocytosis). The first CPP was discovered when it was found that the TAT transactivator protein of the Human Immunodeficiency Virus (HIV) was able to enter human cells. This was followed by the observation that other proteins, such as the α-helical homeobox domain of the antennapedia protein of *Drosphila* were also able to translocate through human cellular membranes.[141,142] Several different CPPs have been fused to peptides derived from the BH3-only proteins studies.; Lutz and co-workers fused a CPP derived from the antennapedia protein (Ant) to Bak BH3-peptide and could observe BH3-mediated apoptosis in HeLa cells.[143] Mutation of key hydrophobic residues of the BH3 peptide abolished its ability to induce cell death, in line with the expected interaction with anti-apoptotic members of the Bcl-2 family. BH3-mediated apoptosis was also blocked by exposing cells to caspase-inhibitors, strongly suggesting that apoptosis is achieved through the mitochondrial pathway. Comparative studies using the CPPs Ant and octa-arginine (R8) fused to the N-termini of Bad, Bax and Bak BH3-peptides on head and neck squamous cell carcinoma (HNSCC) cells revealed that Ant-conjugated peptides were generally more effective at killing HNSCC cells despite R8 more effective than Ant when the CPPs alone were tested. The Ant-Bad peptide yielded superior apoptosis induction to the Ant-Bax and Ant-Bak counterparts.[144]

A different approach to BH3 inhibitors is the application of foldamers. Gellmann and co-workers created oligomers containing α- and β-amino acids residues that are able to mimic the sidechain placements of α-helical peptides to bind tightly (2 nM) to Bcl-x_L whilst exhibiting improved metabolic stability (Figure I.20). Further patterns alternating the α- and β-amino acids in the peptide sequence were tested and indicated that even αααβ-combinations offer improved stability against proteolytic degradation whilst retaining tight binding to Bcl-x_L.[54,145,146]

Another chemical modification used to improve the properties of BH3 peptides is the introduction of chemical staples to maintain an α-helical conformation of the peptide chain. This aims to reduce the entropic cost of folding into an α-helix, improving the free energy of binding but stapling can also improve pharmacological properties. A stapled Bid-derived peptide showed improved performance *in vitro* and *in vivo* compared to its unmodified analogue with an enhanced resistance to metabolic degradation, higher affinity to the anti-apoptotic proteins of the Bcl-2 family, and an improved ability to penetrate cellular membranes. Stapled Bid peptides induced apoptosis *in vivo* through the direct activation of Bax in leukemia cells.[147,148] This technique will be explored in more general terms in the next section.

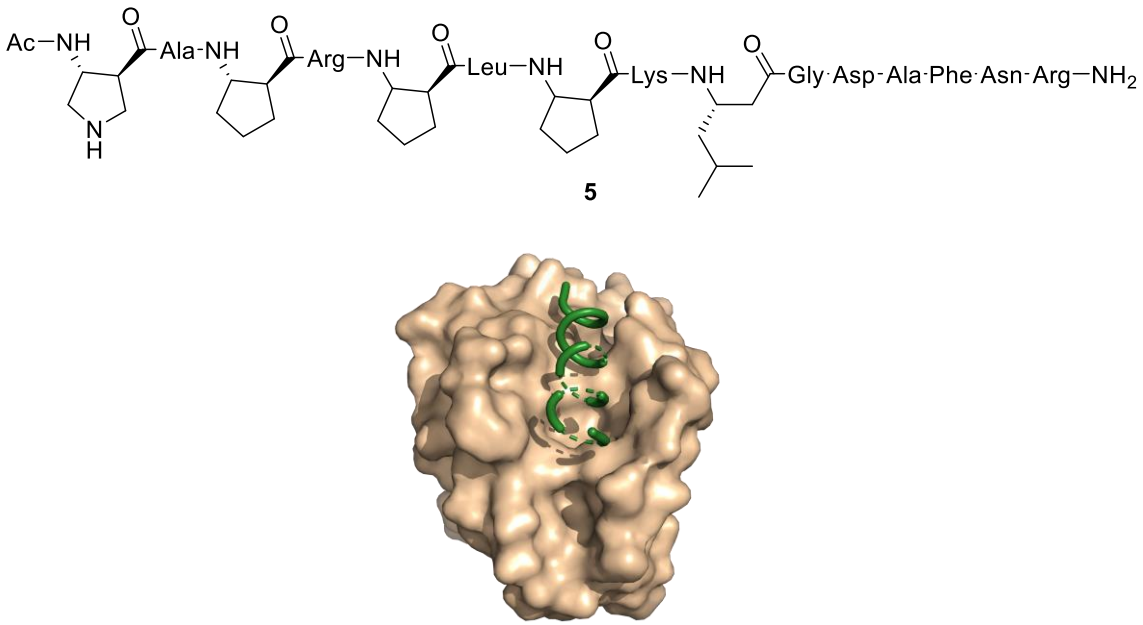

Figure I.20 *The foldamer **5** used by Gellman and co-workers that can mimic α-helical motifs and bind to Bcl-x_L in the hydrophobic groove at 2 nM. (PDB: 3FDM)*

3. Stapled Peptides

a. General Considerations

The α-helix is a very common structural motif that plays a crucial role in many PPIs. As a consequence, methods to mimic α-helical motifs to manipulate PPIs are of widespread interest. Unfortunately, peptides derived from helical regions of proteins are often unstructured, reducing their binding affinity and increasing their susceptibility to proteolytic degradation whilst reducing their membrane permeability. Methods to restore structure to short peptides are therefore keenly sought.[56]

One technique to stabilize loose, linear peptides is to apply a chemical staple between two residues of the sequence, restricting the distance between these residues to reinforce a particular overall conformation. On average, 3.6 amino acids make a turn in an α-helix,[149] so that residues in *i*,*i*+4, *i*,*i*+7, *i*,*i*+11 relationships lie on the same face of the helix (Figure I.21). These pairs of residues can be substituted for non-native amino acids that are then either linked directly together or offer orthogonal reactivity to natural residues apply a chemical *staple*.

BH3 (Bax): *H_2N*-LKRIGDELDS-*OH*

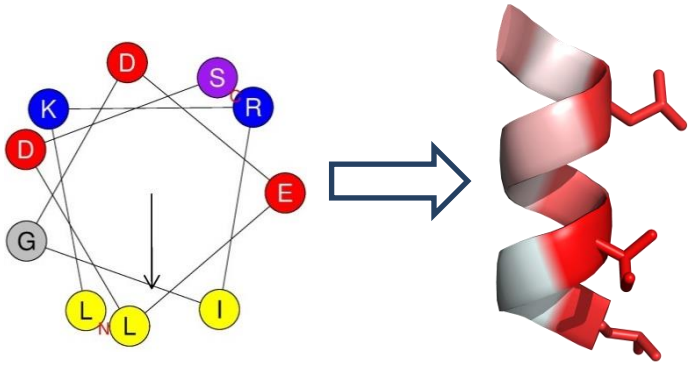

Figure I.21 *Helical wheel depiction of the BH3 region of Bax and the same sequence as an α-helical structure. The arrow in the helical wheel indicates the overall hydrophobicity. The hydrophobic residues Leu and Ile are on the same side of the interface and are marked in red in the alpha helical structure. (PDB: 2XA0).*

Peptides corresponding to individual structural elements may display a significantly lower solubility compared to the full-length protein and attachment of a covalent linker between two polar amino acid residues may further diminish the solubility or lead to aggregation issues, depending on the type of linker. Therefore, peptide sequences may need to be altered in order to decrease the overall hydrophobicity. The position of the staple is usually of great importance and oriented away from the binding interface,[45] but this does not always guarantee that they do not affect binding.[150,151] The introduction of a staple at a given position on the peptide sequence does not guarantee structural reinforcement or enhanced α-helicity, nor is enforced helicity necessarily a guarantee of improved biochemical or biological activity. However, in some cases the stabilization of α-helices using covalent staples has led to promising drug-candidates.

b. Stapling Techniques

Several different macrocyclisation strategies to introduce a chemical staple between two amino acid residues have been reported, falling into two general categories; one-component and two-component reactions. One-component stapling occurs through the formation of a direct intramolecular bond between two amino acid side-chains. As the reactive side-chains are already present in the peptide sequence, selective deprotection strategies may be required during SPPS if the reactive functionalities are not unique within the peptide. Two-component reactions involve an addition of a bi-functional linker that forms covalent bonds with both

reactive side-chains in a stepwise fashion to form a macrocycle. This stepwise reaction makes two-component reactions more prone to by-product formation, potentially including polymerization if the reaction is carried out under insufficiently high dilutions (Figure I.22). The main-advantage of this strategy is that a diverse range of similarly reactive linkers can be introduced to a single parent peptide rather than preparing numerous peptides containing a range of non-native amino acids *via* SPPS for intramolecular cyclisation.[56]

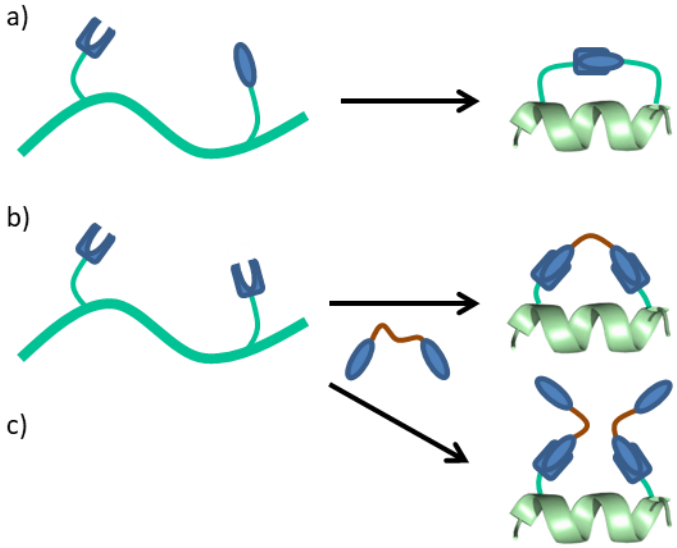

Figure I.22 *a) One-component stapling vs b) two-component stapling. The bi-functional linker used for the two-component stapling reaction bridges two side-chains together but can lead to side-product formation (c).*

Perhaps the most successful approach to introduce staples into a peptide sequence is through a ring-closing metathesis (RCM) reaction resulting in *all-hydrocarbon* linkers (Figure I.23a). Residues bearing olefinic side-chains must first be introduced *via* SPPS before carrying out the RCM reaction. Advantageously, RCM-catalysts such as Grubbs I or Grubbs II can be applied directly to resin-bound peptides allowing straightforward purification. Amino acid pairs suitable for *all-hydrocarbon*-stapling peptides have been reported for *i,i* + 3/4/7 spacings, with subsequent RCM resulting in a compact, robust and relatively innocuous staple. However, a crystal structure of a hydrocarbon-stapled p53 peptide showed that the staple in fact engaged in hydrophobic interactions with the binding site.[150] Other peptides have proved more successful, with Aileron Therapeutics completing the first clinical trial of ALRN-5281, a growth hormone releasing hormone (GHRH) agonist for metabolic disorders, in 2013.[45] Several other

stapled peptides are currently in clinical trials, including ALRN-6924, a stapled peptide mimicking the p53 tumor suppressor protein.[152,153]

Macrolactamisation reactions between the sidechains of ornithine or lysine and aspartic or glutamic acids were amongst the first techniques applied in order to reinforce α-helical structures in peptides (Figure I.23b). Coupling agents, such as dicyclohexyl carbodiimide (DCC) and diisopropyl carbodiimide (DIC) or benzotriazol-1-yl-oxytripyrrolidinophosphonium hexafluorophosphate (PyBOP), are normally necessary to drive the condensation to completion. The first successful examples applied this technique to the stabilization of peptides derived from growth hormone releasing factor *via* the sidechains of lysine and aspartic acids residues in an $i,i+4$ relationship.[154] Whilst the amino acids necessary for the lactam stapling are usually much easier to obtain and to introduce into the sequence compared to other techniques, orthogonal protecting groups are required during SPPS to allow selective deprotection of the particular pair of amine and acid functionalities to be lactamised. Additionally, only $i,i+4$ staples are feasible using lysine and aspartic acid, with larger macrocycles requiring modified amino acids with longer side-chains. Numerous examples of lactam staples exhibit enhanced α-helicity and proteolytic stability compared to their linear precursors, despite the macrolactam being less biologically inert than hydrocarbon stapled peptides.[56] Two-component lactamisations can also be carried out using bi-functional linkers.[155]

The archetypical 'Click'-chemistry copper (I) catalyzed 1,3-dipolar cycloaddition reaction is well suited for bio-orthogonal ligations and has been used to staple amino acid side-chains to form cyclic peptides under very mild conditions (Figure I.23c).[156,157] In order to create a linkage, two non-proteogenic amino acids bearing an azide group and an alkyne group respectively are introduced into the sequence. Studies on a model peptide based on parathyroid hormone-related peptide revealed that for a residue spacing of $i,i+4$, five or six methylene units in the staple are needed in order to enforce α-helicity, whilst other lengths led to irregular secondary structures.[158] This chemistry can be applied for two-component coupling too using double-click linkers. Two azidoornithine residues were introduced into a p53-MDM2 interaction inhibiting peptide in a $i,i+7$ spacing and were then reacted with molecules containing two alkyne functionalities to create a library of functionalized linkers. Cellular uptake was achieved in addition to p53 activation using a linker bearing cationic arginine groups.[157]

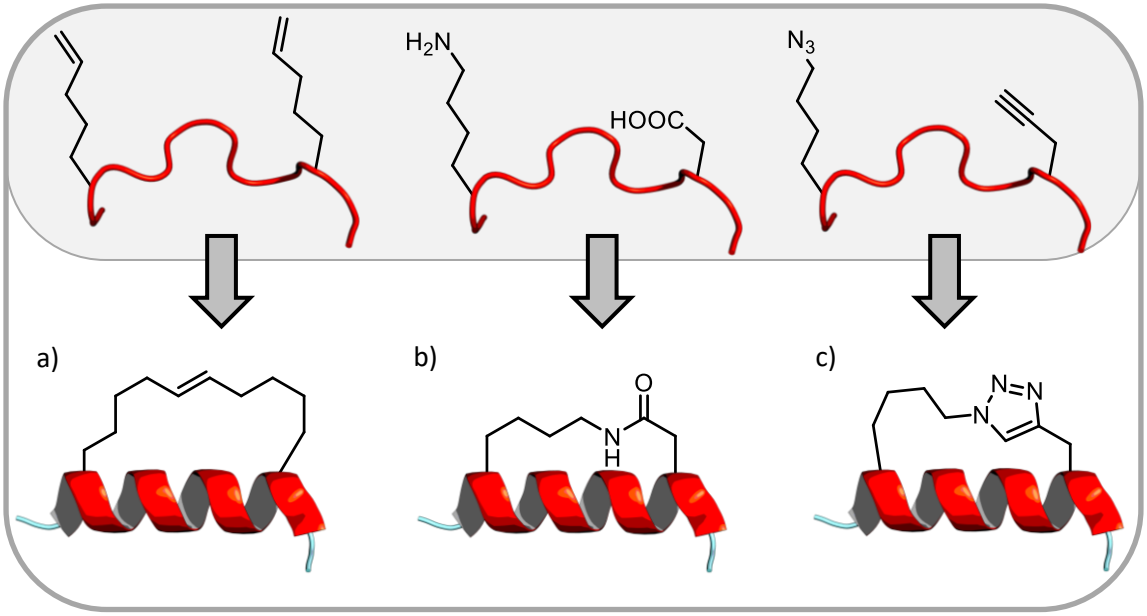

Figure I.23 *Different one-component stapling-techniques to enforce α-helicity in peptides. a) Ring-closing metathesis (RCM) reaction, b) Macrolactamisation reaction, c) Copper(I) catalysed 1,3-dipolar cycloaddition reaction ("Click-reaction").*

Disulfide bridges formed between the sidechains of two cysteine residues can be used as a highly biomimetic staple (Figure I.24e). Cysteine bridges play an important structural role for many proteins and are easily formed by the oxidation of the thiol groups of two spatially proximal cysteine sidechains. Many protecting groups exist for cysteine side-chains allowing a large degree of orthogonality against other common protecting groups. Numerous macrocyclic peptides containing more than one disulfide bridge have been synthesized applying a strategy that involved stepwise deprotection of specific cysteines followed by their oxidation.[159] Disulfide bridges are resistant to acidic and oxidizing environments, making it possible to form the linkages prior cleaving the peptide from the resin using strong acids. However, unlike natural disulfide bonds that are often buried in protein structures, those in short peptide chains are often exposed to the surrounding environment leaving them prone to reduction. This is a major limitation, particularly as the cytosol of cells is a reducing environment.

An alternative approach to harnesses the reactivity of thiol groups is the formation of thioethers. Under modestly basic conditions (pH 8), cysteine side chains readily react with α-bromo amide groups to form thioethers (Figure I.24c). This chemistry has been used to form in *i,i* + 3 and *i,i* + 4 staples by an intramolecular reaction, although it was suggested that thioether stapling might be more suitable to improve α-helicity for shorter *i,i* + 3 spacings with lactam staples preferred for *i,i* + 4.[160] The physical properties of the linkage can be tuned by oxidation

of the thioether to sulfoxide or sulphone using either hydrogen peroxide or performic acid. Oxidation leads to increased polarity and can be used to increase the water-solubility of stapled peptides.[161] Thiols groups can also react with terminal alkyne-or alkene substituted amino acids to form thioethers *via* thiol-yne/-ene chemistry (Figure I23.a). The reaction rate is dramatically enhanced when a radical initiator is employed in order to promote the formation of a sulphide radical and the resulting linkage can also be oxidised as described above.[156,162,163]

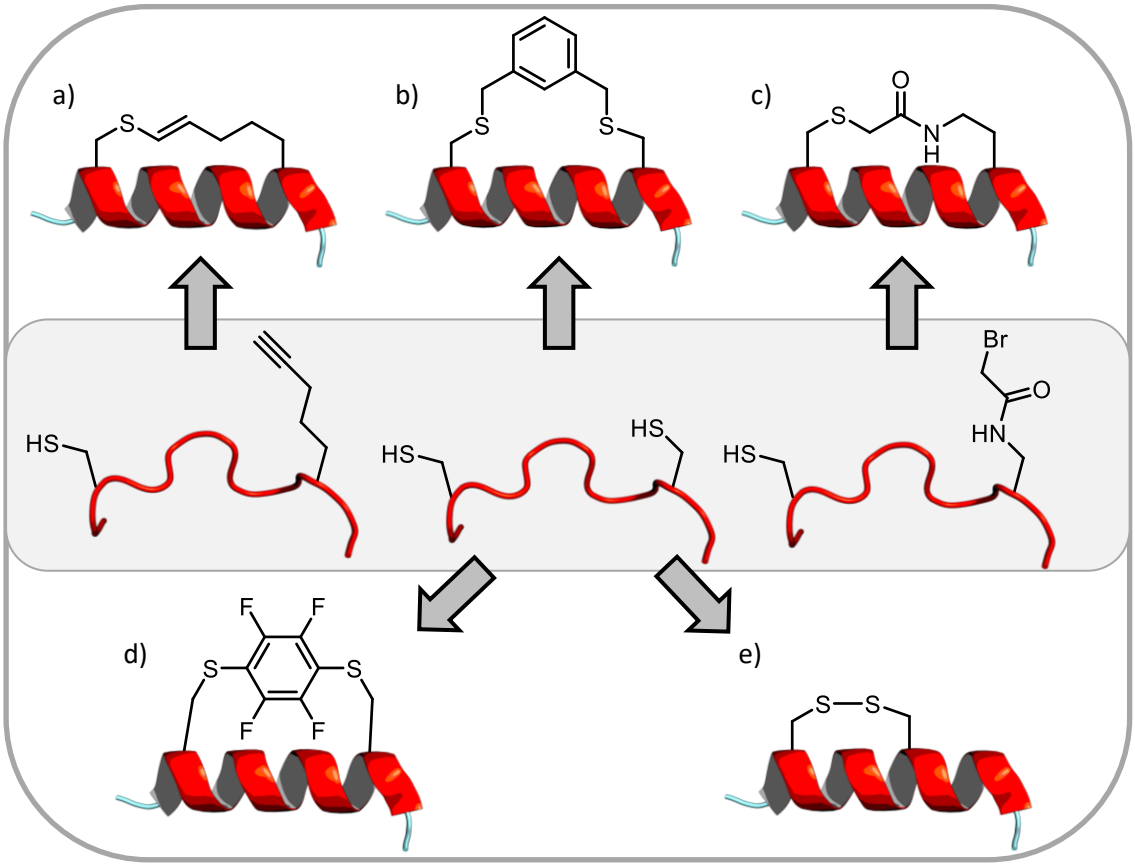

Figure I.24 *Different peptide-stapling techniques involving the cysteine side-chain. a) Thiol-yne/ene reactions, b) S_N2 reactions using benzyl-halides, c) reaction with α-bromo amide groups, d) S_NAr reactions with hexafluorobenzenes, e) disulfide-formation under oxidising conditions.*

The nucleophilicity of the thiol groups in cysteine-residues is also commonly exploited for two-component macrocyclisation reactions. Thiol-groups can be deprotonated under very mild conditions (pH ~8) to greatly increase their nucleophilicity and rate of reaction with appropriate electrophiles. Suitable electrophiles include aromatic substrates containing strongly electron-withdrawing substituents, including hexafluorobenzene where the strong

inductive electron-withdrawing effect allows two fluorine atoms to be displaced (Figure I.24d).[164] When tested on a model-peptide, this modification increased helicity, proteolytic stability, cellular uptake and improved binding. Saturated alkyl halide electrophiles are not typically very reactive towards thiolates, but benzyl- or allyl-halides react usually smoothly (Figure I.24b).[165] Staples containing haloacetamides electrophiles have also found widespread use.

Somewhat less commonly applied are stapling reactions between methionine residues and benzylic bromides, which nevertheless offer excellent functional group tolerance including even cysteine residues.[166] When various benzylic bromides were reacted with autophagy inducing peptides with *i,i* + 4 and *i,i* + 7 spaced methionines, the resulting macrocycles displayed improved proteolytic resistance and cellular uptake due to the positive charges of the resulting sulfonium ions. These ions were found not to be stable in the reducing environment of the cytoplasm, releasing the peptide.

Finally, the properties of the tryptophan side-chain, which can undergo a condensation reaction with aldehydes can also be used to form macrocycles. As tryptophans occur relatively rarely, this approach may limit by-product formation. Activation 4-bromobenzaldehyde was achieved under mild conditions using (1S)-(+)-camphor-10-sulphonic acid. High conversions were obtained for spacings up to *i,i* + 4, which was accompanied by an increased proteolytic stability. However, no increased α-helicity was observed by CD spectroscopy.[167]

c. Stapled BH3 Region-Derived Peptides

Peptides derived from the BH3-regions of the pro-apoptotic proteins of the Bcl-2 family interact more strongly with their target proteins when their native α-helical conformation is reinforced using a chemical staple.[148] Therefore, stapled BH3-peptides are thought to have potential to restore the function of the apoptotic pathway in cancerous cells. When *all-hydrocarbon* staples were applied to BH3-only pro apoptotic Bid- and Bim-derived peptides, Walensky *et al.* referred to the staples peptides as 'stabilized alpha-helix of Bcl-2 domains' (SAHBs). α,α-Disubstituted non-natural amino acids containing olefinic side chains of different lengths were incorporated at different positions into a Bid-derived peptide during SPPS and were cyclised by ruthenium catalyzed olefin metathesis. Circular dichroism showed a significant increase in helicity of the stapled variants (up to 87%) compared to the native peptide (16%), but the effect was strongly dependant on the positioning and length of the hydrocarbon tether. The SAHB displaying the highest degree of helicity was tested further,

displaying significantly enhanced proteolytic stability in mouse serum (~10-fold) and almost 7-fold stronger binding to its target protein compared to the non-stabilized peptide (K_D: 38.8 nM *vs* 269 nM). Cell uptake studies using leukemia cells with stapled and unstapled FITC-labelled Bid peptides showed cytoplasmic localization only for the SAHB. A dose dependent cytochrome *c* release was observed *in vitro* on purified mouse liver mitochondria for the SAHB at concentrations where the Bid-BH3 peptide showed negligible effects. Bak deficient mitochondria did not show any cytochrome *c* release suggesting activation of the apoptotic pathway. Moreover, the SAHB-peptide treatment consistently suppressed leukemia growth in mice models *in vivo*.[148] Further experiments revealed that Bid $SAHB_A$ directly binds to the pro-apoptotic protein Bax, the first verification of a direct interaction between Bid and Bax. The specificity of this interaction was tested using a stapled peptide derived from the sensitizer BH3 protein Bad, as expected, interacted with Bcl-x_L but not Bax.[147]

Initial results using SAHBs suggested that a combination of the presence of the staple and an overall positive peptide charge enabled cellular penetration.[168] However, other literature reports a wide range of stapled peptides that display intracellular activity with overall charges ranging from significantly positive (+3 to +5) to negative (-4).[169] A systematic study using a comprehensive library of *i*,*i* + 4 all-hydrocarbon stapled Bim BH3-derived peptides employed statistical methods to compare the biophysical parameters of various stapling positions to determine the specific properties conferring the ability to penetrate cellular membranes.[168] The overall findings were that a combination of excessive positive charge and hydrophobicity should be avoided in order to prevent non-specific cell lysis. Point mutations suggested that cellular uptake efficiency is best served by lowering the overall pI to 8.8-9.3 while maintaining hydrophobicity. Furthermore, SAHBs containing a hydrocarbon at the boundary between hydrophobic and hydrophilic faces were the most favourable, suggesting that an extension of the hydrophobic surface of the α-helix may be a critical feature. The most promising product of this study contained a staple reinforcing a crucial highly conserved part of the BH3 region containing a hydrophobic residue, a small residue and an acidic residue (XIGDX) (Figure I.25).

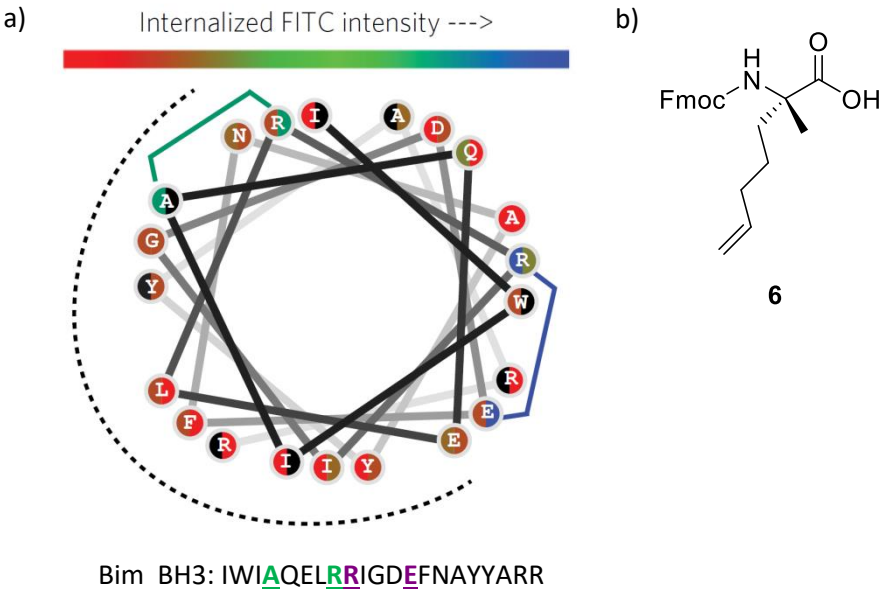

Figure I.25 *a) Wheel depiction of the stapled Bim BH3 α-helix and the wild-type sequence. The dotted line indicates the hydrophobic interaction face of the α-helix. Residues were mutated with* ***6*** *(b) and an all-hydrocarbon staple formed using ruthenium catalyzed olefin metathesis reaction. Stapled amino acid pairs are colour-coded based on the level of measured total internalized fluorescence intensity. Left and right colours correspond to the roles of the amino acids as N- vs. C-terminal staples, respectively. Extension of the hydrophobic surface by the staple resulted in strongest internalized fluorescence intensity (position of the staples indicated in the peptide sequence). (Figure adapted from [*[168]*]).*

Analysis of the binding interface of the anti-apoptotic protein Bfl-1 and the BH3 domain of the pro-apoptotic NOXA revealed a cysteine on the lip of the canonical binding groove of Bfl-1, a feature unique among the anti-apoptotic members of the Bcl-2 family. SAHB-stapled NOXA and Bim-derived peptides containing appropriately placed cysteine residues were shown to form disulfides between the peptides and Bfl-1 under oxidising conditions. Next, further peptides were constructed that instead contained a thiol reactive acrylamide to combine the selectivity of α-helical BH3 domains and enhanced binding affinity of stapled peptides with the capacity to form a covalently bonded irreversible complex (Figure I.26).[170] The peptide was synthesized and tested against wild type Bfl-1 and a mutant with the key cysteine mutated to serine. *In vitro* experiments showed no non-specific reactivity of the cysteine-reactive warhead stapled NOXA and Bim SAHBs in the presence of other cysteine-bearing proteins, underscoring the selectivity towards the cysteine in the binding groove of Bfl-1. Streptavidin pull-down experiments showed non-covalent interactions of the NOXA construct with the anti-apoptotic protein Mcl-1 together with covalent interactions against Bfl-1. In contrast to the non-modified Bim SAHB, the warhead-equipped Bim SAHB construct was able to compete with tBid for Bfl-1 indicating the effectiveness of the selective thiol reaction in driving binding equilibria. While

the NOXA construct showed only limited cellular uptake, the warhead-bearing Bim SAHB could enter A375P cells and displayed induction of higher levels of caspase-3/7 release compared to its unmodified counterpart. A subsequent crystal structure of the NOXA-peptide covalently bound to Bfl-1 revealed an induced conformational change upon binding, data that might help design more specific Bfl-1 inhibitors in future.[171]

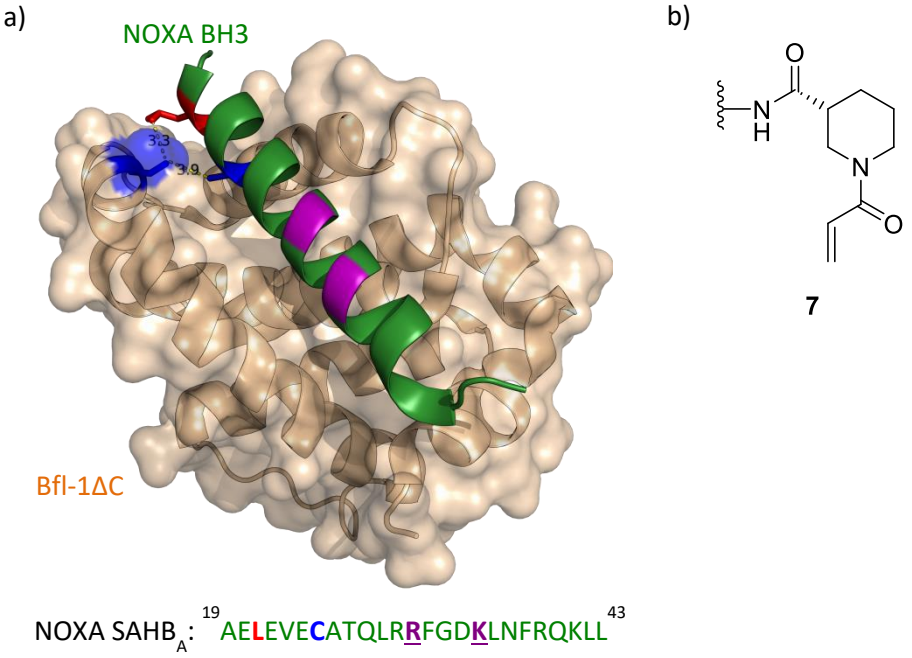

Figure I.26 *a) Noxa peptide in the binding groove of Bfl-1 containing a cysteine residue (blue). The residues mutated for the SAHB$_A$ staple are coloured magenta. Based on the distances between Cys-Cys (3.9 Å) and Cys-Leu (3.3 Å), the leucine residue in the peptide sequence (red) was later replaced with the warhead **7** (b) to obtain covalent binding to the cysteine residue in the binding groove. (PDB: 3MQP)*

A double-click approach was used to generate a library of functionalized stapled peptides for the investigation of human platelet PPIs.[172] Different functional groups were attached to a *meta*-dialkynylphenyl staple (Figure I.27e) and were assessed for platelet uptake using FACS analysis. Despite platelets being anuclear, peptides containing staples bearing a nuclear localization sequence (NLS) and oligo-arginine residues showed the highest uptake. CD experiments showed no improvement in helicity compared to the wild-type peptide, suggesting enhanced uptake is purely due to the additional functionality born on the staple. A Bim BH3-derived peptide containing a pair of azidoornithine residues was equipped with this staple *via* a double CuAAC reaction and was found to successfully trigger platelet activation.

Another recent example of stapled BH3-domain peptides utilized the reactivity of *i,i* + 4 cysteine residues towards decafluorobiphenyl to generate a series of stapled peptides that showed enhanced abilities to penetrate a spheroid model of the blood-brain barrier (Figure I.27c).[173] They found that the stapled peptides displayed improved proteolytic stability and that the penetration depth of the constructs into spheroids was significantly affected by the location of the perfluoroarene within the sequence. This stapling method was then applied to a peptide derived from the BH3-region of Bim and enhanced its ability to cross the blood-brain barrier in mice; the first reported example of increased brain-penetration by a peptide based solely on the addition of a linker.

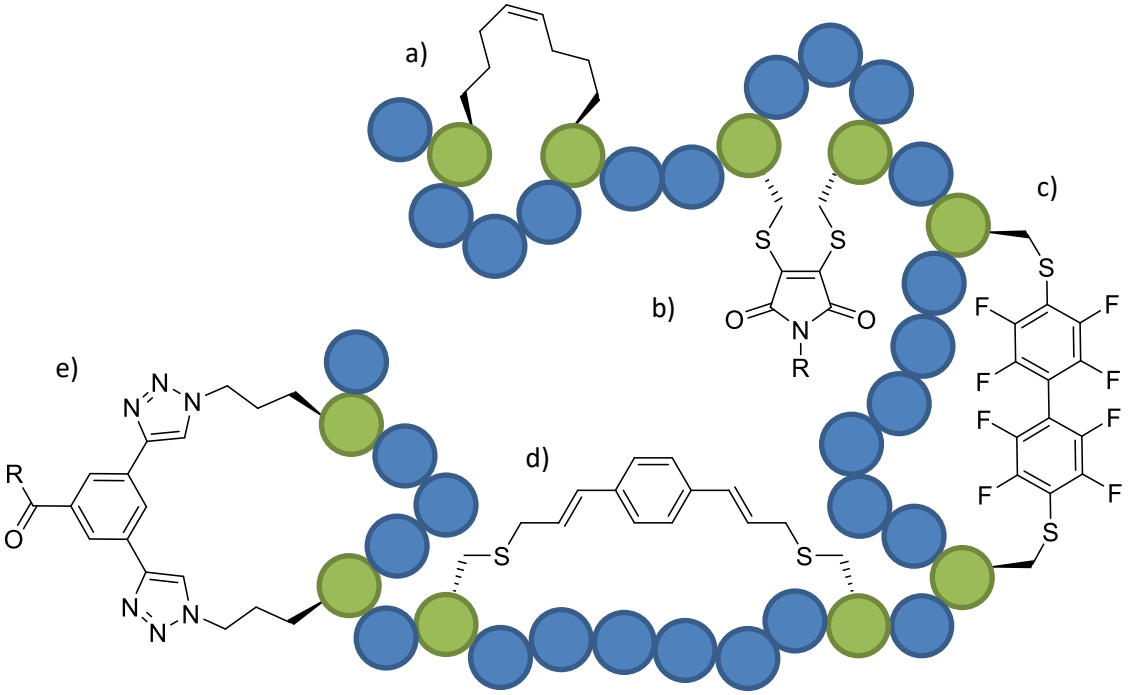

Figure I.27 *Some of the reported one- and two-component stapling strategies used on BH3 peptides. a) All-hydrocarbon staple, b) dibromomaleimide reacted with two cysteine side-chains, c) fluorophenyl-groups used in S_NAr-type reactions, d) halobenzyl and halovinylaryl compounds, e) double-click strategy.*

Dibromomaleimide can be used with cysteines and homocysteines to form a reversible staple that can subsequently be removed by excess thiols (Figure I.27b).[174] An *i,i* + 4 stapled Bid-peptide construct displayed improved α-helicity and proteolytic stability while showing significantly binding to Bcl-x_L compared to the linear peptide. Alkyne-containing dibromomaleimides were then used to conjugate other functionalities, such as fluorescein, PEG-groups and biotin to the peptide using click-chemistry.

A series of Noxa BH3 peptides containing *i,i* + 7 spaced cysteines were reacted with a range of bromobenzyl and bromovinylaryl compounds to introduce staples of varying lengths and rigidities (Figure I.27d).[175] Molecular dynamic simulations to estimate the rigidity of the constraints by the shape of their S-S distance distribution. Subsequent analysis showed that Noxa peptides bearing a staple of a similar S-S distribution compared to the S-S distance of the native helical peptide displayed the highest degree of helicity as well as the tightest binding to Mcl-1. When tested, the more hydrophobic staples yielded the most efficient uptake into HeLa cells.

4. Photo Control of Stapled Peptides

a. Principles of Photo Control

Controlling the secondary structures of peptides or proteins upon irradiation with light offers the opportunity to manipulate PPIs in a non-invasive way with high spatiotemporal resolution. In order to obtain photo control over a peptide, a responsive element needs to be attached. Photo-responsive moieties that allow the selective activation of one of two states in a reversible way can be termed *photoswitches*. Naturally photo-responsive proteins, associated with vision, phototropism, or phototaxis typically involve conformational changes of a closely associated chromophore, such as retinals in rhodopsins or *p*-hydroxycinnamic acid in photoactive yellow proteins respond to light in the visible spectrum.[176] However, these molecules are usually buried deeply into specialised host proteins in order to allow effective signal transduction. A range of other small molecules, more amenable to adding to existing general proteins or peptides are known, including spiropyrans, stilbenes, hemithioindigos, diarylethenes and azobenzenes (Figure I.28). Unfortunately, many of these molecules are most sensitive to shorter wavelengths of light, in the UV region which is non-selectively absorbed by tissue and causes damage to cells. In fact, blood supported tissues allow deep penetration (~ 20 mm) only for the wavelengths between 650-1100 nm (the 'bio-optical-window').[177] As a consequence, the development of photoswitches sensitive to visible or near-infrared light is a high priority. A number of other features also have to be considered during development of new photo-reactive switches, such as the isomeric composition of the photostationary state (PSS), quantum yields, thermal half-life time of the thermodynamically less stable isomer, fatigue resistance, stability against proteolysis and reducing environments and water-solubility.[176,178]

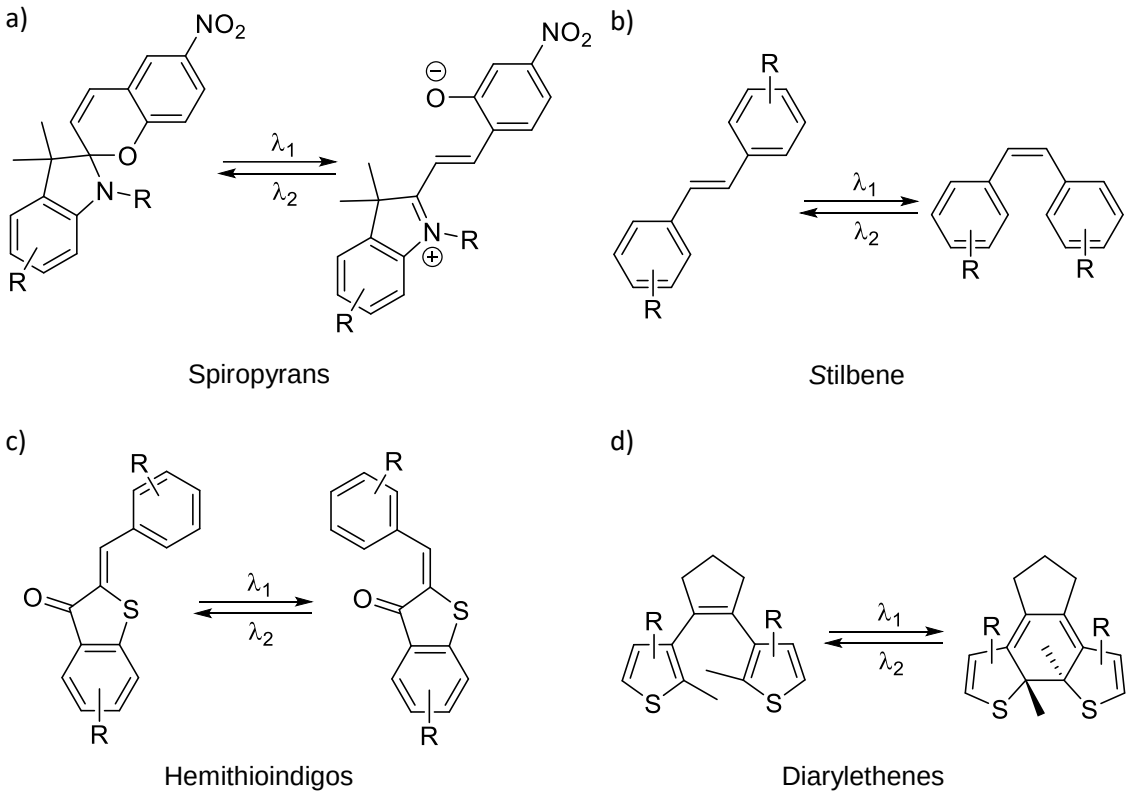

Figure I.28 *Some small molecules capable of photo-induced conformational change. a) Spiropyrans b) Stilbene c) Hemithioindigo d) Diarlyethenes, R is other functional groups.*

Three general strategies exist in order to activate photochromic compounds without the use of UV-light (Figure I.29). The first strategy involves tuning the HOMO-LUMO gap of molecules to a value which can be addressed by photons in the visible region. The most common approach to this is by extending the π-system of a known compound and hence red-shifting its absorption, although this can negatively impact solubility. The second approach utilizes a sensitizer, which is able to absorb multiple photons of long-wavelength light and transfer their combined energy to the switch. Typical sensitizers include upconverting nanoparticles, triplet photosensitizers or two-photon absorber/emitters.[179,180] While a few multi-photon photoswitches are known, organic molecules tend to have low two photon absorption cross sections and it is more common to perform indirect two-photon excitation of photoswitches *via* energy transfer from a sensitizer whose emission overlaps with the absorption band of the photoswitch. The switch and sensitizer are either physically mixed together or covalently connected to create close proximity for efficient energy transfer.[181] In the final strategy, a half-photo switch is used, where switching in one direction is achieved through redox reactions triggered either electrochemically or using a photo-induced electron transfer from or to a sensitizer. The advantage of this final class of systems is that they are not limited by overlap of the absorption

spectra of the isomers, but are thermodynamically driven leading to quantitative isomerization.[176]

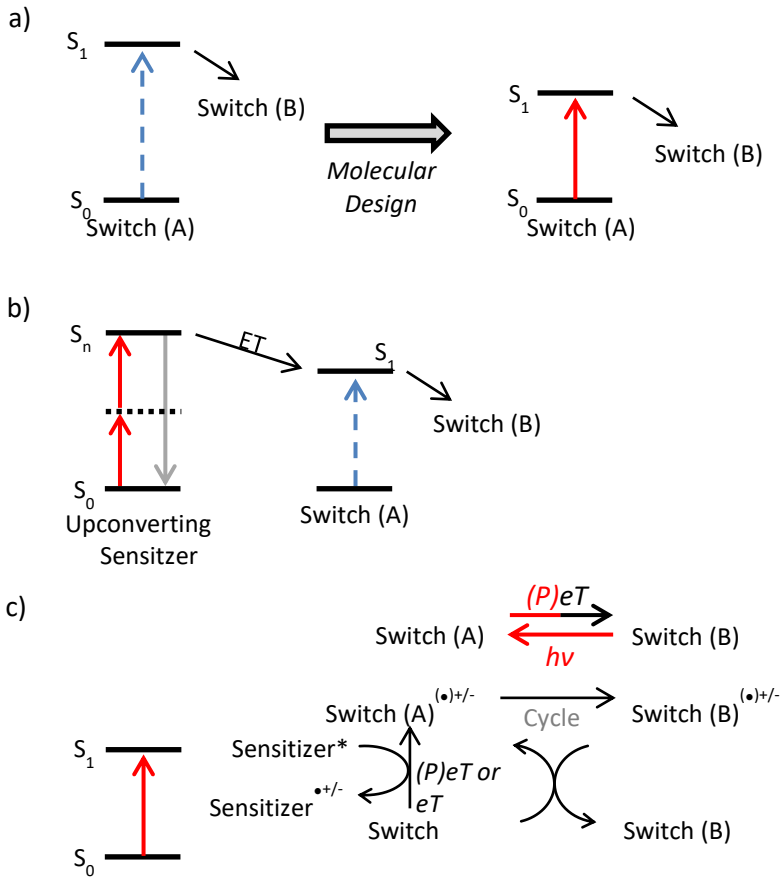

Figure I.29 *Different strategies to replace UV-light with visible light for photochromic compounds. a) Direct photoexcitation. Molecular design of the photoswitch is applied to lower the energy gap so that it can be addressed with visible light. b) Energy transfer from an up-converting sensitizer using visible light followed by an energy transfer to the switch. c) Switching via redox reaction coupled to a sensitizer, which is excited by visible light to initiate the photo-induced electron transfer. (S_0: ground state, S_1: first singlet excited state, ET: energy transfer, (P)eT: (photoinduced) electron transfer). (Figure adapted from [*[176]*]).*

b. Azobenzenes as Photochromic Compounds

i. Photo-Physical Properties of Azobenzene

Azobenzenes are among the best characterized photochromic molecules. They undergo fast photoisomerization, have a symmetric structure that allows high spatial control, a low rate of photo-bleaching and offer relatively high quantum yields with acceptable isomer ratios at their photostationary states. Azobenzenes are readily available and their synthesis can use well established synthetic aromatic chemistry.[182] The ability of azobenzene (**8**) to undergo

photoisomerization was discovered in 1937 and the two isomers were subsequently isolated by extraction utilizing their slightly different solubility properties.[183] The *trans*-isomer is almost planar and has a dipole moment near zero. One of the rings of the *cis*-isomer twists ~55° out of the plane due to the steric and electronic repulsion of the phenyl-rings, resulting in a significant increase of the dipole moment (Figure I.30). The end-to-end distance between the carbons in *para*-positions of the two rings changes by ~3.5 Å from the *trans*- to the *cis*-isomer.[178,184,185]

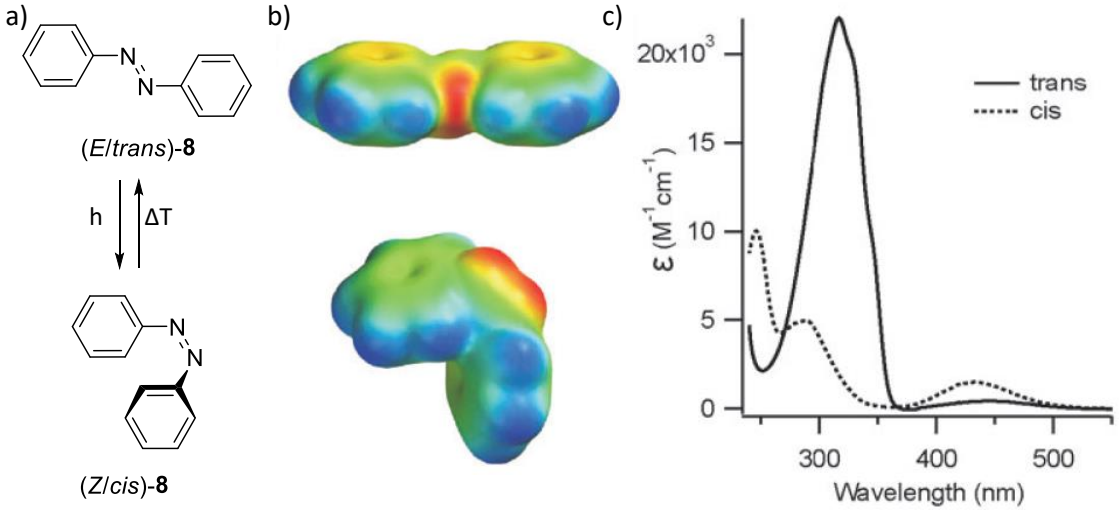

Figure I.30 *a) Structure of trans- and cis-azobenzene (**8**) with a spacefilling model of the electrostatic potential of the isomers (b). c) UV-visible spectra of the two isomers in ethanol. (Figure adapted from [178]).*

The spectra of the *cis*- and *trans*-azobenzene overlap and show distantly different strengths for their n-π* and π-π* transitions as symmetry constraints are broken by isomerisation. In ethanol, t*rans*-**8** displays a strong π-π* transition at 320 nm ($\varepsilon_{440} \approx 22000\ M^{-1}\ cm^{-1}$), whereas the *cis*-**8** shows a band at 280 nm ($\varepsilon_{440} \approx 5000\ M^{-1}\ cm^{-1}$). This trend is reversed for the n-π* transition with a stronger band shown by *cis*-**8** ($\varepsilon_{440} \approx 2000\ M^{-1}\ cm^{-1}$) than *trans*-**8** ($\varepsilon_{440} \approx 600\ M^{-1}\ cm^{-1}$). Both isomers show further bands below 250 nm. The *trans*-**8** isomer is ~10 kcal mol^{-1} more stable than *cis*-**8** and forms >99.99% of the equilibrium population in the dark. *Trans*-**8** can be isomerised to *cis*-**8** through irradiation with 340 nm light, with *trans*-**8** being regenerated either through thermal relaxation to equilibrium or irradiation at 450 nm.[178] While solvent polarity has no effect on the π-π* transition, the quantum yield of the n-π* transition driven *trans*-to-*cis* isomerization increases while the *cis*-to-*trans* decreases with

increasing solvent polarity. The quantum yield of the *trans* to *cis* isomerization is not affected by changes in temperature. However, the reverse isomerization from *cis* to *trans* shows a significant decrease in quantum yield following increasing temperatures, indicating a high dependence on thermal vibrations.[186]

Several mechanisms have been proposed for the isomerization pathway from *trans*-**8** to *cis*-**8** including rotation, inversion, inversion-assisted rotation and concerted inversion. However, the exact mechanism is still a matter of debate. [186] The potential barriers for the rotational- and inversion-mechanisms are subject to external factors including the solvent polarity and viscosity, which can favour one mechanism over the other.[187] Thermal relaxation from *cis*-**8** to *trans*-**8** is considered to proceed *via* the inversion pathway and *ab initio* and molecular dynamics simulations suggested that photochemical *cis*-**8** to *trans*-**8** conversion should proceeds through the rotational pathway**.**[186]

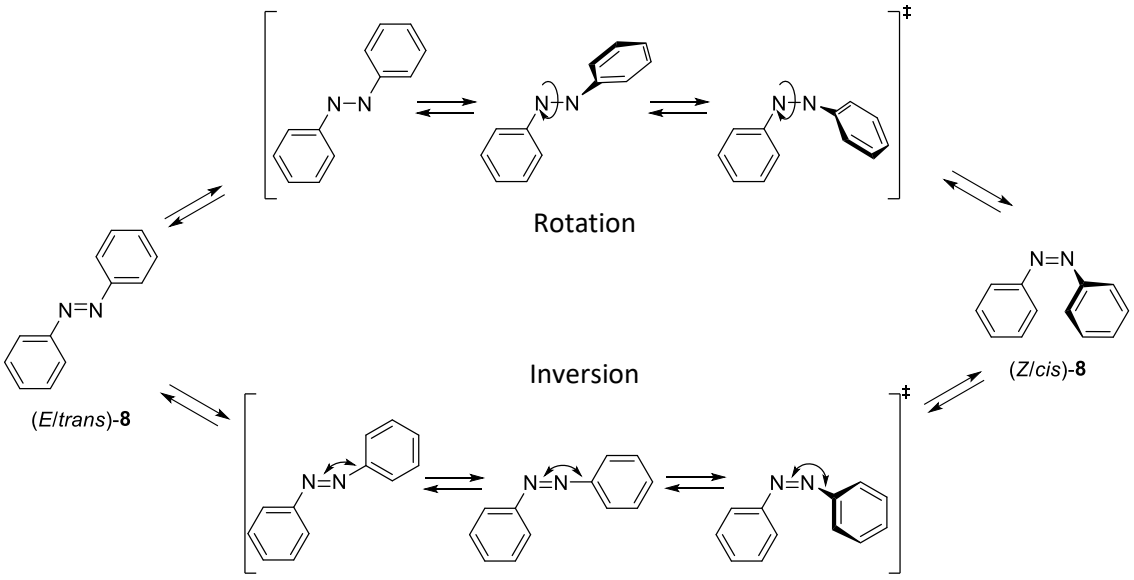

Figure I.31 *Proposed mechanisms for the trans-cis isomerization of azobenzene.*[186,188]

The *trans* and *cis*-conformations of azobenzene molecule have been modelled using the MO-theory. The non-bonding orbital can be considered as a linear combination of the lone pair orbitals of the nitrogen atoms. Excitation of an electron from the n- or π-orbitals into the anti-bonding π*-orbital, leads to a weakening of the N=N double bond character and allows rotation or inversion around the N-N axis. Both isomers show similar n-π* excitation energies due to similar shifts in the energies of the π* and n orbitals in the *trans* isomer. As the twisted conformation of the *cis* isomer reduces the delocalization of the π-electrons, the energy level of the π*-molecular orbital is increased. However, the energy of the n-orbital also increases

leading to a very similar energy gap to the *trans* isomer, resulting in overlapping absorption maxima for the n-π* transitions of the isomers. The energy gap for the π-π* transition changes more significantly in both isomers and the absorption maxima appear well separated.[189]

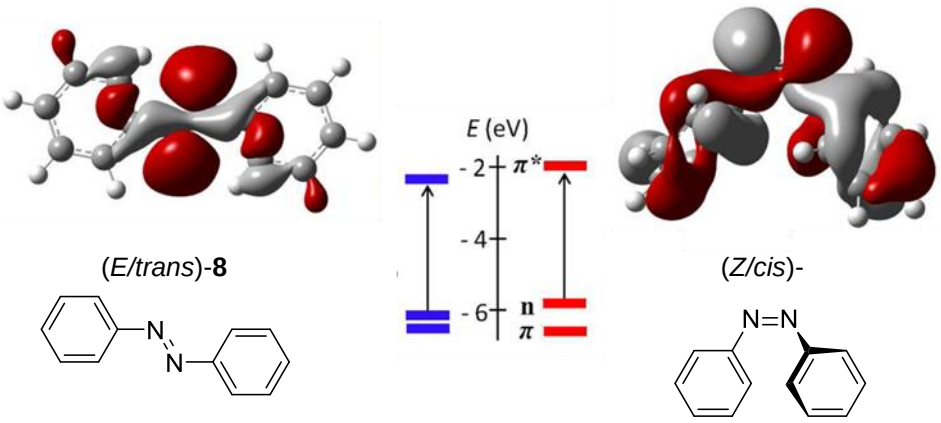

Figure I.32 *Representation of the n-orbitals (HOMOs) and energetic diagrams of the π, n and π* orbitals for the trans- and cis-isomer of* ***8****. (Figure adapted from [*[189]*]).*

ii. Refining the Photoswitching Properties of Azobenzene

Therefore, in order to apply azobenzene structures as visible light photoswitches in biological systems, the n-π* excitation bands of both isomers need to be separated. The better the separation of excitation bands, the more selective isomerization can be, avoiding photostationary states containing mixed isomers. One of the most conceptually straightforward routes to red-shifted absorption spectra is through the extension of the π-system of the photochromic switch in order to lower the HOMO-LUMO gap towards visible wavelengths.

However, extending the conjugated system can diminish the photoswitching performance.[176] One reason for this phenomenon is that an extended π-system can lead to a significantly red-shifted π-π* transition, while the n-π*transition remains mostly unaffected. In many systems, the π-π*band is used to induce *trans* to *cis* isomerization, whereas the n-π* band of the *cis* isomer is utilized to photo-revert the azobenzene back into its *trans* configuration. As a result, in systems with extended π-system, the two bands overlap and can no longer be selectively addressed. Extended systems have also been applied to peptides with larger amino acid spacings, albeit with limited success due to a lack of rigidity or poorly separated isomers at their photostationary states.[190–192]

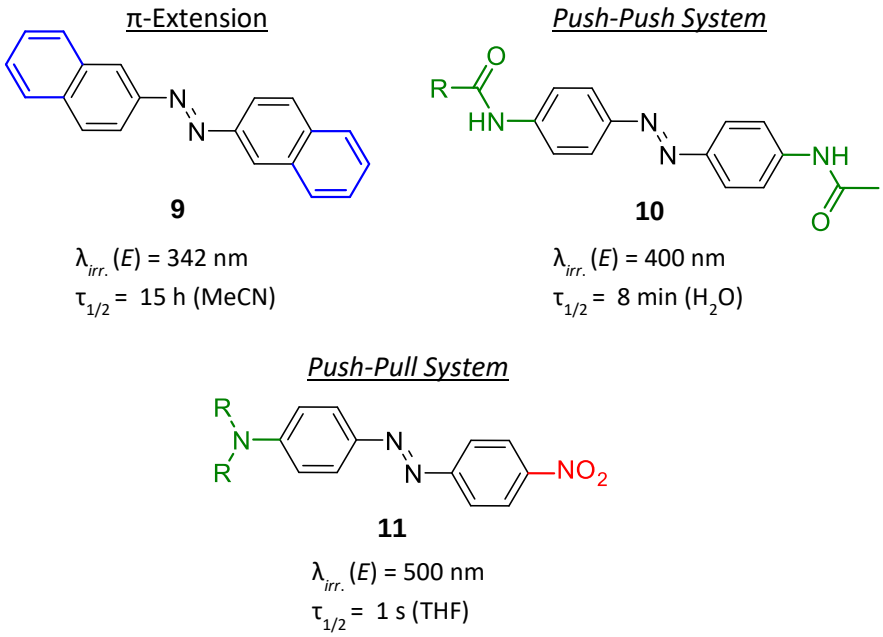

Figure I.33 *Red-shifting azobenzenes through π-extension (**9**), push-push- (**10**) and push-pull-substitutions (**11**).*

Another strategy to red-shift absorption is to introduce electron-donating (EDGs) or withdrawing groups (EWGs) in *ortho*- or *para*-position to the azo-group.[176] However, substituents can also strongly affect the thermal *cis*-to-*trans* relaxation. This effect can be rationalized by how the groups affect the single bond character of the azo-group with groups contributing to an increased dipole character lower the activation barrier for the thermal relaxation.[178] *Push-pull*-azobenzenes contain one electron rich and one electron poor ring causing the π-π* band to be red-shifted to 400-600 nm, at the cost of the thermal stability of the *cis* isomer decreasing in proportion to the strength of the electron donating/accepting substituents (Figure I.33). Typically, the π-π*and the n-π* absorption bands of *push-pull* azobenzenes completely overlap resulting in mixtures of isomers at its photostationary state, and often have *cis* isomer half-lives measured in seconds.[176] These compounds are therefore most useful in systems where little activation is needed in order to trigger an effect or where fast cycling is required.

In surveys of different moieties at the *para* position of azobenzene, a similar clear correlation between an increased electron donating ability red-shifting the π-π* absorption maxima (up to 480 nm) while significantly decreasing the half-life of *cis* isomers was observed (Figure I.34a).[178,193–195] Substituents in the *ortho*-positions can have a variety of influences, from changes in the excitation spectra caused purely by steric effects on the transition state

with alkyl substituents,[196–198] to amino substituents that cause similar red-shifting but slightly less half-life shortening behaviour as in amines the *para*-position (Figure I.34b).[199]

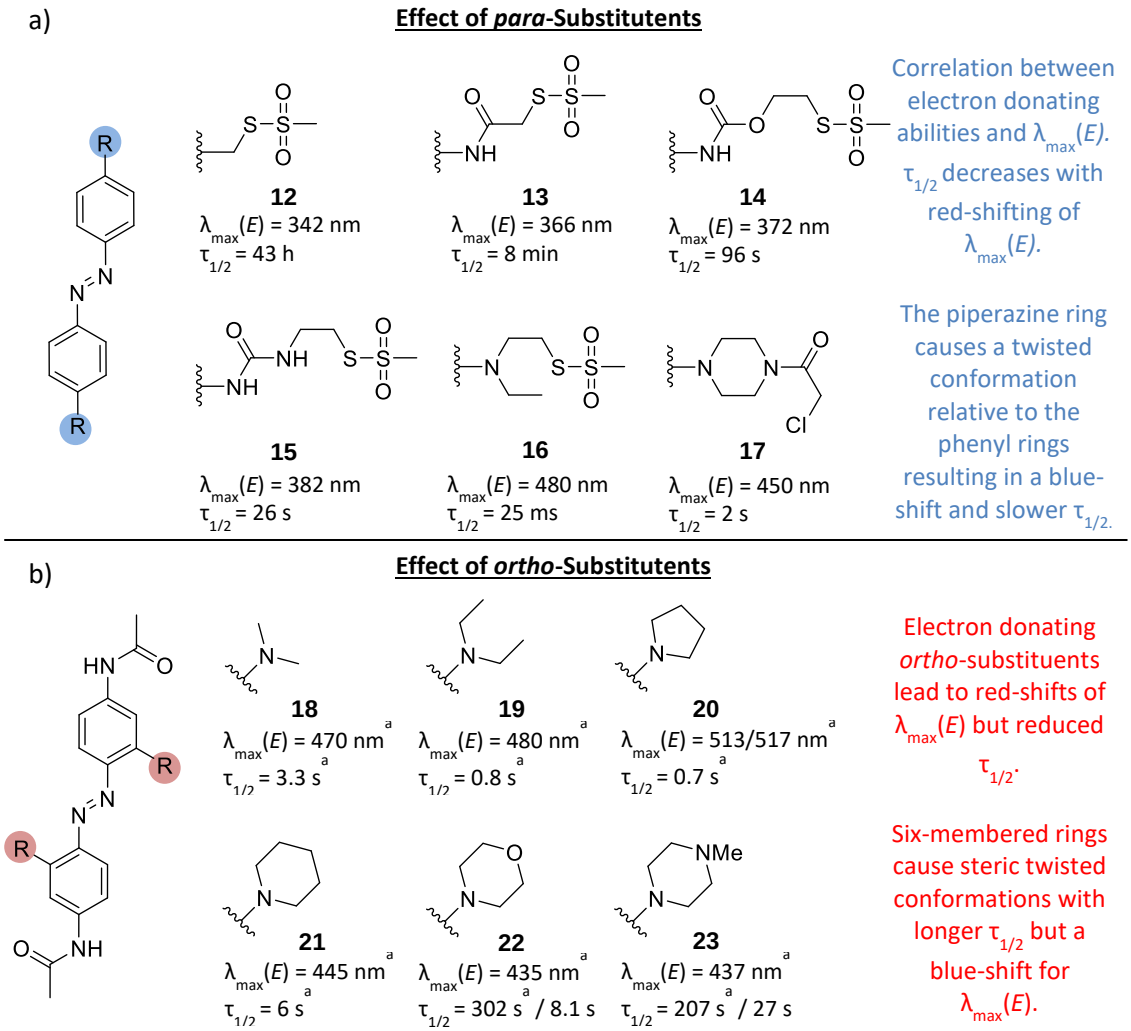

Figure I.34 *a) Photo-physical effect of different substituents in para-position when incorporated into a peptide and b) in ortho-position of azobenzene. Stronger electron-donating substituents lead to a red-shift of the absorption maxima but a reduced half-life time of the cis-isomer. Twisted conformations cause a blue-shift but longer half-life times. [a]: 70% MeCN/H_2O; otherwise measured in aqueous solution (pH 7.0).*[193,195,199]

Speculating that electron-donating substituents might be shifting the absorption maxima with their electronic influence, yet slowing relaxation by their steric influence, different electron-donating groups were examined in *ortho* position to the azo-group in order to combine these properties. A tetra-*ortho*-methoxy azobenzene derivative (**24**) in *trans* (Figure I.35) showed a significant red-shift for its n-π* band compared to the parent structure, while the π-π* transition is blue-shifted.[200] Interestingly, the n-π* band of the *cis* isomer was found to be separated from that of the *trans* isomer by 36 nm, allowing efficient bidirectional switching.

Time-dependent density functional theory (TD-DFT) calculations indicated that *trans*-**24** adopts a conformation where the rings are twisted aplanar, explaining the blue shifted π-π* transition. The difference of the n-π* bands in *cis* and *trans* can be explained by the different steric interaction of the nitrogen lone pairs with the oxygen atoms of the methoxy-groups in both conformations. Green light irradiation (530-560 nm) of the *trans*-isomer yielded ~80% of the *cis*-azobenzene derivative and blue light irradiation (450-460 nm) converted ~85% of the *cis*-isomer back into *trans*, enabling bidirectional light switching. The *cis*-**24** compound also showed very slow relaxation rates, with a half-life of 53 hours in buffer at room temperature. Unfortunately, **24** proved sensitive towards reduction under biomimetic (1 mM) glutathione conditions with a half-life of 1.5 hour limiting its intracellular application.

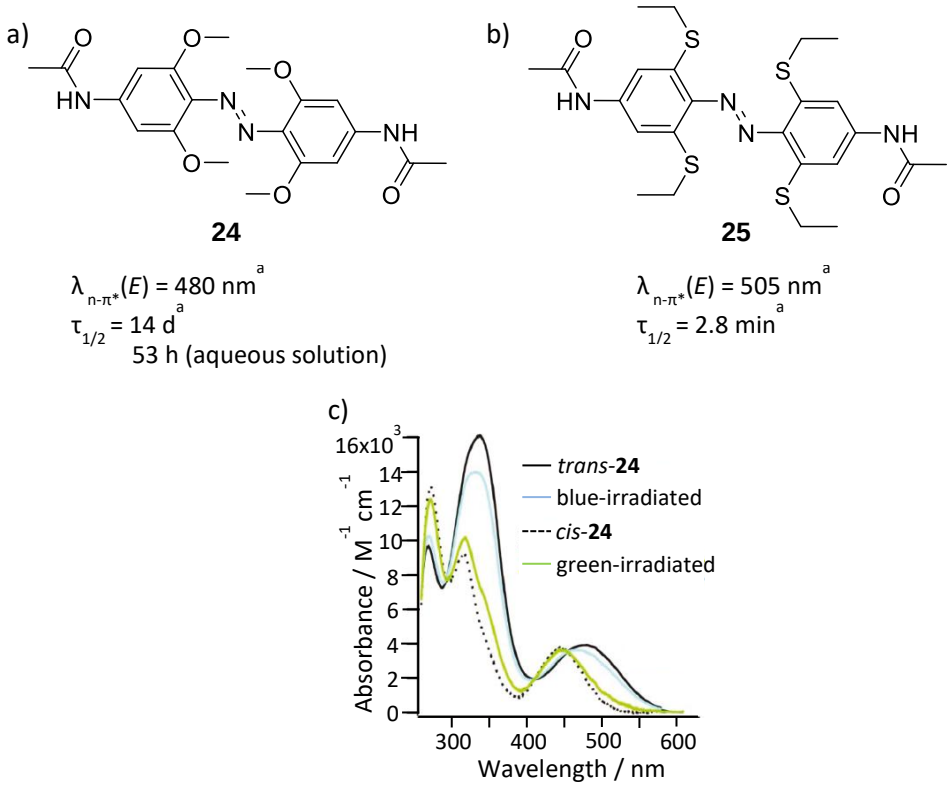

Figure I.35 *a) Tetra-ortho-methoxy- (**24**) and b) tetra-ortho-diethylthioether-azobenzene (**25**) with the wavelength for their n-π* transition band and cis-isomer half-life time. c) UV-visible spectrum of **24** measured in DMSO at 25°C. [a]: DMSO at 25 °C. (Figure adapted from [200]).*

In an attempt to obtain glutathione resistance, an analogue of **24** was synthesized bearing diethylthioether substituents in *ortho* position to the azo-bond (**25**) (Figure I.35).[201] The replacement of the *ortho* substituents led to a >20 nm red-shift and a significant increase in intensity of the n-π* transition band for the *trans* isomer. **25** displayed a strong transition in the blue region of the spectrum. However, no difference between *cis*- and *trans*-**25** were found

for the n-π* transition bands at longer wavelengths, preventing bidirectional photoswitching using visible light. Compound *cis*-***25*** could be formed using green light to obtain ~75% *cis*-isomer at the photostationary state, but it thermally reverted back to *trans*-**25** within minutes in DMSO at 25 °C (**24** displayed a thermal relaxation half-life time of ~14 days). In contrast to **24**, **25** showed the desired resistance against reducing environment and retained the ability to photocycle even after 14 hours incubation in glutathione (10 mM). The weaker hydrogen bonding ability of the thioethers of **25** compared to the ethers of **24** are thought to disfavour protonation of the central azo bond (formation of an azonium-ion) and prevent glutathione reduction with steric effects providing additional steric protection.

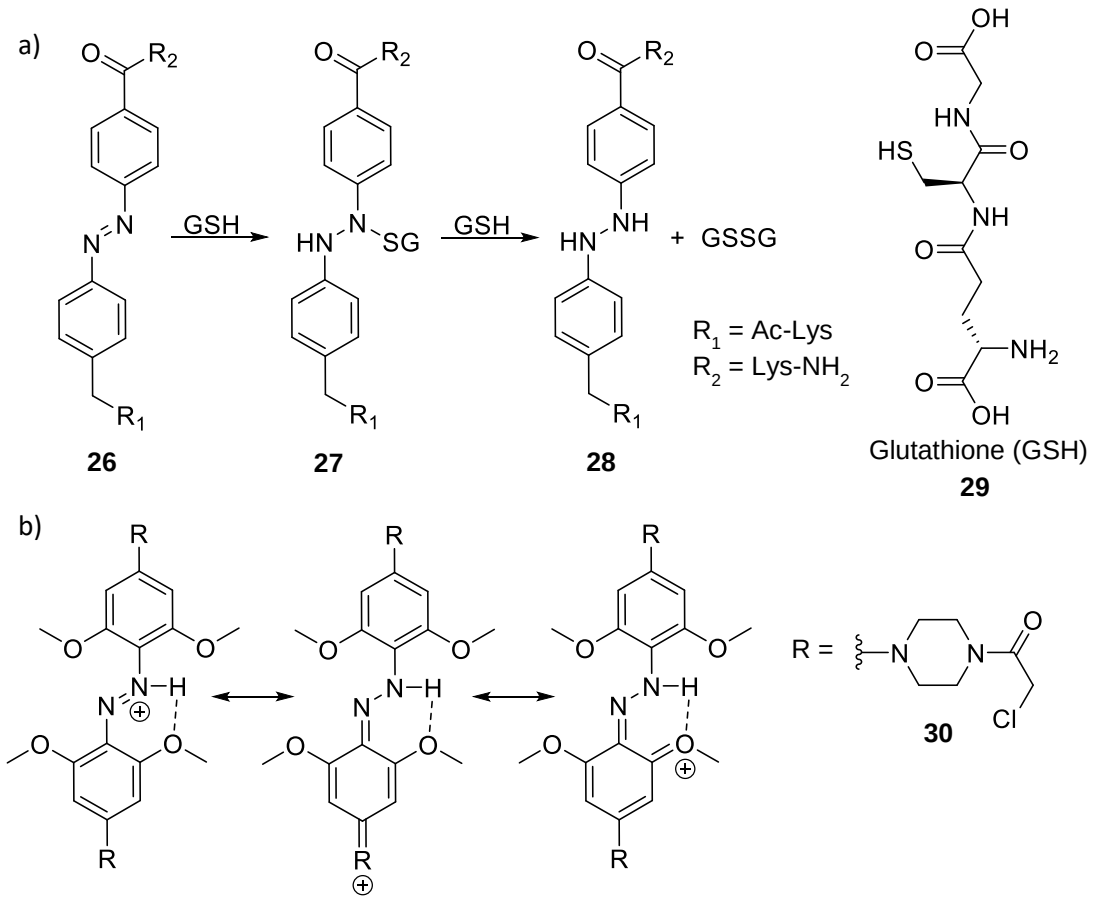

Figure I.36 *a) Reduction of the azobond of the azobenzene **26** with glutathione (**29**).*[202] *b) Stabilization of the azonium-ion through hydrogen-bonding.*

It was envisioned that azonium ions could be used for red-light photoswitching. Typically, azonium-ions show strong absorbance in the red region of the spectrum, but usually display such low pKa values that they hardly exist at physiological pH.[203] Thermal *cis*-to-*trans* relaxation rates of azonium ions are in the range of microseconds due to the loss of the double bond character of the azo bond. However, combining the tetra-*ortho*-methoxy substituents

with a red-shifting amine-group in *para* position increased the pKa value of *trans*-**30**, allowing formation of an azonium ion under physiological conditions.[203] In contrast to neutral *trans*-**30** state, the protonated azonium-ion *trans*-**30**·H^+ displays a planar structure, which supports resonance stabilization and H-bonding with the *ortho*-substituent. Once *trans*-**30** was crosslinked to a test-peptide it could be switched with red light (635 nm) at pH 7.5. Thermal *cis*-to-*trans* relaxation occurred within 10 seconds, around a million times slower than other azonium-ion species due to highly twisted *cis*-**30** no longer being able to hydrogen bond to the azonium ion, significantly reducing the pKa to 5.7). As a result, *cis*-**30** becomes neutral under physiological conditions reverts back to *trans*-**30** much more slowly. However, as reported for previous crosslinkers with similar substitution patterns, **30** was not stable in glutathione solution. Compound **30** was further developed to **31**, capable of absorbing in the near-infrared region of the spectrum when protonated to exploit the biological wavelength window (Figure I.37). Further substitutuents were introduced in *meta* position in order to increase the thermal energy barrier for the *cis*-to-*trans* isomerization.[204] Photoisomerization of *trans*-**31** was achieved using 720 nm light and the thermal reversion half-life of *cis*-**31** was 0.7 seconds. Different *para*-amino substituents were tested to tune the pKa-values, 6-membered rings resulted in steric clashes, leading to a twisted *para*-substituent and lower pKa-value due to diminished delocalisation. However, once again, the system was not stable under reducing buffer conditions.

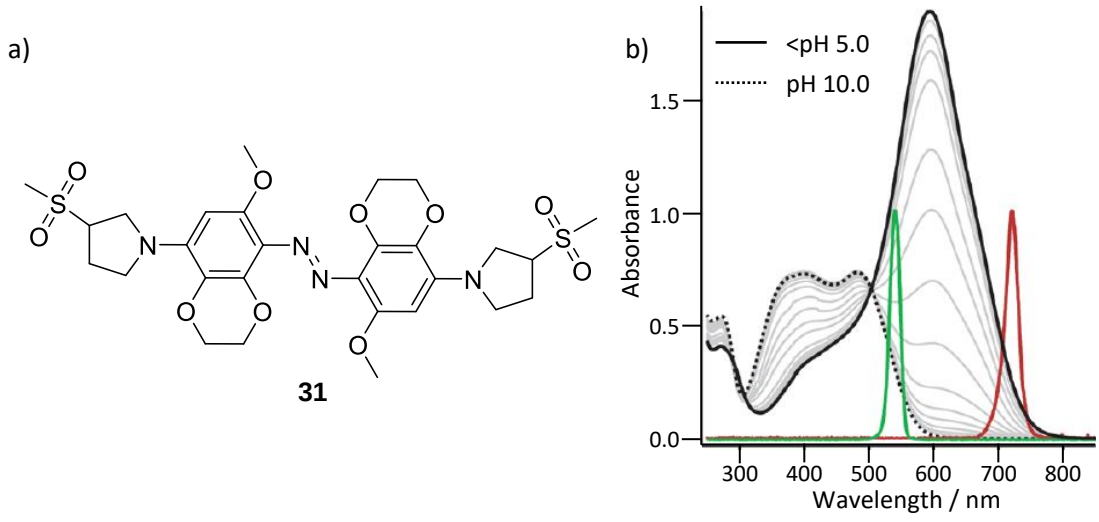

31

Figure I.37 *a) The azobenzene derivative **31** (pK_a: 6.7) can undergo photoswitching using near-infrared light under physiological conditions due to the protonation of the azo-group. b) Absorbance* **31** *at different pH-values. The dotted line (pH 10.0) is the spectrum of the neutral trans-isomer, whereas the solid line is the limiting spectrum of the azonium-ion. During photoswitching-experiments of **31** with 720 nm near-IR-light (red), the absorbance was monitored at 540 nm (green). (Figure adapted from [204]).*

Unlike the tetra-*ortho*-methoxy azobenzenes, tetra-*ortho*-fluoro azobenzene **32** is planar in its *trans* state. The idea behind its synthesis was that fluorine would withdraw electrons and stabilize the non-bonding orbital of the *cis* isomer by reducing the electronic repulsion centered around the azo double bond. This would result in an energy increase of the n-π* transition. The fluorine substituents lower the energy level of the LUMO (π*) for the *trans* form more than for the *cis*-isomer, leading to a n-π* red-shift of the *trans*-isomer. This effect causes a band separation between the *cis* and *trans* isomers, which is greatest (50 nm) when π-electron withdrawing groups are placed *para* to the azo group. The stabilization of the *cis* n-orbital relative to the transition state causes a larger thermal barrier and therefore slower thermal relaxation times. Screening various fluorine-substitution patterns revealed that more than four fluorine-substituents on the system did not lead to any further increase in band separation, which stayed consistently around 40 nm between the two isomers. *Trans*-to-*cis* isomerization using >500 nm light yielded photostationary states of 92% *cis* isomer for both ester and amide derivatives while 410 nm irradiation resulted in *cis*-to-*trans* isomerization to 96% and 97% *trans* isomers for *p*-amide and *p*-ester respectively. A decrease of thermal stability of the *cis*-isomers was observed for the azobenzenes with ester or amide groups in *para* position as they caused stabilization of the reversion transition state, lowering the half-life of the *cis*-isomer.[205]

Tetra-*ortho*-chloro and -bromo substituted azobenzene photoswitches yielded red shifted n-π* transitions for the *trans*-states that could be isomerized using red light (635 nm), with blue light (450 nm) reverting it back from *cis*-to-*trans*.[206] Furthermore, the tetra-*ortho*-chloro azobenzene switch was stable against glutathione reduction in both isomeric forms. It was hypothesized that the combination of the twisted conformation of *trans*-**33** and the inductively electron withdrawing properties of the chloride substituents makes the azo-group less susceptible to reduction. Subsequently, the tetra-*ortho*-chloro crosslinker **33** was attached to a test peptide and yielding a thermal relaxation half-life time of 3.5 hours at 37 °C in sodium phosphate buffer (pH 7.0). When attached to a fluorescein-labelled peptide consisting of D-amino acids and microinjected in zebrafish embryos, switching with red-light produced a change in fluorescence emission indicating successful photoisomerization into its *cis*-state. It was possible to carry out alternate red light/blue light switching for 30 hours with no apparent side-effects. The ability of bidirectional photoswitching using visible light, the long thermal half-life time of its *cis*-isomer and its stability in reducing environment makes **33** one of the most promising azobenzene-photoswitches for *in vivo* application based on its photo-physical properties.

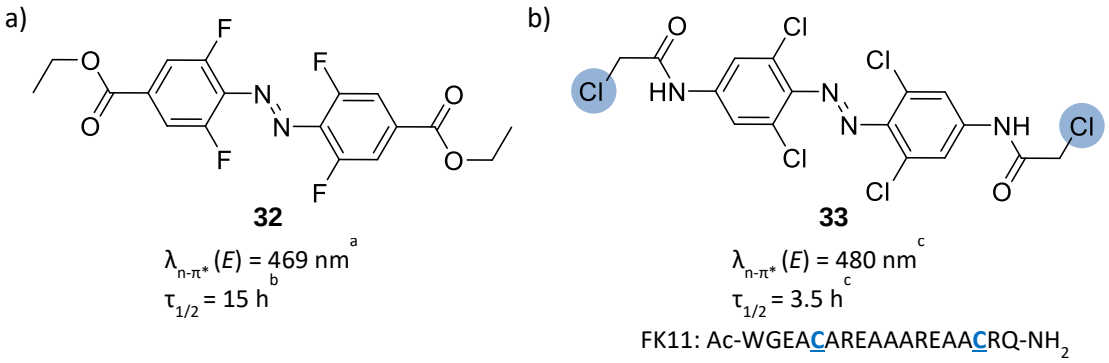

Figure I.38 *a) Tetra-ortho-fluoro azobenzene derivative (**32**) with its n-π* transition bands and cis half-life time. b) The tetra-ortho-chloro azobenzene derivative (**33**) with the n-π* transition bands and cis half-life time after linking it onto the peptide FK11 over the cysteine residues. [a]: MeCN, 25 °C; [b]: MeCN, 60 °C; [c]: aqueous solution (pH 7.0), 37 °C.*[205,206]

Bridged azobenzenes (**34**, Figure I.39), where an *ortho* ethylene bridge constrains the azobenzene, possesses remarkable photo-properties with a separation between the n-π* transition maxima of 86 nm for both isomers. The relative stability of the *cis* and *trans* isomers is also reversed compared to azobenzene.[207] Isomerization from the ground state *cis* isomer to the *trans* isomer occurs upon irradiation with 370-400 nm light and the reverse direction with 480-550 nm light. Chloroacetamido groups were introduced in *para* position to yield **35**, it was attached to the test peptide FK11 and a photostationary state consisting of 70% *trans*-**35** was detected by NMR-spectroscopy after irradiation with 407 nm. Reversion to the *cis* isomer was achieved using 518 nm light. Whilst the *trans*-isomer was completely resistant, the *cis*-isomer was reduced reduction by glutathione-containing buffers approximating biomimetic reduction potentials.[208]

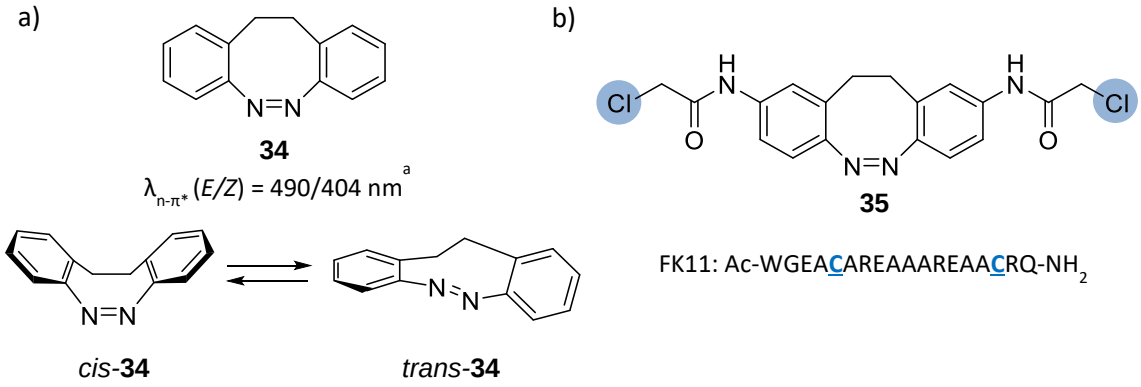

Figure I.39 *a) Constrained azobenzene derivative **34** displays a n-π* transition maxima of its two isomers of 86 nm and was utilized as **35** to obtain photocontrol over the test-peptide FK11 (b). [a]: n-hexane, 25 °C.*[207]

iii. Azobenzene Photo-Control of BH3 Domains

Azobenzene-photoswitches can be conveniently linked to peptides or proteins through the introduction of appropriate *para*-substituents; typically, ester or amide-moieties that can react with specific side-chain residues in the peptide sequence. In particular, *p*-haloacetamide substituted azobenzene linkers that can undergo a substitution reaction with thiol-groups of cysteines have been well utilized. Indeed, the first report of photo-control of the helical content in a short peptide using an azobenzene-based linker employed *p*-iodoacetamido-azobenzene (**36**, Figure I.40) to create a staple between cysteine residues in *i,i* + 7 positions of a soluble, monomeric test peptide known to readily form α-helices.[209] A water-soluble version of this crosslinker **37** bearing electrophilic *p*-chloroacetamido substituents was subsequently developed. Compound **37** requires no organic co-solvents for its peptide conjugation reaction, displays a similar absorption spectrum and an equivalent degree of helical control on a model-peptide compared to **36**. Irradiation of a test-peptide solution at 370 nm yielded 85% *cis*-**37**.[210] Neither **37** nor **36** allow bidirectional photoswitching, relying on thermal-relaxation processes in order to revert *cis* to *trans*. However, the thermal relaxation barrier seems larger for **37** attached to the same test-peptide as the half-life of *cis*-**37** is 12 minutes at 37 °C compares to 2.5 minutes for *cis*-**36**.[210] Access to **37** greatly expanded the scope of peptides and proteins that could be crosslinked by haloacetamido azobenzenes.

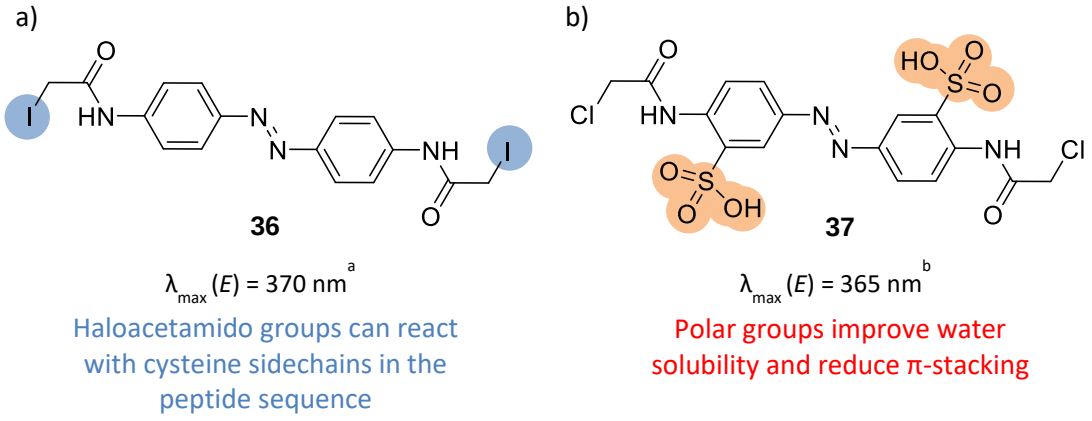

Figure I.40 *a)-b) The two azobenzene derivatives that have been utilized to photocontrol BH3-peptides. [a]: DMSO, 25 °C; [b]: aqueous solution (pH 7.0), 25 °C.* [209,210]

Crosslinker **37** was attached to short BH3 peptides derived from Bak and Bid with several different cysteine spacings; *i,i* + 4 for the Bid-peptide and *i,i* + 7 and *i,i* + 11 for the Bak-peptide.[211] Bulky residues on the same face of the helix as the crosslinker were replaced with amino acids of equivalent character but lesser steric demands. Methionine residues in the Bid-

derived sequence were replaced with isoleucine to increase the stability of the peptide towards oxidation. The UV-Vis spectrum of the crosslinked Bak$^{i,i+11}$ showed a π-π* absorption band with a maximum at 363 nm for the transition. Half-lives of the *cis* states for the crosslinked **37**-Bak$^{i,i+7}$ and **37**-Bid$^{i,i+4}$ were reported to be 174 and 190 minutes respectively at 15 °C. Photostationary states containing 69%, 76% and 80% *cis*-isomers were observed for **37**-Bak$^{i,i+11}$, **37**-Bak$^{i,i+7}$ and **37**-Bid$^{i,i+4}$ respectively under 363 nm irradiation. The end-to-end distance of the crosslinker in its *trans*-state matches the ideal *i,i* + 11 distance for an α-helix so in this spacing, *trans*-**37** stabilises a helical conformation. This was confirmed by CD-spectroscopy experiments with significant changes in the α-helical content observed upon irradiation. In contrast, crosslinked **37**-Bak$^{i,i+7}$ and **37**-Bid$^{i,i+4}$ did not show any great changes in helicity upon irradiation. Binding affinities to the anti-apoptotic protein Bcl-x_L were measured using N-terminal carboxy-fluorescein labeled peptides in florescence anisotropy titrations. For **37-**Bak$^{i,i+7}$ and **33**-Bid$^{i,i+4}$ peptides a ~20 fold difference in affinities was observed for their dark and photostationary states, but only a twofold change was observed for **37**-Bak$^{i,i+11}$. No binding was detected with Hdm2, a negative control protein, using concentrations up to 10 μM, indicating more than 200-fold selectivity. ^{1}H-^{15}N-heteronuclear single-quantum correlation (HSQC) NMR experiments were carried out using a truncated version of Bcl-x_L lacking the flexible loop between helix 1 and 2 and **37**-Bak$^{i,i+7}$ and **37**-Bak$^{i,i+11}$ peptides. Strong chemical shift changes were observed for residues lying in the hydrophobic groove region of Bcl-x_L observed upon incubation with dark adapted **37**-Bak$^{i,i+11}$. Surprisingly, NMR experiments with dark adapted peptide **37**-Bak$^{i,i+7}$ resulted in almost identical chemical shift changes compared to Bak$^{i,i+11}$. It was concluded that isomerization only affects binding affinities to the target protein Bcl-x_L, rather than change in its preferred binding site.[211]

The truncated anti-apoptotic protein Bcl-x_L (1–209, Δ45–84, Δ210–233), excluding the loop and the trans-membrane-region for solubility-reasons, was expressed in ^{15}N and ^{13}C minimal media, purified and mixed with **37**-Bak$_{I81F}^{i,i+11}$. The Bak-sequence containing an I81F mutation is known to enhance the affinity to Bcl-x_L. 3D NMR experiments yielded a full assignment of Bcl-x_L free and liganded with **37**-Bak$^{i,i+11}$. Solution of the NMR-structure revealed that crosslinked Bak$^{i,i+11}$ adopts a slightly distorted helical structure upon binding to the surface groove of Bcl-x_L, which is formed by its α-helices α2 and α5. The distortion of the stapled peptide is mostly centered on the Cys73-residues, which are connected to the crosslinker. Interestingly, Phe81 was found to point away from the binding groove and towards the crosslinker, increasing the hydrophobic contact area.

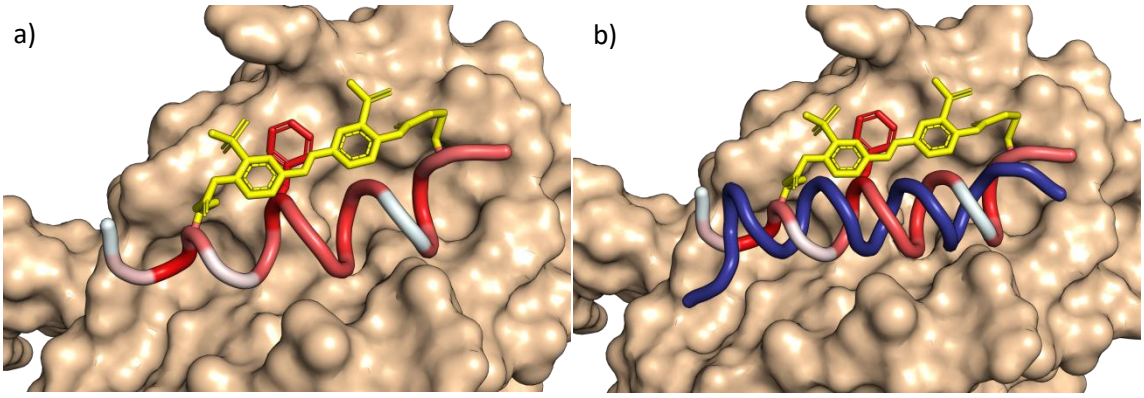

Figure I.41 *a) **37**-Bak$_{I81F}^{i,i+11}$ in complex with the anti-apoptotic protein Bcl-x$_L$. The linker **37** leads to the formation of a slightly distorted α-helix around the anchor point. Phe81 points towards the crosslinker increasing the hydrophobic surface (hydrophobic residues are colored red). (PDB: 2LP8). b) The wild-type sequence Bak$_{wt}$ (blue) binds to the hydrophobic groove with half a helical pitch shift. (PDB: 1BXL).*

Comparing the position of the crosslinked peptide in the binding cleft to the wild-type, a shift of around half a helix pitch towards the N-terminus was observed. Additionally, the positions of the side-chains that make hydrophobic contact with the protein in the crosslinked peptide are slightly different to those in the wild-type, suggesting that the distortions caused by the crosslinker result in a change in position of the hydrophobic side-chains. However, the binding site of Bcl-x$_L$ displays a large degree of flexibility and remodels itself in order to make hydrophobic contact with the peptides. The NMR-structures suggest that the increased affinity of the crosslinked peptide may not only be a result of the helical-pre-organization, but also of the formation of a larger area of hydrophobic contact between the peptide and the surface of Bcl-x$_L$ due to the relocation of Phe81.[212,213]

Carboxyfluorescein-tagged **37**-Bak$^{i,i+11}$ and **37**-Bid$^{i,i+11}$, with affinities of 15 nM and 43 nM, respectively, to Bcl-x$_L$ in their dark-states in fluorescence-polarisation assays, were tested for their ability to photostimulate membrane depolarization and cytochrome *c* release using flow cytometry techniques. Experiments on permeablised human lymphoma SU-DHL-4 cells showed that FAM-**37**-Bak$^{i,i+11}$ initiated mitochondrial dysfunction more efficiently than FAM-**37**-Bid$^{i,i+11}$. However, whilst FAM-**37**-Bak$^{i,i+11}$ induced apoptosis effectively, it only possessed 35% *cis* isomer at its photostationary state and the half-life of the *cis* isomer was only 18 minutes at 37 °C. Ac-**37**-Bak$^{i,i+7}$ was much better, with up to 70% *cis* isomer upon irradiation and an extended half-life of 28 min at 37 °C. Low levels of cytochrome *c* release were observed when cells were treated with the inactive, non-helical *trans*-state of this peptide, which increased more than twofold when the peptide was pre-irradiated.[214] Overall, these experiments

highlight that while BH3-peptides crosslinked with **37** are able to induce cytochrome *c* release triggered with light, improvements need to be made before such peptides are ready for medicinal applications.

5. Aims of the Project in the Context of Current Research

Most apoptotic processes are normally tightly regulated by the Bcl-2 protein family members with abnormal over-expression of anti-apoptotic family members often being observed in cancer cells, rendering intended death-signals futile, immortalizing the cancer-cell. Peptides are naturally good starting points to selectively target PPIs due to their high coverage of the mostly hydrophobic interfaces. Secondary structures of peptides can be enforced using chemical staples in order to increase the binding affinity. Furthermore, the application of azobenzene-photoswitches as peptide-staples gives the opportunity to reversibly stabilize secondary structures in a non-invasive way upon irradiation with light of an appropriate wavelength.

Both isomers of crosslinker **33** have been reported to be formed by the action of visible light. Most importantly, harmless red-light (635 nm) can be used to isomerize **33** into its *cis*-state, which is a significant improvement over existing azobenzene-linker systems operated on UV-visible light. When attached to a test-peptide and injected into zebra-fish embryos, the thermal relaxation half-life of the *cis*-state was 3.5 hours, long enough to control even longer cellular events. However, despite its outstanding photo-physical properties and glutathione resistance, only one example has been described using **33** to alter peptide-conformation.[206]

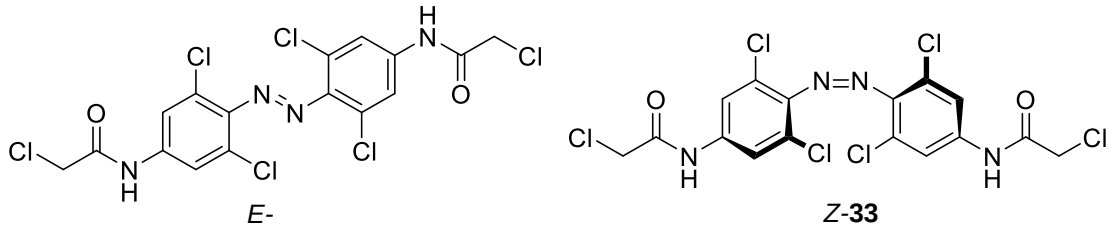

Figure I.42 *Azobenzenes E-**33** can be photo-isomerised to Z-**33** with red light, is stable against glutathione and displays a long cis half-life time.*

Modulation of BH3-peptide conformations to disrupt PPIs using azobenzene photoswitches have only been reported with azobenzenes **36** and **37**. A major drawback of systems based on these molecules has been the relatively short half-lives of their irradiated states and the need for UV-Vis light to *trans-cis* isomerization, effectively limiting their *in vivo* application. In addition, these peptides proved unable to enter cells unaided. The aim of this project was therefore to develop an azobenzene-BH3-peptide system, based on **33** due to its excellent photo-physical properties and *in vivo* stability, which is able to cross cell-membranes to induce apoptosis in intact cells.

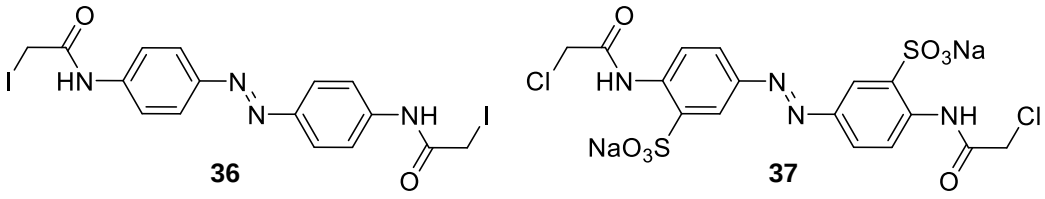

Figure I.43 *Previously used azobenzene derivatives to photocontrol BH3-peptides.*

II. Results and Discussion

1. Azobenzene Photoswitches

a. Aims and Objectives

Due to the promising characteristics of existing azobenzene photo-linkers (chapter I.4.b.ii), it was decided to synthesise some of these bi-functional azobenzene analogues, which are able to react with two cysteine residues in a peptide. A non-substituted azobenzene crosslinker was the first target, to act as a baseline, followed by the synthesis of the tetra-*ortho*-chloro azobenzene crosslinker **33,** which can be addressed using light in the visible range of the spectrum. Subsequently, the photochemical properties of these compounds were to be investigated by NMR and UV-visible spectroscopy. Further modification on the final compounds was undertaken in order to change the reactivity towards the thiol-groups of the cysteines and to obtain reference compounds for cell-culture studies in the later stage of the project.

b. Azobenzene Crosslinker

i. Synthesis

The azobenzene crosslinker **38** was synthesized as described in a one-step procedure from commercial material (Scheme II.1) to represent the most basic azobenzene scaffold. Addition-elimination reactions of the two amines with chloroacetyl chloride yielded a pair of reactive groups able to undergo S_N2 type reactions with nucleophiles, such as the thiol group of cysteines. The reaction was performed in acetonitrile with triethylamine added to neutralize any hydrogen chloride formation during the reaction. A total yield of 87% was obtained for **38** as indicated by NMR spectroscopy.

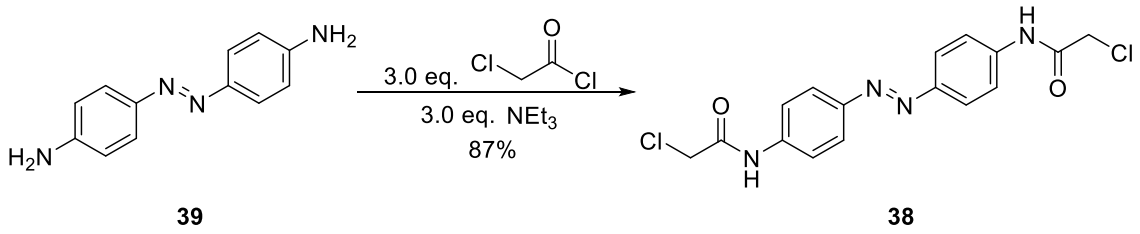

39 **38**

Scheme II.1 *Formation of the unsubstituted azobenzene-crosslinker **38**.*

ii. Photocharacterisation

As the chlorine atoms in **38** are susceptible to hydrolysis, the photocharacterisation was carried out in aprotic DMSO solvent. UV-visible spectra were recorded in the dark state and the photo-stationary state (PSS) under 360 nm and 450 nm illumination. The dark state of **38** in DMSO displays a major band for the π-π* transition at 376 nm and another maximum at 260 nm. The n-π* band, which can be found at 440 nm for *trans*-azobenzene (in ethanol[178]) appears to overlap with the π-π* band, without any distinct maxima. Irradiation with 360 nm light significantly reduces the absorption band at 376 nm. There is a small increase in absorbance for the n-π* band at 449 nm and the π-π* transition band is blue-shifted to 321 nm. Irradiation with 450 nm light yielded a photo-stationary state similar to the dark state in its absorption spectrum (see Figure II.1a). As expected, irradiation with red-light induced no *trans*-to-*cis* isomerization (not shown).

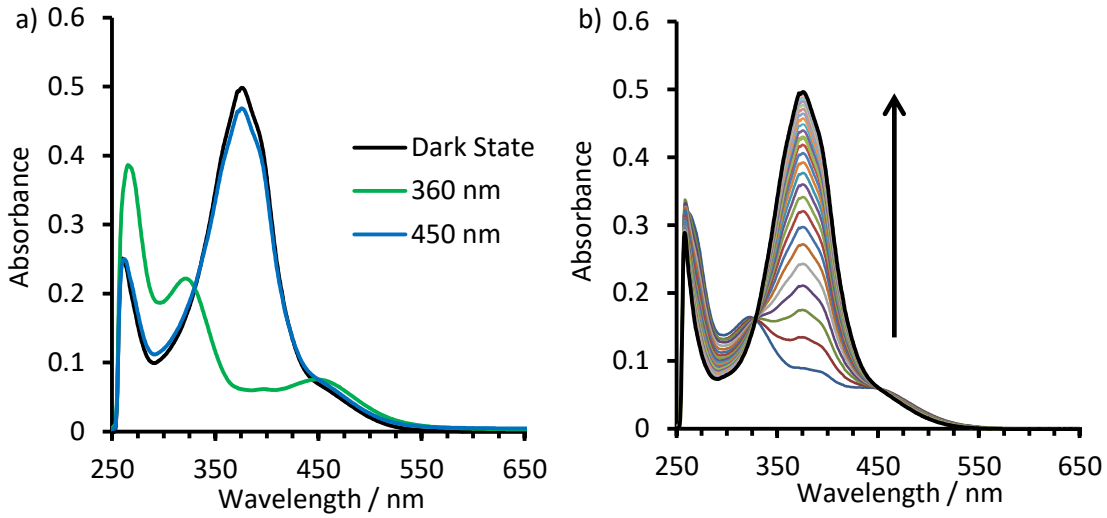

Figure II.1 *a) Absorption spectrum of **38** in DMSO at dark state, $PSS_{360\,nm}$ and $PSS_{450\,nm}$. b) Thermal relaxation profile of **38** in DMSO at 37 °C after 360 nm irradiation, one scan every 20 min is shown.*

Spectra of *cis*-**38** were taken at 37 °C at 20 min intervals after irradiation with 360 nm light to observe thermal relaxation (Figure II.1b). Full reversion to the dark state could be observed after a few hours. The measured half-life time of *cis*-**38** in DMSO was 132 min at 37 °C, significantly longer than the half-lives previously reported for **38** crosslinked to model-peptides (6.4 min at 36 °C,[209] 2.5 min at 37 °C[210]). The difference between the half-life obtained and those previously reported are a combination of the different chemical environment in the

absence of a peptide and the different solvents used for the experiment. The composition of the attached peptide substantially influences the *cis*-to-*trans* relaxation rate as does the spacing of the cysteines used to bind the crosslinker, as the end-to-end distances define how strained the crosslinker is in either state. Peptides, designed to form an α-helix with a cysteine-spacing of *i*,*i* + 11, might therefore show faster relaxation rates compared to peptides with an *i*,*i* + 4 or *i*,*i* + 7 spacing due to the combination of the thermodynamically preferred *trans*-state of the linker and the additional hydrogen-bond interaction promoting an α-helix formation.

The ^{1}H-NMR spectrum of thermally equilibrated **38** in DMSO-d6 showed two overlapping doublets in the aromatic region at 7.88 and 7.81 ppm corresponding to the protons on the phenyl-rings (Figure II.2). The methylene-group appeared as a singlet at 4.32 ppm and the amide-proton could be observed as a broader singlet at 10.66 pm. No other peaks relating to other species could be observed suggesting that the dark state consists of 100% *trans*-**38**.

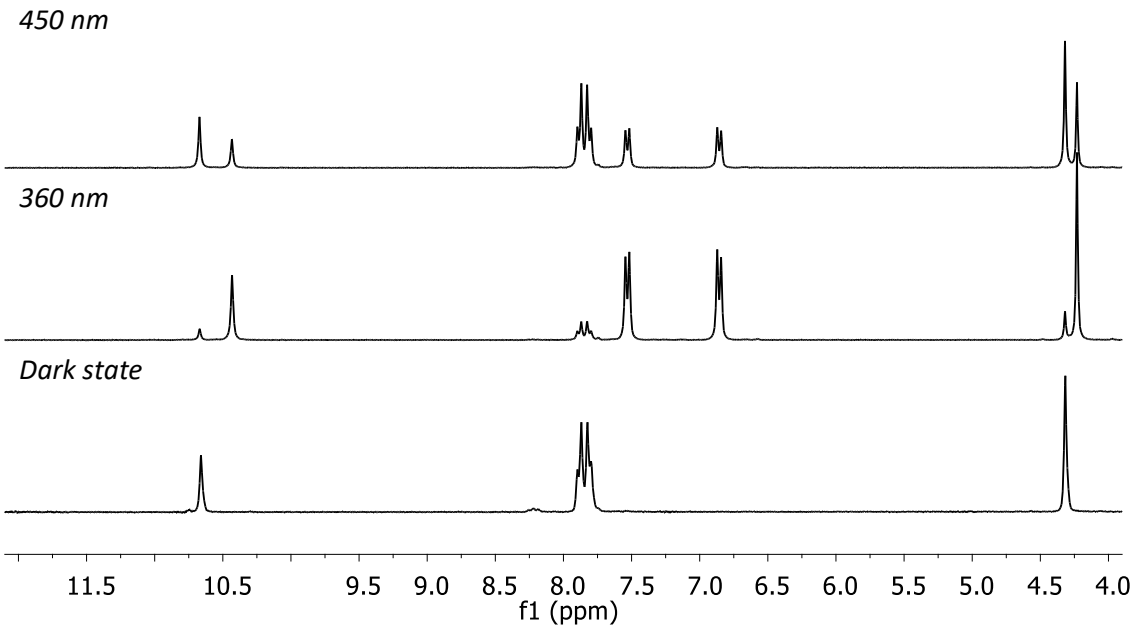

Figure II.2 *^{1}H-NMR spectra of **38** at dark-state, the $PSS_{360\,nm}$ and the $PSS_{450\,nm}$ in DMSO-d6.*

At the photo-stationary state under 360 nm illumination, new peaks emerged in the ^{1}H-NMR spectrum corresponding to the *cis*-**38**. Interestingly, the peaks of the *cis*-**38** uniformly shifted to more shielded electronic environments. This could be explained by the conformational change to a bent structure for the *cis*-isomer, where the phenyl rings are twisted out of the plane to the azo-group. This leads to a loss of the aromaticity between the two phenyl-rings and the electron density becomes more localised within the separated rings. Due to the

diminished delocalisation of the electron density over the azo-bond, the nitrogen-atoms might impose a slight inductive effect further shifting the aromatic signals upfield. As a consequence, the aromatic protons underwent the most significant changes in the spectrum, appearing as doublets at 7.53 ppm and 6.86 ppm. The amide-proton in *para*-position of the phenyl-ring displayed a weaker shift upfield to 10.43 ppm, whereas the methylene-protons (4.23 ppm) were least affected by the shielding effect of the conformational change. Integrating the proton signals revealed of ~83% *cis*-**38** at $PSS_{360\,nm}$. Interestingly, attempted photoreversion by irradiation with 450 nm light led to a $PSS_{450\,nm}$ still containing ~34% *cis*-**38**, despite the UV-visible spectrum indicating almost complete reversion to the dark-state conformation (Figure II.1a). This suggested that estimating the *cis*-/*trans*-isomeric content of azobenzene molecules just by UV-visible techniques could be misleading and should be supported by other techniques as well.

c. *Ortho*-Tetrachloro azobenzene Crosslinker

i. Synthesis

Crosslinker **33** was reported to have excellent photo-physical properties compared to previous azobenzene analogues.[206] *Cis*-to-*trans* photo-isomerization was possible using red light, which was attributed to the tetra-*ortho* substitution pattern of the azobenzene ring. When linked to a test peptide, thermal *cis*-to-*trans* relaxation was observed to occur over a period of 16 h. Furthermore, **33** displayed resistance to reduction by glutathione, which was assessed through incubation experiments using reduced glutathione (10 mM) and high stability towards photobleaching as indicated by the ability of **33** to undergo multiple cycles of red-/blue light switching.

The synthesis of crosslinker **33** was attempted as described in literature reports,[206] however certain changes to the published procedure had to be made to obtain the final product **33** (Scheme II.2). Protection of the amine group in **40** was carried out as described in the literature, yielding **41** in 88% yield. Synthesis of the azo bond was achieved through formation of a nitrosyl cation using sulphuric acid and sodium nitrite. After drop-wise addition of **41**, the solution was stirred for 1 h at 0 °C and then allowed to warm to room temperature. The mixture was poured onto ice-water whereupon a very fine precipitate formed which was left to aggregate for another 2 h to facilitate subsequent filtration. The resulting precipitate of crude **43** was subsequently treated with aqueous sodium hydroxide to release the protecting group.

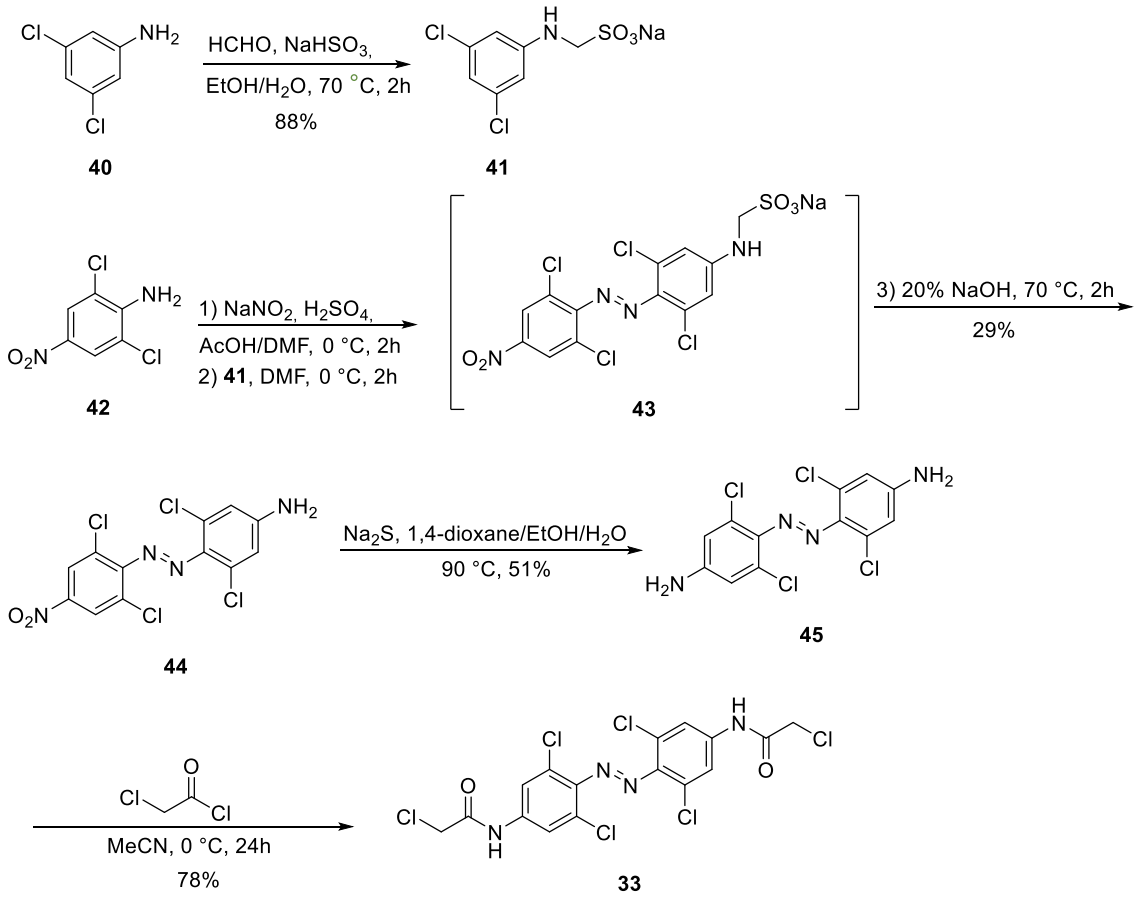

Scheme II.2 *Modified synthetic route for **33**. Synthetic route adapted from [[206]].*

Complete removal of dimethylformamide (DMF) was necessary before the removal of the protecting group to avoid the formation of side products. Formation of the side product **46** (Scheme II.3) was observed when ^{1}H-NMR spectroscopy indicated DMF was not fully removed. Decomposition of DMF under higher temperatures and basic conditions can promote the formation of dimethyl amine, which could subsequently attack the aromatic ring in **43** in a nucleophilic aromatic substitution reaction displacing one chlorine atom to give **46**.

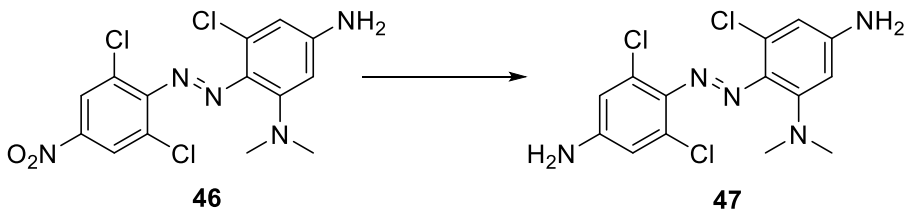

Scheme II.3 *Side product **46** and its reduced azobenzene derivative **47**.*

Full removal of DMF from the crude product **43** proved impossible even after several washes and re-suspensions in ice-cold water or methanol suggesting the formation of a complex between the solvent and **43**. Subsequent analysis of the dried precipitate displayed product-to-DMF peaks in a 3:1 ratio. Removal of DMF was finally achieved by washing the precipitate with lithium chloride (LiCl, 1 M) solution to displace DMF from the putative complex by coordination of LiCl to the DMF molecule (Figure II.3). Compound **43** was then dry-loaded onto magnesium sulfate under reduced pressure and subsequently transferred onto a cellulose-filter. It was washed with cold dichloromethane (DCM) until the eluent ran clear. The lower polarity of DCM allowed selective elution of side products from the magnesium sulfate, as confirmed by TLC analysis, whilst leaving the product sulfate behind. The magnesium sulfate was then washed with acetone to release a red solution containing the intermediate **43** in high purity. The solvent of the red acetone fraction containing the intermediate **43** was removed under reduced pressure and the solid thoroughly dried before the synthesis was continued.

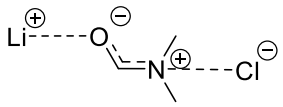

Figure II.3 *Proposed coordination of LiCl to DMF.*

Reduction of **44** to **45** was carried out as reported in recent literature.[206] Three equivalents of sodium sulfide were used as a reducing agent in dioxane, water and ethanol. The reaction mixture was stirred and heated under reflux for 24 h. More sodium sulfide (3.0 eq.) was added and the reaction let to stir for another 5 h until the reduction was complete as judged by TLC-analysis. Extraction and subsequent silica gel chromatography of the crude product yielded **45** as a red solid in 51% yield.

The reduction of the isolated dimethylamine side product **46** was attempted under the same conditions using sodium sulfide in dioxane, water and ethanol under reflux but gave only 17% yield for **47** (compared to 51% for the tetra-chloro derivative **45**). Further reducing agents such as stannous chloride or sodium borohydride were tested but did not yield any of the desired product. One possible explanation for this observation is the more electron rich environment of this azobenzene scaffold due to the electron-donating properties of the dimethyl amine group, which might lead to a higher electron density around the nitro-group, and thus, make

its reduction more difficult. However, no product could be isolated after reaction of the reduced dimethyl amine scaffold with chloroacetyl chloride.

Reaction of chloroacetyl chloride with **45** gave the final product **33**. The literature procedure specified that this step should be carried out in a mixture of diethyl ether and pyridine. However, complete removal of pyridine from the crude product proved challenging and made the identification of the final product by NMR spectroscopy difficult due to overlapping signals in the aromatic region. Purification of the reaction mixture by silica chromatography, extensive washes with copper sulfate or 1 M hydrochloric acid did not yield clean product and NMR showed strong signals of pyridine in a 2:1 pyridine:azobenzene ratio, suggesting potential π-interaction between the aromatic system of the azobenzene and pyridine. The synthesis of the final compound was instead achieved by dissolving **45** in cold acetonitrile and slow addition of chloroacetyl chloride in the presence of diisopropylethylamine (DIPEA) as the base. The solution was stirred overnight and the reaction mixture cooled in an ice-water bath. The precipitate was filtered off and washed with cold acetonitrile to give pure **33** by NMR spectroscopy and mass spectrometry. In general, the overall yield was less than 5%, presumably due to the steric hindrance of *ortho*-substituents disfavouring product formation.

Although initially formed as a side-product, an azobenzene-based crosslinker bearing three chlorine atoms and one dimethyl-amine residue could potentially possess interesting photo-physical properties. The separation of the n-π* transition bands of the *cis*- and *trans*-isomers in similar azobenzene-crosslinkers can be attributed to the tetra-*ortho* substitution pattern, whereas the red-shift and thermal stability of the *cis*-isomer is widely considered a result of the twisted conformation in the *trans*-state. The torsion of the *trans*-state causes destabilization of the HOMO orbitals centred on the azo-nitrogen lone pairs due to the close proximity of the electrons of the other substituents, resulting in a red-shift of the n-π* transition. Furthermore, amine-substituents in *ortho*-position are known to induce bathochromic shifts due to their electron-donating character.[199,201,206] Subsequently, a mixed tetra-*ortho*-substituted azobenzene-linker bearing one dimethyl amine and three chlorine-residues might be expected to further increase the red-shift of **33**. The three chlorine-substituents may still cause enough distortion of the *trans*-state and generate a long-lived *cis*-state useful for bidirectional photoswitching, although the nitrogen lone-pair might also be able to stabilize protonation of the azo-bond and therefore lead to a linker less stable to glutathione-reduction. Further material was obtained by a direct synthesis of the dimethyl amine derivative by addition of dimethylamine hydrochloride to the reaction mixture during the deprotection step and heating to 70 °C for 3 h to give an overall yield of 7% (Scheme II.4).

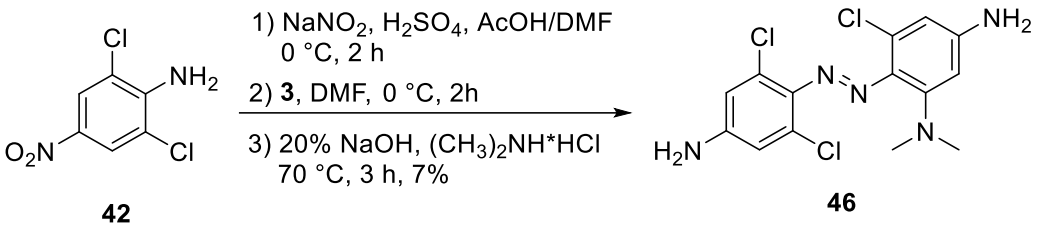

Scheme II.4 *Intentional synthesis of **46**.*

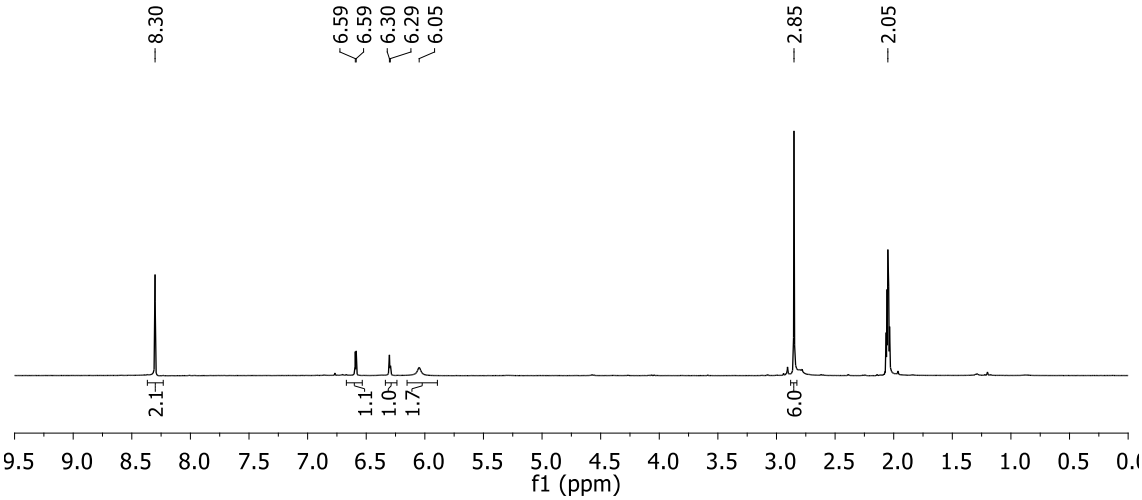

Figure II.4 *[1]H-NMR spectrum of the purified dimethyl-amine side product **46**.*

Compound **46** was characterised using NMR-spectroscopy and mass spectrometry. The ^{1}H-NMR spectrum confirmed the presence of different substitution patterns for the two phenyl rings resulting in two doublets at 6.59 ppm and 6.30 ppm for the ring bearing the dimethlyamine-moiety. The two doublets show *J*-coupling constants of 2.3 Hz, typically corresponding to ^{4}J coupling constants in aromatic systems. A significantly de-shielded singlet corresponds to the two protons on the ring with the nitro-group (8.30 ppm). A broad singlet at 6.05 ppm is due to the amine-protons, whereas a singlet at 2.85 ppm integrating for six accounts for the methyl-protons (Figure II.4). Reduction of **46** to **47** continued to be the limiting factor and further optimisation is necessary. Only a few milligrams of **47** were obtained using the described procedure, leading to difficulties in the subsequent purification step. Small scale reaction of **47** with chloroacetyl chloride again did not lead to any observable product formation so attention returned to the tetra-chloro compound.

ii. Photocharacterisation

UV-visible spectra were recorded for the linker **33** at the dark state, $PSS_{360\,nm}$ and $PSS_{450\,nm}$ in DMSO to avoid hydrolysis of the reactive chloroacetyl moieties. The ability to photo-isomerize using red light was evaluated using 635 nm LEDs. Compared to the unsubstituted azobenzene crosslinker, the π-π* transition band for the dark state appears blue-shifted with an absorption maximum at 333 nm (vs. 360 nm). A weaker absorption band for the n-π* transition could be observed at 461 nm. The photo-stationary state at 360 nm gave a significant decrease of the absorption band for the π-π* transition (327 nm) and a moderate increase of the n-π* absorption band (458 nm). Irradiation using the 635 nm light source led to a stronger decrease of the π-π* transition band and further blue-shift of the absorption maximum to 323 nm. Blue light irradiation resulted in an absorption spectrum similar to the dark state with the maximum of the π-π* transition at 338 nm and the n-π* band at 463 nm (Figure II.5a). Reversibility of photoswitching between those two states was possible for more than 10 cycles without any change in the absorption profile for either of the species.

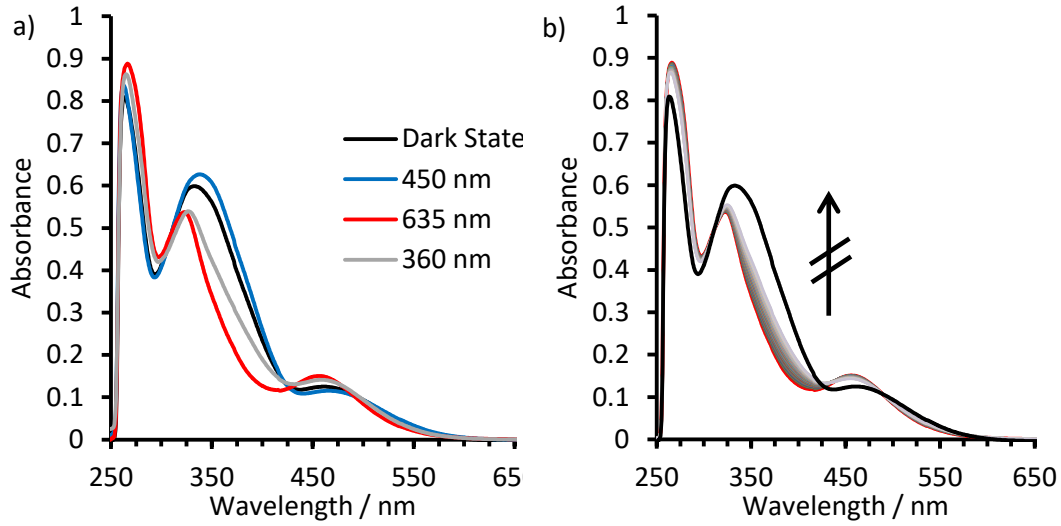

Figure II.5 *a) Absorption-spectrum of **33** for the dark state, $PSS_{450\,nm}$, $PSS_{625\,nm}$, and $PSS_{360\,nm}$. b) Thermal relaxation at 37 °C after 635 nm irradiation, one scan every 60 min is shown. All spectra were obtained in DMSO.*

Thermal relaxation experiments were carried out at 37 °C from $PSS_{625\,nm}$ (Figure II.5b). Relaxation occurred very slowly, with the dark state not reached even after 33 hours. The half-life for the thermal relaxation from the *cis*-to-*trans* isomer at 37 °C in DMSO was calculated to be 2761 min (~46 h). Compared to the non-substituted azobenzene crosslinker **38**, thermal

relaxation occurs significantly slower, indicating a higher thermal *cis*-to-*trans* isomerization barrier. Even at elevated temperatures, the relaxation process was extremely slow and full *trans*-relaxation was only achieved by incubation of a sample in DMSO at 60 °C for several hours. No half-life has previously been reported for the crosslinker alone, but when attached to a test-peptide, the half-life of the conjugate was 3.5 h at 37 °C.[206]

An HPLC-trace of a sample of **33** confirms the strongly hydrophobic character of the crosslinker with *trans*-**33** eluting at ~75% (*v*/*v*) acetonitrile/water (Figure II.6). When an irradiated sample of **33** was subjected to HPLC, a second peak with an earlier retention time could be observed, indicating the presence of the more polar *cis*-**33**. Typically, the *cis*-isomers of azobenzene derivatives display a higher polarity due to the bent phenyl-rings and the subsequent exposure of the lone pairs of the nitrogen atoms of the azo-bond creating a dipole. Chromatographic techniques are a valuable method to determine the number and proportion of isomers present, and to compare their hydrophobicity relative to each another and between crosslinkers.

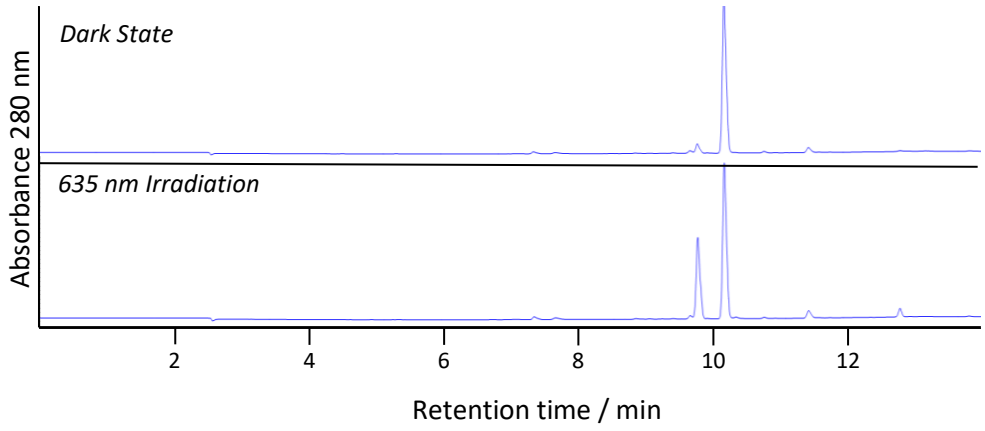

Figure II.6 *HPLC-profile of **33** before and after irradiation with 635 nm.*

UV-visible spectra of *trans*-isomers (dark state) can be recorded without being affected by the *cis*-state for most azobenzene derivatives, but typically corresponding spectra of *cis*-isomers have to be inferred from time-dependent density functional theory (TD-DFT) calculations due to contamination with the *trans*-isomer in real samples. However, in this case a diode-array detector on the HPLC-system was used to scan the absorption values for wavelengths ranging from 250 – 700 nm for each peak that eluted. This allowed the absorption profiles for the *cis*-

33 and *trans*-**33** to be plotted against each other (Figure II.7a). The ratio of the two conformations can also readily be quantified using NMR-spectroscopy.

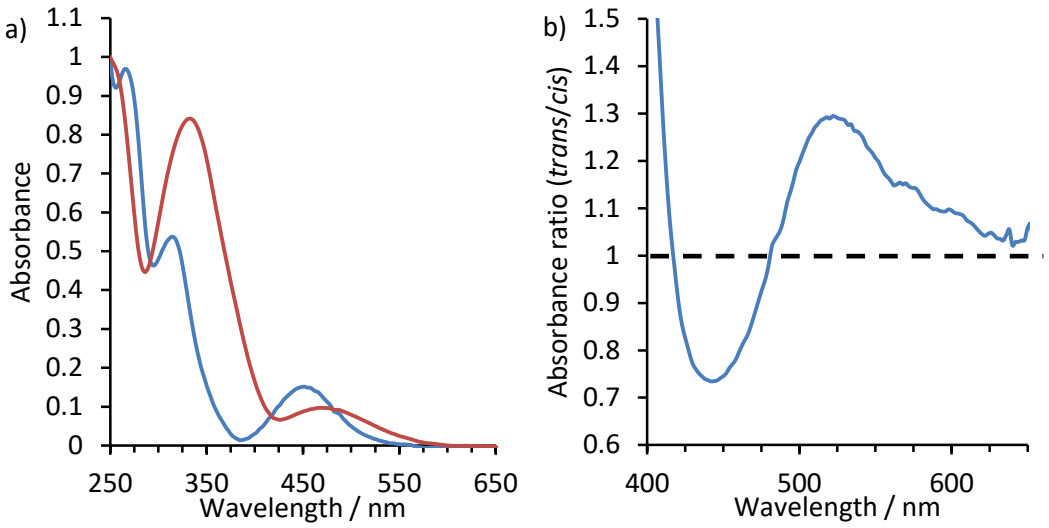

Figure II.7 *a) Extracted absorption profile of the cis- and trans-isomer of* **33** *from the HPLC separation. b) Ratio of the absorbance of the dark-adapted trans-isomer to that of the cis-isomer.*

Figure II.7a shows the UV-visible spectra for the *cis*- (blue) and *trans*-isomers (red). The *trans*-isomer shows a maximum at 332 nm for the π-π* transition and a weaker n-π*band at 466 nm. A shift of these maxima is observed in the *cis*-isomer, with a significantly weaker π-π* transition at 314 nm and a moderately stronger n-π* absorption band at 452 nm. A clear separation between the n-π* transition bands for the two isomers enables direct bidirectional photo-isomerization. Compared to the spectra in Figure II.5a, a shift of ~5 nm can be observed for the n-π* transition of the in both isomers. Those shifts can be mainly linked to the changes in the chemical environment due to the different solvents. Small shifts of the n-π* absorption band of crosslinked peptides have previously been attributed to the variation in solvent hydrogen-bonding to the azo nitrogen atoms and changes in co-planarity of the aromatic rings.[206]

When plotting the ratio of the absorbance of the isolated *trans*- and *cis*-isomer, the relative absorption at a specific wavelength of the two isomers can be seen (Figure II.7b). A value of one indicates that the *cis*- and *trans*-isomer show the same absorption values at this specific wavelength and indicates isobestic points in their spectra. The graph shows a minimum at 442 nm and a maximum at 522 nm displaying the wavelengths with the highest differences for the photo-isomerization of *cis*-to-*trans* and *trans*-to-*cis*, respectively. Isobestic points can be

found at 416 nm and 482 nm in the UV-Vis spectrum. Interestingly, the *trans*-isomer shows a stronger absorbance than the *cis*-isomer from the isobestic point at 482 nm onwards into the red-region of the visible spectrum, as the absorption ratio is greater one. This explains why red-light driven *trans*-to-*cis* isomerization is possible.

The extent of red-light photo-isomerization of **33** was quantified by ^{1}H-NMR-spectroscopy. A sample of *trans*-**33** in DMSO-d6 was irradiated using 635 nm light (Figure II.8). Proton NMR-spectra were run at different time points after irradiation until the photo-stationary state was reached. The ^{1}H-NMR-spectrum of non-irradiated, *trans*-**33** consists of three singlets. The amide-protons could be observed at 10.90 ppm, the aromatic protons at 7.90 ppm and the aliphatic methylene protons at 4.29 ppm. Interestingly, a singlet-signal corresponding to the aromatic protons of the *cis*-isomer at 7.71 ppm integrated for ~7% of the signal from the *trans*-isomer, suggesting that the product obtained from the synthesis exists as an isomeric mixture. Samples of the pure *trans*-isomer as indicated by ^{1}H-NMR spectroscopy (not shown) were obtained following thermal relaxation at 60 °C for 3 hours. Irradiation with red light (635 nm) resulted in the appearance of the slightly upfield signals for the *cis*-isomer. The amide-protons shifted to 10.79 ppm, the aromatic protons to 7.71 ppm and the aliphatic protons to 4.29 ppm. The aromatic protons underwent the greatest chemical shift due to the loss of conjugation to the other phenyl group. In the bent *cis*-conformation, the aromaticity of the crosslinker is greatly diminished and the azo-group imposes an inductive effect on the phenyl-rings causing the upfield-shift. The photo-stationary state at 635 nm consists of 85 % *cis*-isomer. Irradiation with blue light (450 nm) yielded 81% *trans*-isomer and 19% cis-isomer resulting in a ~4.5 fold change for the bidirectional photo-isomerization using those two wavelengths.

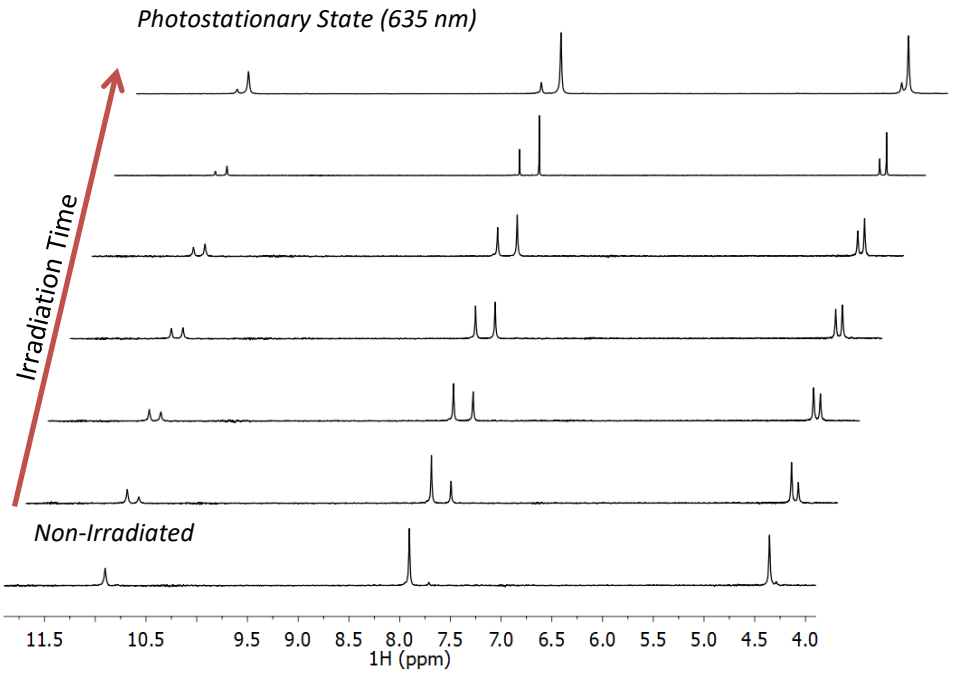

Figure II.8 *^{1}H-NMR spectra of **33** after irradiation with 635 nm at different time intervals.*

iii. Synthesis of Di-Cysteine Crosslinker

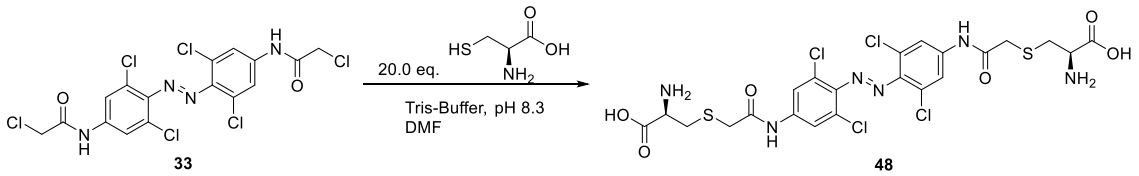

Scheme II.5 *Reaction of **33** with L-cysteine to obtain **48**.*

In order to test the crosslinkers robustness in a cellular environment, its toxicity and uptake abilities, the terminal ends were reacted with *L*-cysteine as the charged N- and C-termini of cysteines were expected to increase the water solubility of the otherwise poorly soluble crosslinker **33**.

The reaction was first attempted under the conditions reported in the literature to attach the crosslinker **33** to peptides. However, reaction overnight at 45 °C did not lead to a soluble product as evidenced by a colourful precipitate and the colourless supernatant. Dimethylformamide (DMF, 50 % v/v) was added in an attempt to dissolve the crosslinker **33** to improve the reactivity towards the cysteines. The reaction was left overnight, but no improvement in solubility was achieved. The obtained precipitate did in fact contain the

intended product according to mass spectrometry, but it was not soluble even in neat in DMF or DMSO. The diminished solubility as compared to the crosslinker on its own could originate from the amphipathic nature of the amino acid, which might contribute to cation-π-interactions with the aromatic rings (Figure II.9) rather than interacting with solvent molecules. Polar interactions could also exacerbate the effects of existing aromatic interactions, such as π-stacking, making the product even less soluble compared to the unmodified crosslinker.

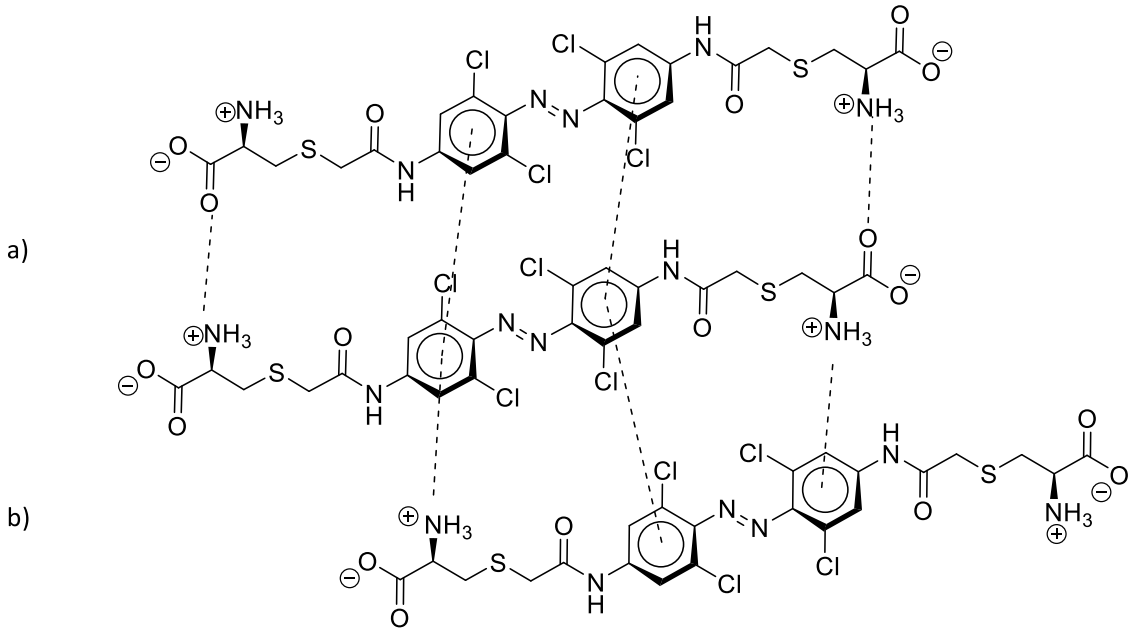

Figure II.9 *Proposed intermolecular interactions decreasing the solubility of **48**. a) π-stacking and b) cation-π-stacking as main-driving force for the formation of aggregates.*

Due to its low solubility, **48** could only be characterised by mass spectrometry. The calculated isotopic pattern of the product was identical to the isotopic pattern of the measured sample and a handful of other fragment peaks were observed (Appendix 1), suggesting successful synthesis of **48**. Further testing in mammalian cell culture lab was deemed impractical due to the adverse physical properties of **48**.

d. Halide Exchange Reaction

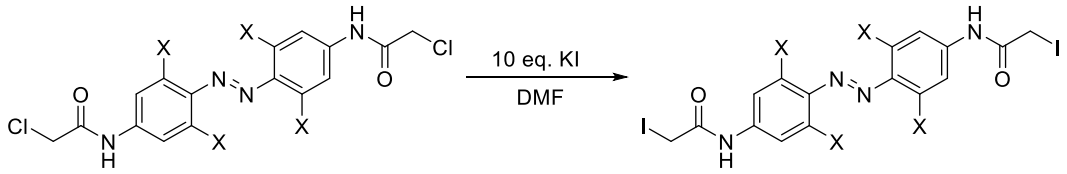

X: Cl **33**
X: H **38**

X: Cl **49**
X: H **36**

Scheme II.6 *Finkelstein-reaction to exchange the chloride with iodide in* ***33*** *and* ***38****.*

In order to increase the reactivity of the crosslinkers **33** and **38** towards nucleophilic groups, a halide exchange of the chlorides with iodide was performed *via* a modified Finkelstein procedure. Potassium iodide is approximately 16-fold more soluble in DMF than potassium chloride pushing the halide exchange equilibrium towards the desired product.[215] Crosslinkers were dissolved in DMF, excess potassium iodide was added and the reaction was stirred overnight at 45 °C. The precipitation of potassium chloride indicated successful synthesis. The products were then isolated by pouring the reaction mixture into dilute hydrochloric acid, precipitating them whilst dissolving potassium halide salts. Acidic conditions were chosen to prevent hydrolysis of the iodoacetates. The precipitate was then washed with acetonitrile and diethyl ether to remove any water, then dried under vacuum to yield **49** and **36**. Compared to the acetyl chloride analogous **33** and **38**, the chemical shifts of the methylene protons are most affected by the new substituent and appear more shielded in the ^{1}H-NMR spectra (3.87 ppm vs. 4.31 ppm for **36** and 3.88 ppm vs. 4.36 ppm for **36**, Appendix 2). This is due to the weaker electronegativity of iodine compared to the chlorine substituents leading to a less polarised carbon atom and hence a more shielded proton environment.

e. Conclusion

Azobenzene crosslinkers **38** and **33** were synthesised and their UV-Vis spectra and photo-stationary states at their dark states, 360 nm, 450 nm and 625 nm, respectively were characterised. *Cis*-to-*trans* relaxation spectra were recorded and the half-life times for relaxation of the isolated crosslinkers in DMSO were calculated. Both isolated azobenzenes showed significantly longer half-lives than literature-values for their half-lives when conjugated to peptides. Their photo-stationary states were analysed by ^{1}H-NMR spectroscopy to determine the ratio of the *cis*- and *trans*-species. Separation of the isomeric mixture of **33**

by HPLC and subsequent analysis using a diode-array detector gave access to the isolated UV-visible absorption spectra of the *cis*- and *trans* conformation. Plotting the absorption ratio for the *trans*/*cis*-isomers explains why red-light photo-isomerization from *trans*-to-*cis* can be applied with azobenzene **33**.

Several steps of the synthesis of **33** required modification to be successful. During the synthesis an interesting side-product, **46**, was formed that may possess promising photo-physical properties when converted into a crosslinker. A synthetic procedure was established to synthesise **46** directly, but the final steps to convert **47** into an azobenzene crosslinker remained problematic. Halide-exchange reactions were carried out for **33** and **38** to improve their reactivity towards nucleophiles.

2. Synthesis of Pro-Apoptotic BH3 Peptides for the Photochemical Control over Cell Fate

a. Aims and Objectives

Synthetic biochemical tools for controlling apoptosis could help unravel the complex pathways governing cell fate and provide new therapeutic agents for disease. Using light to control the activity of molecules enables the generation of transient or localised effects that are difficult to realise with traditional chemical methods. Peptides derived from the pro-apoptotic BH3 domain were therefore synthesised such that, when combined with azobenzene crosslinkers, they would induce apoptosis in a light dependent manner. The peptides contained various cysteine-spacings for different light-driven responses and terminal cell-penetrating peptide (CPP) sequences to allow cellular uptake. Previous reports stated that a BSBCA (**37**)-crosslinked Bid$^{i,i+4}$ peptide showed a ~20 fold difference in binding affinity to the target protein Bcl-x_L in its dark and light states.[211] However, this design was of limited application as this conjugate is not cell permeable. Therefore, the initial focus was to establish an effective synthetic route for the Bid$^{i,i+4}$ peptide with and without a CPP. Other pro-apoptotic peptides bearing cysteine residues in alternative spacings (*i,i* + 7*, i,i* + 11*)* were also investigated. Different strategies were tested to synthesise the pro-apoptotic peptides including recombinant expression using *Escherichia coli* and solid-phase peptide synthesis. In addition, a novel enzymatic ligation approach was employed to conjugate CPP- and BH3-peptides together.

b. Bio-Synthesis of Pro-Apoptotic Peptides

Octa-arginine (R_8) is a cell-penetrating peptide (CPP) sequence widely used to facilitate the uptake of peptides or proteins by cancerous cell lines, such as HeLa, KG1a or A431.[216,217] A BH3-R_8 peptide construct was designed with the high-dynamic range *i,i* + 4 cysteine spacing. Based upon previous reports on the production of peptides by recombinant expression in *E. coli*, a similar recombinant production strategy was attempted.[217] A plasmid containing DNA encoding a BH3$^{i,i+4}$-R_8 peptide repeats fused to a sequence encoding ketosteroid isomerase protein was used. Codons for methionine were located between each BH3$^{i,i+4}$-R_8 gene repeat for downstream peptide processing. From this plasmid, the ketosteroid isomerase fused peptides were expressed in inclusion bodies using the BL21 (DE3) strain of *E. coli* grown in auto-inducing media (100 μg/mL of ampicillin) for 72 h at 25 °C. The protein was purified by washing in three different buffer systems of increasing ionic stength before dissolving the pellet in guanidinium hydrochloride solution (6 M) and dialysis against water.

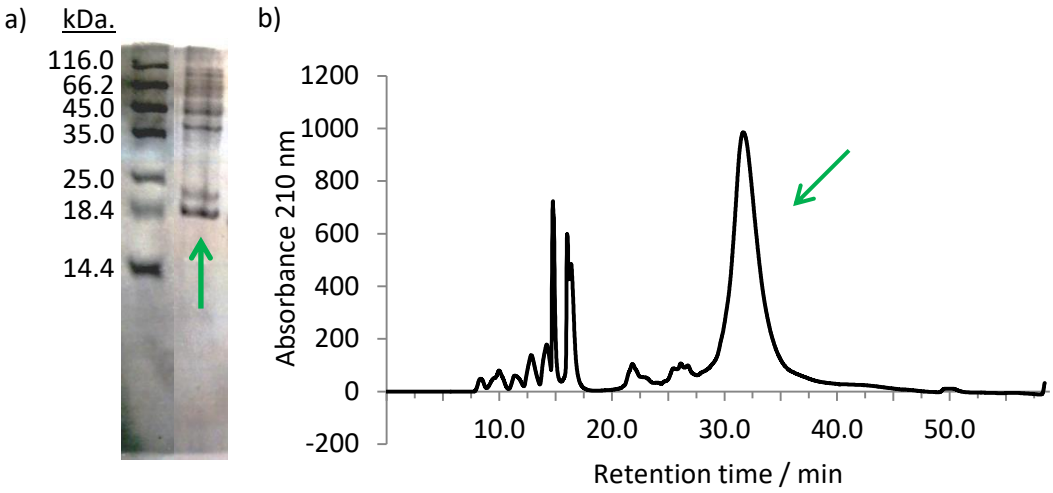

Figure II.10 *a) SDS-gel of KSI-tag fused to Bid$^{i,i+4}$-R$_8$ (total mass: 17.3 kDa.) b) HPLC-profile of Bid$^{i,i+4}$-R$_8$ after CNBr cleavage. The green arrow indicates the target band and peak in the SDS-gel and HPLC-chromatogram, respectively.*

Analysis by SDS-PAGE showed a clear band at the expected mass for the protein (17.3 kDa.) (Figure II.10). However, the band size indicated a relatively low level of overexpression. The precipitate was treated with cyanogen bromide to cleave the protein at the methionine residues and liberate the Bid$^{i,i+4}$-R$_8$ peptides as C-terminal homoserine lactones. The crude peptide mixture was separated by HPLC (Figure II.10) and the main fraction (30.0 – 35.0 min) collected. However, characterisation *via* mass spectrometry was unsuccessful, possibly due to the eight arginine residues, giving complex and ambiguous mass spectra. To see if the product obtained was consistent with similar peptides, a SDS-polyacrylamide gel was prepared containing 20% acrylamide other peptides, previously synthesized by similar or solid-phase peptide synthesis methods, were used as standards (Figure II.11). (6)[FAM]-Bid$^{i,i+4}$-NH$_2$, Tat-Bid, Bid$^{i,i+4}$-R$_8$ and Bid$^{i,i+7}$-R$_8$ were used as reference compounds. The gel was treated according to standard protocols and stained with Coomassie Brilliant Blue. No bands were observed for the reference peptide (6)[FAM]-Bid$^{i,i+4}$-NH$_2$ indicating that the peptide ran through the gel within the time (60 min) and voltage (150 V) of the electrophoresis process. This could be due to the additional negative charge of the FAM-tag, which accelerates the transport through the gel. Another reason could be the lack of reactive sites for the staining agent due to the overall negative charge. The synthesised Bid$^{i,i+4}$-R$_8$ and Tat-Bid showed one band at the same height indicating pure compounds of a similar molecular weight.

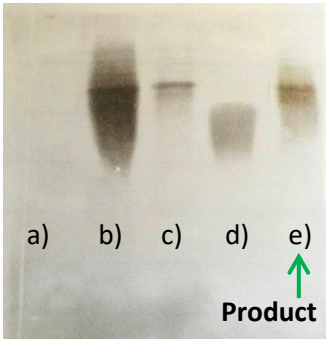

Figure II.11 *SDS-PAGE (20% acrylamide) of synthesised Bid$^{i,i+4}$-R$_8$ (e) against (6)[FAM]-Bid$^{i,i+4}$-NH$_2$ (a), Tat-Bid (b), reference peptide Bid$^{i,i+4}$-R$_8$ (c) and Bid$^{i,i+7}$-R$_8$ (d).*

As mass-spectrometry repeatedly failed to characterise the peptide, an alternative method was required to establish whether the synthesised peptide was in fact functional Bid$^{i,i+4}$-R$_8$. Bcl-x$_L$ has a specific and well-characterised interaction with BH3 helices that can be probed using solution-state NMR and chemical shift perturbations, which are already known for other BH3 peptides, such as Bak$^{i,i+11}$. The synthesised peptide Bid$^{i,i+4}$-R$_8$ (232 µM, 1.1 eq.) was therefore incubated with a sample of ^{15}N-Bcl-x$_L$ (211 µM, 1.0 eq.) to visualise potential binding interactions by ^{15}N NMR spectroscopy. Certain residues of ^{15}N-Bcl-x$_L$ undergo significant and distinct chemical shifts upon a BH3-domain peptide binding to its hydrophobic groove.[213] However, addition of the peptide to the protein-sample resulted in the formation of a precipitate. The supernatant of the sample showed a significant loss of unbound-protein signal. Although no peptide-protein-complex was directly observed by NMR, interaction between peptide and protein is a likely cause for the formation of precipitate and indicates that the Bid$^{i,i+4}$-R$_8$ may well have been synthesised.

As it was suspected that either the R$_8$ tag or some other event during treatment with cyanogen bromide was preventing characterisation by mass spectrometry, an alternative approach was attempted to synthesise Bid$^{i,i+4}$ as a reference-peptide. Short peptides are poorly expressed in *E. coli*, so a plasmid was designed containing DNA encoding a His$_6$-tag, a GB1-protein fused to a TEV (Tobacco Etch Virus, a nuclear-inclusion endopeptidase) cleavage site followed by the Bid$^{i,i+4}$ sequence (total mass: 10.74 kDa.) (Figure II.12). Primers were designed and the DNA sequence coding for Bid$^{i,i+4}$ was copied from the plasmid used for the Bid$^{i,i+4}$-R$_8$ expression using polymerase chain reaction (PCR) techniques. The PCR product was then inserted into an existing acceptor plasmid by Golden Gate ligation to give the target plasmid.[218]

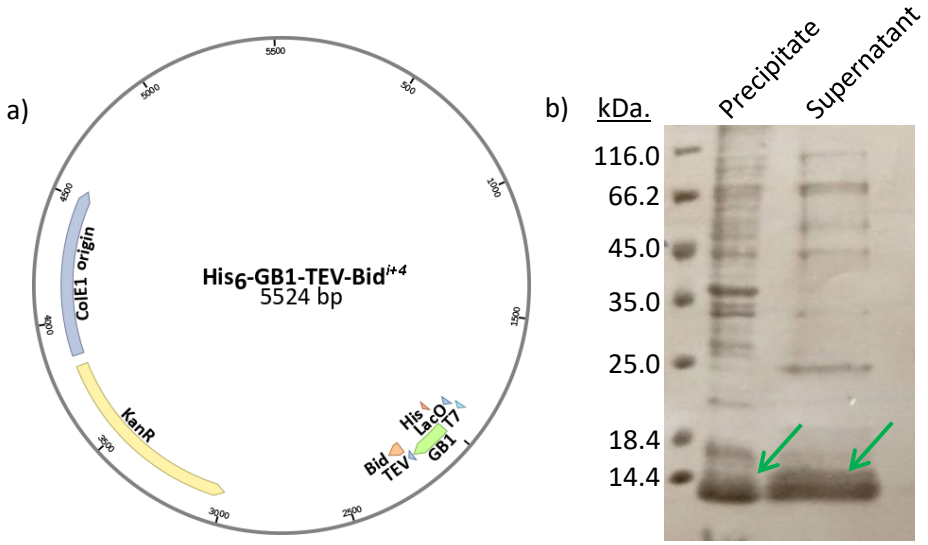

Figure II.12 *a) Plasmid-map displaying key parts of the BH3-Bid peptide with TEV protease recognition sequence, solubility tag GB1 and His_6-tag under T7 promoter, kanamycin resistance cassette and ColE1 origin of replication. b) SDS-PAGE of the expressed, purified and concentrated N-His_6-GB1- BH3-Bid protein (10.74 kDa.) prior to TEV protease digestion.*

The $Bid^{i,i+4}$ peptide-containing fusion protein was expressed in *E. coli* BL21 (DE3) RP cells. A single colony was grown in LB media (50 µg/mL of kanamycin) for 16h at 16 °C. The protein was purified using a Ni-NTA column with an imidazole gradient (5 - 500 mM) to first wash, then elute the product from the column. The product fractions were concentrated on an Amicon filtration system using a 5.0 kDa cut-off membrane. The imidazole buffer was exchanged for a high salt buffer (500 mM NaCl and 100 mM Na-phosphate, pH: 7.5) and the sample was concentrated. Formation of precipitate was observed at 4 °C, which returned to solution upon warming to room temperature. Analysis of the precipitate by SDS-PAGE indicated protein with minor impurities while the supernatant consisted of purer protein (Figure II.12). The concentrated sample was treated with TEV protease in the presence of tris(2-carboxyethyl)phosphine (TCEP), centrifuged to remove any precipitates and applied to a Ni^{2+}-NTA column. Analysis of the flow-through by mass spectrometry confirmed the presence $Bid^{i,i+4}$-peptide (Appendix 3).

Following the successful synthesis and characterisation of the $Bid^{i,i+4}$-peptide, two complementary restriction enzyme cleaving sites for *Bsa*I were introduced into the plasmid after the sequence encoding the BH3 peptide using PCR techniques and the presence of the desired sequence was confirmed by DNA sequencing. *Bsa*I cuts DNA outside its recognition site and creates unique overhangs that can be used in combination with a ligase to rapidly assemble DNA parts. The post-ligation plasmid lacks *Bsa*I sites and remains uncut in the presence of the enzyme.

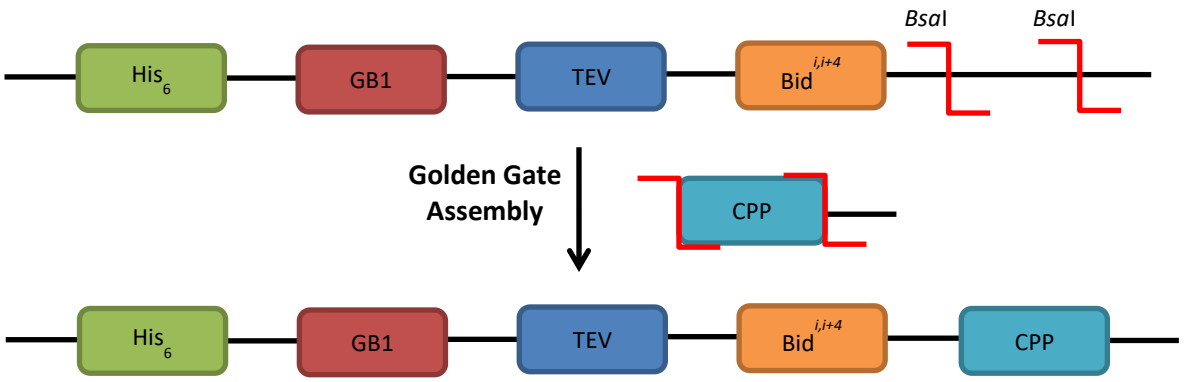

Figure II.13 *Schematic map of the new acceptor-plasmid containing BsaI protease sites for the rapid insertion of CPP-tags.*

The *Bsa*I site-containing plasmid could therefore be used as a template to introduce different tags or CPPs on the C-terminus of the Bid$^{i,i+4}$ sequence using oligonucleotides with corresponding *Bsa*I sites *via* Golden Gate techniques (Figure II.13). However, upon critical reflection, doubts were raised about the ability of biosynthesis to deliver the necessary quantities of material and alternative synthetic strategies were investigated.

c. Solid-Phase-Peptide Synthesis and Enzymatic Ligation

i. Overview

Recombinant peptide production suffers from low yields and challenges with expression of small peptides that are frequently unexpressed or proteolytically digested during production. The small size means peptides have to be produced fused to larger proteins, which reduce yields. Therefore, a solid state synthetic approach was taken before further progress was attempted with recombinant synthetic techniques. A clear challenge with this approach is that, different to automated systems, the manual peptide synthesis can be time and labour intensive.

In order to investigate a large number of peptide constructs with different CPPs a modular synthetic approach was required. Solid-phase peptide synthesis (SPSS) is a well refined method and can be performed either by automated systems, or more slowly but with a greater degree of control by manual peptide synthesis. The C-terminus of an N-terminal protected amino acid is first anchored onto a solid-support. Iterative deprotection and coupling steps, using soluble reagents and new amino acids, which can be washed from the resin after reaction is complete

lead to a growing peptide chain. The N-terminal Fmoc-protecting groups on the amino acids can be released using basic conditions while the protecting groups of reactive side-chains and the linkage to the solid support are acid-labile. Compared to the recombinant approach, SPPS offers a greater degree of flexibility, enabling the use of a wide variety of unnatural, isotopically labelled and enantiomeric amino-acids. However, aggregation and low yields with increasing chain lengths limit the practical application of SPPS to peptides <100 amino acids.

A number of different ligation strategies exist that have been exploited to combine peptide fragments to a bigger sequence to achieve the desired modular synthesis of BH3 and CPP components. Chemical ligation techniques often involve the modification of N- or C-terminal residues to ensure reactivity between the peptide chains. In contrast, enzymatic ligations only rely on the introduction of specific recognition sequences to ligate two peptide strains. Asparaginyl endopeptidases from *Oldenlandia affinis* (OaAEP1) hydrolyses C-terminal asparagine residues, ligating them to the N-terminus of another peptide. The reversibility of the reaction requires a large excess of one of the peptides in order to drive the equilibrium towards the product. The recognition sequence for OaAEP1 consists of three amino acids for the peptide to be ligated through its C-terminal end: Asn-X-Leu, with X being any of the other proteinogenic amino acids except Pro. A Gly-Leu motif on the N-terminus of the second peptide has been used as a nucleophile during the ligation (Scheme II.7).[219]

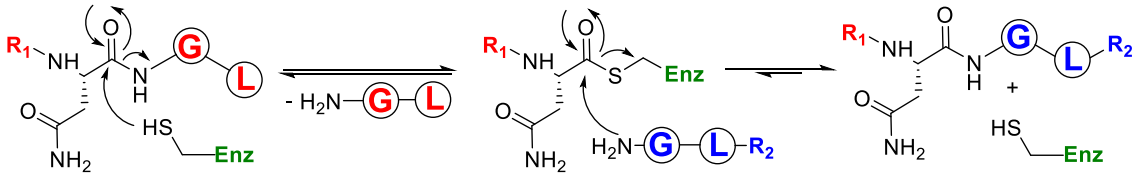

Scheme II.7 *Reaction scheme of the enzyme OaAEP1. The recognition sequences Asn-Gly-Leu and Gly-Leu are shown for both peptides.*

It was anticipated that, using OaAEP1, a library of peptides consisting of various BH3-peptides and different CPPs could be easily accessible. The chosen synthetic route would involve the BH3-peptide being crosslinked prior to ligation, making its preparation more difficult, so the CPP-peptide would then be added in excess to push the equilibrium to the product side. Following the difficulties analysing Bid$^{i,i+4}$-R_8 using mass spectrometry, an alternative CPP, the Ant sequence derived from the antennapedia protein was used instead. This sequence has

been demonstrated by Lutz and co-workers to enhance apoptosis in HeLa cell through fusion to the N-terminus of a related BH3-peptide.[143] A number of peptides comprising the *Ant* and Bid$^{i,i+4}$ sequence of varying lengths and enzyme recognition sequences were synthesised by SPPS and purified by HPLC to explore the suitability of this approach (Table II.1).

Table II.1 *Synthesised peptides for the ligation with the enzyme OaAEP1.*

Peptide	Length	Sequence
Bid$^{i,i+4}$-NH_2	5-mer	GL-DIIRN-NH_2
	Full-length	GL-DIIRNIARHLACVGDCIDRSI-NH_2
Ant-NH_2	5-mer	MKWKK-NGL-G-NH_2
	Full-length	RQIKIWFQNRRMKWKK-NGL-G-NH_2
	Full-length	RQIKIWFQNRRMKWKK-NCL-G-NH_2

ii. Short Fragment Peptide Ligation

Different conditions were screened to test the applicability of OaAEP1-mediated ligation using truncated models of Bid and Ant in preliminary experiments as single repeats (Table II.1). The 5-mers of Bid and Ant containing the corresponding enzyme recognition site on their N- and C-termini, respectively, were synthesised and purified. Expression, purification and activation of OaAEP1 were kindly carried out by Simon Tang (Cardiff University). Samples were reacted in sodium acetate buffer at pH 5.0 and at 37 °C and with an OaAEP1 concentration of 100 nM. Peptides were added in ratios with concentrations ranging from 100 µM to 2 mM and the reaction progress monitored by LC-MS at time points ranging from over 3 hours (Table II.2).

Table II.2 *Different peptide ratios and time points used for the ligation of the short fragments GL-Bid5 (GLDIIRN) and Ant5-NGLG (MKWKKNGLG).*

	GL-Bid5 : Ant5-NGLG (100 µM)					
	1 : 5	**5 : 1**	**1 : 10**	**10 : 1**	**1: 20**	**20 : 1**
Reaction time	1 h	1 h	1 h 2 h	1 h 2 h	1 h 2 h	1 h 2 h

			3 h	3 h	3 h	3 h

Samples of reactions were quenched by the addition of hydrochloric acid (10% *v*/*v*, 1 M) at different time points to evaluate the progress of the ligation and to compare to samples exposed to the same conditions without any enzyme. Bid5 and Ant5 separated well by HPLC owing to their very different degrees of hydrophobicity. After enzymatic ligation, a new product peak was observed between the two starting materials, suggesting the desired combination of the hydrophilic properties of the CPP with the hydrophobic character of the BH3 peptide, which gave a mass spectrum corresponding to product. In all cases, no further product formation was observed after 1 hour. No side-products could be detected during the enzymatic ligation step. Figure II.14 shows the elution profile at 210 nm of 100 µM Bid5 and 500 µM Ant5 without addition of OaAEP1 and after 1 hour of reaction using the enzyme. No other products were detected at 210 nm or by the total ion chromatogram (TIC) of the reaction mixture. Deconvolution of the mass-spectrum for the newly emerged peak suggested the formation of the expected product.

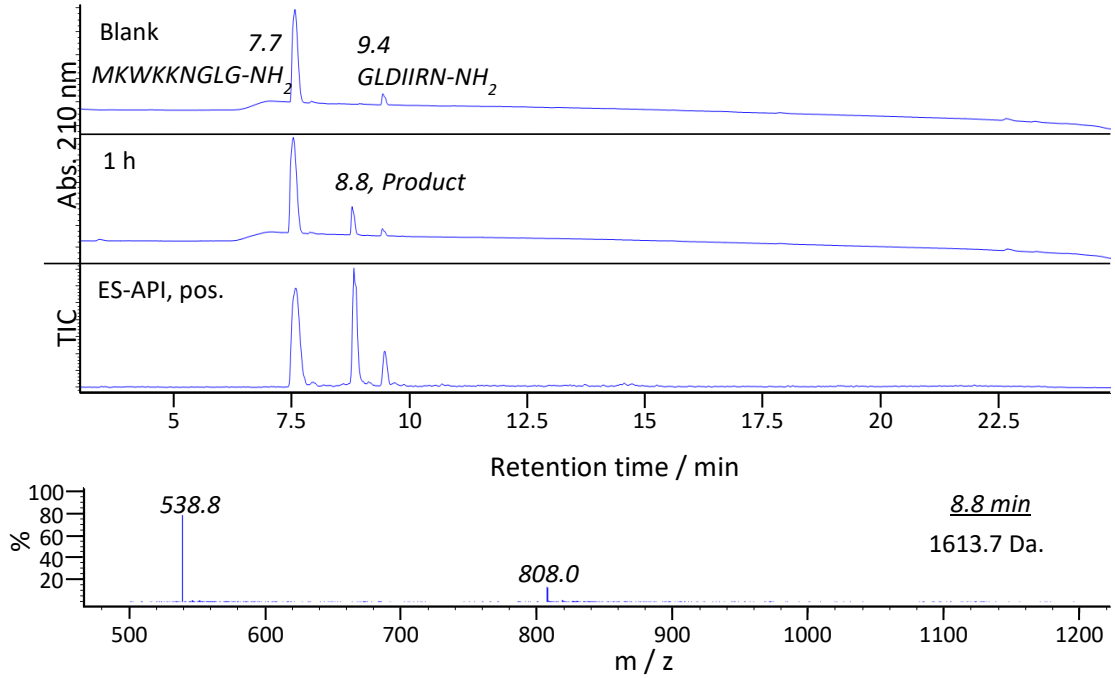

Figure II.14 *LC-MS traces of the enzymatic ligation of the short peptide sequences for 100 µM GL-Bid*$^{i,i+4}$ *and 500 µM Ant-NGLG. Elution profile without and with the enzyme OaAEP1 after 1 h at 210 nm and TIC of the reaction mixture after 1 h. Mass-spectrum for the isolated peak eluting at 8.8 min corresponding to the expected ligation product (calc.: 1615.0, obsv.: 1613.7).*

The peptides show different absorption profiles at 210 nm due to their differing number of peptide bonds and side-groups. As a result, the integrated peaks cannot be compared to each other directly to quantify the composition of the reaction mixture without further calibration. However, assuming that the amount of peptide shows a linear correlation to its absorption value at 210 nm, a qualitative estimation can be made based on the peak area before and after the reaction. A significant change of the ratio between the two starting materials indicates depletion of either one and that the equilibrium is shifted towards the product (Table II.3).

Table II.3 *Reduction in the integrated peak area of the limiting reagent as a percentage of the total integrated reagent area compared to a reaction lacking enzyme (peptide concentration in 100 µM).*

	Bid5:Ant5 Ratio (100 µM)					
	1:5	**1:10**	**1:20**	**5:1**	**10:1**	**20:1**
Limiting reagent	Bid5	Bid5	Bid5	Ant5	Ant5	Ant5
% Limiting reagent in blank	6.7%	13.8%	10.7%	41.5%	26.7%	16.7%
% Limiting reagent in reaction	3.7%	1.1%	0%	38.7%	0%	12.8%
Estimated limiting reagent remaining	55%	8%	0%	75%	0%	77%
Estimated conversion	**45%**	**82%**	**100%**	**25%**	**100%**	**23%**

Interestingly, only the samples with a GL-Bid5:Ant5-NGLG ratio of 10:1 and 1:20 showed a complete depletion of Ant5-NGLG in the 210 nm trace. Likewise, very little GL-Bid5 remained after 1 hour when reacted in a ratio of 1:10. In contrast, the ratio of the integrated peaks of the two peptides showed hardly any change for a 20:1 GL-Bid5:Ant5-NGLG ratio. Overall, these results support the assumption that excess starting material is needed to drive the product formation. However, the type of peptide in excess seems to play an important role as shown by the reactions with 1:20 and 20:1 ratios.

Product formation by OaAEP1 is governed by two equilibria (Scheme II.7); reversible attack of the enzyme on Ant5-NGLG, and hydrolysis of the peptide bond to release a NH_2-Gly-Leu-Gly-NH_2 peptide. This tripeptide competes with GL-Bid5 and reaction can proceed either through re-attack of the tripeptide to reform the starting material or product formation through attack by GL-Bid5. Based on the observations in Table II.3, addition of excess GL-Bid5 promotes back-reaction, whereas excess addition of Ant5-NGLG seems to promote the formation of ligated product in the second equilibrium. No Ant5-NGLG peptide remained after the reaction when GL-Bid5 was used in 10:1 excess according to the analytical HPLC-profile before and after the enzymatic reaction for 1 h (Figure II.15a). In contrast, the reverse ratio led to some GL-Bid5 peptide remaining in the mixture following the reaction albeit greatly diminished (Figure II.15b). The much stronger extinction coefficient of the Ant5-NGLG peptide at 210 nm compared to GL-Bid5 is also evident in Figure II.15a where GL-Bid5 is in 10-fold excess.

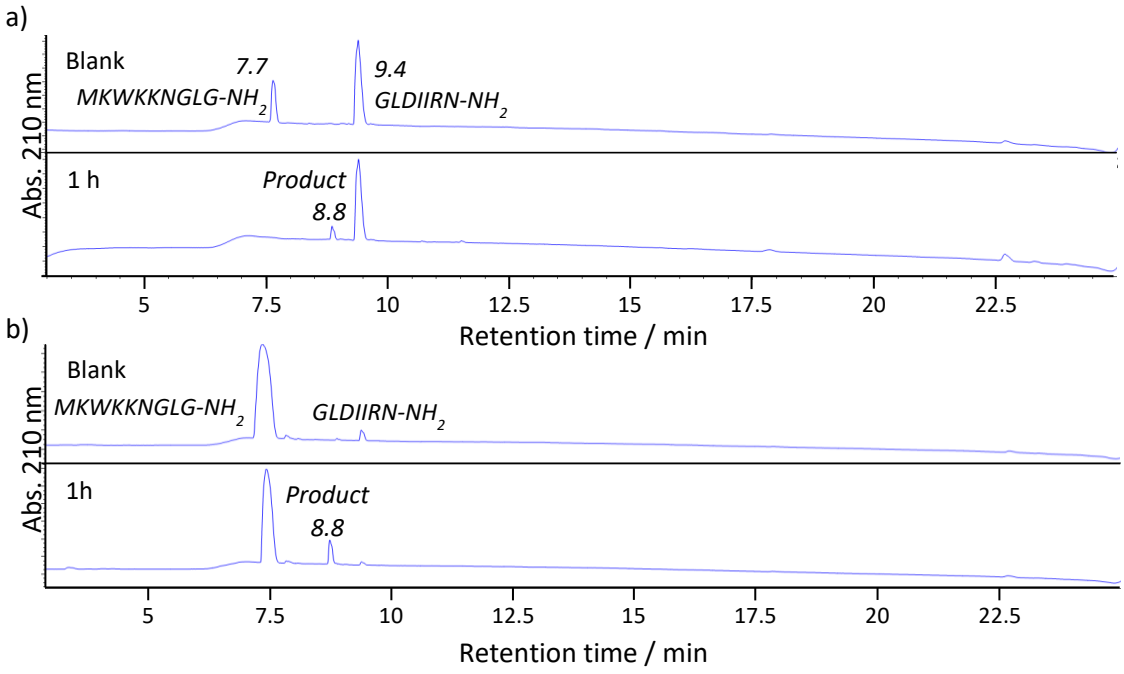

Figure II.15 *HPLC-traces at 210 nm of the shortened sequences of GL-Bid5 (GLDIIRN-NH_2) and Ant5-NGLG (MKWKKNGLG-NH_2) without and with OaAEP1 after 1 h in ratios of (a) 10:1 and (b) 1:10.*

iii. Full-Length Peptide Ligation

Following the successful ligation of the truncated model peptides, full length GL-Bid$^{i,i+4}$-NH_2 and Ant-NGLG-NH_2 peptides were synthesised by SPPS and purified by HPLC for enzymatic ligation.

As the eventual goal was to carry out the ligation on a preparative scale, the right balance between appropriate peptide-ratio and availability of the peptides needed to be struck. Therefore, the enzymatic ligation-reactions were first carried out for peptide-ratios of 10:1 and 5:1 (Ant-NGLG-NH_2 : GL-Bid$^{i,i+4}$-NH_2) on an analytical scale. The conditions used for the full-length peptide ligation were the same as for the short-fragment ligation.

Ant-NGLG-NH_2 and GL-Bid$^{i,i+4}$-NH_2 were also easily separated by HPLC (Figure II.16). The difference in amino acid composition and length of the peptides resulted in a generally stronger absorption of Ant-NGLG compared to GL-Bid$^{i,i+4}$ at 210 nm. The enzymatic ligation reaction was carried out for 1 hour, and LC-MS analysis showed a new peak at 11.3 min corresponding to the ligation product (m/z = 4865.80). The retention time of the product lay between those of the two starting material-peptides, suggesting the correct combination of hydrophobic and hydrophilic characters for the ligated product. Due to the strong absorption of Ant-NGLG-NH_2, the peaks for the product and GL-Bid$^{i,i+4}$-NH_2 appear relatively small at 210 nm and seem negligible. However, analysis of the TIC showed the presence of the product and GL-Bid$^{i,i+4}$ starting material (Figure II.16). Samples with a peptide ratio of 10:1 (Ant-NGLG-NH_2 : GL-Bid$^{i,i+4}$-NH_2) showed no apparent improvement over the product-to-starting-material distribution compared to the reaction that was set at the ratio of 5:1 (Figure II.16).

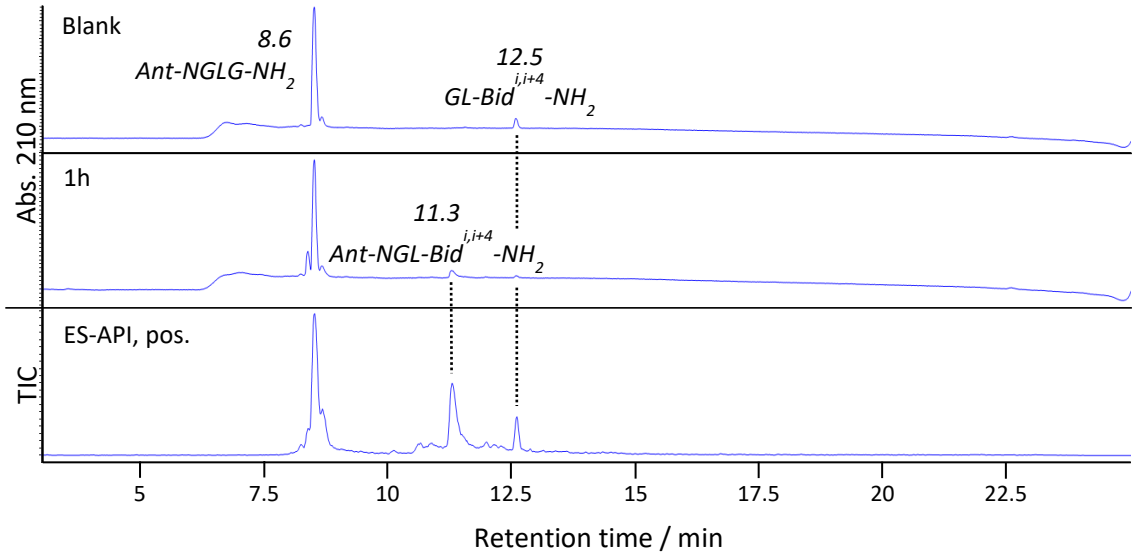

Figure II.16 *HPLC-traces of the ligation of full-length GL-Bid$^{i,i+4}$-NH_2 and Ant-NGLG-NH_2 without (blank) and with OaAEP1 after 1 h in the ratio of 5:1.*

The enzymatic ligation of the full-length peptides was attempted on a larger scale using 500 µM Ant-NGLG-NH_2 and 100 µM GL-Bid$^{i,i+4}$-NH_2 (ratio 5:1) in a total volume of 30 mL (i.e.: 7.6 mg of GL-Bid$^{i,i+4}$-NH_2, 38.9 mg of Ant-NGLG-NH_2). The reaction was monitored by LC-MS and quenched with HCl (10% v/v, 1 M) after 1 hour. Similar to the ligation reaction carried out on an analytical scale (Figure II.16), both starting material-peptides and the product could be detected by LC-MS at 210 nm and TIC. However, only < 1 mg of ligated product was recovered after HPLC purification along with ~27 mg of Ant-NGLG-NH_2, making further optimisation of the reaction necessary.

A major hurdle issue with the enzymatic ligation is the reversibility of the reaction. The product contains the OaAEP1 substrate sequence and can be re-attacked by the enzyme to form the starting material. Excess addition of starting material can shift the equilibrium towards product side but may not be practical or economical on a bigger scale. To eliminate at least one of the equilibria, the product of the enzymatic cleavage could be removed from the reaction mixture or made unreactive. Pyruvic acid readily reacts with cysteines to form thiazolidine derivatives even at similar reaction conditions.[220,221] It was therefore anticipated that by changing the recognition sequence of the CPP Ant from NGLG to NCLG and the addition of pyruvate, an unreactive thiazolidine-derivative would be formed (Scheme II.8). The formation of a heterocycle using the thiol-group of cysteine would remove the nucleophilic character of the N-terminus and drive the first equilibrium of the ligation reaction.

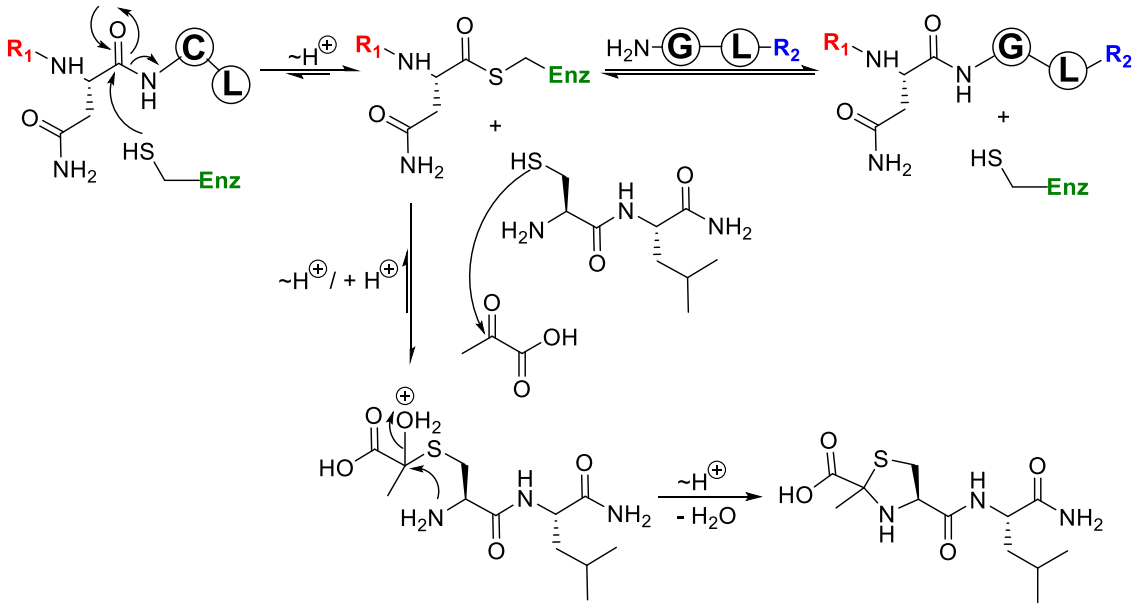

Scheme II.8 *Reaction of pyruvic acid with the side-chain of an N-terminal cysteine leads to the formation of a thiazolidine product, eliminating the first equilibrium of the enzymatic ligation.*

The appropriate Ant-NCLG peptide was synthesised and purified in order to test this hypothesis (Table II.1). Due to the expected irreversibility of the first reaction, the ligation was carried out using the peptides Ant-NCLG-NH_2 and GL-$Bid^{i,i+4}$-NH_2 in 1:1 and 1.5:1 ratios in the presence of 10 equivalents of pyruvic acid. After ensuring that the pH was correctly buffered at 5.5, the reaction was carried out for 1 hour at 37 °C. Samples without any enzyme and samples lacking pyruvic acid were subjected to the same conditions as a control.

In all samples, another peak close to the Ant-NCLG-NH_2 starting material was observed with a retention time of 8.4 min (Figure II.17). The extent of absorption for this species at 210 nm varied throughout the samples, suggesting a non-uniform formation of this side-product. Analysis by mass spectrometry suggested a mass corresponding to Ant-N-OH (2360.84 Da.), which could suggest hydrolysis, but probably originates from non-enzymatic N-terminal cysteine/pyruvic acid condensation due to the presence of this peak in the no-enzyme control samples (Figure II.17).

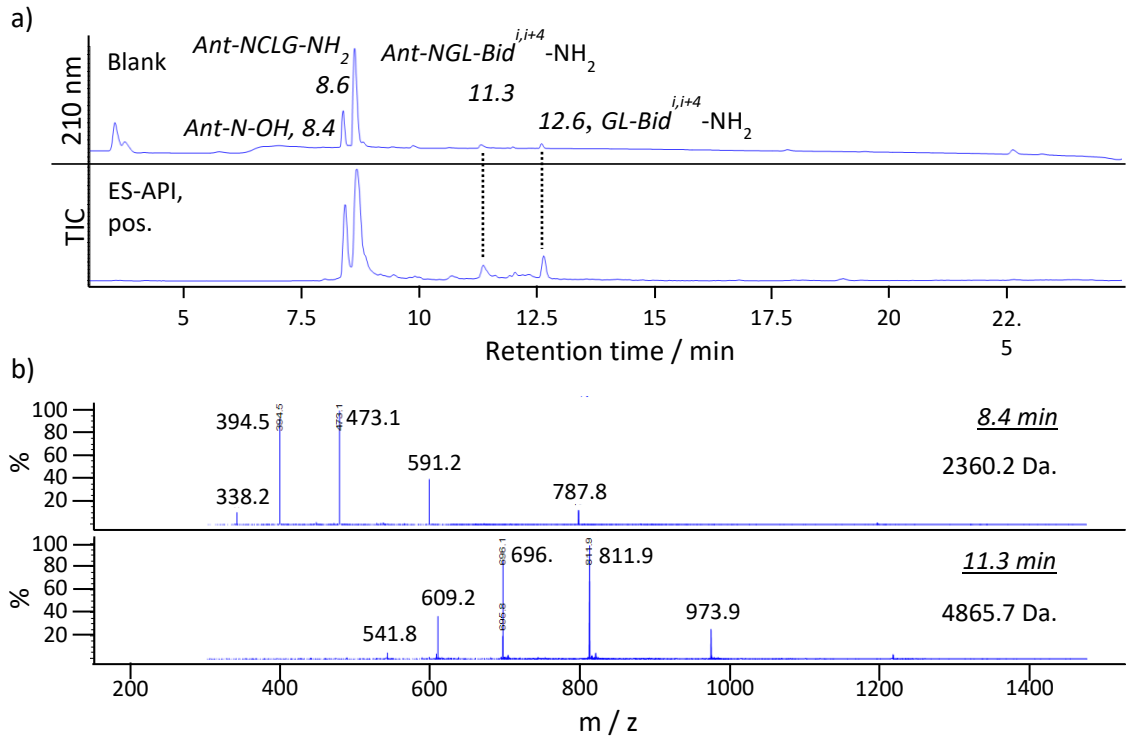

Figure II.17 *a) LC-MS trace of the reaction mixture without any enzyme using Ant-NCLG-NH_2 and GL-$Bid^{i,i+4}$-NH_2 in a ratio of 1.5:1 with 10 eq. of pyruvic acid after 1 h. b) Mass-spectra of the*

peak at 8.4 min corresponding to the hydrolysed Ant-N-OH and 11.3 min corresponding to ligated product (calc.: 4865.8).

Substrate specific self-cleavage is known for a number of proteins during which an internal segment is usually excised from the original sequence.[222] Non-enzymatic peptide-bond cleavage reactions have been reported for peptides containing aspartate and asparagine adjacent to cysteine residues, where the formation of a cyclic succinimide intermediate plays a crucial role.[223] The initial step for the cleavage of the peptide bond is the attack on a carbonyl-group by the cysteine side-chain to yield a thioester, which can undergo hydrolysis. Typically, the attack of an Asn-residue onto the thioester leads to the liberation of a segment from the polypeptide. Possibly, the close proximity of Asn-Cys residues and reaction conditions might lead to a similar reactions and the subsequent release of C-terminal-cyclised Ant-N-OH (Scheme II.9). Subsequent hydrolysis of the cyclised succinimide intermediate would free the Asn-residue to yield Ant-N-OH as indicated by mass-spectrometry. Samples of Ant-NCLG-NH_2 incubated in pure water gave a single peak, suggesting that a combination of the elevated temperature, buffer system and reaction-time promoted the auto-cleavage of the substrate rather than any inherent instability.

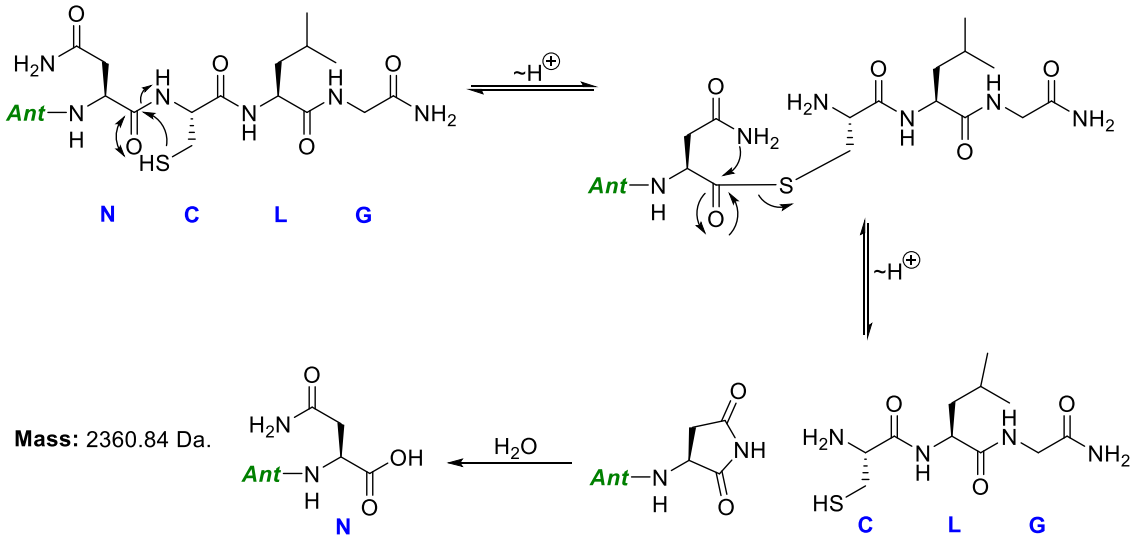

Scheme II.9 *Proposed mechanism for the internal trans-thioesterification that lead to the auto-cleavage of the NCLG-motif. Ring-opening of the cyclised C-terminus by either hydrolysis or nucleophilic attack of a peptide could lead to the truncated peptide as suggested by mass spectrometry.*

Surprisingly, all samples contained traces of ligated product (m/z 4865.80) even in the absence of the enzyme, as indicated by mass spectrometry and absorption at 210 nm (Figure II.17). Ligated product was also observed in samples lacking pyruvate, suggesting that the mechanism of product formation involves the substrate only. Samples containing larger quantities of the truncated peptide Ant-N-OH seemed to show more ligated product as estimated by the extent of 210 nm absorption. One possible explanation is that the cyclic succinimide of the truncated peptide Ant-N can undergo ring-opening through the nucleophilic attack of water (hydrolysis) or GL-Bid$^{i,i+4}$-NH_2 to give the ligated product. The amount of product formed would then depend on the degree of autolysis of Ant-NCLG-NH_2 and the competitive ring-opening reaction with water. The observation of product coincides with a diminished GL-Bid$^{i,i+4}$-NH_2 peak compared to reference samples at 210 nm, supporting the assumption of a potential reaction. Addition of enzyme to the samples did not lead to a significant increase in product (Figure II.18), suggesting that the conditions were suboptimal for catalysis.

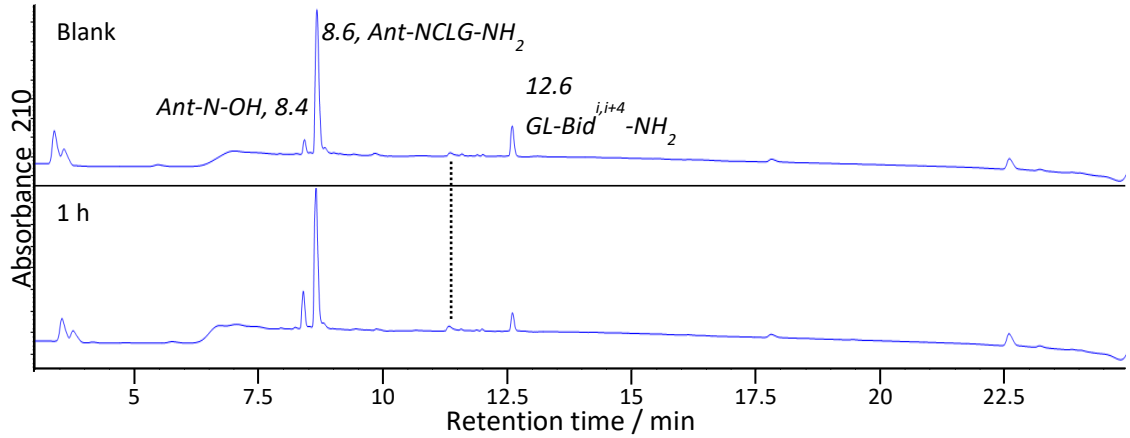

Figure II.18 *210 nm trace of the reaction mixture without any enzyme using Ant-NCLG-NH_2 and GL-Bid$^{i,i+4}$-NH_2 in a ratio of 1:1 with 10 eq. of pyruvic acid after 1 h. The dotted line marks the peak for the ligated product Ant-NGL-Bid$^{i,i+4}$.*

Further evidence supporting non-enzymatic, cysteine-mediated autolysis was gathered by analysing old samples containing the peptide GL-Bid$^{i,i+4}$-NH_2. Decomposition of the peptide up to ~26% (based on the integration of the 215 nm absorbance values) could be seen in all batches of the peptide tested, even those stored as a dry powder at -20 °C. Decomposition of the peptide may have occurred during the freeze-drying after the HPLC purification or thawing process prior their further application. Rather than the Asn-Cys-motif described above, an Asp-Cys sequence is present in this peptide that could lead to the truncation (Scheme II.10).

Autolysis would proceed *via* an initial thioesterification, similar to the proposed mechanism for the truncation of the peptide Ant-NCLG-NH_2. The thioester intermediate could then be cleaved by the adjacent Asp residue giving a truncated C-terminal cyclic peptide and the sequence CIDRSI-NH_2 (mass: 704.83). Ring opening through hydrolysis would give a peptide fragment of the sequence GLDIIRNIARHLACVGD-OH (mass: 1836.13). The analysis of a seven month old peptide sample (stored at -20 °C) by LC-MS techniques showed four peaks at the wavelength of 215 nm (Figure II.19). Mass spectrometric analysis suggested the peaks at 10.5 min and 17.0 min correlated to the truncated products described in the proposed mechanism. The mass spectrum of the peak at 16.6 min corresponded to the peptide GL-Bid$^{i,i+4}$-NH_2 containing a disulfide-bond between the cysteine-residues and that of the main peak at 18.2 min (92% of the total integrated signal) corresponded to the parent peptide.

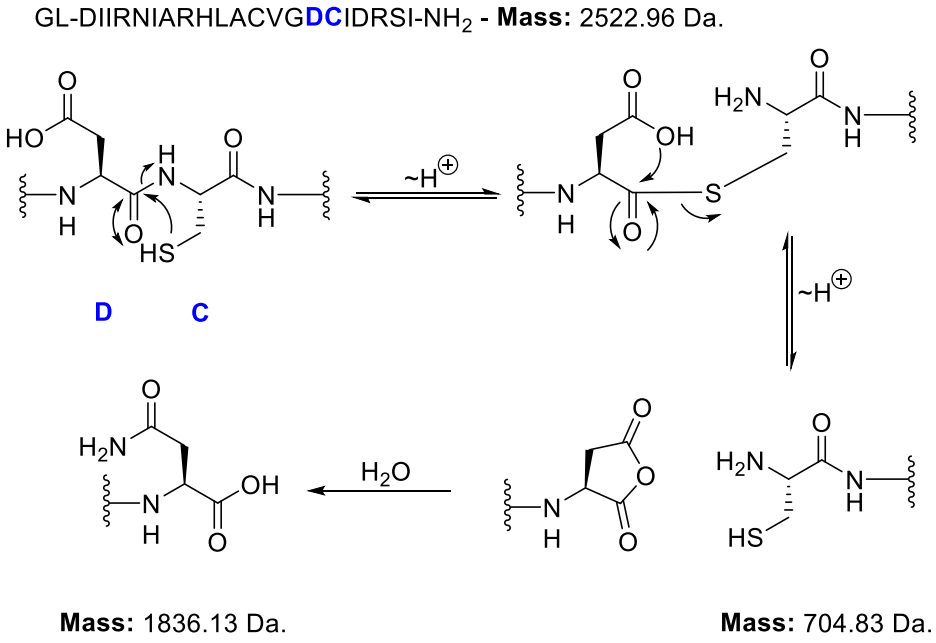

Scheme II.10 *Potential autolysis mechanism of the peptide sequence of GL-Bid$^{i,i+4}$-NH_2 leading to the observed truncated peptides.*

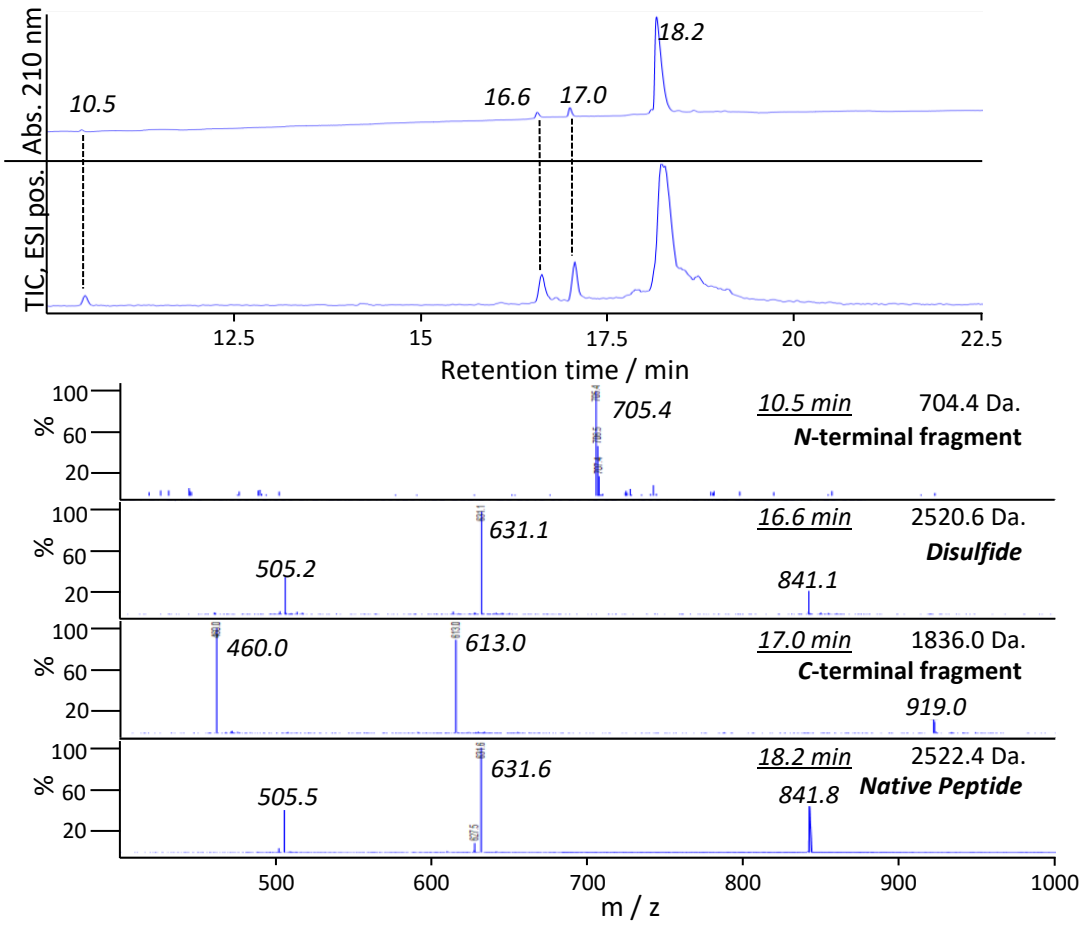

Figure II.19 *LC-MS analysis of the peptide GL-Bid$^{i,i+4}$-NH$_2$ ~7 months after its purification and storage at -20 °C indicating decomposition and truncation.*

The peptide bond is known to be particularly stable and very few cases of its self-cleavage without any exogenous cofactors are known, such as in protein-splicing or when certain non-proteinogenic amino acids are introduced to a sequence.[224,225] However, those mechanisms require specific conditions such as certain amino acid compositions, conformations or pH. Surprisingly, no decomposition of the peptide GL-Bid$^{i,i+4}$-NH$_2$ was observed during the enzymatic ligation. Peptide degradation was only observed in tested batches (5 in total) of purified peptide-samples indicating that the cleavage of the peptide might have occurred under the specific conditions, such as during the freeze-drying process following the peptide-purification or during the thawing of the samples prior use.

Further studies were carried out on the enzymatic ligation using OaAEP1 to optimise the conditions and to shift the equilibrium of the enzymatic ligation towards the product side using formyl phenyl boronic acid (FPBA) by Simon Tang *et al.*[219] Similar to the application of pyruvic acid, a thiazolidine group is formed during the condensation with the terminal cysteine

quenching the reverse reaction of the enzyme. These optimised conditions with 0.1 mol% OaAEP1 were applied to the enzymatic ligation of a 4:5 mixture of Ant-NCLG-NH_2: GL-Bid$^{i,i+4}$-NH_2 in 2-(*N*-morpholino)ethanesulfonic acid (MES) buffer at pH 5.5 and 20 °C. The reaction progress was monitored by the absorption at 210 nm at an analytical HPLC with no further conversion observed after 4 hours of reaction (Figure II.20).

The reaction yield was estimated by the integration of the peaks for the peptides on their own and in the reaction mixture to be ~50%. Interestingly, no truncated Ant-NCLG-NH_2 was observed under these optimised conditions, suggesting that the previously observed auto-cleavage of the peptide might be caused by specific conditions, such as the buffer or elevated temperatures. However, although the yield of the ligation was significantly higher than previously obtained, no preparative scale of the enzymatic ligation was carried out. The potential of this enzymatic ligation for synthesising libraries of peptides through a modular approach is good, but its application on larger scales and even under optimised conditions is limited by the ~50% conversion of starting material. Peptides were therefore synthesised by SPPS directly to avoid the multiple lengthy purification steps that were necessary to purify first the starting materials, then the enzymatic ligation reaction mixture.

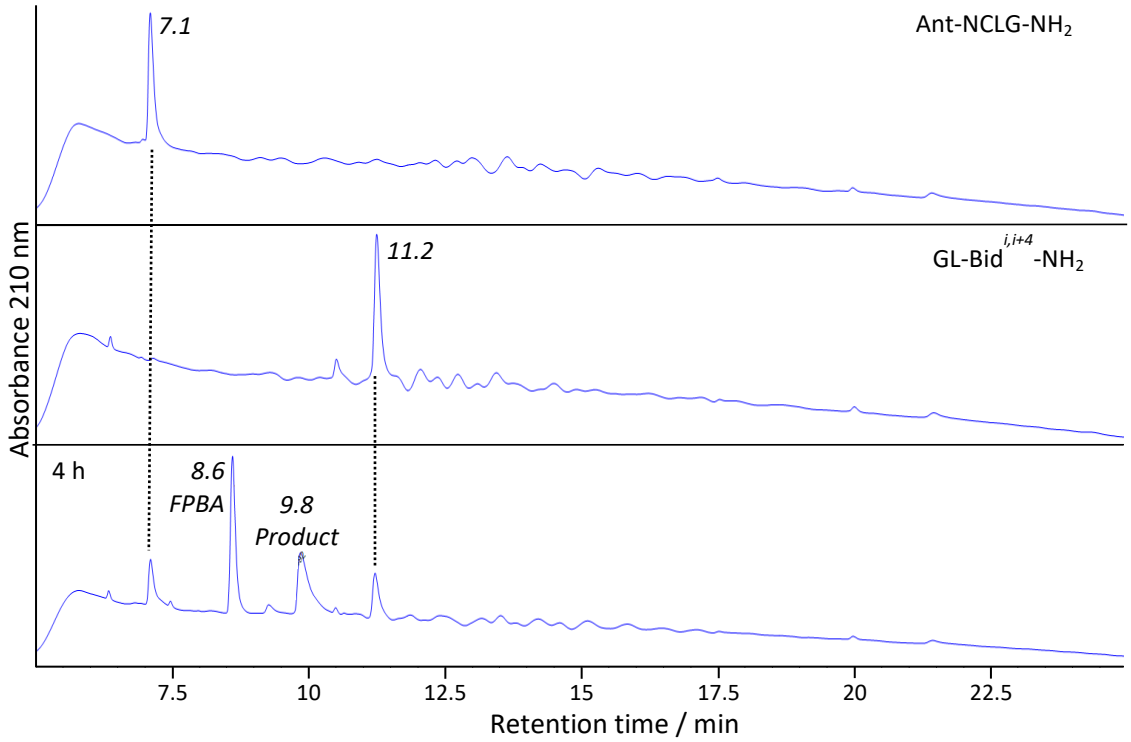

Figure II.20 *Ligation of Ant-NCLG-NH_2 and GL-Bid$^{i,i+4}$-NH_2 in a ratio of 1:1.2 using optimised conditions and formyl phenyl boronic acid (FPBA) as an additive.*

d. Conclusion

This chapter describes two approaches to generate CPP-BH3-peptide-conjugates; recombinant expression and enzymatic ligation. In the recombinant approach, the synthesis of BH3-peptides attached to cell-penetrating sequences using biological techniques was successfully carried out. Recombinant peptide production was achieved using a plasmid harbouring DNA encoding $Bid^{i,i+4}$-R_8 fused to an insoluble ketosteroid isomerase. Post-translational modification and purification furnished a soluble peptide. Although no conclusive mass-spectrum could be obtained, analysis by SDS-PAGE and 210 nm HPLC trace suggested the presence of the desired product. A new plasmid was created harbouring DNA encoding a His-tag, solubiity tag, a TEV cleaving site and $Bid^{i,i+4}$. The expressed protein was purified by Ni-NTA-column followed by TEV cleavage and the presence of the desired peptide confirmed by mass spectrometry. The plasmid was further modified to include two *Bsa*I recognition sites following the DNA encoding $Bid^{i,i+4}$. This new acceptor plasmid can be used in future to generate a library of sequences, which are fused to the C-terminus of a $Bid^{i,i+4}$ peptide by Golden-Gate ligation.

An approach combining biological and synthetic chemistry techniques was applied next. Peptides containing the BH3- and the CPP-sequence of the antennapedia protein were synthesised by SPPS and ligated using the asparaginyl endopeptidase OaAEP1. Short sequences of the peptides containing the recognition sites were synthesised and ligated at different concentrations to explore the suitability of this approach. Generally, addition of excess peptide containing the recognition site on its C-terminus seemed superior to excess peptide bearing the N-terminal recognition site. Following model studies, ligation of the full-length peptides was carried out using excess CPP containing the recognition site on the C-terminus. However, despite a preparative scale (46.5 mg of combined peptide), only negligible amounts of ligated product could be isolated (<1 mg). It was anticipated that the reaction equilibrium could be strongly shifted towards the product if the cleavage byproduct could be made to undergo an irreversible reaction, removing it from the equilibrium. The recognition sequence was changed so that the by-product contained a N-terminal cysteine residue. Addition of pyruvate would then cause a reaction with this cysteine residue to form an unreactive thiazolidine, preventing the back-reaction of the enzymatic ligation. However, the amount of ligated product did not significantly improve as indicated by HPLC analysis, and introduction of the cysteine residue seemed to promote enzyme-independent autolysis of the peptide. Optimised conditions for the enzymatic ligation developed by Simon Tang using formyl phenyl boronic acid (FPBA) as an additive yielded ~50% product on an analytical scale.

Auto-cleavage of GL-Bid$^{i,i+4}$ and Ant-NCLG peptides was narrowed down to their Asp/Cys and Asn/Cys sites, respectively. While the truncation of the peptide GL-Bid$^{i,i+4}$-NH_2 is likely a product of its storage and treatment following its purification, Ant-NCLG-NH_2 showed auto-cleavage only under certain conditions, such as those applied during the initial enzymatic ligation. However, the exact mechanism of this fragmentation remains unclear and further investigation would be necessary to fully elucidate it.

3. Peptide-Stapling

a. Aims and Objectives

The efficient synthesis of azobenzene crosslinked peptides in high yields remains a significant challenge. Typically, photo-crosslinker attachment is performed after peptide synthesis and cleavage from the resin in a buffered aqueous solution at a pH that selectively deprotonates thiol-groups on the side chain of cysteine residues. This process can suffer from low yields, particularly when peptides have limited solubility and/or adopt significant degrees of secondary structure. Purifying peptides before and after the stapling reaction can be extremely time-consuming, especially in cases of limited peptide solubility. To address these issues, methods for crosslinking on resin as part of the SPPS procedure were investigated with the aim of simplifying crosslinking procedures and reducing the number of purification steps to a single HPLC purification. A series of apoptosis inducing peptides including short test peptides and full length BH3-peptides, CPP linked peptides and fluorophore-labelled peptides were synthesised on a preparative scale using SPPS methods (Table II.4). As the selective deprotection of the cysteine-thiol-protecting groups was crucial to ensure reactivity with the crosslinker, different protecting group and deprotecting regimes were tested.

Table II.4 *Pro-apoptotic BH3-domain peptides and the corresponding sequences, which were to be synthesised. $[PEG]_n$ denotes a polyethyleneglycol polymer of n monomer units consisting of H_2N-(PEG)-COOH (linker length: 9 atoms) each.*

Peptide	**Sequence**
GL-Bid$^{i,i+4}$-NH_2	GL-DIIRNIARHLACVGDCIDRSI-NH_2
(5)[FAM]-GL-Bid$^{i,i+4}$-NH_2	(5)FAM-GLDIIRNIARHLACVGDCIDRSI-NH_2
Bid$^{i,i+7}$-NH_2	DIIRNIASCLASVGDCIDRSI-NH_2
Ant-Bid$^{i,i+4}$-NH_2	RQIKIWFQNRRMKWKKDIIRNIARHLACVGDCIDRSI-NH_2
(5)[FAM]-Ant-Bid$^{i,i+4}$-NH_2	(5)FAM-RQIKIWFQNRRMKWKKDIIRNIARHLACVGDCIDRSI-NH_2
Bim$^{i,i+4}$-NH_2	IWIAQELRCIGDCFNAYYARR-NH_2
Bak$^{i,i+11}$-NH_2	GCVGRALAAIGDCINR -NH_2
$[PEG]_3$-Bak$^{i,i+11}$-NH_2	NH_2-$[PEG]_3$-GCVGRALAAIGDCINR -NH_2
(5)[FAM]-$[PEG]_3$-Bak$^{i,i+11}$-NH_2	(5)FAM-$[PEG]_3$-GCVGRALAAIGDCINR -NH_2

b. Solution Phase Stapling

i. Screening Solution Phase Crosslinking Conditions

Crosslinking conditions were screened using a 12-amino acid Bid$^{i,i+4}$ peptide which was synthesised, cleaved form the resin and purified as described (see chapter IV.2c). The previously synthesised, non-substituted crosslinker **38** was used for experiments to establish baseline solution phase conjugation yields. The stapling reaction was carried out in 100 mM tris-ethanolamine (Tris) buffer including 0.5 mM tris(2-carboxyethyl)phosphine (TCEP). The pH of the crosslinking buffer was adjusted to 8.3 to deprotonate the cysteine sidechain thiols, and the peptide was pre-equilibrated in the buffer for 30 min at 45 °C in a total concentration of 0.5 mM to ensure reduction of any disulfides. Crosslinker **38** was then added in 1 µL portions from a 50 mM DMSO stock solution to obtain a final ratio of 50% (*v*/*v*) DMSO:Tris-buffer. After addition, the reaction vessel was shaken to ensure complete mixing of the reagents. Different ratios of peptide-to-linker from 1:1 to 1:4 were tested, and the reaction mixtures were shaken at 450 rpm for 16 h at 45 °C, prior to LC-MS analysis.

Formation of precipitate was observed in all samples, so the suspensions were centrifuged at 13,200 rpm for 5 min and the supernatant was injected into the LC-MS. The precipitate was dissolved in 1:1 (*v*/*v*) acetonitrile:water then analysed by LC-MS. Generally, a peptide-to-linker ratio of 1:1 seemed to be sufficient to obtain crosslinked peptide with only a trace amount of starting material detectable in the reaction mixture. Higher concentrations of crosslinker did not seem to have a significant effect, with no side-product formation evident in UV-Vis absorbance traces (Appendix 4). Both precipitate and supernatant samples contained some crosslinked peptide, but whereas the precipitate sample mostly consisted of crosslinked peptide and unreacted crosslinker, the supernatant sample had numerous peaks at different wavelengths (210, 280, 360, 440 nm) indicating the formation of a significant number of unidentified side-products. This suggested that the side-products formed during the crosslinking reaction were mostly soluble in the buffer/DMSO mixture with the final product and unreacted crosslinker largely remaining insoluble.

Reaction of crosslinker **38** with the 12-amino acid peptide resulted in a shift in retention time for the crude crosslinked adduct of the major peak from 10.2 min to 11.4 min (Figure II.21). A later retention time corresponded to an increased hydrophobicity, supporting successful attachment of **38** to the peptide. Furthermore, significant absorbance was observed at 360 nm, characteristic of the presence of crosslinker. The mass spectrum of the main peak at

11.4 min corresponded to the double-charged state of the peptide-crosslinker product (calc.: 1555.8).

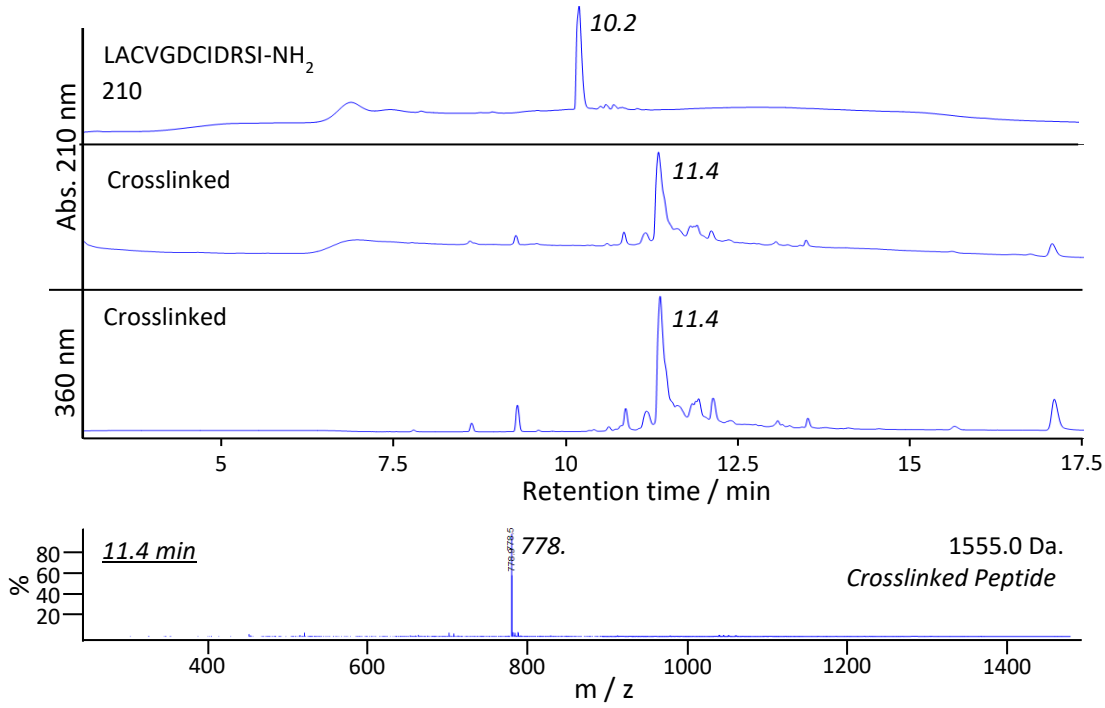

Figure II.21 *210 nm traces of the purified starting material peptide and the crude crosslinked peptide at 210 and 360 nm. Mass spectrum of the peak at 11.4 min corresponded to the crosslinked peptide (calc.: 1555.8). Shown traces are for the purified 12-mer peptide and the reaction mixture containing peptide:linker in a ratio of 1:1 (precipitate)***.**

ii. Full Length Stapling

The ultimate aim was to staple the peptides listed in Table II.4 using the red-shifted azobenzene linker **33**, so the optimised crosslinking conditions for the shorter peptide (100 mM TRIS pH 8.3, 0.5 mM TCEP) were applied to the reaction of **33** with full-length Ant-Bid$^{i,i+4}$-NH_2, but no full-length stapled peptide could be isolated. This was hypothesised to be caused by the solubility of the peptide or its secondary structure due to the longer peptide limited cross-linking, so guanidinium chloride (8.0 M) was added to the reaction. Guanidinium is a chaotrophe, disrupting hydrogen bonding and hydrophobic interactions, and is frequently used to denature proteins and peptides. Formation of **33**-stapled Ant-Bid$^{i,i+4}$-NH_2 was observed by LC-MS, so high guanidinium salt concentrations were therefore used to react all the peptides of Table II.4 with 1.5 eq. of **33**. As the solubility of the crosslinker was poor under these reaction conditions, **33** was added portionwise and the reaction mixture was mixed thoroughly before overnight incubation. If conversion of the starting material was noted to

have halted by LC-MS, further TCEP and **33** were added. Stapling reactions of peptides containing the Bid$^{i,i+4}$ sequence all yielded multiple major peaks, which made the subsequent purification steps challenging, leading to a maximum yield of 22%.

Typically, 0.1% TFA was used as an additive to the HPLC-solvents when purifying the reaction mixture, whereas LC-MS analysis was carried out with 0.1% formic acid in the mobile phase to improve the ionisation of the peptides. Compound **33**-crosslinked peptide Ant-Bid$^{i,i+4}$-NH_2 gave a broad peak when analysed by LC-MS, suggesting incomplete protonation. In contrast, when 0.1% TFA was used as an additive, a sharper peak-shape and a shift in retention time were observed (Figure II.22). A wider, tailing peak-shape suggested more than one mechanism of analyte retention on the solid phase may be at work, such as polar interaction of the amino acids residues with residual silanol groups of the silica support.[226] The LC trace at 210 nm and 360 nm contained an additional peak in the purified sample around 8.7 min that persisted even after multiple rounds of purification implying the presence of an equilibrium of conformers or a mixture of the *cis*- and *trans*-form of the crosslinker, as all peaks displayed the same mass spectrum corresponding to crosslinked Ant-Bid$^{i,i+4}$-NH_2 (m/z 5011.5).

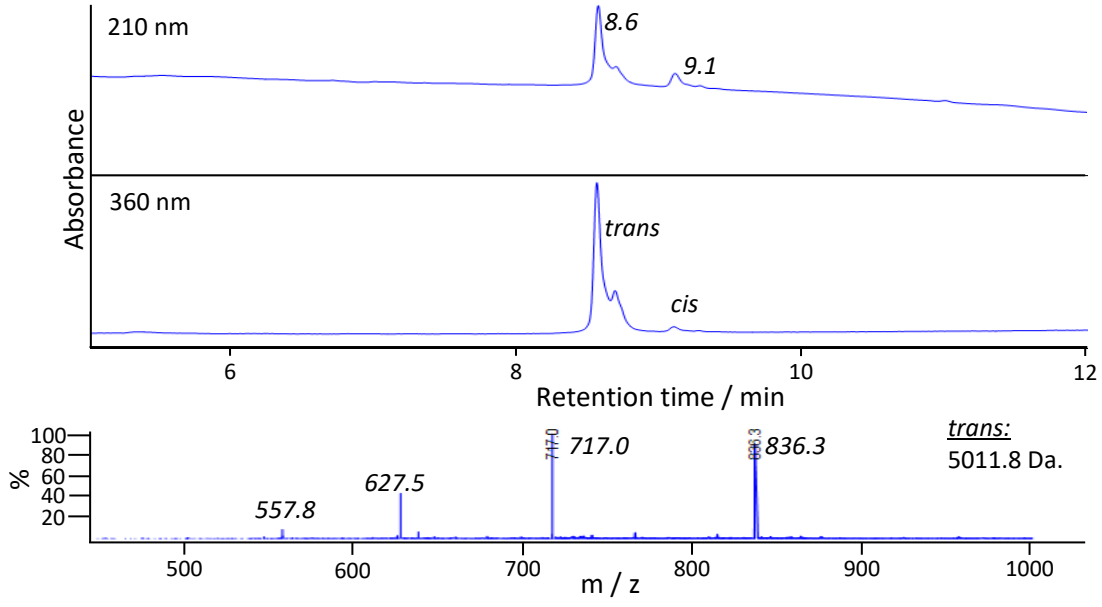

Figure II.22 *Analytical LC-trace at the wavelengths 210 nm and 360 nm for the **33**-crosslinked peptide Ant-Bid$^{i,i+4}$-NH_2 (TFA used as additive), mass spectrum of the peaks obtained by the LC-MS analysis run with formic acid as an additive corresponded to the crosslinked peptide (calc.: 5011.5).*

GL-Bid$^{i,i+4}$-NH_2 was stapled with both, the red-shifted linker **33** and the water-soluble azobenzene-derivative **37** (Appendix 5) for use as controls in protein-binding assays and for comparison with previous results.[211] The N-terminal Gly- and Leu- residues were added to maintain consistency to the previously synthesised peptides. A total yield of 28% was obtained when crosslinking with **33**, but only 6% for the water-soluble linker **37**. In contrast to crosslinked Ant-Bid$^{i,i+4}$-NH_2, no peak tailing or secondary peaks were observed on the LC-MS, hinting that incomplete protonation or distinct conformational states of the CPP-tag were the cause of this phenomena. **33**-staped GL-Bid$^{i,i+4}$-NH_2 also showed mixed *cis*-/*trans*-isomers in the dark-state of the sample (Figure II.23). (5)[FAM]-GL-Bid$^{i,i+4}$-NH_2 was stapled with **33** and **37** (Appendix 6) for fluorescence anisotropy (FP) binding assays with Bcl-x_L.

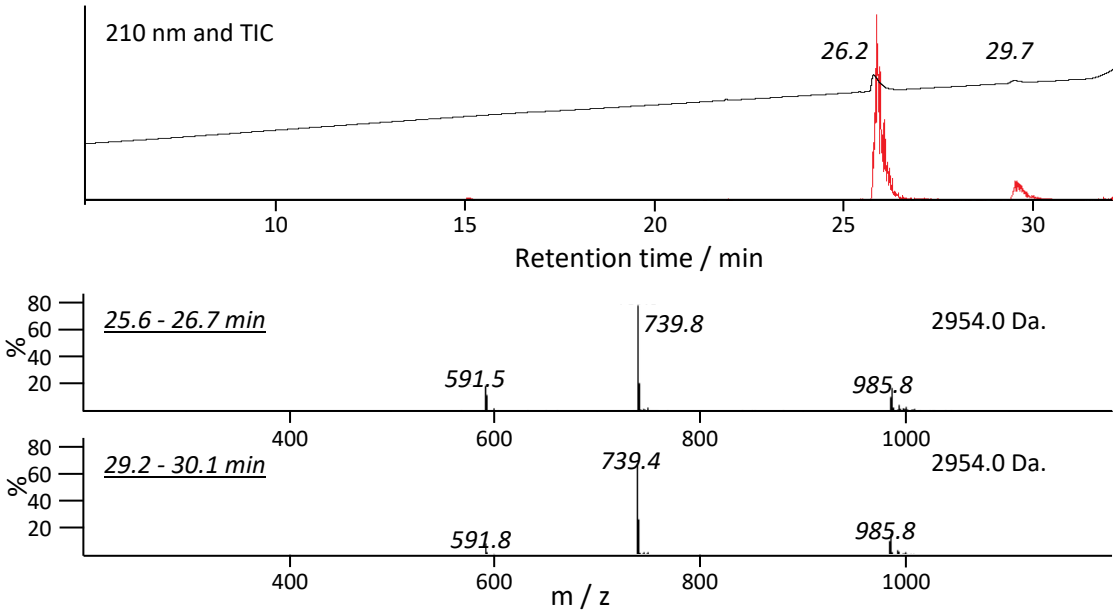

Figure II.23 *LC-MS trace of the **33** crosslinked peptide GL-Bid$^{i,i+4}$-NH_2. 210 nm (black) and TIC (red)-trace are overlapped. Mass spectra of the two peaks are shown and the obtained mass corresponded to the final product within the standard deviation of the de-convoluted mass (calc.: 2953.0).*

A common observation during the purification step of the stapling-reaction was the isolation of starting material, even when no starting material peak could be observed during reaction monitoring. This was attributed to the oxidation of cysteines and the formation of disulfide-bonds leading to new species with different retention times. Oxidised starting material was often recovered and could be easily reduced to its original state by the addition of TCEP

(Figure II.24). Several peaks corresponding to oxidised starting material suggested the presence of multiple oxidised species containing intra- and intermolecular disulfide bridges.

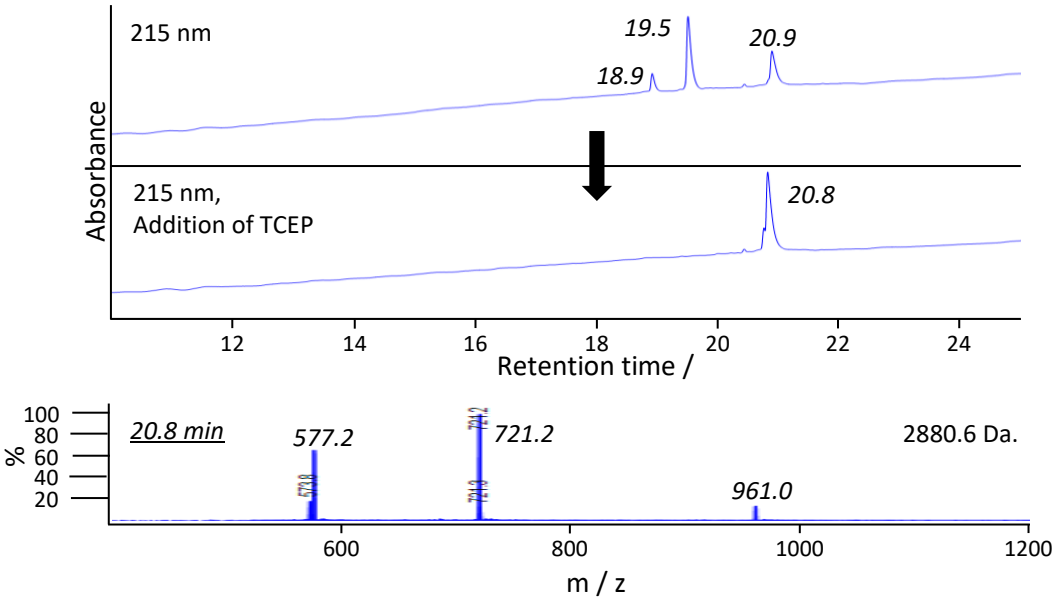

Figure II.24 *Isolated starting material from the HPLC purification of the crosslinking reaction with (5)[FAM]-GL-Bid$^{i,i+4}$-NH$_2$. Addition of TCEP lead to conversion of the three peaks to one at 210 nm, which was confirmed to be starting material by mass spectrometry (calc.: 2881.3).*

Stapling reactions could be carried out using one equivalent of TCEP to reduce any disulfides in peptide reagent. However, if the peptides predominantly existed in their reduced state when added to the reaction mixture, excess TCEP would exist in solution and is known to react with the crosslinker chloroacetamides. To minimise any side-product formation, peptides were dissolved in the crosslinking buffer and the cysteines oxidised by bubbling compressed air through the sample over-night. Oxidation was confirmed by LC-MS, then the buffer containing the oxidised peptide was degassed under reduced pressure to remove dissolved oxygen, and the peptide reduced using one equivalent of TCEP. Argon was bubbled through the reaction mixture prior the addition of the crosslinker to minimise the chance of oxidation. Peptides that were crosslinked following this procedure contained significantly fewer side-products, simplifying subsequent purification of the reaction mixture.

Walensky and co-workers investigated the BH3-domain of the pro-apoptotic peptide Bim regarding the optimal positioning of an all-hydrocarbon linker. The resulting construct displayed a significant increase in α-helicity, cellular uptake and successful induction of apoptosis in various cancer cell lines even without any attached CPP-sequences.[168,227]

Following these results, the peptide Bim$^{i,i+4}$-NH_2 was synthesised and stapled with **33** to obtain another light-switchable activator BH3-domain peptide. The azobenzene crosslinker was positioned between the same amino acids as the all-hydrocarbon linker reported by Walensky and co-worker. The analysis of the crude reaction mixture by HPLC indicated multiple side-products. The product could be purified in 25% yield and showed two peaks (74.3% *trans*, 25.7% *cis*) corresponding to the mass of the peptide-construct at the dark-state in LC-MS analysis (Appendix 7).

In previous work, binding interactions between **37** crosslinked Bak$^{i,i+11}$-NH_2 and Bcl-x_L were examined by NMR spectroscopy,[213] so **37-**stapled Bak$^{i,i+11}$-NH_2 was synthesised to reproduce these results and **33-**stapled Bak$^{i,i+11}$-NH_2 to determine if the binding mode remained the same in the absence of the polar sulfonate groups. As these NMR experiments are conducted in purely aqueous solutions, a polyethylene glycol (PEG) tag (H_2N-(PEG)-COOH, linker length 9 atoms) was added to the N-terminus of the peptide sequence to increase the water-solubility of the crosslinked peptides. PEG-groups are highly hydrophilic, flexible chains unlikely to cause undue steric hindrance when conjugated to a peptide or protein. Three repeating units of PEG-groups ($[PEG]_3$) were added to the N-terminus of Bak$^{i,i+11}$-NH_2 during synthesis. As this solubility tag contributed more than 20% of the total mass of the peptide, a significant improvement in solubility was expected even when stapled with a bulky hydrophobic crosslinker. The PEG-spacer also provided sufficient distance between the BH3-sequence and the fluorophore to rule out potential interference of the fluorophore with the binding groove during NMR or fluorescence polarisation assays.

The crude reaction mixtures of the stapled Bak$^{i,i+11}$-peptides showed fewer side-products compared to Bid peptides, which facilitated ready identification of the product peaks and purification of the crosslinked peptide by HPLC and significantly greater yields (54% yield) than for the Bim$^{i,i+4}$ (25% yield) and Bid$^{i,i+4}$ (6-28% yield) peptides. The azobenzene crosslinker seemed to react more selectively with peptides containing a wider spacing of the cysteine residues. Without a chemical staple or protein-context, these peptides predominantly exist in a random structure in the reaction mixture.[228] An azobenzene staple can function as a secondary structure-forming element depending on the cysteine-spacing in the peptide and the isomeric form of the linker. For peptides containing *i,i* + 4 and *i,i* + 7 cysteine-spacings, the longer end-to-end distance of the *trans*-isomer stretches the peptide out of an α-helical structure. For peptides with a *i,i* + 11 cysteine spacing, an α-helical structure is distorted by the shorter end-to-end distance of the *cis*-isomer.

Compound **33** crosslinked Bak$^{i,i+11}$-NH_2 (Figure II.25) and (5)[FAM]-[PEG]$_3$-Bak$^{i,i+11}$-NH_2-peptides (Appendix 8) exhibited two peaks in LC-MS analysis, indicating the presence of both *cis*- and *trans*-stapled peptide in the dark-state. The first peak corresponds to the less hydrophobic *cis*- and the peak with later retention time corresponds to the *trans*-conformer as indicated by comparison of their 210 and 360 nm absorption profiles.

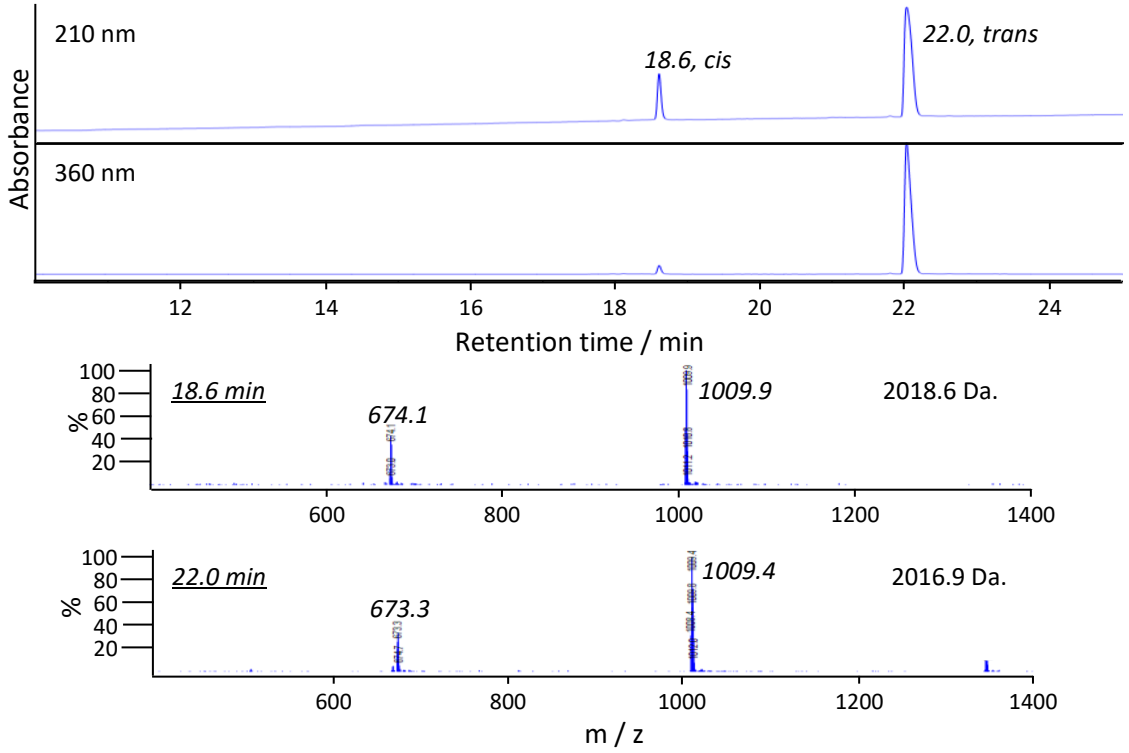

Figure II.25 *LC-MS traces of the **33**-crosslinked peptide Bak$^{i,i+11}$-NH_2. The obtained mass spectra of the two peaks correspond to the two isomers of the stapled product within the standard deviation of the de-convoluted mass (calc.: 2017.9).*

This observation supports the expectation that helical conformations of BH3-domain peptides should display a stronger hydrophobic character due to the formation of a stripe of hydrophobic residues on one side of the helical wheel (Figure II.26). Based on the integration of the 210 nm trace, 17% *cis*-conformer was present.

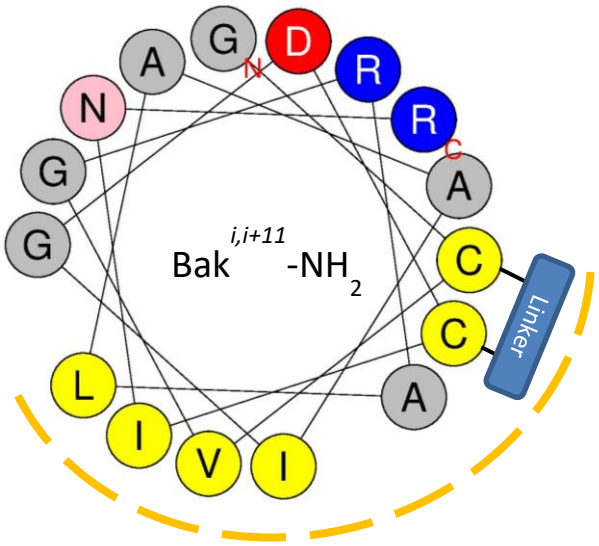

Figure II.26 *Helical wheel illustration of the stapled peptide Bak$^{i,i+11}$-NH$_2$ with the attached linker that leads to an extension of the hydrophobic surface (dotted line).*

The reactivity of functional groups other than the thiols could be a potential source of side-product formation when stapling the peptides in solution. The reaction of the cysteine-thiols with the crosslinker can be controlled by adjusting the pH of the buffer so that other potentially nucleophilic residues are not deprotonated in solution. However, as the pK_a-values of N- terminal amine (8.0-9.0) lies close to the pK_a-value of the cysteine side-chain (8.1), the **33**-stapled peptide Bak$^{i,i+11}$-NH$_2$ was subjected to an enzymatic digestion assay followed by LC-MS analysis to confirm the correct position of the crosslinker. Trypsin was used to cleave the peptide on the C-terminal side of Arg and Lys residues (Figure II.27). When stapled through the thiol groups of the cysteines, the digested peptide would exist as a linear sequence with hydrolysed ends of the peptide bond at the arginine residue. In case the crosslinker was misplaced to the N-terminal end of the peptide sequence, the digestion assay would result in two peptides that could be isolated and identified by LC-MS techniques with a mass of 920.6 Da. and 1115.3 Da. (Figure II.27).

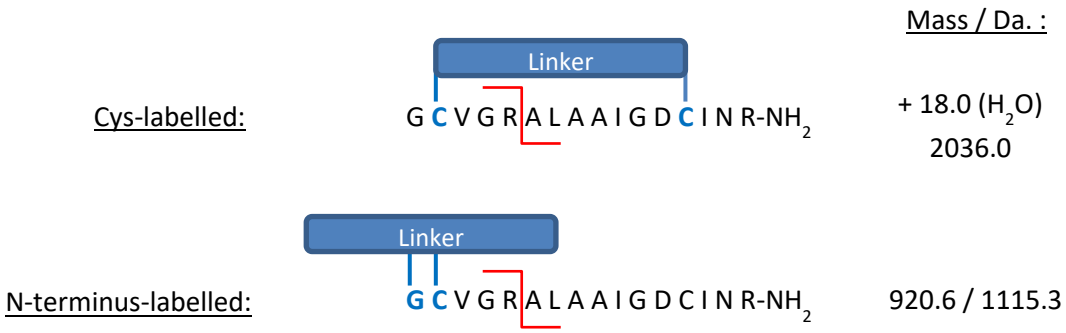

Figure II.27 *Trypsin digest assay with **33**-stapled Bak$^{j,i+11}$-NH$_2$ and resulting masses of the peptides when labelled through the cysteine-residues and the N-terminus. As the peptide bond plays a crucial role during the amino acid recognition process of the enzyme, the C-terminal arginine was not expected to be cleaved by trypsin.*

Samples were first denatured in 8 M urea by heating to 60 °C for 60 min. The digestion reaction was then diluted in Tris HCl (pH 7.8. 50 mM) and incubated with an aliquot of MS-grade trypsin to a trypsin:peptide ratio of 1:20 (*w*/*w*) at 37 °C for 24 hours in buffer containing dithiothreitol (DTT) to prevent disulfide formation. The reaction was quenched by addition of 5% (*v*/*v*) of formic acid to the sample and analysed by LC-MS (Figure II.28).

The 280 nm absorbance trace showed five major peaks at 10.1 min, 15.3 min, 15.9 min, 19.4 min and 19.7 min. The first peak at 10.1 min was identified as trypsin by mass spectrometry, but the latter four peaks exhibited crosslinker-**33**-specific absorption at 360 nm and 450 nm. The following pairs of peaks corresponded to the two isomers of the hydrolysed, cleaved peptide (*trans* at 15.3 min and *cis* at 15.9 min) and unreacted peptide (19.4 min and 19.7 min).

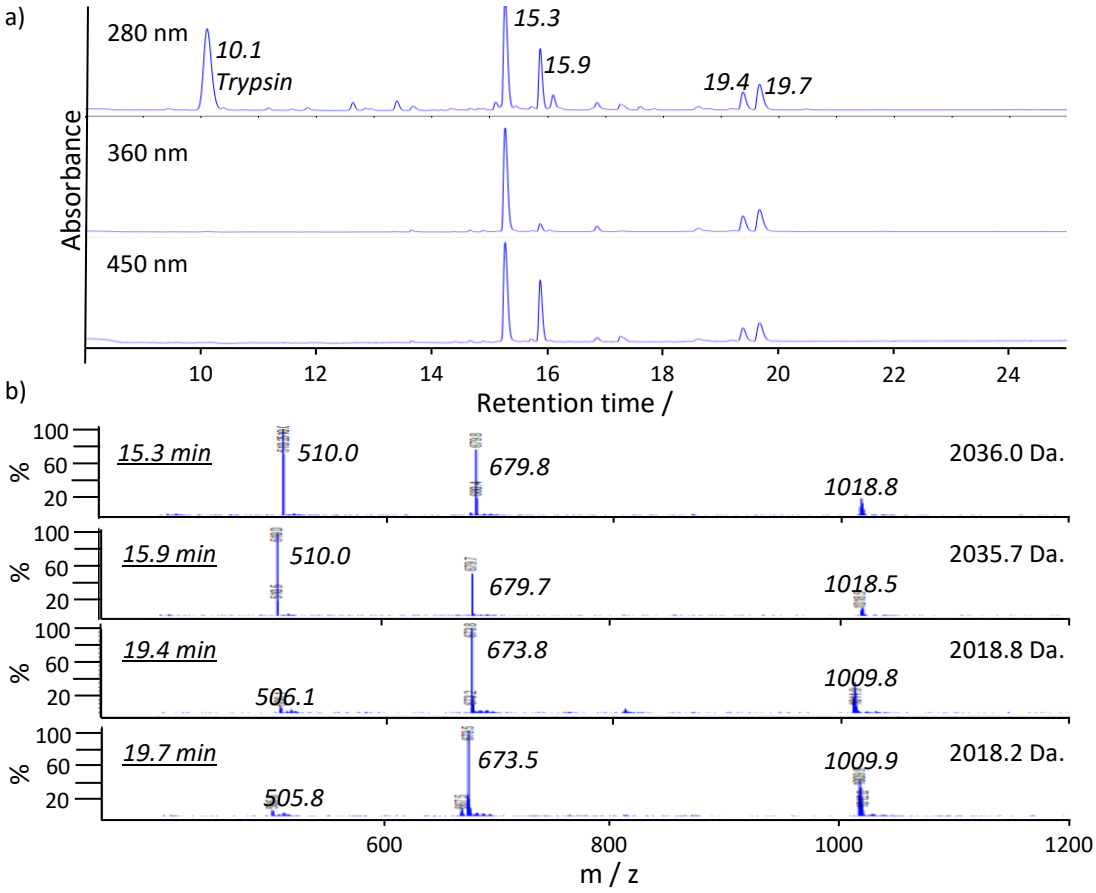

Figure II.28 *LC-MS analysis of the peptide digestion of **33**-stapled Bak$^{i,i+11}$-NH$_2$ using trypsin. a) UV-Vis absorbance of the reaction mixture at 280 nm, 360 nm and 450 nm. b) Mass spectra with deconvoluted masses of the obtained four main-peaks.*

iii. Methyl-Cysteine Labelling

An alternative to cysteine conjugation was reported by the research group of Li and co-workers, who developed a macrocyclization strategy based on a chemoselective alkylation process of methionine residues (Figure II.29a).[26] Methionine amino acids were introduced into a model peptide and then reacted for 24 hours with various alkyl halides in 30:70 MeCN:H_2O (*v*/*v*) containing 1% formic acid to generate cyclic peptides of different ring sizes. The product contained two additional positive charges, causing the *bis*-alkylated peptides to have better solubility and cellular uptake in addition to imparting greater stability towards proteolytic enzymes than the linear parent peptides. This strategy was successfully applied to create cyclic peptides that were able to induce an autophagic flux in HeLa cells.[27]

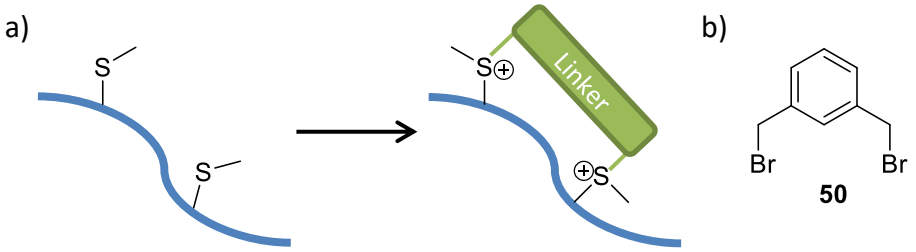

Figure II.29 *(a) General principle of methionine-alkylation used by Li and co-workers*[166,229] *and (b) one of the linkers (**50**, α,α'-dibromo-m-xylene) used for the stapling of the methyl-cysteine residues.*

It was hoped that this conjugation approach would counteract the poor solubility of the **33**-crosslinked peptides. Methyl-cysteines were used instead of methionines to limit the flexibility of the product and improve photo-control and were introduced in place of cysteines into the GL-Bid$^{i,i+4}$-NH_2 sequence. The methyl-cysteine stapling reaction with **33** was carried out at 45 °C. The reaction mixture was centrifuged and the supernatant analysed by analytical HPLC. No product formation was observed after 24 hours. DMF (30 vol.%) was added to increase the solubility of the crosslinker **33**, but there was still not show any reaction after 24 h as indicated by analytical HPLC (Figure II.30a). The subsequent addition of α,α'-dibromo-*m*-xylene (Figure II.29b), a linker used in previous publications for stapling of methionine residues[166,229], to the reaction mixture resulted in a significant decrease of the starting material signal and three new peaks (Figure II.30b). LC-MS analysis of the new peaks revealed that two of them originated from small molecules (obtained mass < 400 Da.) and to the formic acid-adduct of the successfully **50**-stapled peptide (calc.: m/z 2700.1).

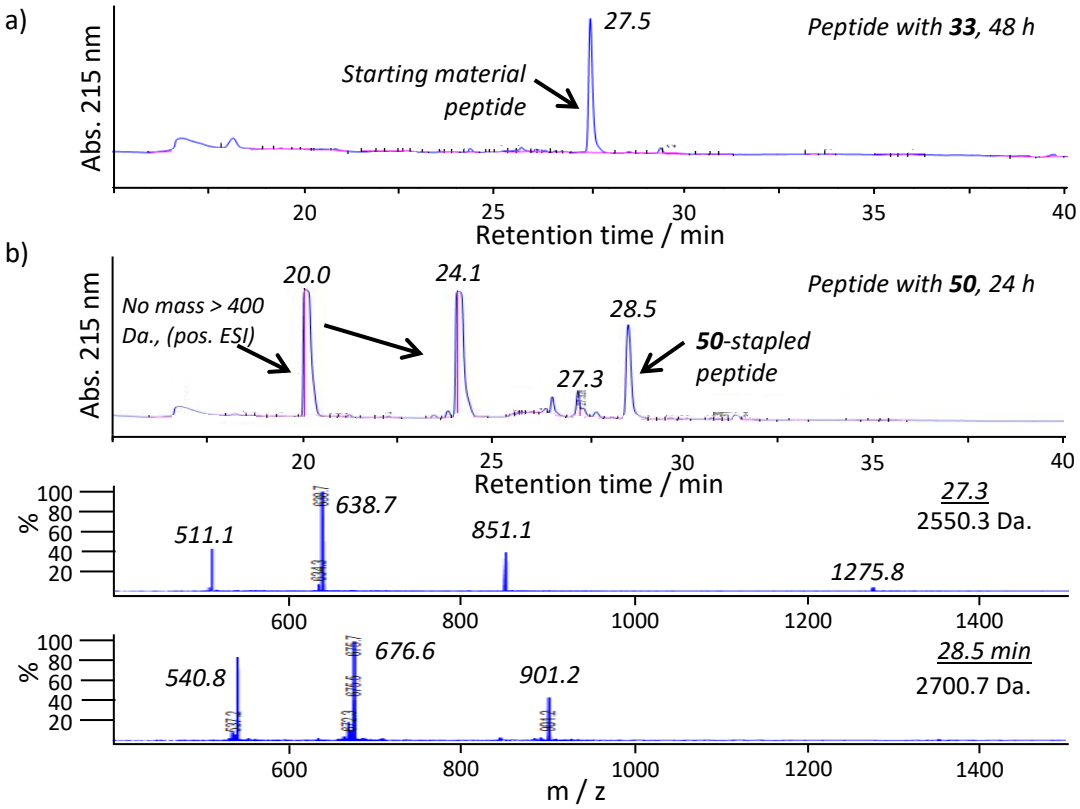

Figure II.30 *HPLC-traces of the reaction mixture containing the peptide GL-Bid$^{i,i+4}$-NH$_2$ with methylated cysteines. a) The azobenzene linker **33** after 48 h shows only starting material. b) Addition of the staple **50** leads to the formation of multiple peaks. The peaks at 20.0 and 24.1 min did not show any mass > 400 Da. in ESI pos. mode. The peak at 27.3 min corresponded to starting material (m/z 2251.0) and the peak at 28.5 min to **50**-stapled peptide (2655.1 + 45.0 (formic acid): m/z 2700.1).*

One potential reason for **50** reacting when **33** does not, is the proximity of the bromine to the sp^2-hybridised aromatic ring that has an electron withdrawing effect on the attached carbon atom and a stabilising effect on the partial positive charge formed during the reaction. To increase the reactivity of the crosslinker **33**, a halide-exchange reaction was carried out to replace the chloride with iodine (**49**, chapter II.1.d). However, no reaction between **49** and the peptide was observed, even at 45 °C. Although the electrophilicity of alkyl-iodides is significantly greater than alkyl-chlorides, an even more reactive staple seemed to be necessary for the reaction with methyl-cysteines. Only staples where the halide was connected to a carbon-atom in α-position to a sp^2-center showed reactivity towards methionine residues in recent literature, suggesting that the lack of an sp^2 centre in the crosslinker was hindering its reactivity.[166,229]

c. Solid Phase Stapling

A major limitation in the production of azobenzene stapled peptides are the required multiple HPLC purification steps to separate the non-stapled and stapled peptides. The purification is particularly challenging when several side-products show *cis*/*trans* isomeric mixtures with similar retention times to the desired construct, significantly reducing the final yield. Due to the hydrophobic nature of the azobenzene scaffold, precipitation of the linker in the aqueous stapling buffer was thought to reduce the amount of formed product. Furthermore, the analysis by LC-MS techniques of the multiple potential products after the HPLC separation proved to be time consuming making the stapling process very inefficient in terms of time and material costs. On resin crosslinking of peptides was investigated as a means to improve the overall yield of crosslinked peptide synthesis by addressing solubility issues in typical stapling buffers, minimising potential side-products during the stapling reaction, and reducing the total number of purification steps required. This approach requires orthogonal cysteine protecting groups that can be removed selectively without affecting the nascent peptide (Figure II.31).

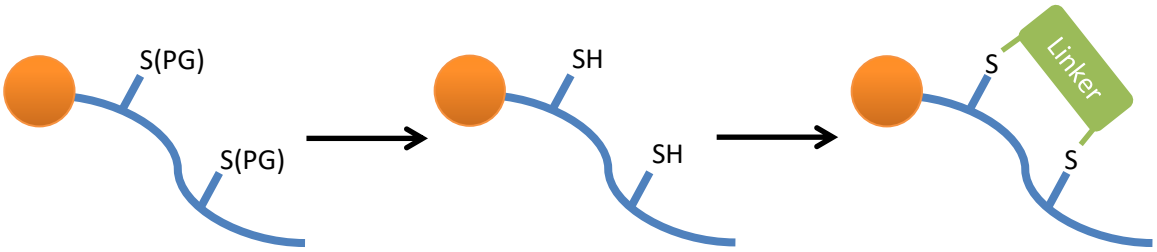

Figure II.31 *Solid-phase crosslinking: The peptide is still anchored onto the solid support and the cysteine-protecting groups (PG) have to be removed in a selective fashion in order to allow the linker to react with the free thiol-groups.*

The azobenzene-linker dissolved in organic solvent could then react with the free thiol groups and any unreacted material would be removed by washing as usual for solid phase synthesis. The stapled peptide would remain anchored to the resin and the peptide sequence could be further modified with fluororphores or other sequences, such as solubility tags or CPPs. Following release of the peptide from the resin under acid, a single purification step would provide the final stapled peptide-construct.

i. Selective Deprotection of Peptides Containing Cys(Trt)-OH and Cys(S^{t}Bu)-OH

Selective deprotection of the cysteine side-chains is crucial to avoid side product formation. Initial experiments were carried out on a 12 amino acid long Bid$^{i,i+4}$-NH_2 sequence where the cysteine-thiols were protected with trityl-groups. To avoid any reaction with the peptide N-terminus, the Fmoc-group was only removed after the crosslinking reactions with **38**.

The trityl-protecting group is generally acid-labile and can be removed using dilute TFA solutions (1-3% v/v). The released trityl cation is very stable and gives the supernatant a yellow colour. The deprotection reaction is reversible, as the thiol group can react with the product trityl cation, so additives are typically used with the cleavage cocktail to quench the cation. After swelling the peptide on the resin, it was repeatedly exposed to a mixture of 1% trifluoroacetic acid (TFA) and 1% triisopropylsilane (TIPS) in dichloromethane (DCM) (9 x 5 min). This was followed by 1% TFA and 99% DCM to check if the reaction was complete by absence of yellow unquenched trityl cations. However, a yellow colour was observed in the solution even after repeated exposure to the cleaving cocktail, meaning complete deprotection could not be readily achieved with this protecting group.

Methoxytrityl (Mmt)-groups have been reported to be more quickly and more efficiently removed from thiol groups than trityl groups. In a recent literature report,[230] Cys(Mmt) was introduced into a peptide sequence, deprotected using 2% TFA and the resulting peptide stapled with an all-hydrocarbon linker while still on the resin. However, quantification of the degree of deprotection remained challenging, as visual assessment of deprotection progress by colour was prone to error and conditions used to cleave test peptides from the resin for analysis also removed any remaining (methoxy)trityl groups. Repeated treatments may also remove trityl groups from other amino acids, with their unprotected side-chains potentially leading to side-products.

Based on these initial experiments, the introduction of a cysteine-protecting group that is orthogonal to the acidic cleavage was considered superior to continuing to use acid-labile groups as they would allow monitoring the selective deprotection progress by LC-MS after cleavage from the resin. Disulfides are typically stable under acidic conditions and are readily removed under mild conditions by exposure to reducing agents. Disulfides are also stable during the base-induced N-terminal Fmoc-deprotection step, allowing complete flexibility in monitoring deprotection and crosslinking reactions by LC-MS.

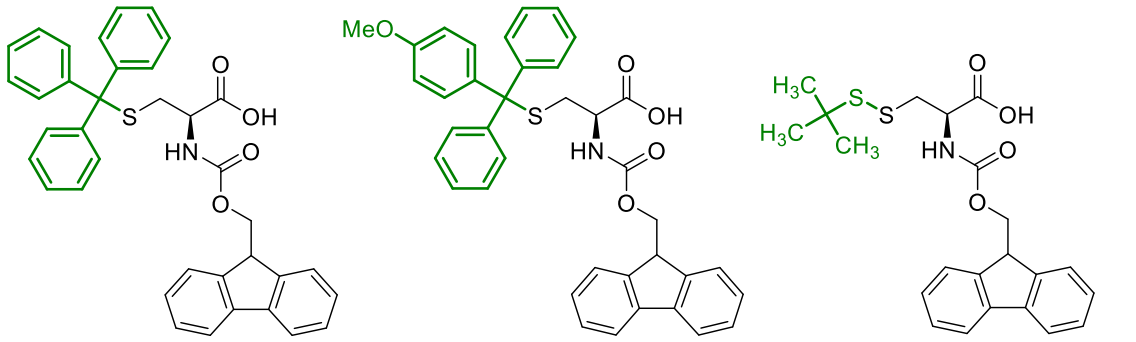

Fmoc-*L*-Cys(Trt)-OH Fmoc-*L*-Cys(Mmt)-OH Fmoc-*L*-Cys(S^{t}Bu)-OH

Figure II.32 *Structural differences of three Fmoc-Cys(PG)-OH building blocks for SPPS. The different protecting groups are highlighted in green.*

The cysteine building block Fmoc-Cys(S^{t}Bu)-OH, consisting of a *tert*-butyl sulfide attached to the thiol group (Figure II.32), was incorporated into a 13 amino acid long Bid$^{i,i+4}$-NH_2 sequence. A number of different reducing agents have been reported to deprotect peptides containing ^{t}Bu-disulfide protecting groups, including: DTT[231], a combination of *N*-morpholine and β-mercapto-ethanol,[232] and tributylphosphine.[233] However, only small amounts of deprotected product were detected by LC-MS under any of these conditions, even after 24 hours. A maximum of 15% deprotection (estimated from 210 nm absorption trace) was achieved when tributylphosphine was mixed with the peptide and β-mercaptoethanol and the solution left to react overnight. This difficulty in removing the protecting group could potentially be caused by the peptide adopting a coiled structure in which the *t*Bu-protecting groups were not accessible to the added reducing agents. If that were true, reduction of the S^{t}Bu-protecting group should have been facilitated by releasing the peptide from the solid support. However, even prolonged exposure to a reducing agent did not lead to a significant increase in deprotection by LC-MS in the solution phase. Further scrutiny of the scientific literature suggests deprotection of Cys(S^{t}Bu) amino acids in peptides may be challenging in general, as conditions to fully deprotect the cysteine-residues required thorough optimisation in a number of reports.[231–233]

ii. Synthesis and Reaction of Cys(STmp)-OH with Bid$^{i,i+4}$-NH_2

The trimethoxyphenylthio (STmp) cysteine protecting group was developed by Albericio and co-workers.[234] The protecting group was reported to be rapidly removed (5 minutes) using mild reducing agents. It showed good stability under both SPPS conditions and TFA cleavage

when incorporated into a test-peptide. However, on a different model peptide, exposure to 95% TFA compromised the stability of the group and lead to deprotection of 8% of the cysteine side-chains. Following the unexpectedly high resilience of the S^{t}Bu-protecting group to reducing agents, the potential moderate instability of STmp against TFA exposure seemed like an acceptable compromise, particularly as stability against TFA is only useful for measuring incomplete deprotection of the peptide. The synthesis of Fmoc-Cys(STmp)-OH was adapted from literature procedures (Scheme II.11).

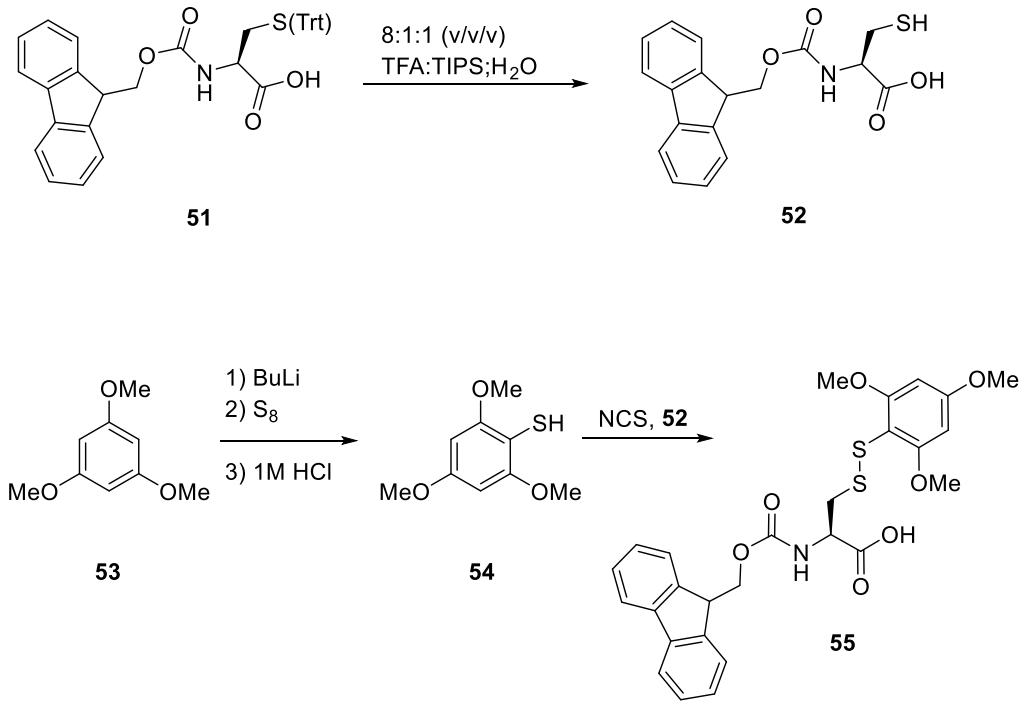

Scheme II.11 *Synthesis of the new Cys-building block for SPPS; Fmoc-Cys(STmp)-OH (**55**).*

Deprotection of **51** was achieved by stirring it in a mixture of 8:1:1 (v/v/v) TFA:TIPS:H_2O for 1 hour. The reaction mixture was concentrated and the precipitate obtained was washed several times with hexane. **53** was then reacted with 1 equivalent of sulphur and 0.9 equivalents of butyl lithium (2.5 M in hexanes). The reaction product was crystallised from hexane and a few drops of dichloromethane at -78 °C. N-chlorosuccinimide was recrystallized from water and dried prior to suspending in dichloromethane at -78°C whereupon a solution of **54** and **52** in tetrahydrofuran was added drop-wise. Overnight reaction and subsequent silica gel chromatography yielded impure **55** by ^{1}H NMR spectroscopy. The main impurity appeared to be Fmoc-cysteine, possibly due to strong π-interactions with **55**. Several silica gel

chromatography conditions were tried, but purification of **55** was eventually achieved by reverse-phase HPLC yielding a white powder (47%, lit.: 76%) after freeze drying the combined product fractions. LC-MS analysis indicated that the purity of the isolated material was greater than 96% (Appendix 9).

The new protected cysteine building block was incorporated into a 13 amino acid Bid$^{i,i+4}$-NH_2 sequence by standard Fmoc-SPPS chemistry. Analysis of the cleaved peptide by LC-MS indicated that the synthesis was unsuccessful. Different cleaving cocktails were tested as well as removal of the STmp-group prior to cleaving the peptide from the resin in order to rule out any interference with the analysis by the new protecting group, but the results did not change. As a consequence, portions of the peptide were cleaved from the resin after the incorporation of each amino acid and analysed by LC-MS. The results indicated that the incorporation of the second cysteine as the tenth amino acid was successful but major side-product formation occurred upon addition of alanine as the eleventh amino acid. No product could be observed after the incorporation of the twelfth amino acid (Figure II.33). These observations were surprising as alanine does not carry any protecting groups that could interact with the newly introduced Cys(STmp) and cause the decomposition of the peptide.

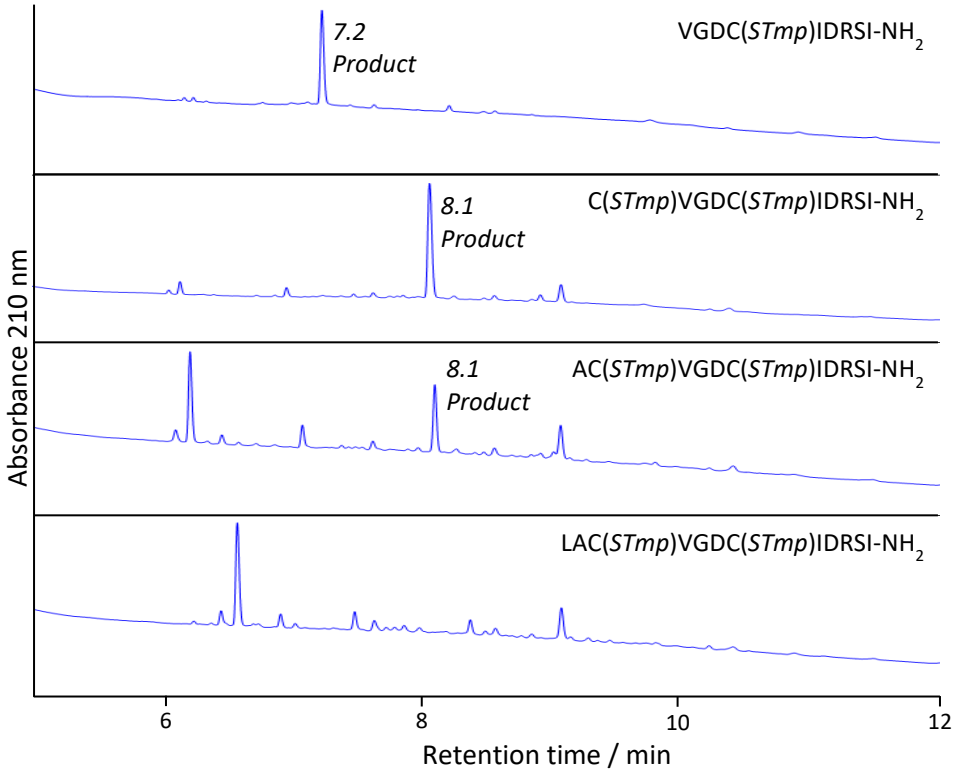

Figure II.33 *Test-cleaving of the peptide after incorporation of each amino acid revealed that decomposition of the peptide takes place after the introduction of the second cysteine.*

A 10 amino acid long Bid$^{i,i+4}$-NH_2 sequence was synthesised to investigate the cause of the peptide degradation. Integration of the 210 nm HPLC trace estimated a purity of ≥95% for the crude 10-mer and suggested that the protecting group is mostly stable against the cleaving conditions. One possibility for the degradation of the peptide on the resin was interaction of an activated amino acid monomer with the STmp-protecting groups. To test for this type of reaction, Fmoc-Ala-OH was activated with DIC and oxyma and incubated with the Fmoc-protected 10 amino acid long peptide. The resulting 210 nm trace consisted mostly of the desired product, with few side-product peaks emerging. Different Fmoc-deprotection-cocktails were tested (2% DBU + 0.5% piperidine in DMF instead of 10% (*w*/*v*) piperazine in NMP/EtOH (9:1)+ 0.1 M HOBt) but produced the same outcome as previously observed, with product purity falling to ~40%. Glycine was used in place of alanine to investigate any potential steric effects, but displayed a similar level of side-product formation (product purity ~30%), indicating that the effect is independent of the amino acid. Changing the activating agents from DIC and oxyma to HBTU and HOBt also had no effect suggesting, the cause of degradation might be related to the internal spacing of the cysteines.

The STmp-protecting groups of the 10 amino acid Bid$^{i,i+4}$-NH_2 sequence were selectively removed using a solution containing 5% (*w*/*v*) DTT in DMF (3 x 5 min), with loss of the hydrophobic groups causing a significant shift of the retention time from 8.1 min to 6.3 min relative to the parent protected peptide (Figure II.34). In a test-reaction, the STmp-deprotected peptide was reacted with the azobenzene crosslinker **38** and DIPEA overnight. The Fmoc-group was removed and the peptide cleaved off the resin using standard techniques. The analysed sample showed a single major peak at 360 nm indicating a crosslinked species (Figure II.34).

Next, reactions were conducted to produce the crosslinked 12 amino acid Bid$^{i,i+4}$-NH_2 sequence by on-resin crosslinking of the 10-mer sequence, followed by the addition of the remaining two amino acids. The result of the LC-MS analysis of the released peptide was compared against the previously obtained results for the in solution stapled 12 amino acid long peptide of Bid$^{i,i+4}$-NH_2 (Figure II.35). The stacked traces displayed the same retention time for the main product and similar amounts of side-products absorbing at 360 nm suggesting that the attached crosslinker did not interfere with adding additional amino acids. However, even though this result indicates that crosslinking of a peptide using an azobenzene linker during SPPS is possible, multiple additional signals in the 210 nm and 280 nm (not shown) traces corresponding to side-products indicated that further optimisation of this technique is necessary.

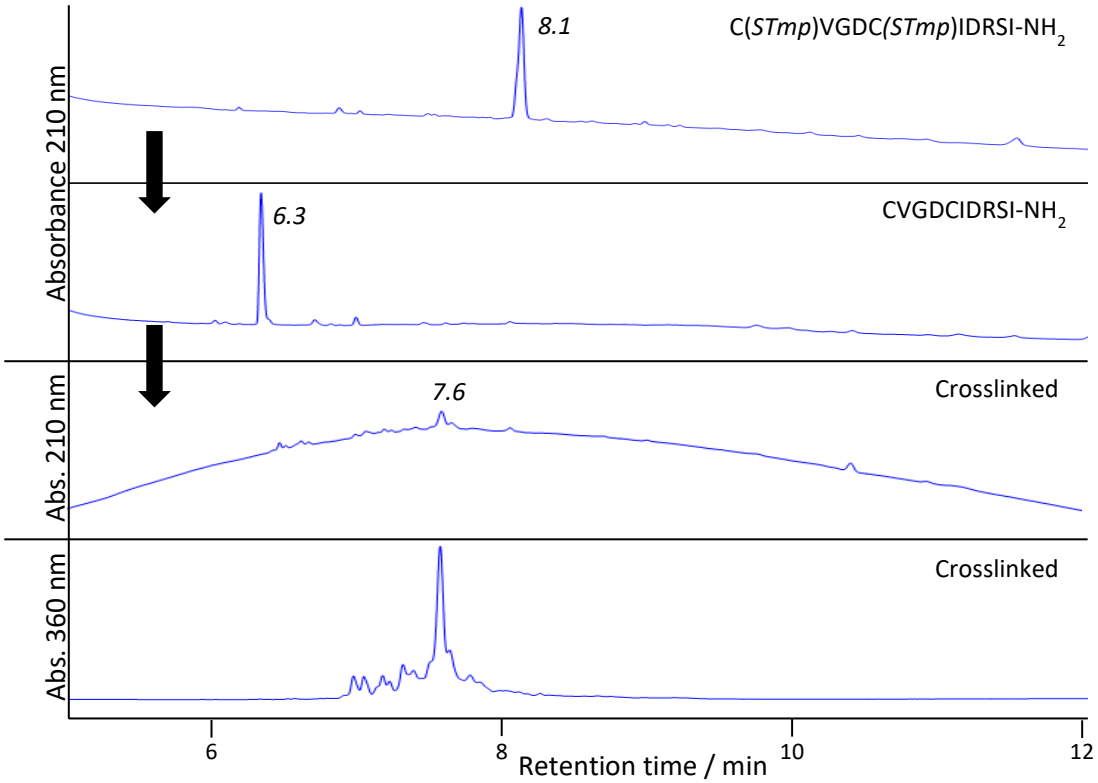

Figure II.34 *10 amino acid long peptide containing the synthesised cysteine before and after the selective deprotection of the STmp-protecting groups. Crosslinking with non-substituted azobenzene linker* ***38*** *yielded a main peak at 360 nm.*

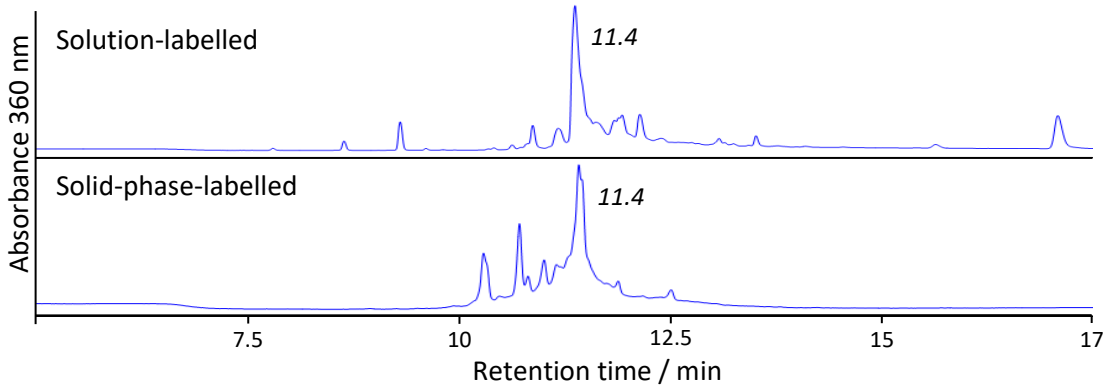

Figure II.35 *Stacked LC-traces at 360 nm wavelength comparing the obtained product of the solution- and solid-phase-labelling process with azobenzene* ***38****.*

iii. Synthesis and Labelling of Bid$^{i,i+7}$- Cys(STmp)

As the results of the 12-mer Bid$^{i,i+4}$-NH_2 synthesis implicated internal interactions of the aromatic protecting groups, Fmoc-Cys(STmp)-OH was used to synthesise Bid$^{i,i+7}$-NH_2, a BH3

domain peptide with a wider cysteine spacing. Analysis of the crude peptide indicated one predominant species, identified as the desired Bid$^{i,i+7}$-NH$_2$ peptide containing two STmp protecting groups (Figure II.36).

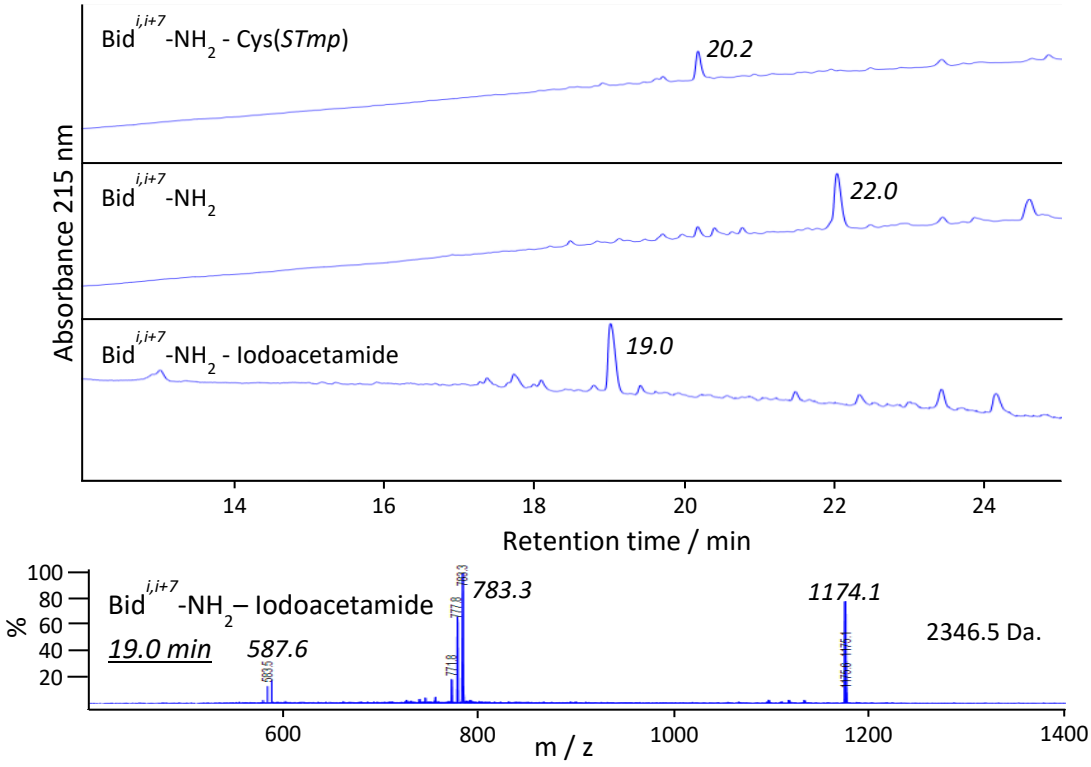

Figure II.36 *The peptide Bid$^{i,i+7}$-NH$_2$ containing the two cysteine protecting groups STmp before and after selective deprotection. The STmp removal was followed by reaction with iodoacetamide and the main-peak identified as product by mass spectrometry (calc. mass: 2347.7).*

Removal of the protecting groups was achieved using 5% DTT in DMF (3 x 5 min), but unexpectedly resulted in a product with a later retention time than the protected Bid$^{i,i+7}$-NH$_2$ peptide. Overall, these results confirmed that the distance between the cysteine-protecting groups is crucial, with significant byproducts observed when using Fmoc-Cys(STmp)-OH for the Bid$^{i,i+4}$-NH$_2$ 12-mer but not Bid$^{i,i+7}$-NH$_2$. However, incubation of the deprotected Bid$^{i,i+7}$-NH$_2$ with the linker **38** and DIPEA overnight did not yield any crosslinked peptide by LC-MS. Multiple peaks with absorbance at 210 nm, 280 nm and 360 nm indicated the presence of several crosslinker/peptide products, suggesting low selectivity, but mass-spectrometry failed to detect any mass correlating to the desired product. Basic reactivity towards alkylation was tested using iodoacetamide to mimic the halide-acetamide motif of the crosslinker.

Iodoacetamide and DIPEA were added to the deprotected peptide and let to react overnight. Analysis of the crude-peptide, cleaved from the resin, by LC-MS showed a major peak at a shorter retention time with a mass correlating to diacetylated product (calc.: m/z 2347.7, obsv.: m/z 2346.5) (Figure II.36).

As a result of the successful reaction of iodoacetmaide with the deprotected peptide, **38** was subjected to a halide-exchange reaction to replace the chloride with iodine in order to increase its reactivity towards thiol-groups (chapter II.1.d). The iodide version of **38**, **36**, was incubated with the STmp-deprotected peptide and DIPEA overnight, the resin was then washed multiple times with DMF prior the Fmoc-removal and removal of the peptide from the resin using TFA. Analysis of the crude peptide by LC-MS showed corresponding major peaks in 210 nm and 280 nm chromatograms (Figure II.37).

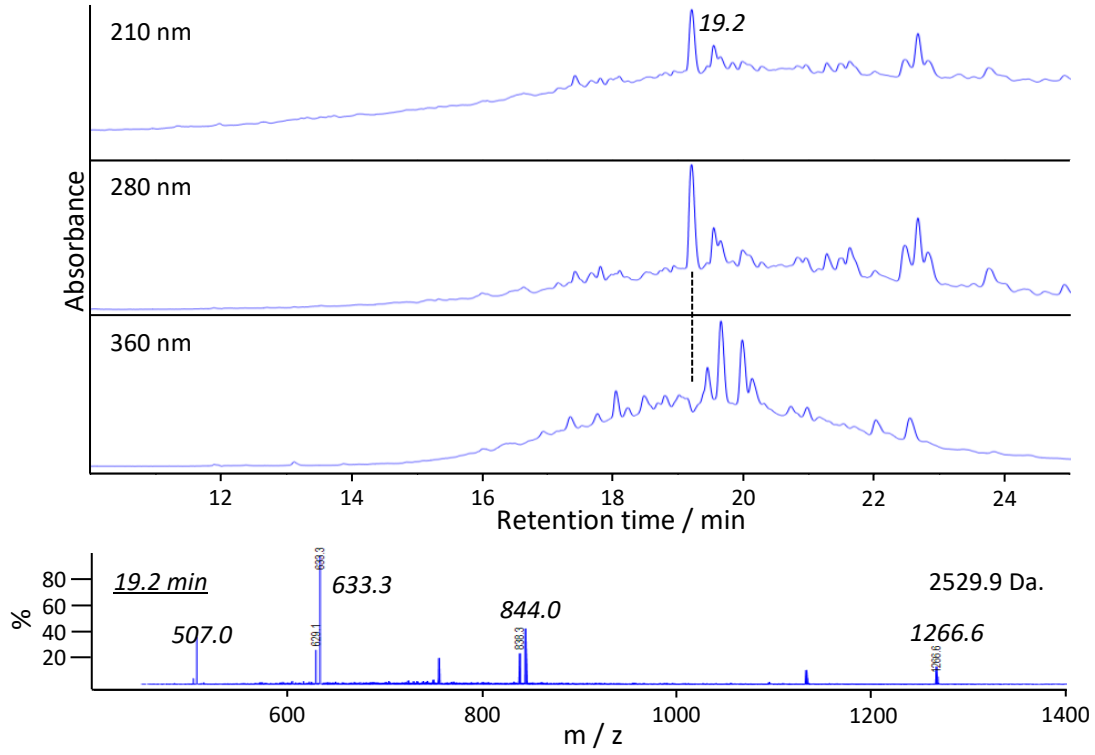

Figure II.37 *LC-MS analysis of the crude product obtained from the solid-phase stapling reaction of **36** with the peptide Bid$^{i,i+7}$-NH$_2$. The obtained mass for the peak at 19.2 min corresponded to the stapled peptide within the standard deviation of the deconvolution and calibration of the mass-spectrometry (calc.: m/z 2525.9, obsv.: m/z 2529.9).*

The later retention time of the main-peak compared to the diacetylated sample was consistent with the expectation that the addition of **36** to the peptide should increase the overall

hydrophobicity and the mass spectrum suggested formation of the desired product (Figure II.37, calc.: m/z 2525.9, obs.: m/z 2529.9, the difference of four mass units was attributed to calibration difficulties). However, no absorption of the main-peak at 360 nm could be observed (dotted line), inferring the peak corresponding to the *cis*-isomer of the crosslinker. Several side-products had formed during the reaction as indicated by the multiple other peaks. Although the stapling-conditions needed further improvement, this experiment did demonstrate that crosslinking peptides on the resin using azobenzene linkers is possible, but the successful incorporation of Cys(STmp) requires a certain minimal spacing between the two protected cysteines.

d. Conclusion

Two different approaches to stapling BH3-domain peptides were explored with the peptide either in solution or on a solid-phase support. While a 12 amino acid long Bid$^{i,i+4}$-NH_2 sequence was successfully stapled in solution under several different conditions, no stapled peptide was obtained when optimised conditions were applied to a 37 amino acid long peptide sequence containing an N-terminal CPP sequence in addition to the BH3-domain of Bid. However, product formation was observed in the presence of a high concentration of chaotropic agents.

Purification of stapled peptides by HPLC was a significant challenge, a protocol was developed involving the complete oxidation and reduction of the peptides to minimise side-products that could arise from disulfide-formation prior to crosslinking. Stapling peptides with a greater spacing between cysteine residues, such as Bak$^{i,i+11}$-NH_2, resulted in much higher overall yields and cleaner HPLC profiles suggesting that the amount of side-product formation correlates with the distance between the two anchor points.

Stapling peptides while they were still anchored to the resin during or after SPPS offered a promising solution to the high number of purification steps required and the prospect of increasing the overall yield. It was anticipated that the higher solubility of the azobenzene-linker in DMF compared to the aqueous buffer systems would also improve product formation. Reliable, complete and selective removal of the cysteine protecting group was crucial for the selective reaction with crosslinkers, and following a series of test reactions on the selective deprotection of protected cysteine residues, Fmoc-Cys(STmp)-OH was synthesised for use during SPPS. Complete deprotection of this disulfide-group was achieved upon short exposure of the peptide to mild reducing agents, with the disulfide-group otherwise stable even under the TFA conditions used for cleaving from the resin. It was planned that the synthesis of the

peptide should be carried out before the stapling reaction, in order to minimise any potential side-reactions of the crosslinker during SPPS. However, incorporation of Fmoc-Cys(STmp)-OH into a short Bid$^{i,i+4}$-NH_2 sequence resulted in catastrophic loss of purity of the peptide during SPPS. Careful experiments showed that this degradation did not take place before the introduction of a second Cys(STmp) into the sequence, indicating that interactions between the two protected residues might lead to the observed decomposition. Subsequently, a peptide was synthesised until the incorporation of the second Cys(STmp) four residues after the first, stapled using an azobenzene crosslinker. The sequence of the stapled peptide was then successfully extended by the addition of further amino acids, suggesting that the process to staple peptides that were still anchored onto the resin using this approach was possible.

Bid$^{i,i+7}$-NH_2 was successfully synthesised using Fmoc-Cys(STmp)-OH, which were selectively deprotected. As this peptide contained a similar amino acid composition but a wider cysteine spacing than Bid$^{i,i+4}$-NH_2, this result supports the hypothesis that peptide-degradation might be related to the internal interaction between the STmp groups. Initial crosslinking experiments were not successful, but exchanging the halide of the cross-liker to improve its reactivity resulted in a single major peak which corresponded to the desired peptide-construct by LC-MS. Although the LC traces obtained showed that conditions still could be further improved to address the formation of side-products, crosslinking peptides on the resin using azobenzene linkers was shown to be possible with the introduction of Cys(STmp) into a peptide sequence allowing rapid, reliable, and selective deprotection of the Cys-side chains. However, the spacing between these protecting-groups seemed to have a significant effect on the peptide stability.

4. *In Vitro* Characterisation of Crosslinker-Peptide Complexes

a. Aims and Objectives

Following the synthesis and purification of the crosslinked peptides (Table II.5), the biophysical properties of the constructs were tested to investigate if binding to an anti-apoptotic protein could be controlled by red light. Fluorescence-polarization (FP) assays were used to detect binding, requiring crosslinked peptides also be labelled with a fluorophore. NMR experiments using labelled protein were performed to obtain further information about the location of binding sites; photo-physical properties were evaluated by UV-Vis spectroscopy, the extent of *cis*-/*trans*-isomerization by analytical HPLC techniques and secondary structure propensities by circular dichroism (CD) spectroscopy.

Table II.5 *Crosslinked-apoptotic BH3-domain peptides and the corresponding sequences, which were investigated during the in vitro studies.*

Peptide	Sequence
33-GL- Bid$^{i,i+4}$-NH_2	GLDIIRNIARHLACVGDCIDRSI-NH_2
33-(5)[FAM]-GL-Bid$^{i,i+4}$-NH_2	(5)[FAM]-GLDIIRNIARHLACVGDCIDRSI-NH_2
37-(5)[FAM]-GL-Bid$^{i,i+4}$-NH_2	(5)[FAM]-GLDIIRNIARHLACVGDCIDRSI-NH_2
33-Ant-Bid$^{i,i+4}$-NH_2	RQIKIWFQNRRMKWKKDIIRNIARHLACVGDCIDRSI-NH_2
33-Bim$^{i,i+4}$-NH_2	IWIAQELRCIGDCFNAYYARR-NH_2
33-Bak$^{i,i+11}$-NH_2	GCVGRALAAIGDCINR-NH_2
33-(5)[FAM]-$[PEG]_3$-Bak$^{i,i+11}$-NH_2	(5)[FAM]-$[PEG]_3$-GCVGRALAAIGDCINR-NH_2

b. Photo-Characterisation of Stapled Peptide Complexes

The *cis*-/*trans*-isomerisation of the stapled-peptides were characterised using UV-visible spectroscopy and LC-MS techniques. In order to obtain the greatest dynamic range for cell-experiments, the switching wavelengths used need to have the highest possible proportions of either *active* or *inactive* states. As the application of UV light is toxic to cells, light of the visible range of the spectrum and ideally red-light-switching was preferred as it displays higher tissue penetration and lower toxicity than shorter wavelengths of visible light.

Peptides stapled with **33** could be isomerized using red-light (635 nm), as demonstrated by the change in their UV-visible spectrum upon illumination (Figure II.38). Maximal relaxation to the thermodynamically more stable *trans*-state was achieved by heating solutions to 60 °C. Pleasingly, blue light (450 nm) could be used to obtain a photostationary state that was almost identical to the dark state (60 °C), allowing bidirectional switching using red and blue light. UV light produced an intermediate photostationary state. As for free *cis*-**33**, the *cis*-**33**-stapled peptides were long-lived with slow thermal relaxation at 37 °C. The measured half-life time for *cis*-**33**-Ant-Bid$^{i,i+4}$-NH_2 at 37 °C in water was ~13 hours, long enough to cover most cellular events. This half-life was, however, significantly shorter than free **33** in DMSO (46 hours, 37 °C), due to the differences in the solvents and the destabilising steric effect of the peptide on *cis*-**33**.

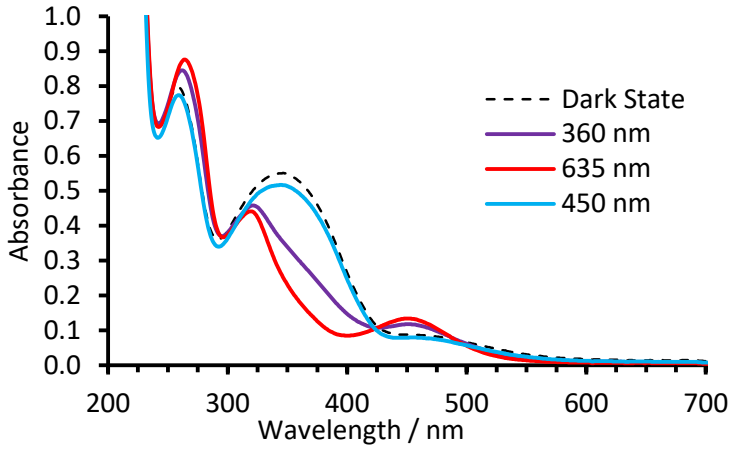

Figure II.38 *UV-visible spectra of **33**-GL-Bid$^{i,i+4}$-NH_2 in a thermally induced dark state and at PSS_{360nm}, $PSS_{450\,nm}$ and $PSS_{635\,nm}$.*

When shorter peptides, such as GL-Bid$^{i,i+4}$-NH_2, were stapled with **33** the half-lives of their *cis*-isomers remained long even at elevated temperatures (11 hours at 60 °C). However, due to the lower net-charge of these constructs, organic solvents were required to solubilise most of the **33**-stapled peptides. For example, while **33**-Ant-Bid$^{i,i+4}$-NH_2 was readily soluble in water, the addition of acetonitrile (33% v/v) was necessary to dissolve **33**-GL-Bid$^{i,i+4}$-NH_2, which lacks the highly polar CPP sequence.

Peptide constructs that employed the water-soluble linker **37**, displayed significantly faster thermal relaxation than **33**-stapled peptides. The observed half-life time of the **37** stapled peptide **37**-(5)[FAM]-GL-Bid$^{i,i+4}$-NH_2 at 20 °C was 81 min (Figure II.39). Due to the photo-

bleaching of the carboxyfluorescein-group under blue-light, all (5)[FAM]-labelled peptides had to be thermally relaxed back into their native state.

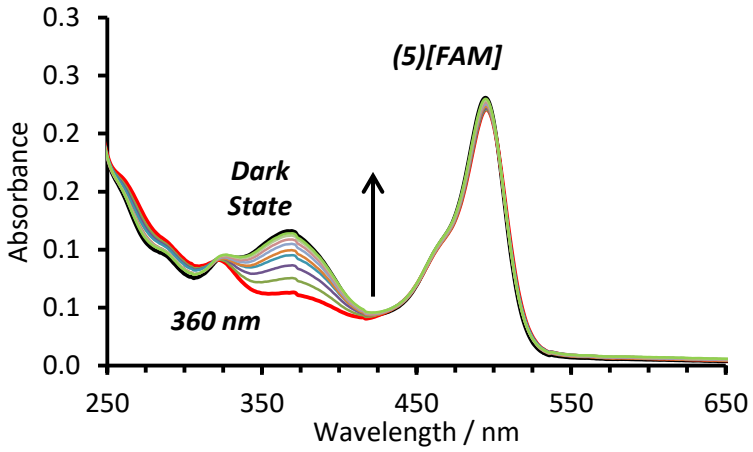

Figure II.39 *UV-visible spectra showing thermal relaxation of **37**-(5)[FAM]-GL -Bid$^{i,i+4}$-NH$_2$ at 20 °C from PSS$_{360nm}$. Spectra were recorded every 30 minutes ($t_{1/2}$ = 81 minutes).*

LC-MS was used to quantify the extent of *cis*-/*trans*-isomerization of a sample of **33**-Ant-Bid$^{i,i+4}$-NH$_2$. The two isomeric forms were easily separated on an analytical HPLC-column due to the differences in hydrophobicity between the two states and the peak areas under the 210 nm absorbance trace were integrated to assess the *cis*-/*trans*-isomer ratio (Figure II.40).

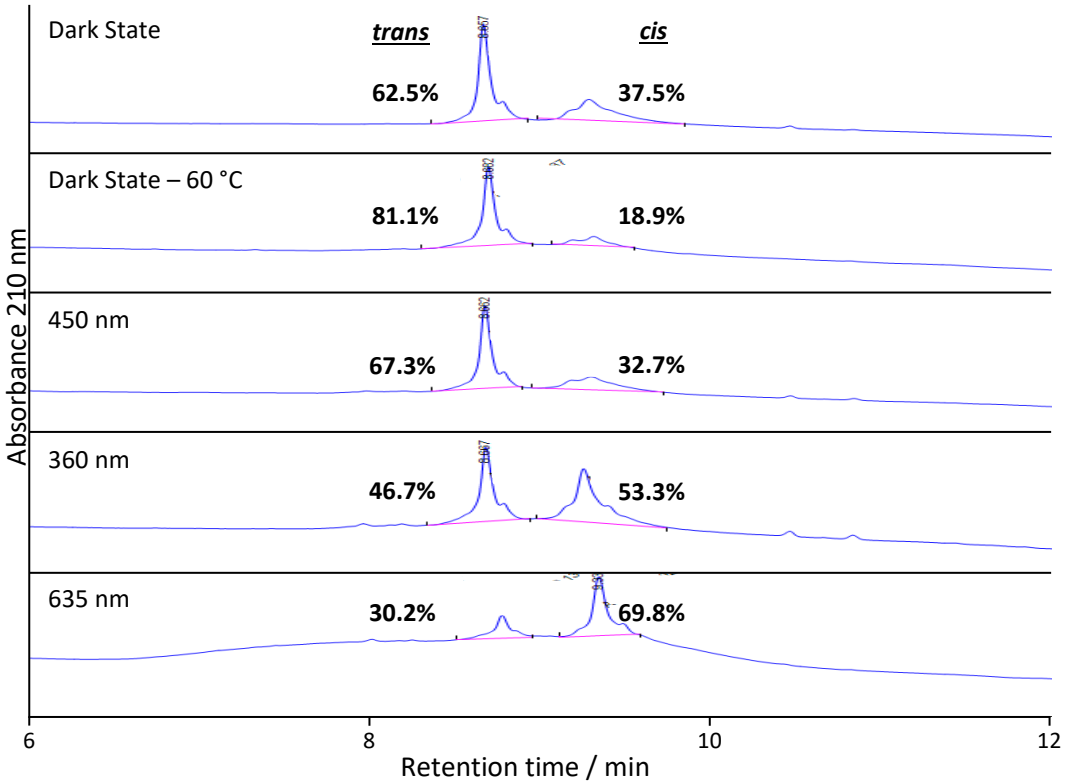

Figure II.40 *HPLC traces of **33**-Ant-Bid$^{i,i+4}$-NH$_2$ showing isomer ratios under different conditions. Maximum discrimination is achieved in the dark at 60 °C and under red light (635 nm).*

A sample of **33**-Ant-Bid$_{i,i+4}$-NH$_2$ equilibrated in the dark at room temperature in aqueous solution contained 62% *trans* and 38% *cis* isomer. Heating this sample to 60 °C achieved a state containing significantly more *trans*-isomer (81%), suggesting that the energy barrier of isomerisation at room temperature prevents easy access to the thermodynamic ground ratio. Irradiation with blue light (450 nm) resulted in a similar quantity of *cis*-isomer (33%) to the room temperature sample, whilst irradiation with 360 nm resulted in a 2.8-fold enrichment of the *cis*-isomer compared to the dark state at 60 °C. Red-light irradiation (635 nm) caused the biggest change between dark- and light-state with a 3.7-fold increase of the *cis*-isomer compared to the dark state sample at 60 °C. **33**-Bim$^{i,i+4}$-NH$_2$ in buffer supplemented with acetonitrile displayed a similar 3.4-fold increase in *cis*-isomer compared to the dark state (to 89% from 26%) when exposed to red-light at room temperature.

The wider cysteine spacing in **33**-Bak$^{i,i+11}$-NH$_2$ results in α-helical conformation matching the end-to-end distance of the *trans*-azobenzene staple, imposing additional tension on the *cis*-isomer of the crosslinker compared to narrower spacings. LC-MS determined a dark-state sample in aqueous solution supplemented with acetonitrile to contain 83%

trans-**33**-Bak$^{i,i+11}$-NH_2 at room temperature. When the sample was irradiated with red light (635 nm), a 2.7-fold increase in peak area of the *cis*-isomer was seen to 45%.

In conclusion, the **33** and **37** stapled peptides displayed photo-physical properties that echoed the properties of the free crosslinkers. Compound **33** was attached to a number of pro-apoptotic peptides and could then be switched between its *cis* and *trans* isomers by irradiation with 360 nm, 635 nm and 450 nm light sources. The greatest difference in isomer populations were obtained using red-light irradiation and thermal relaxation of the constructs at 60 °C.

c. Circular Dichroism Spectroscopy

The aim in crosslinking pro-apoptotic peptides is to control their conformation so that an α-helical peptide mimics the BH3 domain of a pro-apoptotic protein in binding to the hydrophobic groove of anti-apoptotic Bcl-2 proteins. Circular-dichroism (CD) experiments were therefore carried out to examine changes in helical propensity upon light-induced *trans-cis* isomerization of the attached crosslinker.

Spectra of peptides (typically 50 µM) were recorded in potassium phosphate buffer (5 mM, pH 8.0) containing DTT (1 mM) in a 1 mm path length cuvette with at 20 °C. However, all **33**-stapled peptides were insoluble under these conditions, even when incubated for extended durations at increased temperatures. Addition of DMSO as a co-solvent resulted in a strong background absorbance at 204 nm. Therefore, attention was then focussed on native, non-stapled peptides. Surprisingly, Bim$^{i,i+4}$-NH_2 was not soluble either, but GL-Bid$^{i,i+4}$-NH_2 and Bak$^{i,i+11}$-NH_2 could be analysed by CD-spectroscopy in buffer (Table II.5).

Table II.5 *Mean residue ellipticity and helical content of peptides at 20 °C.*

Peptide	$[\Theta]_{r,222}$ / deg cm^2 dmol^{-1}	Helicity / %
Bak$^{i,i+11}$-NH_2	-737	3
GL-Bid$^{i,i+4}$-NH_2	-1118	3
Ant-Bid$^{i,i+4}$-NH_2	-868	2
33-Ant-Bid$^{i,i+4}$-NH_2 (Dark state)	-4079	11
33-Ant-Bid$^{i,i+4}$-NH_2 ($PSS_{450\ nm}$)	-4939	14
33-Ant-Bid$^{i,i+4}$-NH_2 ($PSS_{635\ nm}$)	-4479	13

Compound **33**-Ant-Bid$^{i,i+4}$-NH_2 was insoluble in buffer but was soluble in water, suggesting that solubility issues of the constructs could be connected to cation-π stacking interactions that are significantly reduced in deionised water, or that even the weak buffer was sufficient to screen mutually repulsive charges. Ant-Bid$^{i,i+4}$-NH_2 and **33**-Ant-Bid$^{i,i+4}$-NH_2 were therefore analysed in water rather than buffer (Figure II.41).

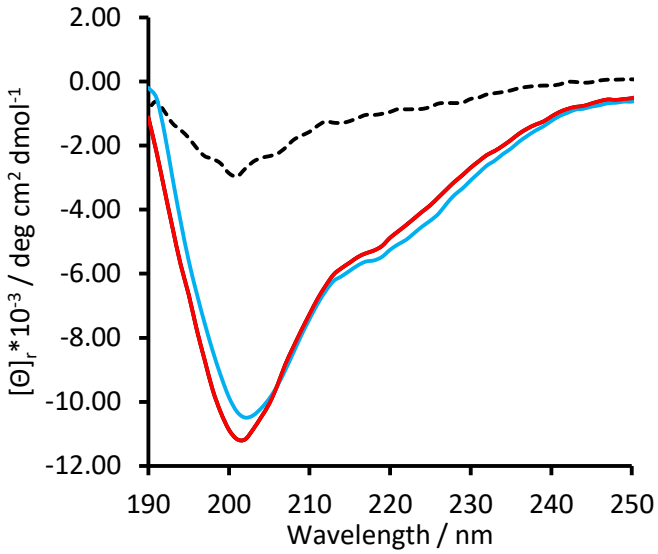

Figure II.41 *CD-spectra of the non-stapled peptide Ant-Bid$^{i,i+4}$-NH_2 (black dotted line) and **33**-Ant-Bid$^{i,i+4}$-NH_2 in its dark state (black line), $PSS_{635\ nm}$ (red line, overlaps with black line) and $PSS_{450\ nm}$ (blue line).*

As expected, non-stapled peptides displayed very low α-helical content, roughly estimated as 2-3% based on a their mean residue ellipticities at 222 nm.[235] Attaching the azobenzene staple to Ant-Bid$^{i,i+4}$-NH_2 resulted in an increase of α-helicity to 11%. Contrary to expectations, red-light irradiation did not lead to a significant increased helicity (13%) whereas the irradiation with blue light created a nominally higher α-helical content of 14%. Although these results seemed to contradict the hypothesis that α-helicity can be induced by *cis*-azobenzene formation, similar results were observed in the past for **37**-stapled Bid$^{i,i+4}$-peptides.[211,236] It is thought that the stabilisation of binding interactions are more significant than initial conformations for controlling the affinity of BH3 peptides.[237]

d. Fluorescence-Polarisation Binding Assays

In vitro binding experiments were carried by mixing fluorescently tagged-peptides in their dark and light states with the anti-apoptotic protein Bcl-x_L in fluorescence-polarization (FP) assays. It

had previously been reported by Kneissl *et al.* that the azobenzene-staple **37** had an effect on the binding properties of a number of pro-apoptotic BH3-domain peptides with **37**-Bid$^{i,i+4}$-NH_2 and **37**-Bak$^{i,i+11}$-NH_2 reported to show 23-fold and 2-fold differences in specific target-binding between their light and dark states.[235]

Stock solutions of the peptides were prepared, with peptide concentrations determined by the extinction coefficient of their carboxyfluorescein group at 492 nm in sodium hydroxide solution (0.1 M). Peptide-stock solutions (typically ~100 mM) were diluted in phosphate buffer (100 mM, pH 7.5) containing sodium chloride (10 mM) to a final concentration of 10 nM. TCEP reducing agent was added to samples of non-crosslinked peptides to avoid disulfide-formation. Crosslinked peptides were thermally relaxed by incubating them at 60 °C for 16 hours prior to the experiment. Light states were maintained by irradiating the sample every 5 min with an appropriate light source for 2 min during the experiment. Bcl-x_L was expressed in *E. coli* BL21 (DE3), purified by affinity chromatography and concentrated using a spin-column. Protein concentrations were determined using a known extinction coefficient at 280 nm. Measurements were carried out using a Perkin-Elmer LS-55 fluorescence spectrometer exciting at 495 nm and detecting fluorescence emission at 525 nm. During the experiment, the protein was titrated into the solution of fluorophore-labelled peptide in concentrations from 10 nM to 2 µM (resulting in a total increase in volume of <2.5 vol%) and the changes in fluorescence anisotropy recorded. All measurements were recorded in triplicate unless otherwise stated. The background signal of the measurement was removed by subtracting the initial anisotropy-value of the (5)[FAM]-labelled peptide before protein addition from the remaining values. To rule out interference from a CPP, **33**-stapled constructs GL-Bid$^{i,i+4}$-NH_2 and Bak$^{i,i+11}$-NH_2 were tested first.

Titration curves were fitted to the Hill-Langmuir equation, simplified by the assumption that only one binding site exists for the peptides on the target protein. Based on the Hill-Langmuir equation, the obtained anisotropy values were fitted to two different binding models: specific binding and total-binding (Figure II.42a). Specific binding only takes the interaction of the peptide with the protein into account whereas the total binding includes specific and non-specific binding interactions. It is assumed that the amount of non-specific binding is directly proportional to the concentration of protein, and thus becomes more significant at higher concentrations. The B_{max} term represents the maximum specific binding of the function and can never be fully reached when the binding curve is described by specific interactions only. B_{max} can also be used to normalize different data sets by division of the receptor-ligand complex to yield fractional binding values. K_D is the equilibrium binding constant; the

concentration that is needed to achieve a half-maximum binding at equilibrium, commonly used to describe specific protein-ligand interactions. Binding curves are often displayed on a log-scale to give a sigmoid curve where the $\log_{10}(K_D)$ value lies at the inflection point (Figure II.42b). Linear binding curves can be misleading as a slower increase of the anisotropic values can be misinterpreted as a saturation of the binding sites. However, when plotting the same values on a logarithmic scale, it often becomes more apparent by the shape of the sigmoid curve if sufficient sample points were measured. The dissociation constants were reported with their standard deviation (SD) and 95% confidence interval (95% CI) based on their binding model used to fit the experimental data.

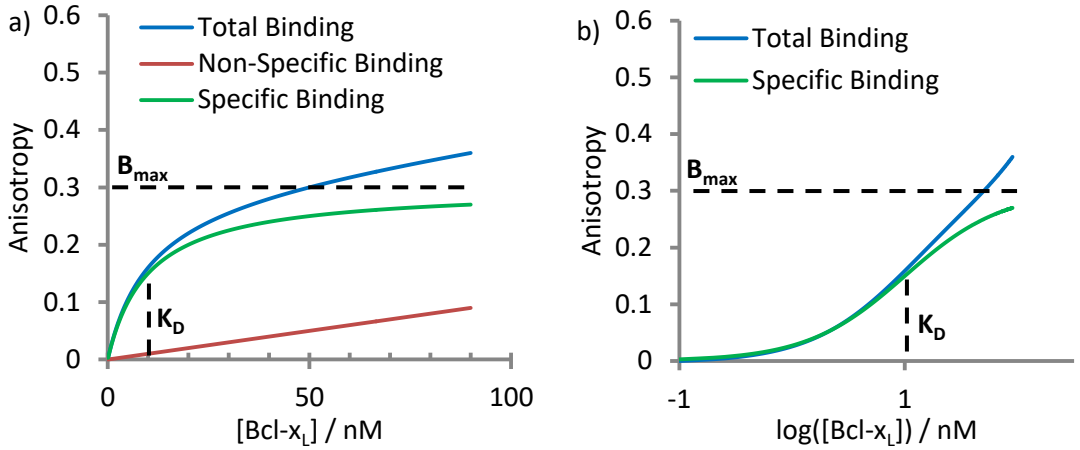

Figure II.42 *Simulated binding curves using the Hill-Langmuir equation with a K_D of 10 nM and B_{max} of 0.3 on a linear plot (a) and on a logarithmic plot (b). The total binding is based on the assumption that non-specific binding is proportional to the added concentration of the protein Bcl-x_L.*

(5)[FAM]-GL-Bid$^{i,i+4}$-NH_2 was titrated with Bcl-x_L and the anisotropy values obtained were fitted to both binding models (Figure II.43a). A significant linear increase of the anisotropy values was observed from ~200 nM onwards suggesting a strong contribution of non-specific binding. The close-up of the plots up to 200 nM (Figure II.43b) showed that even at lower protein concentrations the total-binding model offers the best fit for the data. Plotting the residuals of the specific model (Figure II.43c) against the protein concentration suggested that the specific model suffers from systematic errors while the random distribution of the values around zero in the total-binding model indicated to be a more appropriate fit (Figure II.43d). The discrepancy between the two binding models became also visually apparent when the experimental data was plotted on a logarithmic scale (Figure II.44a). As the two binding models

resulted in very different K_D values for the same data set (35 nM vs. 201 nM), the curves showed only little overlap implying a strong contribution of non-specific binding. Using the more sophisticated model, specific binding could be observed despite a non-specific linear effect, (Table II.6) however the large errors made it difficult to accurately determine a dissociation constant.

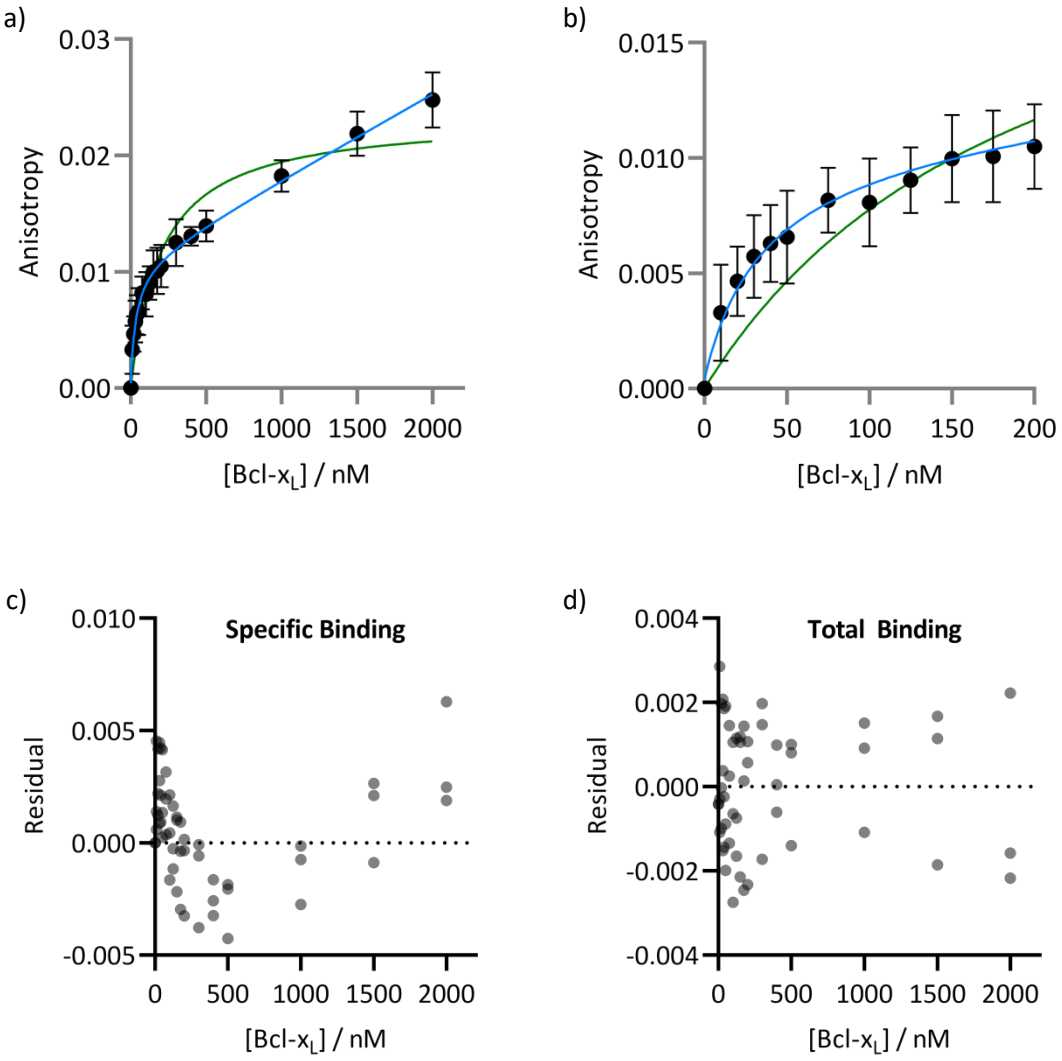

Figure II.43 *Binding curves and residual plots for (5)[FAM]-GL-Bid$^{i,i+4}$-NH$_2$. a-b) Experimental values were plotted against the total-binding (cyan line) and the specific-binding model (green line). c-d) Residuals of the binding models show that the total-binding model was a more appropriate description of the experimental data based on its random distribution.*

Table II.6 *Dissociation constants obtained for (5)[FAM]-GL-Bid$^{i,i+4}$-NH$_2$.*

Peptide / Model	Total Binding / nM			Specific Binding / nM		
	K_D	95% CI	SD	K_D	95% CI	SD
(5)[FAM]-GL-Bid$^{i,i+4}$	35	78 - 18	60	201	279 - 143	138

The obtained K_D-values differed from previously reported values (117 ± 48)[235] for (5,6)[FAM]-Bid$^{i,i+4}$-NH$_2$, and it was thought that the additional hydrophobic glycine and leucine residues in (5)[FAM]-GL-Bid$^{i,i+4}$-NH$_2$ must contribute to the increased non-specific binding, and thus the large errors in the measurement. A stored sample (5)[FAM]-Bid$^{i,i+4}$-NH$_2$ (previously synthesised and purified by Dr. Robert Mart) was tested against Bcl-x$_L$ in a single repetition and the data fitted with both binding models (Figure II.44b).

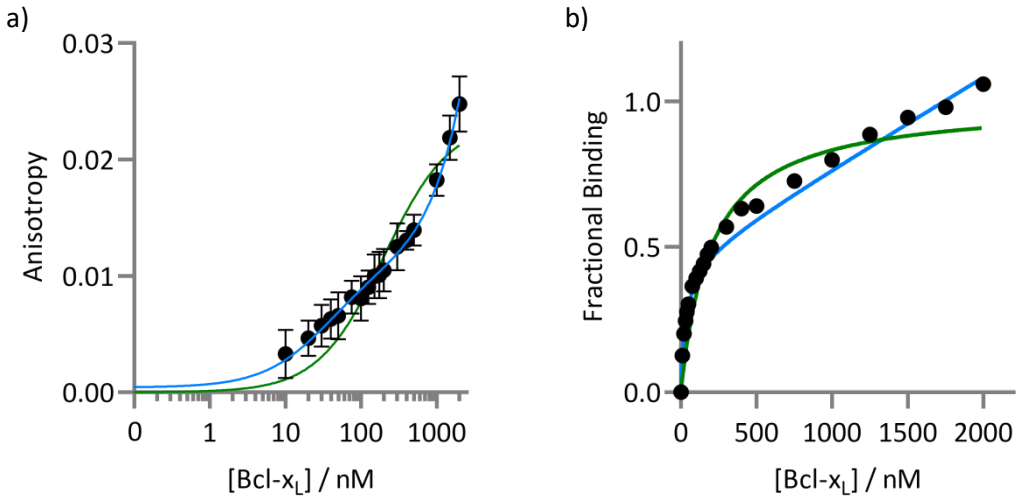

Figure II.44 *a) Binding curve of the peptide (5)[FAM]-Bid$^{i,i+4}$-NH$_2$ plotted on a logarithmic scale with the fits of the specific-binding model (green line) and the total-binding model (cyan line). b) Previous fit curves for the specific-binding (green line) and total-binding (cyan line) of the peptide (5)[FAM]-GL-Bid$^{i,i+4}$-NH$_2$ overlaid upon the experimental data of (5)[FAM]-Bid$^{i,i+4}$-NH$_2$.The similarity of the data points to the total-binding model indicated that the additional glycine and leucine residues in the peptide sequence did not alter the binding properties of the peptide.*

Again, the model including non-specific binding provided a superior fit across the whole concentration range and when the data were overlaid with the fits previously obtained for (5)[FAM]-GL-Bid$^{i,i+4}$-NH$_2$ (Figure II.44b), the additional residues appeared to have little impact

on the balance between specific and non-specific interactions. The K_D values obtained from total binding fits for (5)[FAM]-Bid$^{i,i+4}$-NH_2 were similar to those obtained for (5)[FAM]-GL-Bid$^{i,i+4}$-NH_2 (50 nM, 95% CI: 67-38 nM; SD ± 32 nM).

Discrepancies between these fits and those previously reported might also be explained by the lesser contribution of non-specific binding at lower concentrations, e.g. (5)[FAM]-GL-Bid$^{i,i+4}$-NH_2 for protein concentrations up to 200 nM (Figure II.45a).

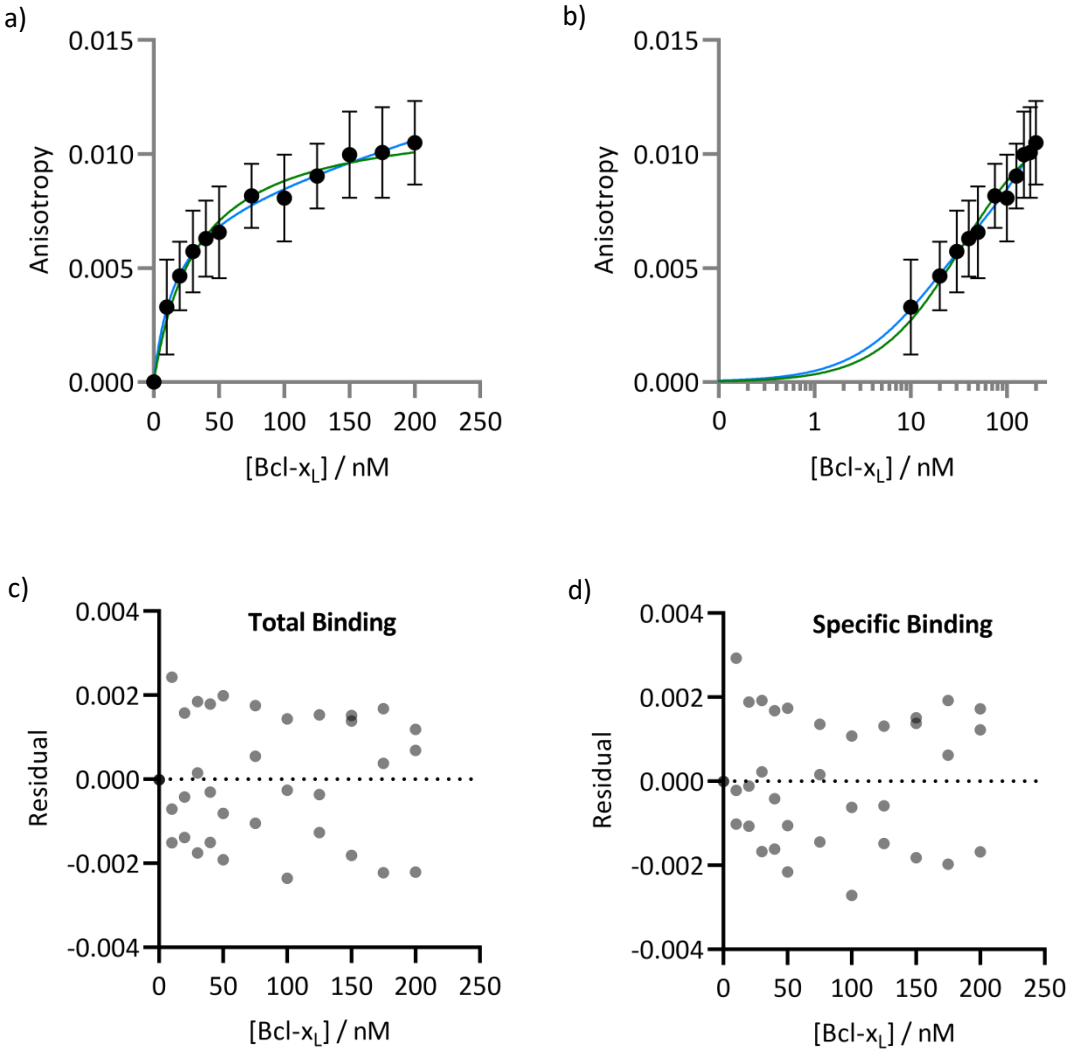

Figure II.45 *Binding curves and residual plots for the peptide (5)[FAM]-GL-Bid$^{i,i+4}$-NH_2 for a protein concentration up to 200 nM. The experimental values were plotted against the total-binding (cyan line) and the specific-binding model (green line) on a linear scale (a) and a logarithmic scale (b). c-d) Residuals of the binding models showed that both models describe the binding accurately at low concentrations indicating that little non-specific binding is dominant at lower concentrations.*

The plateau at the higher end of the concentrations resembled the shape of an ideal binding curve without any significant non-specific binding. Both models describe the data-points well within their errors, as can also be seen when plotting the data on a logarithmic scale (Figure II.45b). The residuals of the total (Figure II.45c) and the specific-binding model (Figure II.45d) showed a random distribution, in marked contrast to their application to wider concentration ranges (Figure II.43) suggesting that the K_D-binding dominates at low concentrations. Indeed K_D values derived from both binding models were similar for this narrower concentration range (Table II.7), and the K_D-value for the specific-binding model for up to 200 nM protein concentration (33 nM) correlates well with the dissociation constant of the total-binding model for the titration curve over the entire concentration range (35 nM). The total binding model will be more accurate over wider concentration ranges and in cases of stronger non-specific (ie. hydrophobic) interactions or weaker specific binding.

Table II.7 *Obtained dissociation constants for the peptide (5)[FAM]-GL-Bid$^{i,i+4}$-NH_2 up to 200 nM protein concentration with 95% confidence interval and standard deviation.*

Peptide / Model	Total Binding / nM			Specific Binding / nM		
	K_D	95% CI	SD	K_D	95% CI	SD
(5)[FAM]-GL-Bid$^{i,i+4}$ *[0 - 200 nM]*	16	99 - 1.8	77	33	56 - 19	29

In conclusion, non-specific binding dominated for (5)[FAM]-GL-Bid$^{i,i+4}$-NH_2 at higher concentrations of Bcl-x_L where specific interactions were saturated. Large errors made an accurate determination of the dissociation constant challenging. The total-binding model was equivalent to the non-specific model over a lower concentration range, but described the full-range concentration data set more accurately. The glycine and leucine residues of (5)[FAM]-GL-Bid$^{i,i+4}$-NH_2 were shown to have little effect on binding behaviour, suggesting that non-specific binding is an intrinsic property of the peptides investigated.

Compound **33**-(5)[FAM]-GL-Bid$^{i,i+4}$-NH_2 was tested next, with a degree of optimism as previously reported results with **37**-(5,6)[FAM]-Bid$^{i,i+4}$-NH_2 indicated significant differences between the dark and light states.[235] However, non-specific binding dominated even at low concentrations in both light and dark states, with large errors in the calculated properties (Figure II.46a).

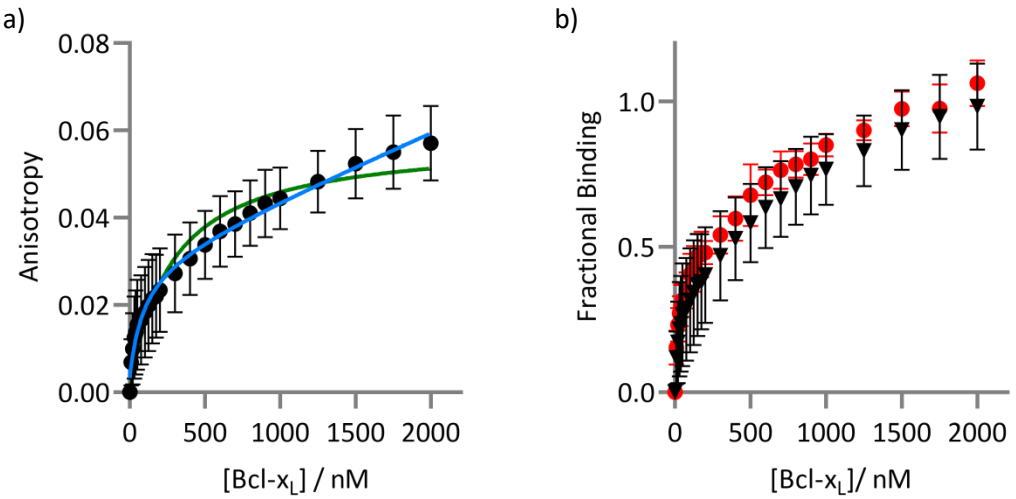

Figure II.46 *a) Binding curve for dark state **33**-(5)[FAM]-GL-Bid$^{i,i+4}$-NH$_2$ with the values fitted to a specific-binding (green line) and total-binding (cyan line) model. b) Overlaid dark (▼) and light state (●)**33**-(5)[FAM]-GL-Bid$^{i,i+4}$-NH$_2$ curves.*

The irradiated sample showed a significant overlap with dark state sample implying that no difference in protein affinity with respect to their isomeric state (Figure II.46b), but close comparison of the dissociation constants proved impossible due to the magnitude of the errors (Table II.8).

Table II.8 *Dissociation constants, 95% confidence intervals and standard deviations obtained for **33**-(5)[FAM]-GL-Bid$^{i,i+4}$-NH$_2$ in its dark and light states.*

Construct / Model	Total Binding / nM			Specific Binding / nM		
	K_D	95% CI	SD	K_D	95% CI	SD
33-(5)[FAM]-GL-Bid$^{i,i+4}$ *Dark State*	92	708 - 18	818	266	413 - 173	284
33-(5)[FAM]-GL-Bid$^{i,i+4}$ *PSS$_{635\ nm}$*	59	118 - 32	103	171	221 - 132	105

One possible explanation for these observations could be self-aggregation of the peptide, with the low concentration of monomeric peptide remaining in solution could then lead to large experimental errors. The **33**-stapled peptides were generally insoluble in buffer systems and

although the constructs were soluble in the stock solution (0.1 M NaOH), dilution to 10 nM might have led to micro-precipitation. The overall shape of the binding curve indicates nM-concentration range interactions with a strong contribution from non-specific binding, possibly *via* interactions between the crosslinker and hydrophobic or aromatic residues on the surface of the protein.

To examine the effect of solubility issues, the water-soluble azobenzene linker **37** was stapled to the peptide to compare the results directly to the previously published data.[235] Compound **37**-(5)[FAM]-GL-Bid$^{i,i+4}$-NH_2 differs to the reported construct only in the glycine and leucine residues, previously shown to exert little effect (Figure II.44b). Titration data indicated a significantly tighter binding compared to the equivalent peptide crosslinked with **33** (Figure II.47a,b). Inspection of residual plots (Figure II.47c) suggested the total-binding model remained a better fit than the specific binding model. When dark and light states were plotted together, the observed affinities were within each other's error bounds, suggesting that the *cis*-/*trans*- state of the linker did not in fact affect the binding (Figure II.47d). However, the dissociation constants were very low in both of the models implying a tight binding of the construct (Table II.9) and below the range at which they could sensibly be determined using 10 nM peptide solutions.

This observation was in stark contrast to the previously published results, where a 23-fold difference in binding was reported upon light-induced isomerisation. Moreover, both calculated constants lie within a standard deviation of the dissociation constant for the non-stapled peptide, implying that the crosslinker may not lead to an improved binding over the unstapled peptide. The error bars of the measurement were, however, significantly smaller than those obtained from the previous binding experiments, possibly due to the improved solubility of the **37**-stapled construct over the **33**- and non-stapled peptide (5)[FAM]-GL-Bid$^{i,i+4}$-NH_2 leading to more monomeric peptide in solution.

Table II.9 *Obtained dissociation constants for the construct **37**-(5)[FAM]-GL-Bid$^{i,i+4}$-NH_2 with 95% confidence interval and standard deviation in its dark and light state.*

Peptide / Model	Total Binding / nM			Specific Binding / nM		
	K_D	95% CI	SD	K_D	95% CI	SD
37-(5)[FAM]-GL-Bid$^{i,i+4}$ *Dark State*	14	17 - 11	7	30	37 - 24	15

37-(5)[FAM]-GL-Bid$^{i,i+4}$ PSS_{360nm}	7	13 - 3.6	11	19	28 - 12	19

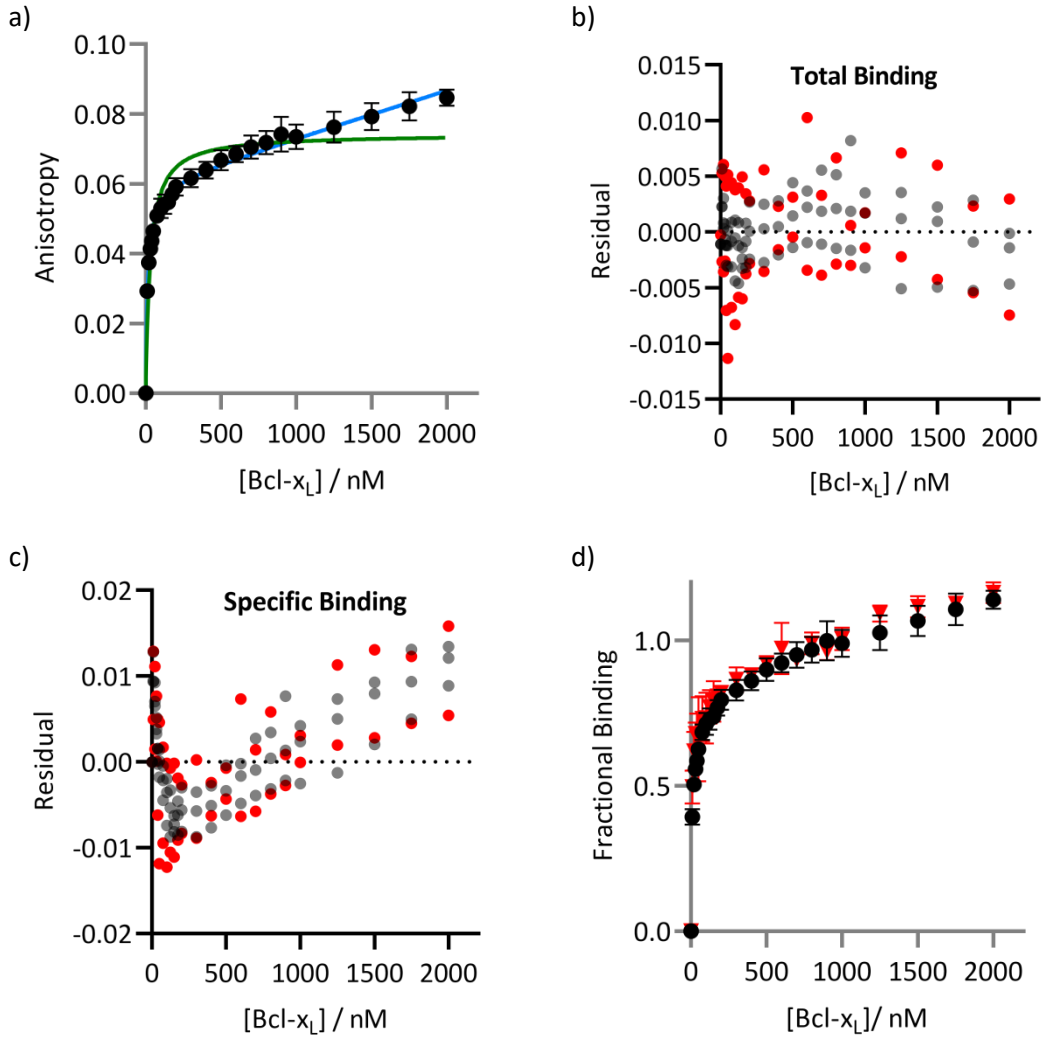

Figure II.47 *Binding curves and residual plots for* ***37****-(5)[FAM]-GL-Bid$^{i,i+4}$-NH$_2$. a) The experimental values were plotted with the total-binding (cyan line) and the specific-binding model (green line) on a linear scale for the dark state. b-c) Residuals of the binding models showed that the total-binding models describes the binding accurately - ● Dark state, ● Light state . d) Overlaid, normalized values for the dark state (●) and the light state (▼).*

Upon closer examination of the previously published data,[235] it became apparent that the experimental values were only plotted against the specific binding model, disregarding non-specific interactions. Different data sets seemed to have been compared to each other without normalizing them correctly to their intrinsic B_{max}-value leading to unrealistic fractional binding values between the dark and light states of the tested constructs. Data points for the anisotropy values were not collected at the same concentrations for both states and therefore

did not account the non-specific binding for both isomers equally. Normalising the two isomeric states then resulted in an apparent tighter binding for the light state due to the fewer measurement points at higher concentrations. Furthermore, no error bars were reported for each measurement making it impossible to judge if the anisotropy values for the dark and light state overlapped. The raw data for the reported binding, which was produced by Dr. Sabine Kneissl, were obtained, re-plotted and processed in the same manner as described above (Figure II.48).

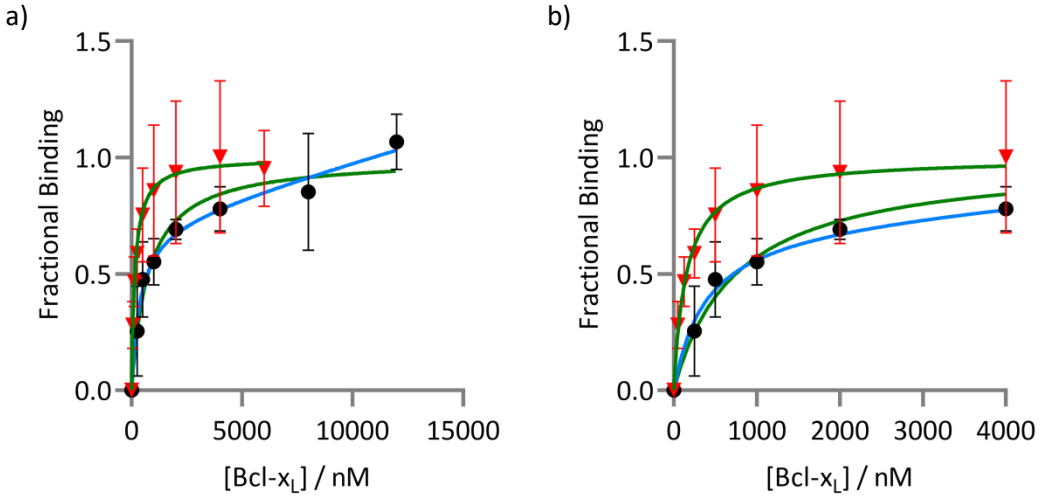

Figure II.48 *a) Re-plotted binding data for **37**-(5)[FAM]-Bid$^{i,i+4}$-NH$_2$ originally recorded by Dr. Sabine Kneissl.*[235] *b) Zoomed-in section of up to 4000 nM protein concentration shows the overlap of the error bars for each measurement.*

Although a difference between the light and dark state was evident, the error bars of each data set overlapped throughout the entire titration curve. The values for the light state seemed to be more accurately described by the specific-binding model whereas the dark state was better described by the total-binding model. However, this might be a result of the data points at the higher concentration range, which led to a greater contribution from non-specific binding. Few data-points were collected for the concentration range where specific binding would be expected to dominate, leading to an inaccurate determination of B_{max} and significantly bigger errors for the dissociation constant (Table II.10). Overall, these up-dated results are in alignment with the previously reported CD-spectroscopic data where no significant difference in induced helicity was found for the dark (16%) and light state (15%) of the **37**-stapled peptide Bid$^{i,i+4}$-NH$_2$.[236]

Table II.10 *Dissociation obtained constants from the raw data recorded by Dr. Sabine Kneissl (**37**-(5,6)[FAM]-GL-Bid$^{i,i+4}$-NH$_2$) in its dark and light state.*

Peptide / Model	Total Binding / nM			Specific Binding / nM		
	K_D	95% CI	SD	K_D	95% CI	SD
37-(5,6)[FAM]-Bid$^{i,i+4}$ *Dark*	362	1167 - 96	641	747	1320 - 411	544
37-(5,6)[FAM]-Bid$^{i,i+4}$ *PSS$_{360\ nm}$*	156	631 - 45	381	152	283 - 76	135

Wysoczanski *et al.* previously solved a solution structure of a complex between apoptosis activating **37**-Ac-Bak$^{i,i+11}$-NH$_2$ peptide and the anti-apoptotic protein Bcl-x$_L$,[213] finding the peptide to be bound in the hydrophobic groove binding site. As no other solution or solid state structures of pro-apoptotic, azobenzene stapled peptides in complex with Bcl-x$_L$ have been reported, this drove the expectation of the specific single-site binding that was observed for the stapled peptide **37**-Ac-Bak$^{i,i+11}$-NH$_2$. Furthermore, previous CD-spectroscopy results of the same construct showed that the dark and light states display significant differences in α-helicity (100% and 44%), which stands in strong contrast to the construct **37**-Ac-Bid$^{i,i+4}$-NH$_2$ where no significant differences were observed.[235,236] Whilst modest control of the Bcl-x$_L$ binding affinity of **37**-Ac-Bak$^{i,i+11}$-NH$_2$ had been reported, the superior *cis*:*trans* ratio at PSS$_{635\ nm}$ and slow relaxation of **33** suggested it would perform far better if its poor solubility compared to **37** could be overcome. To increase water-solubility when using the more hydrophobic **33**, three [PEG]-groups were added onto the N-terminus of the peptide. PEG-groups are flexible, hydrophilic chains that usually cause little steric hindrance. As the molecular weight of the solubility tag contributed to more than 20% of the total mass of the peptide, a significant improvement in solubility was expected, even when peptides were stapled with the **33**. This modification could also be used to distance an N-terminal carboxyfluorescein dye from the rest of the peptide to rule out non-specific binding interactions with the hydrophobic groove, allowing a suitably dye-tagged, crosslinked peptide to be examined by both NMR and FP techniques.

The FP binding curve of (5)[FAM]-[PEG]$_3$-Bak$^{i,i+11}$-NH$_2$ displayed a good overlap for both models indicating that specific binding is dominant with negligible contribution by non-specific binding over the entire range of measured protein concentrations (Figure II.49a). This is further

supported by the very small error bars and obtained dissociation constants, which were similar for both binding models with low standard deviations (Table II.11).

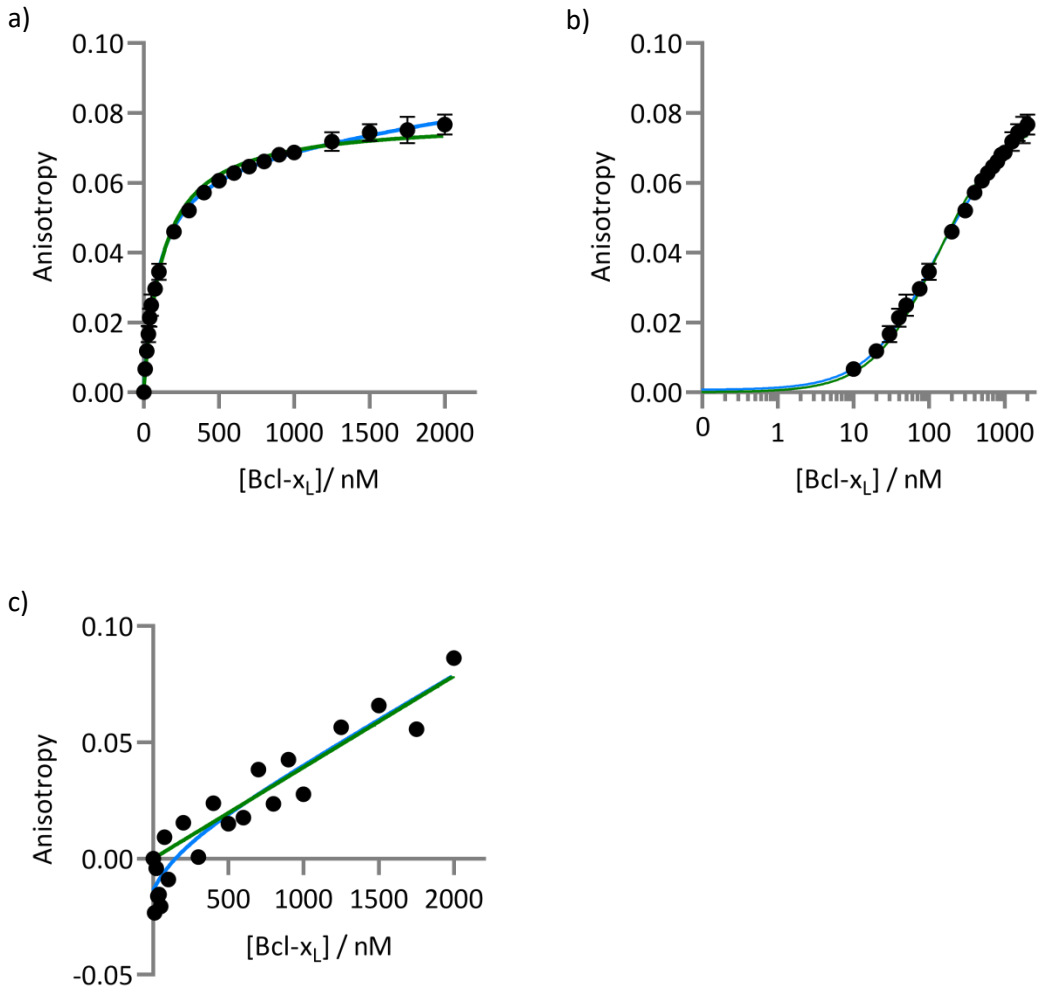

Figure II.49 *Binding curves on a linear (a) and logarithmic (b) scales for (5)[FAM]-[PEG]$_3$-Bak$^{j,i+11}$-NH$_2$ displayed specific binding over the entire concentration range. (c) Addition of a crosslinker resulted in* ***33****-(5)[FAM]-[PEG]$_3$-Bak$^{j,i+11}$-NH$_2$*

Table II.11 *Calculated dissociation constants for the (5)[FAM]-[PEG]$_3$-Bak$^{j,i+11}$-NH$_2$.*

Peptide / Model	Total Binding / nM			Specific Binding / nM		
	K_D	95% CI	SD	K_D	95% CI	SD
(5)[FAM]-[PEG]$_3$-Bak$^{j,i+11}$	102	119 - 88	34	127	139 - 117	25

The quality of this data highlighted the importance of the improved solubility, and supported the hypothesis that solubility issues could be the cause for the larger errors obtained for the

33-stapled and non-stapled peptide (5)[FAM]-GL-Bid$^{i,i+4}$-NH_2. The logarithmic plot of the data confirmed the initial observation and showed a sigmoidal curve implying specific binding over the tested range of protein concentration (Figure II.49b). However, only random scattering was observed for the dark state of the stapled construct **33**-(5)[FAM]-$[PEG]_3$-Bak$^{i,i+11}$-NH_2 suggesting that the attachment of the staple **33** prevented specific binding. This could be due to the precipitation of the construct through self-aggregation or rapid non-specific aggregation with protein.

e. NMR Characterisation of Peptide-Protein Complexes

If the disappointing fluorescence assay result for **33**-(5)[FAM]-$[PEG]_3$-Bak$^{i,i+11}$-NH_2 was indeed due to self-aggregation, this could either be due to the presence of **33**, or to π-stacking interactions between the N-terminal carboxyfluorescein group and **33**. The proposed protein NMR work was therefore continued as it could answer this question by omitting the dye and confirm the location of the specific binding the non-crosslinked construct by observing the chemical shift perturbation. Bcl-x_L was expressed in M9 minimal media supplemented with $^{15}NH_4Cl$ (99% ^{15}N) and purified as described. Product fractions were dialysed three times against sodium phosphate buffer (5 mM, pH 7.3), then concentrated by ultrafiltration to a 400 μM. NMR samples were supplemented with 5% D_2O and recorded at 298 K using a Bruker DPX-600MHz spectrometer equipped with QCI-P cryoprobe and preamplifiers using a ^1H-^{15}N-HSQC pulse sequence. Peptides were added in varying concentrations to a protein:peptide ratio of at least 1:1. ^{15}N-HSQC spectra were compared to those of pure protein and the published assignments for the Bcl-x_L/**37**-Ac-Bak$^{i,i+11}$-NH_2 complex.[212,213]

The ^1H-^{15}N-HSQC spectrum of pure Bcl-x_L showed generally well dispersed peaks, indicative of a folded protein (Figure II.50). Peaks at the top right corner of the spectrum arise from amide-interactions of asparagine and glutamine residues (blue box) and at the bottom left corner of the spectrum contains signals due to the aromatic side-chain amine peaks pf tryptophan (green box). Changes in the protein-structure upon binding of a ligand were more easily observed in these less-crowded regions. The spectra obtained overlapped well with previously recorded spectra, confirming Bcl-x_L was correctly folded (not shown).

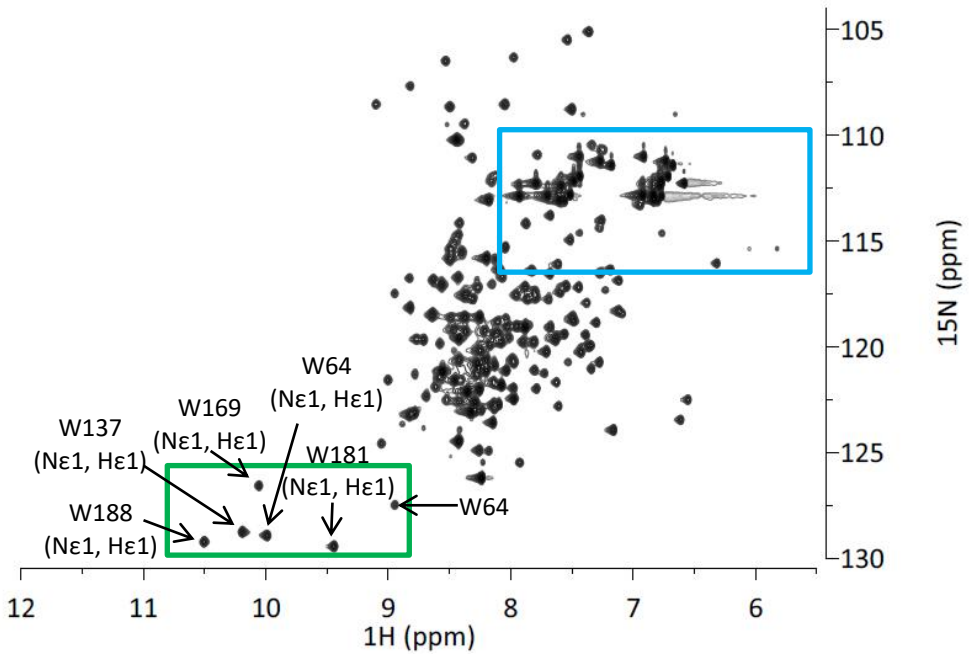

Figure II.50 *^{1}H-^{15}N-HSQC-spectrum of Bcl-x_L. The center of the spectrum is dominated by the backbone amide interactions whereas the blue box by the amide-interactions of the aparagine and glutamine residues. Aromatic amines in the green box arise from tryptophan residues.*

Incubation of Bcl-x_L with 1.4 eq. of the non-stapled peptide Bak$^{i,i+11}$-NH_2 gave a spectrum suggestive of incomplete binding, with peaks present in locations corresponding to both peptide-bound and free Bcl-x_L (Figure II.51). Integration of the Trp169 amine peak indicated 28% of the Bcl-x_L had bound peptide, but a loss of NMR-resolution started to become visible.

More peptide was added to the sample (total 5.7 eq.) to try to achieve saturation, but a precipitate formed. The sample was centrifuged and the supernatant re-analysed by NMR. The tryptophan amine peak now solely corresponded to shifts characteristic of bound peptide, with no peaks for the unbound protein visible (Figure II.52). However, the overall resolution of the spectrum was now generally very poor, presumably due to loss of signal from precipitated peptide-protein complexes leading to little protein remaining in solution.

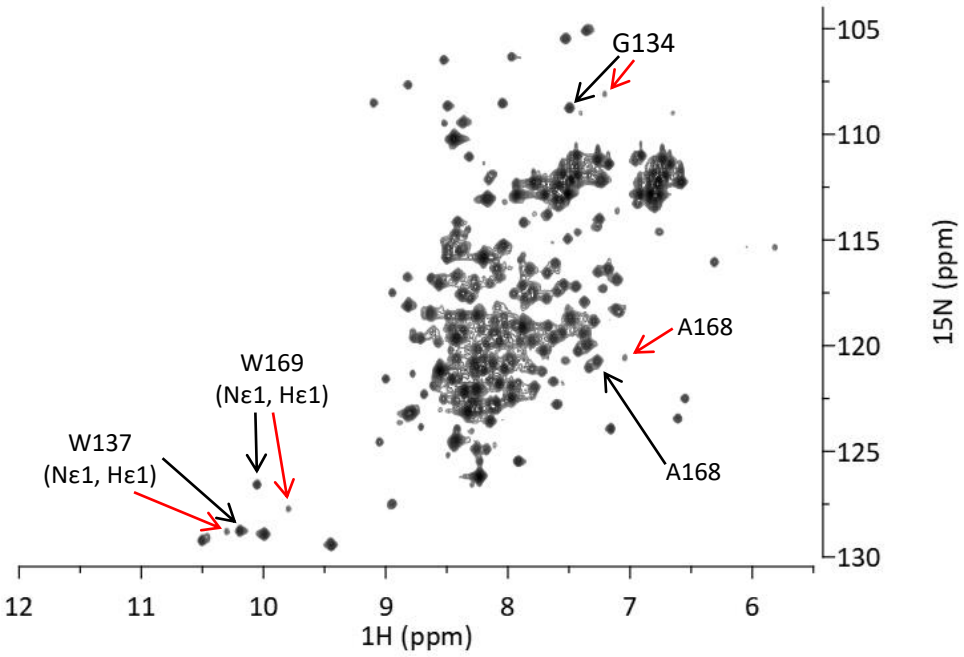

Figure II.51 *^{1}H-^{15}N-HSQC-spectrum of the protein Bcl-x_L with 1.4 eq. of unstapled peptide Bak$^{i,i+11}$-NH_2. Red arrows indicated new peaks arising from the bound complex whereas black arrows mark the peaks corresponding to the unbound protein.*

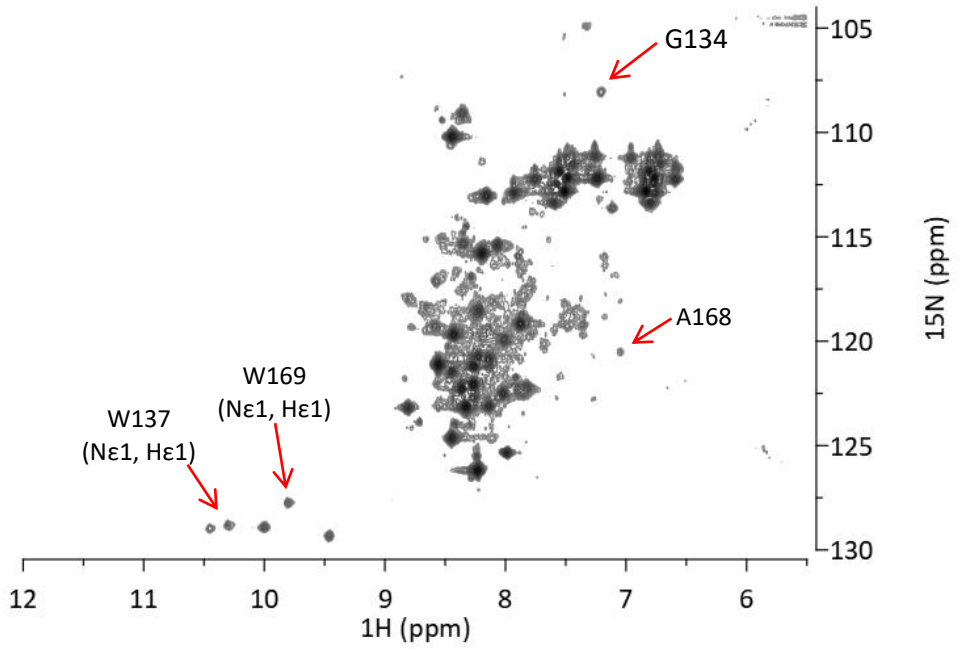

Figure II.52 *^{1}H-^{15}N-HSQC-spectrum of Bcl-x_L with 5.7 eq. of Bak$^{i,i+11}$-NH_2. Red arrows indicated new peaks arising from the peptide-protein complex.*

Precipitation or aggregation of protein samples upon addition of a ligand is a common problem, most often addressed by lengthy buffer optimizations.[238,239] Interestingly, the previously published NMR-solution structure work used a different procedure to prepare NMR samples, involving a second concentration step after the addition of the construct implying either that precipitate had formed or precipitation was mitigated by mixing the peptide and protein in a more dilute solution, then concentrating them.[213]

Curiously, when 1.1 eq. of the azobenzene stapled construct **33**-Bak$^{i,i+11}$-NH_2 was added to a sample of ^{15}N-labelled Bcl-x_L no binding was observed. More stapled peptide was added (total 2.7 eq.), but no peaks for peptide-bound protein were seen (Figure II.53). Although the NMR-spectrum obtained was of lower resolution than the spectrum of the protein on its own, no precipitation was evident either and the red colour of the NMR sample indicated solubilised **33**-Bak$^{i,i+11}$-NH_2.

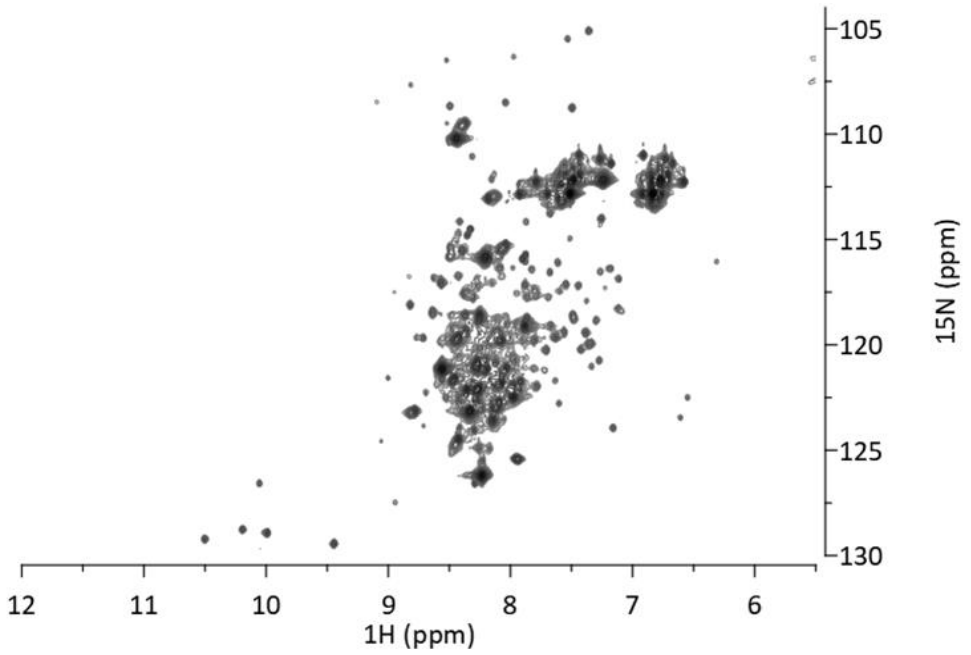

Figure II.53 *^{1}H-^{15}N-HSQC-spectrum of Bcl-x_L with 2.7 eq. of **33**-Bak$^{i,i+11}$-NH_2.*

In a control experiment **33**-Bak$^{i,i+11}$-NH_2 remained insoluble when incubated with the NMR buffer in the absence of protein, implying that interactions with the protein increased its solubility. One explanation for loss of signal without precipitation could be the aggregation of the peptide-protein complex leading to a slower tumbling complex. Larger molecules show faster relaxation for transverse magnetisation (T_2) and the enhanced relaxation leads to line broadening, degrading resolution and increasing signal overlap in crowded areas of spectra.

Slower tumbling of macromolecules also reduces longitudinal relaxation, leading to longer T_1 and necessitating longer recovery-delays between scans. These factors can combine to reduce the sensitivity of the NMR-experiments, leading to a lower signal-to-noise ratio.[240,241] Unlike **37**-Ac-Bak$^{i,i+11}$-NH_2, **33**-Bak$^{i,i+11}$-NH_2 did not seem to engage with the hydrophobic groove of the protein Bcl-x_L in a manner detectable by NMR spectroscopy, although the presence of protein increased its solubility in buffer. In contrast to **33**-Bak$^{i,i+11}$-NH_2, **33**-Ant-Bid$^{i,i+4}$-NH_2, Bim$^{i,i+4}$-NH_2, and **33**-Bim$^{i,i+4}$-NH_2 were insoluble in the NMR buffer even in the presence of the protein Bcl-x_L.

Finally, the effect of an N-terminal carboxyfluorescein was investigated using NMR-techniques. Although soluble, NMR spectra after the addition of (5)[FAM]-Bak$^{i,i+11}$-NH_2 to Bcl-x_L suggested limited binding. Integration of the Trp169 signals indicated only up to 16% binding, in marked contrast to the full binding observed using the non-dye-labelled version of this peptide. When a PEG-spacer was added between the fluorophore and the pro-apoptotic peptide in (5)[FAM]-$[PEG]_3$-Bak$^{i,i+11}$-NH_2, a greater (36%) shift in signals was observed (Figure II.54). However, addition of excess (5)[FAM]-$[PEG]_3$-Bak$^{i,i+11}$-NH_2 did not lead to increased binding.

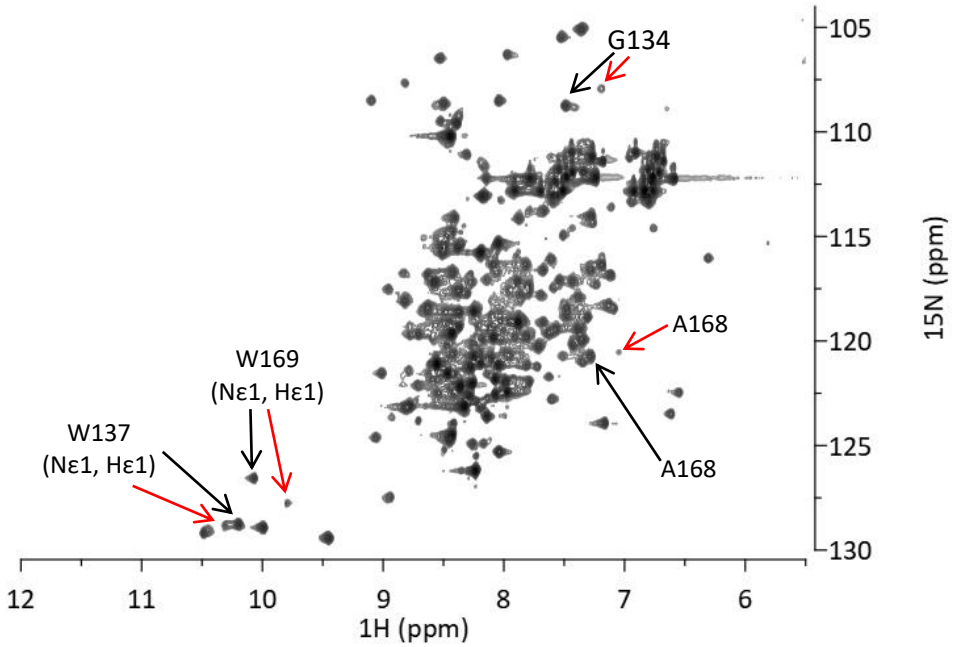

Figure II.54 *^{1}H-^{15}N-HSQC-spectrum of Bcl-x_L with (5)[FAM]-$[PEG]_3$-Bak$^{i,i+11}$-NH_2. Red arrows indicated new peaks arising from the bound peptide-protein complex whereas black arrows mark the peaks corresponding to the unbound protein.*

The equivalent peptide lacking the fluorophore, $[PEG]_3$-Bak$^{i,i+11}$-NH_2 showed full binding accompanied by the formation of precipitate and a significant loss of signal. These results were

analogous to the behaviour of GL-Bid$^{i,i+4}$-NH_2, which also showed full-binding when incubated with the protein sample (Appendix 10), but none with up to 4.0 eq. of (5)[FAM]-GL-Bid$^{i,i+4}$-NH_2. Nor did the fluorophore labelled CPP-BH3 peptide (5)[FAM]-Ant-Bid$^{i,i+4}$-NH_2 show any sign of binding, but it did give an orange precipitate suggesting that it is simply insoluble in buffer which was confirmed by control experiments.

In conclusion, the NMR-experiments showed that only the non-labelled and non-stapled peptides caused a shift in ^{15}N-^{1}H HQSC signals to positions characteristic of protein-peptide complexes. Addition of an N-terminal fluorophore diminished or abolished binding in all cases. This effect was counteracted to an extent when a linker was placed between the fluorophore and peptide as in (5)[FAM]-$[PEG]_3$-Bak$^{i,i+11}$-NH_2. Attachment of an azobenzene crosslinker was universally detrimental, leading to no observable binding and frequent precipitation. Even non-crosslinked sequences containing more hydrophobic residues such as Bim$^{i,i+4}$-NH_2 showed no sign of binding. The analogous peptide to that used in the published NMR structure, **33**-Bak$^{i,i+11}$-NH_2, was the only peptide soluble in the presence of the protein, but again no binding could be detected. Attempts to draw wider conclusions are complicated by the formation of aggregates when using the fluorophore, leading to a lower sensitivity of the NMR signals which may hide binding or bound species may precipitate.

f. Conclusion

In this chapter, the physical properties of stapled peptides were investigated, including tests on their isomerization, structure and binding to Bcl-x_L. These properties are critical to any future application of the constructs in a medicinal context. Attachment of azobenzene linker **33** to peptides led to a mixture of *cis*- and *trans*-isomers in most peptides, indicated by the presence of a recurring second peak observable by HPLC analysis. Red-light switching of the azobenzene linker was established and monitored by analytical HPLC. The relaxation rate of the isomerized crosslinked peptides still remained very low, retaining the desired conformation of the construct over the time scales of cellular events.

Generally, the attachment of the linker **33** to the peptides led to their insolubility in common buffers preventing their further analysis and characterisation. However, the **33**-stapled peptide Ant-Bid$^{i,i+4}$-NH_2 was soluble in deionised water and subsequently analysed using CD-spectroscopy. No significant changes in α-helicity could be observed upon irradiation of the construct using red-light. This was in accordance with previous observations where it was reasoned that a helix-inducing motif, such as a protein binding partner, is needed in order to

observe a change in helical propensity. Interestingly, these observations suggested that the previously observed increase in hydrophobicity using HPLC analysis and thus shift in retention time upon irradiation may not strictly be due to an increase in α-helical content. As the *cis*-isomer of the linker **33** is more polar than the *trans*-species, its later retention time by reverse phase HPLC can only be a result of a different conformational alignment of the peptide leading to an increased exposure of hydrophobic residues.

Fluorophore-labelled peptides were used to perform fluorescence polarisation binding assays. All tested peptides showed specific binding to some degree, with large margins of error making it challenging to determine the accurate dissociation constants. The standard deviation of the measurements were significantly reduced when the water-soluble crosslinker **37** was attached to the peptide (5)[FAM]-GL-Bid$^{i,i+4}$-NH_2, presumably as a result of an increased solubility of the peptide. However, the dissociation constants obtained for an **37** stapled construct did not differ significantly from the non-stapled peptide (5)[FAM]-GL-Bid$^{i,i+4}$-NH_2 suggesting that the linker increases solubility, but not necessarily binding affinity. No significant differences in binding properties were detected between the *cis*- and *trans*-isomers, an observation in accordance with CD-spectroscopic data where only little difference in the α-helical content could be observed upon irradiation. Previously published data were reanalysed, to show they also bound with little difference between dark and light state.

Large error bars were observed when *tetra-ortho*-chloro azobenzene stapled construct **33**-(5)[FAM]-GL-Bid$^{i,i+4}$-NH_2 was tested with Bcl-x_L, making it impossible to determine the dissociation constant accurately. This was most likely a result of aggregation of peptide-precipitation in solution due to the hydrophobic crosslinker, but no differences between dark and light state could be observed for this construct either. Utilizing the solubilizing PEG-group in (5)[FAM]-$[PEG]_3$-Bak$^{i,i+11}$-NH_2 resulted in much smaller errors and increased specific binding, presumably due to the increased solubility. Sadly, attachment of **33** obviated this improvement and no binding was observed, again possibly due to the limited solubility of the stapled construct.

Binding events were further investigated using NMR, where peptide was added to a sample of ^{15}N-labelled anti-apoptotic protein Bcl-x_L. The extent and specificity of the binding could then be estimated by comparison of the chemical shifts before and after addition. No binding could be seen for any of the **33**-stapled constructs, possibly due to the formation of aggregates leading to a diminished resolution. Interestingly, the protein seemed to possess a solubilizing effect for **33**-Bak$^{i,i+11}$-NH_2. Fluorophore-labelling appeared to severely compromise binding of non-crosslinked peptides that otherwise produced clear shifts, but the non-labelled and non-

stapled peptides all showed full binding, except the very hydrophobic $Bim^{i,i+4}$-NH_2. Interactions between the fluorophore with the protein-might have lead to incomplete binding or the formation of aggregates. Precipitations frequently caused reduced signal to noise levels, and was likely the result of protein-peptide interactions.

Unfortunately, **33**-stapled peptides showed only a limited degree of specific binding, presumably due to non-specific interactions of the aromatic crosslinker with the protein. The diminished solubility of the constructs caused major problems during characterisation and was not counteracted by the addition of a solubilizing tag. The addition of N-terminal fluorophores seemed to alter the binding properties of the peptides under NMR conditions, other label-free assays, such as ITC, might be a better in choice in future experiments.

5. Delivery of the Constructs and Light-Induced Activation of Cell Death in Mammalian Cells

a. Aims and Objectives

Using light as a stimulus to activate cell death through the natural apoptotic pathway offers the potential for non-invasive, spatiotemporal control of cell fate. Although azobenzene crosslinkers can enable the photo-control of peptides by influencing their secondary structure, the cellular uptake of larger molecules is often inefficient, limiting *in vivo* and therapeutic applications. Cell-penetrating peptide (CPP) sequences aid cellular uptake of covalently attached cargo molecules by enhancing either direct translocation across the outer membrane or endocytosis. CPPs with both cationic and amphipathic character have been demonstrated to transport peptides and proteins into cells, with the size and properties of the cargo molecule dictating the mechanism of uptake. Endosomal uptake typically occurs with larger cargo molecules, as direct translocation is energetically disfavoured due to the greater free energy penalty of desolvation and limitations in the size of the pores within the outer membrane created by CPPs. However, for therapeutic agents endosomal uptake is less desirable than direct translocation, as the cargo becomes entrapped within endosomes that are acidified over time leading to the degradation of the cargo even before they can reach the cytosol. Thus, a mechanism for endosomal escape is crucial for cytosolic delivery systems to effectively transport large functional molecules into mammalian cells. The synthesised apoptotic peptides GL-Bid$^{i,i+4}$-NH_2 and Ant-Bid$^{i,i+4}$-NH_2 crosslinked with azobenzene photoswitch **33** were tested to establish whether CPPs could allow cellular uptake and enable the control of cell fate using light. Studies were carried out on HeLa cells, derived from cervical cancer cells, to examine uptake by fluorescence-activated cell-sorting (FACS) experiments. Co-incubation experiments with a peptide consisting of an endosome escape sequence, E5-TAT, were carried out to identify endosomal entrapment of the administered peptides and enable release to the cytosol. The effect of peptides on cell viability using Celltiter Blue assays, with experiments employing **33**-stapled constructs, was carried out with peptides in dark and light-states to explore if cell death can be triggered selectively.

b. Uptake Studies of the Non-Stapled Peptides

A wide range of natural and synthetic CPPs have been used to allow the uptake of peptides, proteins, nucleotides and small drug molecules into cells.[242] CPP sequences are typically cationic, enabling direct interaction with negatively charged phospholipid bilayers. Addition of

a hydrophobic tag or a short hydrophobic peptide sequence, such as the *penetration accelerating sequence* (Pas), was reported to increase the uptake and intracellular delivery of arginine-rich sequences by improving membrane insertion.[243] Previous studies showed that adding Pas (FFLIPKG) to the C-terminus of CPP-Ant afforded little improvement, but adding it to the N-terminus of Ant led to a 15-fold increase in internalization.[244] However, even after attachment of a CPP-sequence, peptide and protein conjugates can display poor cytosolic delivery due to endosomal entrapment. As the endosomes mature, their lumen becomes more acidic, activating latent proteases that degrade the endosomal contents. One strategy to encourage endosomal escape is to use peptides that show membrane lytic activity under acidic conditions. This enables specific lysis of the lipid bilayer of the endosomes whilst preventing the disruption of other cellular membranes. HA2 is an endosomolytic peptide derived from the N-terminus of the HA2 subunit of influenza hemagglutinin (HA) that lyses membranes in a pH-dependent manner.[245] The mechanism involves the protonation of glutamate residue sidechains allowing insertion into membranes and formation of pores.[246] The chimeric peptide HA2-TAT consists of the endosomolytic peptide sequence fused to the CPP TAT (GRKKRRQRRR), which is derived from the HIV Trans-Activator of Transcription protein. Co-incubation experiments have demonstrated improved delivery of proteins into live cells when HA2-TAT was added to the media.[247] E5 (GLFEAIAEFIENGWEGLIEGWYG) is a HA2 analogue that displays higher solubility and endosomolytic activity compared to the wild type HA2. When combined with TAT as E5-TAT, this construct showed improved endosomal release of FITC-dextran and the fluorescent protein mCherry.[248]

To investigate whether CPPs enabled efficient uptake of the apoptotic peptides, peptides were *N*-terminally labelled with (5)carboxyfluorescein. Cell uptake experiments were carried out using HeLa cells seeded into a 24-well plate (250,000 cells/well) and incubated overnight at 37 °C. The media was then removed and the cells incubated with the peptide sample for a given time. Following incubations, the cells were washed with heparin, a negatively charged glycosaminoglycan to ensure that the positively charged CPPs were removed from the negatively charged surface of the outer cell membrane. Excess heparin was washed off using phosphate-buffered saline (PBS) and cells detached with trypsin prior to assaying with a S3e Cell Sorter (Bio-Rad). For each experiment, a minimum of 10,000 events were collected in triplicates.

HeLa cells were first incubated with (5)[FAM]-Ant-Bid$^{i,i+4}$-NH_2 and (5)[FAM]-Pas-Ant-Bid$^{i,i+4}$-NH_2 (10 μM) for times ranging from 30 minutes to 8 hours, then cellular fluorescence measured by FACS to establish suitable experimental conditions to compare peptide uptake. A clear

increase fluorescence was observed for the peptide (5)[FAM]-Ant-Bid$^{i,i+4}$-NH_2 over time (Figure II.55a). The sigmoidal shape of the curve obtained indicating saturation at longer incubation times. The fluorescence measured for (5)[FAM]-Ant-Bid$^{i,i+4}$-NH_2 after 4 hours was 83% of the signal recorded at 8 hours, so the shorter time point was deemed a viable compromise between uptake and time expended for future incubation/cell-viability experiments.

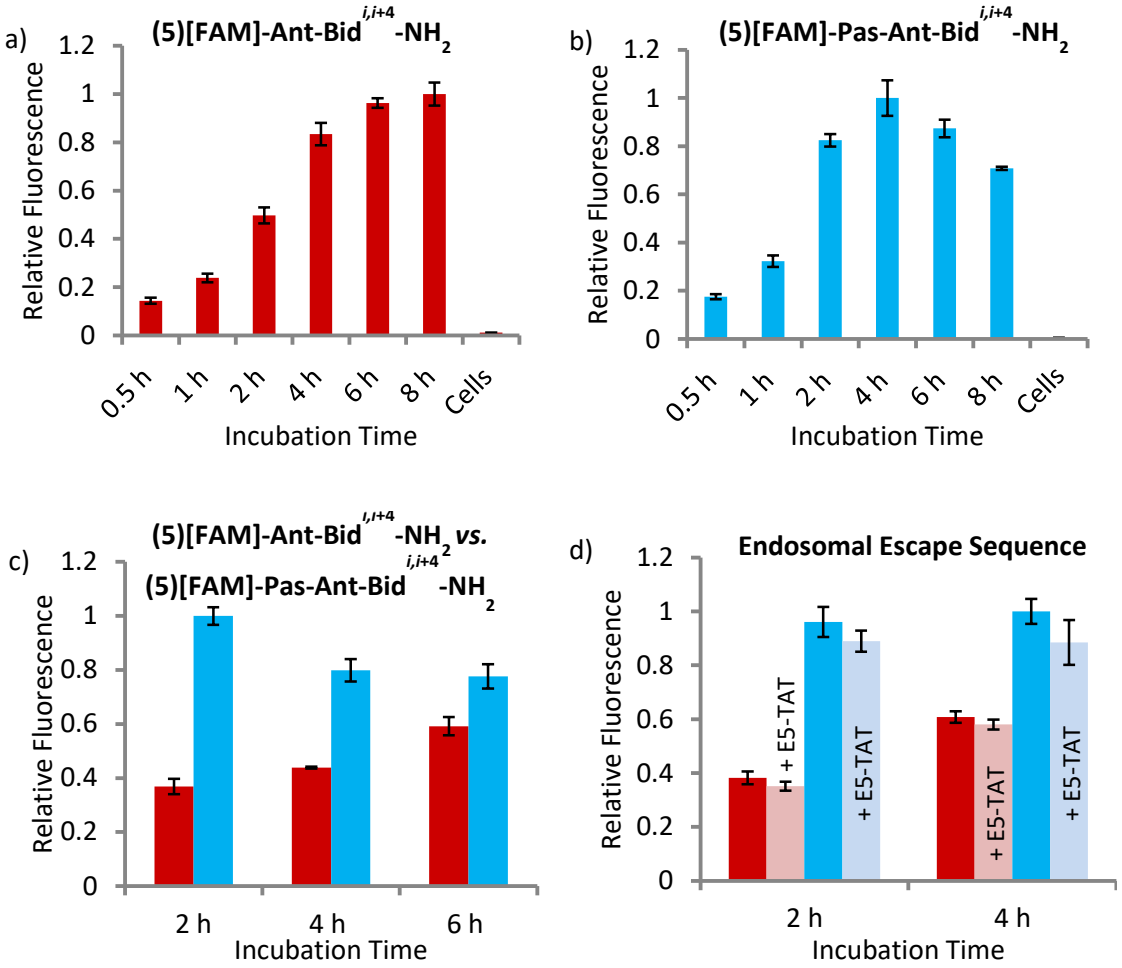

Figure II.55 *Time dependent uptake studies with (5)[FAM]-Ant-Bid$^{i,i+4}$-NH_2 (red) and (5)[FAM]-Pas-Ant-Bid$^{i,i+4}$-NH_2 (blue) by flow-cytometry. a,b) Incubation of the peptides between 0.5-8 hours. c) Comparison of the two peptides at 2, 4 and 6 hours showed higher uptake of the peptide containing the N-terminal Pas-sequence. d) Co-incubation with E5-TAT as an endosomolytic peptide sequence did not indicate enhanced cytosolic delivery of the peptides.*

In contrast, the peptide containing the Pas-sequence, (5)[FAM]-Pas-Ant-Bid$^{i,i+4}$-NH_2 (10 µM) displayed a bell-shaped uptake-curve over the time course (Figure II.55b). Maximum uptake was achieved at 4 hours and fluorescence decreased after 6 hours. It is possible that the

fluorophore was either degraded or endosomally entrapped during the experiment, as carboxyfluorescein displays a much lower emission when at pH <7. The cellular delivery of the two peptides was then directly compared, with cells incubated with 10 µM concentrations of both peptides measuring fluorescence at 2, 4 and 6 hours (Figure II.55c). (5)[FAM]-Pas-Ant-Bid$^{i,i+4}$-NH_2 displayed a higher uptake at all times, with 2.7-fold greater uptake at 2 hours, which decreased to 1.3-fold more uptake at 6 hours as the uptake for (5)[FAM]-Ant-Bid$^{i,i+4}$-NH_2 slowly increased. Despite the decrease of the overall fluorescence over time, the addition of an N-terminal Pas-sequence to the apoptotic peptide significantly improved the cellular uptake.

To test the possibility that the peptides were stuck in endosomes, co-incubation experiments were performed with the endosomal escape sequence E5-TAT (Figure II.55d). E5-TAT (GLFEA IAEFI ENGWE GLIEG WYGGR KKRRQ RRR-NH_2) was synthesised on a rink-amide resin using SPPS techniques and added to the incubation media at a concentration of 2.5 µM, as previous literature had shown that this is the highest concentration without detrimental effects on cell viability.[248] No significant differences were observed for the cell-uptake in the co-incubation studies suggesting that the observed decrease in cytosolic delivery of (5)[FAM]-Pas-Ant-Bid$^{i,i+4}$-NH_2 was not related to endosomal entrapment. However, no other endosomolytic compounds or peptides that were known not to escape the endosomes were tested. To confirm that the CPP and PAS peptide sequences increased uptake, cells were treated with 10 µM of (5)[FAM]-GL-Bid$^{i,i+4}$-NH_2, (5)[FAM]-Ant-NGLG-NH_2, (5)[FAM]-Ant-Bid$^{i,i+4}$-NH_2 or (5)[FAM]-Pas-Ant-Bid$^{i,i+4}$-NH_2 for 4 hours and their fluorescence was compared (Figure II.56).

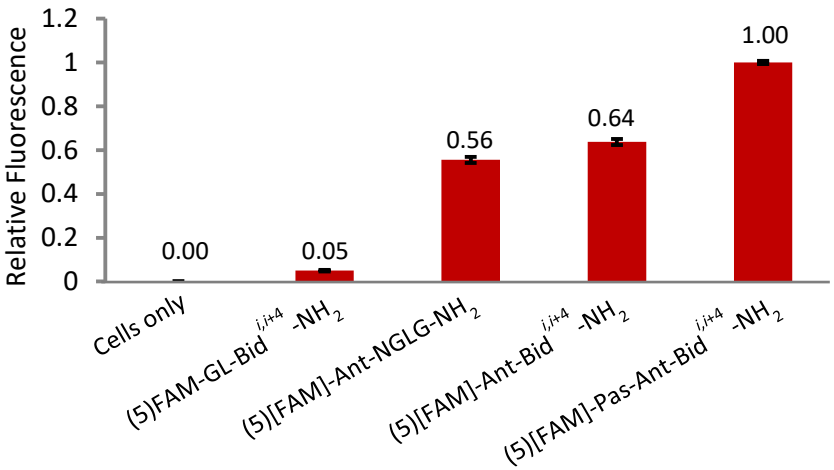

Figure II.56 *Uptake-studies of the peptide (5)[FAM]-GL-Bid$^{i,i+4}$-NH_2, (5)[FAM]-Ant-NGLG-NH_2, (5)[FAM]-Ant-Bid$^{i,i+4}$-NH_2 and (5)[FAM]-Pas-Ant-Bid$^{i,i+4}$-NH_2 by flow-cytometry. The obtained relative fluorescence values are displayed over the corresponding bars.*

The pro-apoptotic peptide lacking the CPP-sequence showed little uptake compared to either the CPP alone (5)[FAM]-Ant-NGLG-NH_2, or the full-length apoptotic construct (5)[FAM]-Ant-Bid$^{i,i+4}$-NH_2. As previously described, uptake was further improved by addition of the Pas-sequence to the N-terminus. These results confirmed that the Ant CPP sequence confers the ability to enter cells, which is crucial for therapeutic applications. The lack of effect of the endosomal release peptide suggests that release from the endosomes is not limiting for the constructs tested, so cell viability experiments were carried out using 4 hours incubation periods to assess the functionality of peptide constructs after uptake.

c. Cell-Viability Assays of the Peptides and Stapled-Constructs

i. Non-Stapled Peptides

Cytotoxicity assays were carried out with the non-stapled construct over a panel of concentrations to determine the EC_{50} value. Assays were performed using 96-well plates (20,000 cells/well) in which cells were incubated with peptides for 4 hours, then washed with heparin and PBS and left in media overnight at 37 °C. To measure the cell viability, cells were treated with Celltiter® Blue (Promega) for 4 h. Intact cells will convert this redox dye into a fluorescent product, whereas cells that have lost their metabolic capacity will be unable to perform this reaction. Fluorescence measured at 585 nm on a plate reader therefore indicated cell viability. Untreated cells were used as a positive metabolic control and considered 100% viable whereas cells that were incubated with 0.01% Trition X-100 to compromise the cells outer and mitochondrial membranes were used as control non-viable cells.

As expected from the lack of uptake in FACS assays, GL-Bid$^{i,i+4}$-NH_2 did not show any significant effect on cell viability (Figure II.57a). Similar results were obtained for the Bim$^{i,i+4}$-NH_2 peptide, which had no effect on the cells up to a concentration of 300 µM (Appendix 11), but the CPP-BH3-peptides: Ant-Bid$^{i,i+4}$-NH_2 and Pas-Ant-Bid$^{i,i+4}$-NH_2 exhibited significant toxicity at concentrations from 10-100 µM. The presence of the Pas sequence led to no significant difference in cell-viability values (Figure II.57b), despite the higher uptake observed for the peptide containing a Pas-sequence by FACS-analysis. The Pas sequence was therefore omitted from later studies. To ensure the observed cytotoxicity was derived from the BH3 sequence, cells were incubated with Ant-NGLG-NH_2 over the same concentration range (1 nM-100 µM, Appendix 12). No cytotoxic effect was observed for the CPP alone, proving that the lethal effect was due to BH3 sequence.

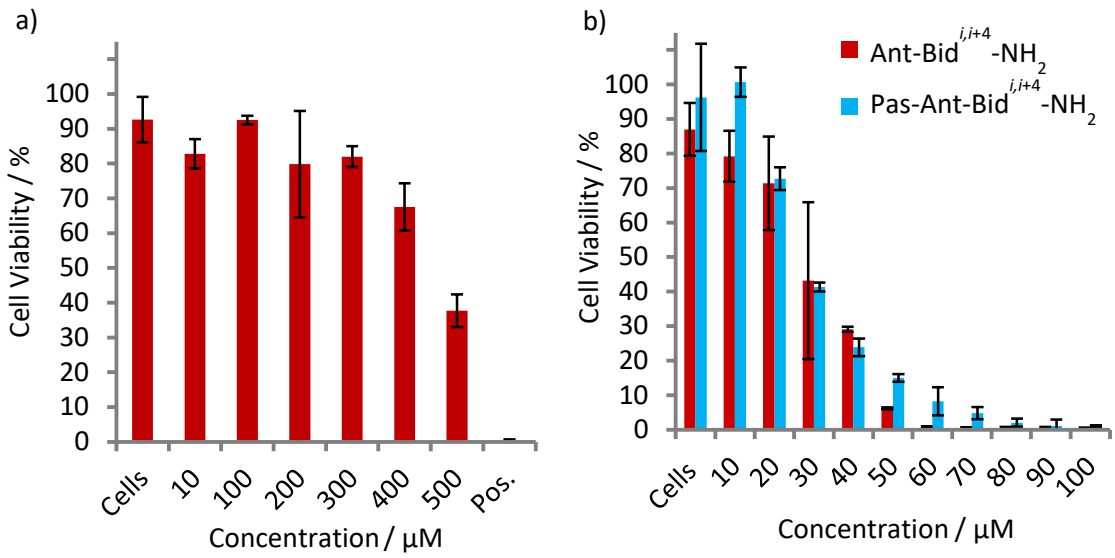

Figure II.57 *Cytotoxicity of the non-stapled peptides GL-Bid$^{i,i+4}$-NH$_2$ (a) and Ant-Bid$^{i,i+4}$-NH$_2$ and Pas-Ant-Bid$^{i,i+4}$-NH$_2$ (b). The CPP-sequence facilitates the cellular uptake and leads to an increased cytotoxicity. Triton-X (0.01%) was used as a positive control of cell death.*

ii. Stapled-Peptides

With the CPP-fused pro-apoptotic peptides shown to be able to direct cell fate *in vivo*, the crosslinked constructs were next investigated to determine if photo-control could also be established *in vivo*. Insolubility made the testing of the **33**-stapled constructs **33**-Ant-Bid$^{i,i+4}$-NH$_2$ and **33**-GL-Bid$^{i,i+4}$-NH$_2$ significantly more difficult than the non-crosslinked peptides. Whilst **33**-Ant-Bid$^{i,i+4}$-NH$_2$ was soluble in water, neither of the stapled constructs were soluble in common buffer systems or cell culture medium (DMEM), so stock solutions were made up in DMSO. The stock-solution was either incubated at 60 °C for 16 hours to obtain a maximum *trans* dark state or illuminated under red-light to reach the PSS$_{635\ nm}$ to achieve the maximum *cis* isomer population, then diluted into the cell culture media to reach the desired concentrations.

When the constructs were diluted from DMSO stocks into the cell culture media, precipitate was observed to form over a time span of ~20 min. Precipitated samples of the stapled peptide **33**-Ant-Bid$^{i,i+4}$-NH$_2$ that were treated to isomerize into *cis* and *trans* overnight, did not show any cytotoxic effects, suggesting that either addition of the crosslinker completely obviated cytotoxic activity, or precipitation occurred quantitatively and only negligible amounts of monomeric construct remained in solution (Appendix 12). As a consequence, samples were diluted in DMEM from their stock solution and immediately (<1 minute) incubated with the cells in the 96-well plates for 4 hours. The final concentration of DMSO in the samples was

maintained below 1% to avoid any cytotoxic effects from the vehicle. The construct **33**-Ant-Bid$^{i,i+4}$-NH_2 was incubated with the HeLa cells in this fashion in both its dark and $PSS_{635\ nm}$ states alongside the non-crosslinked parent peptide and cell-viabilities were measured on a plate reader (Figure II.58).

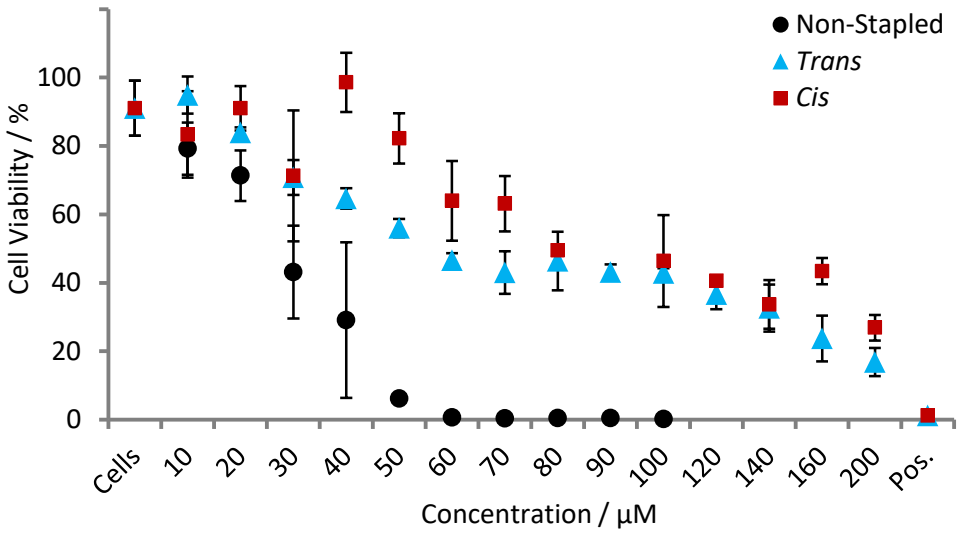

Figure II.58 *Cytotoxicity of the **33**-stapled and non-stapled peptide Ant-Bid$^{i,i+4}$-NH_2 for its dark trans- and cis-rich light states over a concentration gradient. The observable cytotoxic effect of the stapled peptide is significant weaker than the cytotoxicity of the non-stapled peptide.*

Cell death was observed for both the light and dark states, although the overall toxicity was reduced in both cases compared to the non-stapled peptide control. Complete cell-death was not observed for either isomer, even when the concentration was increased to 200 µM, approximately 10 fold higher than the EC_{50} of the non-crosslinked control peptide. The light and dark states appeared to show similar toxicity profiles, with only small differences between 40-70 µM. Within this concentration range the *trans*-isomer unexpectedly displayed a stronger cytotoxic effect than the *cis*-species. As the isomers have a similar profile overall, it is unclear whether the observed effect is due to genuine differences in toxicity or errors in concentrations arising from solubility of stapled peptides. Insolubility is likely responsible for the reduced lethality of the stapled peptide compared to the unstapled parent either due to reduced cellular uptake or compromised activity in the intra-cellular space hindering the activation of cell-death. When precipitated samples and their supernatants were applied to the cells no significant cytotoxic effect could be observed, implying rapid and quantitative precipitation that reduces the effective concentration of monomeric construct in solution creating a limited window of time for cellular uptake to be achieved.

The **33**-crosslinked peptide GL-Bid$^{i,i+4}$-NH_2 was tested to investigate if the azobenzene staple on the peptide leads to an increased cytotoxic effect. As this construct lacks the CPP-sequence, uptake would be expected to be poor and non-stapled parent peptide showed no cytotoxic effects up to a concentration of 500 µM (Figure II.57a). However, Bim BH3 peptides have been reported to be cell permeable when stapled with an all-hydrocarbon linker, possibly due to an increased hydrophobic surface and constrained size of the α-helical conformation.[249] When the dark and light state samples of **33**-GL-Bid$^{i,i+4}$-NH_2 were tested, no effect was observed up to a concentration of 50 µM (Figure II.59). Lower cell viability was evident for both states of the construct at 100 µM and 150 µM, with the dark state again showing a greater cytotoxic effect than the light state. This result suggested uptake was significantly improved for the stapled construct compared to its non-stapled analogue.

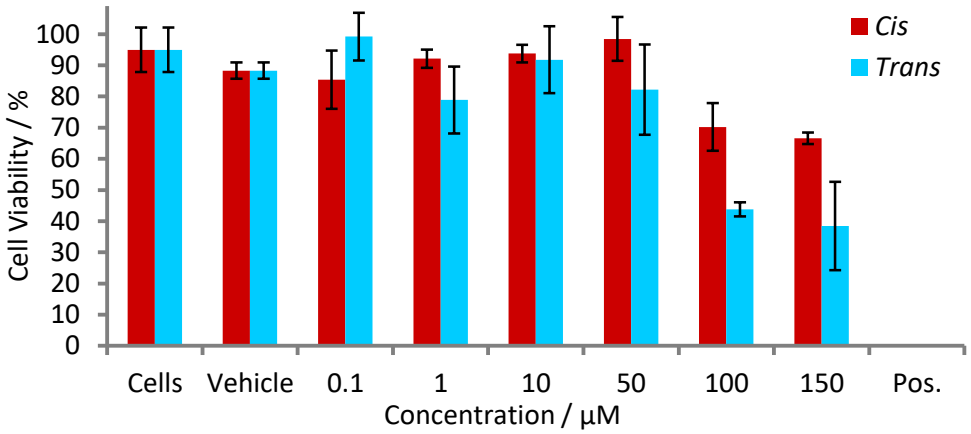

Figure II.59 *Cytotoxicity of the **33**-stapled GL-Bid$^{i,i+4}$-NH_2 for its dark (cyan) and light (red) states over a concentration gradient. A cytotoxic effect can be observed at higher concentrations although no CPP sequence is present in the sequence.*

The light (*cis*-enriched) state of the constructs not displaying higher cytotoxicities than the dark states for GL-Bid$^{i,i+4}$ was contrary to the initial assumption of the project. However, the results were supported by the previously analysed CD- and FP-data, where no increased α-helical formation or selective binding could be observed for the **33**-stapled peptide of Bid. The differences between the dark and light state could therefore be a direct result of the different physical properties of the isomeric forms of the linker. The *trans*-form of the **33** exhibits a stronger hydrophobic character compared to the *cis*-isomer, and might as a result interact more strongly with membranes accelerating its uptake; a concept familiar from certain CPP sequences or the Pas sequence.[243,250] In an attempt to test the two isomeric forms of the

crosslinker **33** for their cytotoxic properties, the linker was reacted with the thiol-groups of two cysteines to mimic the chemical environment when it is bound to a peptide (chapter II.1.c.iii). However, the final product showed only very limited solubility even in organic solvents and thus, was not tested on mammalian cells.

d. Conclusion

In this chapter, the effect of a selection of non-stapled and **33**-stapled constructs on the viability of mammalian cancer cells were tested. Uptake of the constructs and induction of cell death by non-stapled CPP peptides were proven using FACS and cytotoxicity assays. Cytosolic delivery was greatly improved by the inclusion of a CPP-sequence over the peptides lacking a membrane-penetrating sequence (12.8-fold). Control experiments showed that the cell uptake ability was solely derived from the CPP and toxicity from the BH3 sequence. The addition of an N-terminal Pas sequence further increased the amount of cytosolic peptide, but time-dependent uptake studies revealed a bell-shaped curve for the Pas-sequence peptides, indicating that the amount of delivered peptide reached a maximum more rapidly but was degraded at a faster rate. Although this could be due to endosomal acidification leading to lower fluorescence, time-dependant experiments adding the endosomal release peptide E5-TAT showed no differences, suggesting that the peptide is instead cleared from the cells by a different mechanism. Cell viability tests revealed that the increased uptake of the peptide containing the Pas sequence did not lead to higher cytotoxicity. Peptides lacking a CPP-sequence showed little effect on cell viability until very high concentrations, underlining the importance of a cell-penetrating sequence for effective cytosolic delivery.

The stapled constructs were tested in their light (*cis*-enriched) and dark (*trans*) states, but their low solubility reduced activity and compromised the interpretation of the results. Precipitation of the constructs occurred in all common buffer systems used for cell culture. Re-suspended precipitates and their supernatants showed no cytotoxic activity, implying that precipitation occurred quantitatively and left only negligible amounts of monomeric construct in solution. In contrast, samples that were applied to the cells quickly after thorough mixing and before formation of precipitate was observed did show a cytotoxic effect on the HeLa cells. However, the observed cell viability for the **33**-stapled construct **33**-Ant-Bid$^{i,i+4}$-NH_2 was consistently higher than for the non-stapled constructs. It was hypothesised this could be a result of the lower solubility reducing the effective concentration of monomeric construct in solution rather than a reduced affinity for the target proteins. Cytotoxicity was observed for the stapled

peptide **33**-GL-Bid$^{i,i+4}$-NH_2 lacking a CPP sequence, indicating that cytosolic delivery was achieved when the linker was attached to the peptide. However, zero cell viability could not be achieved, possibly due to solubility issues of the construct leading to a less effective concentration of monomeric species in solution. No additional cell death was observed for the light states of either **33**-stapled construct, contradicting the initial hypothesis of the project that suggested a higher cytotoxicity of the constructs in their light-states due to an increased α-helical content and subsequent improved binding to the target-proteins. However, the results were in alignment with the previously obtained CD- and FP-data (chapter II.4.c-d). The higher cytotoxic activity observed for the dark (*trans*) state, may well be linked to the physical properties of the *trans*-crosslinker as increased hydrophobicity could lead to a stronger interactions with cellular membranes.

III. Conclusion and Future Work

1. Overview and Context of the Work

The aim of the project was to develop and characterise a system that is able to induce apoptosis upon a stimulus of light. Peptides have shown to be highly specific therapeutics with relatively few adverse effects. However, peptides also have to adopt certain secondary structural motifs to engage with their target proteins, thus, enabling spatiotemporal control of peptide activity by control of their conformations is highly desirable. Stapling peptides with an azobenzene photo-linker is one strategy to gain structural control, as the staple can influence adoption of the biologically active conformation, triggering an effect inside the cell. Light of a long (red-shifted) wavelength displays a higher tissue penetration depth and is non-toxic, which makes it the preferred choice for these systems. An ideal application for a system like this would be the interruption of the Bcl-2 family network in cancer-cells where certain family members are overexpressed, resulting in the cells being essentially immortal and immune to common apoptotic-stimuli. To date, no system has been described that targets the anti-apoptotic proteins of the Bcl-2 family inside cells with stapled peptides using harmless and deep-penetrating red light.

The synthesis of a novel photo-controllable peptide-construct was divided into four main steps that, ideally, should be addressed in a sequential manner (Figure III.1). The first step involved the synthesis of an appropriate photo-element that resembles the desired properties for the system. Next, peptides were to be synthesised that could address the biological target protein, with an appropriate cysteine spacing to attach the synthesised linker onto the peptides. Bio-physical characterisation of the constructs was necessary to validate binding properties in a simplified environment in *in vitro* assays, where little side-reaction or off-target effects can occur. Once specific target-binding was ensured, the constructs could be tested on cells to test their biological effect on more complex systems. However, as difficulties emerged, a sequential workflow was difficult to maintain; solubility related problems required sequences to be redesigned and limited training opportunities led to an altered order of the steps, so that bio-physical characterisation was carried out after the mammalian cell-testing.

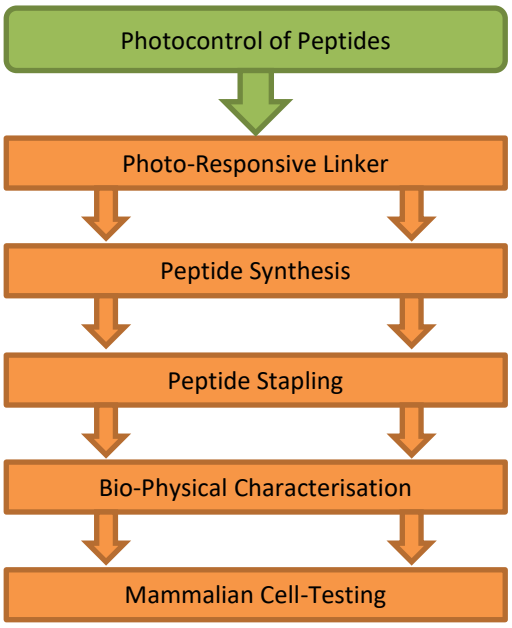

Figure III.1 *Main steps towards the development of photo-controllable peptides. Each of these steps is described in a separate chapter of this work.*

2. Photo-Responsive Linker

As the system was intended to be used in an intracellular environment, the photo-crosslinker should exhibit stability towards reduction, a long excited-state half-life and be addressable using red-light. Photo-responsive elements based on azobenzene benefit from the symmetry of the parent molecule, relatively good synthetic accessibility, documented stability trends and predictable geometric changes upon isomerisation. Different substituents on the aromatic rings can modulate the energy needed for the *trans-cis* isomerization and regulate the thermal stability of the *cis*-isomer. The tetra-*ortho*-chloro azobenzene linker **33**, developed by Woolley and co-workers, embodies many of these desirable properties, including stability against glutathione and bidirectional switching with visible light.[206] In their work, the crosslinker **33** was attached to a fluorescein-labelled test-peptide and the photoisomerization tested *via* fluorescence-quenching of this FRET-system in zebrafish embryos *in vivo*. The construct was microinjected into the zebrafish embryos and was reported to be soluble in PBS buffer to a concentration of 1.0 M. The reported properties and promising results from their *in vivo* studies made this linker the preferred choice for the targeted application. However, despite the advantageous properties of this linker, many of the encountered problems in this project seemed rooted in the limited solubility of **33**. Precipitation of the linker was observed at several stages of this product, even when attached to peptide-sequences that should have improved its solubility. This was possibly caused by aromatic (π-stacking) interactions leading

to aggregation and subsequent precipitation. As the linker dictates most of the photo-physical properties of the system, extra effort should go into designing a system that still exhibits the properties described but displays an increased solubility. Different functional groups on the azobenzene-scaffold might be used to disrupt any potential linker-aggregation caused by stacking-interactions. However, this is not any easy task as a change in the pattern of substituents can affect one of the other key-properties, such as stability against reductive environment or being addressable with red-light.

3. Peptide Synthesis and Peptide Stapling

The synthesis of pro-apoptotic BH3-peptides was carried out using SPPS techniques. Peptides derived from secondary structure motifs from apoptosis-inducing proteins lose their structural integrity when taken out of their protein context. The introduction of a chemical staple helps to regain the secondary structure that is required to engage with the target-proteins. In this work, a number of different BH3-peptides were synthesised and stapled over introduced cysteine residues. Three different azobenzenes were used: the non-substituted linker **38**, which was predominantly used for screening reactions to evaluate crosslinking conditions or novel stapling protocols, the water-soluble staple **37**, which was utilized so synthesise constructs used as reference compounds and the previously synthesised crosslinker **33** to obtain the desired target-constructs that can be addressed using red-light.

The synthesis of these stapled constructs remained difficult due to low yields and the formation of side-products. Shorter cysteine spacings seemed to be a major cause of side-product formation, with wider spacings giving significantly higher yields and fewer side-products. Crosslinking conditions were optimised in order to reduce the amount of side-products and on-resin stapling was explored as a strategy to reduce the number of purification steps necessary. Different cysteine-protecting groups that could be selectively removed orthogonally to the protecting groups of other residues were explored for this purpose. This strategy seemed very promising but has been carried out only on an analytical scale so far. Further refinements and optimisation of the conditions are necessary to apply this system on a preparative scale in the future.

However, successfully stapling the peptides with the linker **33** was accompanied by serious solubility issues in various aqueous buffer systems. The addition of a CPP or a solubilizing sequence onto different peptides did not overcome these problems and organic co-solvents were necessary to solubilize the final compounds. Future work should involve the

identification of an amino acid composition that improves the solubility of the linker and incorporate this into a bioactive sequence to address an in cell target using the linker.

4. Bio-Physical Characterisation

The synthesised constructs were subjected to UV-visible spectroscopy and LC-MS analysis. Both isomeric states of **33** could be separately addressed using red and blue-light. The thermal half-life of the *cis*-state for the construct stapled with **33** was long enough to cover any cellular events, whereas constructs stapled with **37** displayed half-life times that were significantly lower. Analysis of the peptide conjugates by CD-spectroscopy was complicated by the limited solubility of the constructs in appropriate buffers. Compound **33**-stapled Ant-Bid$^{i,i+4}$-NH_2 could be analysed in deionised water, but did not show any increase in helical structure upon irradiation. Similar results had previously been reported for a Bid$^{i,i+4}$ peptide stapled with the water-soluble azobenzene linker **37**.[211] It was previously argued that a helix-inducing motif in the solution is needed to obtain an increased α-helical content as observed for the **37**-stapled Bak$^{i,i+11}$ peptide in previous work.

Binding studies were carried out using fluorescence polarisation assays. The anti-apoptotic protein Bcl-x_L was titrated into solutions of non-stapled and stapled N-terminally (5)carboxyfluorescein labelled peptides and the change in anisotropy measured. Non-specific binding was observed for most peptides at higher concentrations, with **33**-stapled constructs showing a strong contribution of non-specific binding possibly due to aggregation or precipitation in the applied buffer. Furthermore, no difference in binding selectivity was observed between the dark and light state of the **33**-stapled construct. The Bid$^{i,i+4}$ peptide was stapled with the water-soluble linker **37**, but in stark contrast to previous publications that reported a 23-fold difference, no difference between the dark and light states could be observed with **37**. This result concurs with observed and previously reported CD-data.[211] As the Bak$^{i,i+11}$ peptide showed a change in helicity *via* CD-spectroscopy, this peptide was synthesised with a N-terminally attached PEG-tag to increase the overall-solubility when stapled with **33**. Predominant specific binding was observed using this non-stapled peptide, however when stapled only random scattering was obtained, indicating that attachment of the linker leads to precipitation.

Binding experiments were also conducted by NMR using samples of ^{15}N-labelled Bcl-x_L into which peptides were titrated. Chemical shift perturbances for a bound BH3-peptide-protein complex have been reported previously and were used to assess the amount of specific

binding through the integration of significant aromatic peaks. Generally, samples of the peptides that displayed full binding suffered from precipitation and a loss of resolution. Addition of excess fluorophore-labelled peptide did not result in protein precipitation or complete binding as determined by the still observable peaks of the unbound protein. A linker between fluorophore and pro-apoptotic peptide lead to an improvement in the ratio of bound-to-unbound signal, suggesting that the N-terminal fluorophore might disfavour binding to the target protein. Only unbound complex was observed for the **33**-stapled constructs as they did not seem to bind to the protein in a specific fashion.

Future binding assays should consider techniques that do not require peptide modifications to better mimic cellular conditions and to avoid non-specific binding effects caused by the *N*-terminal modifications. For example, isothermal titration calorimetry (ITC) could be used to obtain a binding curve without the need to introduce further modifications to the peptide. The previously recorded CD-data suggested that a change in α-helicity can be observed for the **37**-stapled Bak$^{i,i+11}$ and that this peptide sequence could display a different target-specificity for their dark and light states. However, **33**-stapled pegylated Bak$^{i,i+11}$ did only show a random scattering in the fluorescence polarization assay, possibly due to solubility issues. Future work should involve this promising peptide sequence with a different linker system to target anti-apoptotic proteins.

5. Mammalian Cell-Testing

Peptides were tested on HeLa cells to determine their cellular uptake using FACS-techniques and cytotoxicity by Celltiter® Blue (Promega) viability assays. The ability to cross cellular membranes was only conserved in peptides containing an N-terminal CPP-sequence. The addition of a Pas-sequence to the CPP was explored, which led to further increase of cellular uptake as indicated by the increase of the fluorescent signal. However, cell-viability assays did not indicate an increased cytotoxicity of this peptide despite its enhanced uptake. The **33**-stapled constructs suffered from a low solubility in the buffer systems and showed no cytotoxic effects a short while after being mixed with cell culture buffers. It was assumed that this was caused by the formation of aggregates preventing its uptake or target binding. As a consequence, the cellular uptake of the constructs seemed impeded and a lower effective construct-concentration in solution was likely. **33**-stapled peptides lacking a CPP-sequence showed an increased cytotoxic response over their non-stapled analogues, indicating that cytosolic delivery was enhanced by the attachment of **33**. The dark (*trans*) state of the

constructs showed a higher cytotoxicity than the *cis*-enriched light state, which was attributed to the physical properties of the linker that displays an increased hydrophobicity and therefore stronger interaction with the cellular membrane in *trans*. To test this assumption, the linker **33** was reacted with two cysteines to mimic the chemical environment of a peptide sequence to be used in cytotoxicity assays. However, the limited solubility prevented further testing.

Future work of the cell-testing is highly dependent on the solubility of the constructs. Once a soluble linker has been synthesised, future testing should involve cytotoxicity assays using caspase-markers to validate if the observed cytotoxic effect is a result of apoptosis or non-regulated cell death. The stapled constructs could then be further characterised using established small molecule inhibitors for anti-apoptotic proteins, such as ABT-263 (Navitoclax), to see if a drug combination could enhance the anti-tumour activity of the synthesised constructs.

IV. Materials and Methods

1. Organic Synthesis Methods

a. Materials

All chemicals and solvents were purchased from Sigma-Aldrich UK (Poole, United Kingdom), Apollo Scientific UK (Cheshire, United Kingdom) or Fisher Scientific Ltd (Loughborough, United Kingdom) and used without further purification or distillation unless otherwise stated. 15 MΩ H_2O was used throughout.

b. NMR-Spectroscopy

^{1}H and ^{13}C NMR spectra were recorded on a Bruker Fourier 300 MHz, a Bruker Avance 500 MHz and a Bruker DPX 400 MHz spectrometer. Chemical shifts (δ) are quoted in parts per million (ppm) and referenced to tetramethyl silane, using residual protonated solvents as internal standards (D_2O at 4.79 ppm, $CDCl_3$ at 7.26 ppm, DMSO-d6 at 2.50 ppm and acetone-d6 at 2.05 ppm). Abbreviations used in the description of resonances are: s (singlet), d (doublet), t (triplet), q (quartet), m (multiplet), br (broad).

c. Mass-Spectrometry

Both, high and low resolution mass spectra of the small molecules were submitted to the analytical department of Cardiff University for analysis. Samples were dissolved in methanol and masses recorded on a Waters LCT premier XE with an electrospray ionisation source using a time-of-flight mass detector.

d. Thin Layer Chromatography

TLCs were run on pre-coated G/UV_{254} silica plates on an aluminium support and compounds visualised using UV-light (UVGL-58 handheld UV lamp) and/or using a cerium molybdate (CAM) or permanganate solution. For the CAM-solution, 12 g of ammonium molybdate were mixed with 0.5 g of ceric ammonium molybdate, 15 mL of conc. sulphuric acid and 235 mL of deionised water. The permanganate solution was made up using 7.5 g of potassium permanganate and 50 g of potassium carbonate that was dissolved in deionised water, 6.25 mL of a 10 wt.% sodium hydroxide solution was added and the solution further diluted to 1 L using deionised water.

e. Synthetic Procedures

i. Synthesis of the Unsubstitued Azobenzene Linker (**38**) and Derivatives

(1) Synthesis of the Linker (E)-*N*,*N*'-(diazene-1,2-diylbis(4,1-phenylene))*bis*(2-chloroacetamide) (**38**)

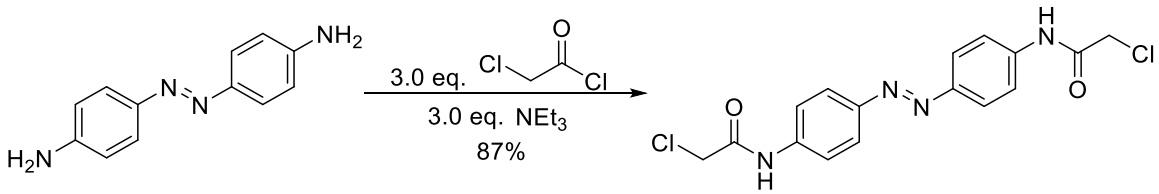

39 **38**

To a solution of **39** (0.15 g, 0.71 mmol, 1.0 eq.) in acetonitrile (40 mL) was added dropwise triethylamine (0.21 g, 2.12 mmol, 3.0 eq.) and it was allowed to stir for 30 min. Chloroacetyl chloride (0.24 g, 2.12 mmol, 3.0 eq.) was added dropwise and the reaction was allowed to stir for 24 h. The solvent was removed under reduced pressure and the solid obtained was washed with hydrochloric acid (1 M, 40 mL) and filtered off. The solid was washed with acetonitrile (30 mL) and dried in air to yield 0.22 g (87% yield) of **38** as an orange/red solid.

R_f: 0.2 (methanol/dichloromethane) (10:90 (*v*/*v*)). **^{1}H NMR** (300 MHz, DMSO-d_6) δ (ppm): 10.65 (s, 2H), 7.87 (d, *J* = 8.9 Hz, 4H), 7.82 (d, *J* = 9.0 Hz, 4H), 4.31 (s, 4H). **^{13}C NMR** (500 MHz, DMSO-d_6) δ (ppm): 165.1, 148.0, 141.2, 123.6, 119.7, 43.7. **HR-MS** (ESI) $C_{16}H_{15}Cl_2N_4O_2$ $[M+H]^+$ Calculated: 365.0572, $[M+H]^+$ found: 365.0554.

(2) Synthesis of (E)-*N*,*N*'-(diazene-1,2-diylbis(4,1-phenylene))*bis*(2-iodoacetamide)) (**36**)

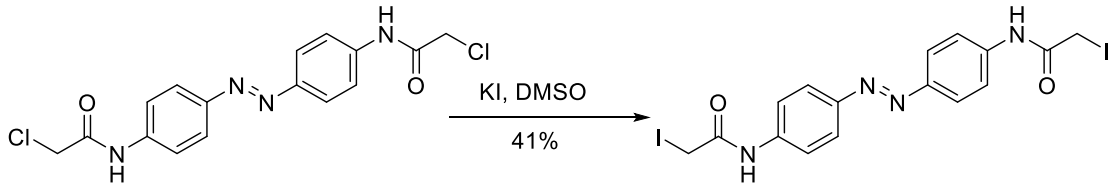

38 **36**

Compound **38** (10 mg, 0.027 mmol, 1 eq.) was dissolved in 1 mL of DMSO and 50 mg (0.30 mmol, 11.2 eq.) of KI was added to the solution. It was shaken until all precipitate was dissolved. The yellow solution was reacted at 45 °C for 16 h under shaking to give a cloudy solution. The reaction mixture was poured into 15 mL of 0.1 M HCl to yield a yellow precipitate of **36**. It was centrifuged and the pale yellow solution decanted. The obtained precipitate was carefully washed with ice-cold acetonitrile (5 mL) and diethyl ether (5 mL) and dried on air to give 6 mg of **36** (0.011mmol, 41% yield).

^{1}H NMR (500 MHz, DMSO-d_6) δ (ppm): 10.65 (s, 1H), 7.87 (d, *J* = 9.0 Hz, 2H), 7.78 (d, *J* = 9.0 Hz, 3H), 3.87 (s, 2H). **^{13}C NMR** (500 MHz, DMSO-d_6) δ (ppm): 167.1 (s), 147.9 (s), 141.5 (s), 123.5 (s), 119.3 (s). **HR-MS** (ESI) $C_{16}H_{15}I_2N_4O_2$ $[M+H]^+$ Calculated: 548.9284, $[M+H]^+$ found: 548.9286.

ii. Synthesis of the Tetra-*Ortho*-Chloro Azobenzene Linker (**33**) and Derivatives

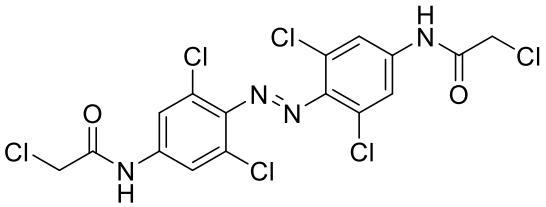

33

The synthesis of **33** widely followed a previously published procedure [206]. However, certain steps had to be modified in order to be successful.

(1) Synthesis of sodium (E)-((3,5-dichloro-4-((2,6-dichloro-4-nitrophenyl)diazenyl)phenyl)amino)methanesulfonate (**41**):

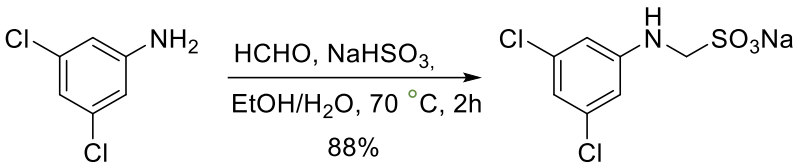

40 **41**

To a solution of sodium hydrogen sulfite (9.63 g, 92.59 mmol, 1 eq.) in water (20 mL) was added 37% formaldehyde-solution (6.89 ml, 27.80 g, 92.59 mmol, 1 eq.) and it was stirred for 1 h at room temperature. The reaction mixture was diluted with 80 mL water and a solution of **40** (15.0 g, 92.59 mmol, 1 eq.) in EtOH (100 mL) was slowly added. The reaction was stirred at 70 °C for 24 h, cooled down to room temperature and the EtOH removed under reduced pressure. The reaction mixture was cooled in an ice bath, the formed precipitate filtered off and washed with cold DCM and dried *in vacuo* to give 22.740 g of pure product (88% yield).

R_f: 0.5 (methanol/dichloromethane) (20:80 (*v*/*v*)). **^{1}H NMR** (300 MHz, DMSO-d_6) δ (ppm): 6.87 (t, *J* = 6.9 Hz, 1H), 6.71 (d, *J* = 1.8 Hz, 2H), 6.56 (t, *J* = 1.8 Hz, 1H), 3.86 (d, *J* = 6.9 Hz, 2H). **^{13}C NMR** (500 MHz, DMSO-d_6) δ (ppm): 150.5, 133.9, 114.1, 110.8, 59.8. **LR-MS** (ESI) $C_7H_6Cl_2NO_3S$ $[M\text{-}Na]^-$ Calculated: 253.95, $[M\text{-}Na]^-$ found: 253.93.

(2) Synthesis of sodium (E)-((3,5-dichloro-4-((2,6-dichloro-4-nitrophenyl)diazenyl)phenyl)amino)methanesulfonate (**43**):

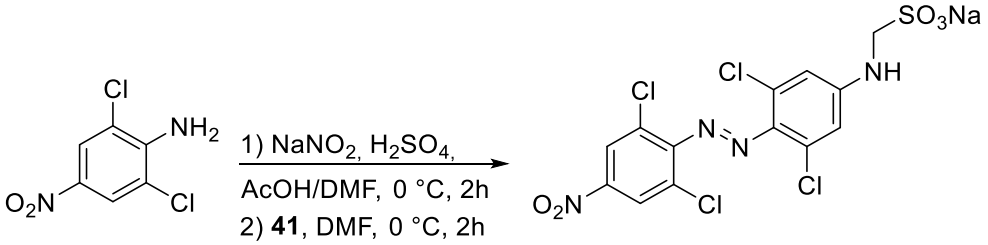

42 **43**

Sodium nitrite (0.20 g, 2.88 mmol, 2 eq.) was added to 2 mL of concentrated sulphuric acid and the reaction mixture was heated to 70 °C and then cooled to 0 °C in an ice-bath whilst stirring. A solution containing 0.60 g (2.88 mmol, 2 eq.) of **42** in acetic acid/DMF (3.5 mL: 9 mL) was

added to this. It was stirred for 2 h at 0 °C and a solution of **41** (0.40 g, 1.44 mmol, 1 eq.) in DMF (6 mL) was added drop-wise. The temperature was kept at 0 °C for 1 h and allowed to warm up to room temperature whilst stirring for 72 h. The mixture was poured on ice, the precipitate let to aggregate for 2 h and filtered off, washed with ice-cold water (5x 20 mL), 1 M LiCl (2x20 mL) and dried on air. The precipitate was dissolved in acetone and magnesium sulfate added. The solvent was removed *in vacuo* and the solid transferred onto a cellulose-filter. It was washed with ice-cold DCM until only clear solvent passed through the filter. The precipitate was then washed with ice-cold acetone until it was colourless and the organic fraction collected separately. The organic solvent of the acetone fraction was removed under reduced pressure and the remaining solid dried *in vacuo*.

^{1}H NMR (300 MHz, DMSO-d_6) δ (ppm): 8.39 (s, 1H), 6.99 (s, 1H), 4.37 (s, 1H). **LR-MS** (ESI) $C_{13}H_7Cl_4N_4O_5S$ $[M\text{-}Na]^-$ Calculated: 473.08, $[M\text{-}Na]^-$ found: 472.89.

(3) Synthesis of 3,5-dichloro-4-[(2,6-dichloro-4-nitrophenyl)diazenyl]aniline (**44**)

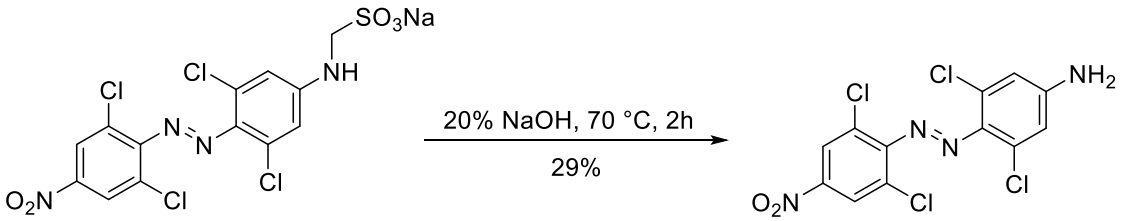

43 **44**

The isolated intermediate **43** was further basified with 20% aqueous sodium hydroxide (20 mL) and heated to 70 °C for 2 h. The reaction mixture was cooled down to room temperature and extracted with EtOAc. The combined organic layers were dried over magnesium sulfate and the organic solvent removed under reduced pressure. The crude product was purified with a silica gel column chromatography over a gradient of 0-80% EtOAc in hexane (*v*/*v*) to yield **44** (159 mg, 29% yield over two steps) as a red-brown solid.

R_f: 0.14 (ethyl acetate/hexane) (20:80 (*v*/*v*)). **^{1}H NMR** (300 MHz, DMSO-d_6) δ (ppm): 8.45 (s, 2H), 7.02 (s, 2H), 6.80 (s, 2H). **^{13}C NMR** (500 MHz, DMSO-d_6) δ (ppm): 153.6, 152.6, 145.8, 133.0, 126.2, 124.7, 113.9. **HR-MS** (ESI) $C_{12}H_9Cl_4N_4O_2$ $[M+H]^+$ Calculated: 380.9294, $[M+H]^+$ found: 380.9288.

(4) Synthesis of 3,5-dichloro-4-[(2,6-dichloro-4-aminophenyl)diazenyl]aniline (**45**)

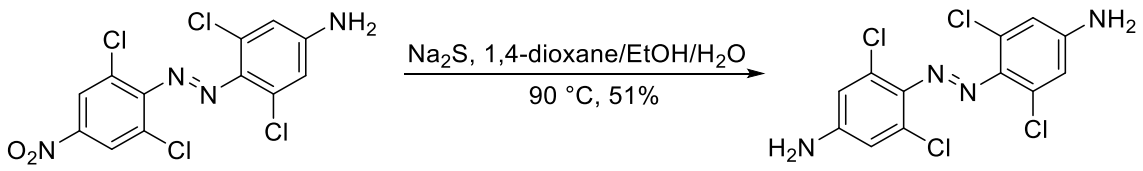

44 **45**

44 (312 mg, 0.82 mmol, 1 eq.) was dissolved in a mixture of dioxane/EtOH/water (16 mL:4 mL:1 mL) and 200 mg (2.56 mmol, 3 eq.) of Na_2S was added. The reaction mixture was heated to 90 °C for 24 h. The reaction was cooled down to room temperature and concentrated under reduced pressure and extracted with ethyl acetate. The combined organic fractions were washed with brine, dried over magnesium sulfate and concentrated under reduced pressure. The crude product was purified using silica gel chromatography with a gradient of 0-100% EtOAc in hexane (*v*/*v*) to give **45** (146 mg, 0.42 mmol, 51% yield) as a red solid.

R_f: 0.56 (ethyl acetate/hexane) (40:60 (*v*/*v*)). **^{1}H NMR** (300 MHz, DMSO-d_6) δ (ppm): 6.71 (s, 4H), 6.27 (s, 4H). **^{13}C NMR** (500 MHz, DMSO-d_6) δ (ppm): 150.6, 135.1, 129.5, 113.6. **HR-MS** (ESI) $C_{12}H_9Cl_4N_4$ $[M+H]^+$ Calculated: 350.9552, $[M+H]^+$ found: 350.9567.

(5) Synthesis of of diazene-1,2-diylbis(3,5-dichloro-4,1-phenylene)bis(2-chloroacetamide) (**33**)

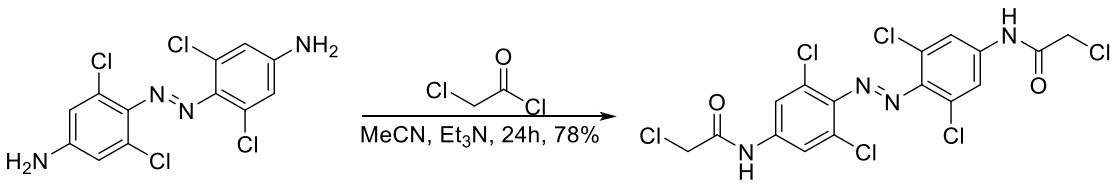

45 **33**

To a solution of **45** (140 mg, 0.37 mmol, 1 eq.) in acetonitrile (45 mL) was added drop-wise triethylamine (155 µL, 113 mg, 1.11 mmol, 3 eq.) and allowed to stir for 30 min. Then, chloroacetyl chloride (88 µL, 125 mg, 1.11 mmol, 3 eq.) dissolved in acetonitrile (20 mL) was added drop-wise and the reaction was allowed to stir for 24 h. The reaction mixture was heated up to 50 °C for 3 h, cooled down to 0 °C using a water-ice bath and the precipitate

filtered off. The obtained solid was washed with ice-cold acetonitrile and dried in air to yield 144 mg (0.29 mmol, 78% yield) of **33** as a dark red solid.

R_f: 0.25 (methanol/dichloromethane) (10:90, (*v*/*v*)). **^{1}H NMR** (300 MHz, DMSO-d_6) δ (ppm): 10.91 (s, 1H), 7.91 (s, 2H), 4.36 (s, 2H). **^{13}C NMR** (500 MHz, DMSO-d_6) δ (ppm): 166.2 (s), 142.2 (s), 140.9 (s), 128.0 (s), 120.1 (s), 44.0 (s). **HR-MS** (ESI) $C_{16}H_{11}Cl_6N_4O_2$ $[M+H]^+$ Calculated: 502.8984 $[M+H]^+$ found: 502.8981.

(6) Synthesis of (E)-*N*,*N*'-(diazene-1,2-diylbis(3,5-dichloro-4,1-phenylene))*bis*(2-iodoacetamide) (**49**)

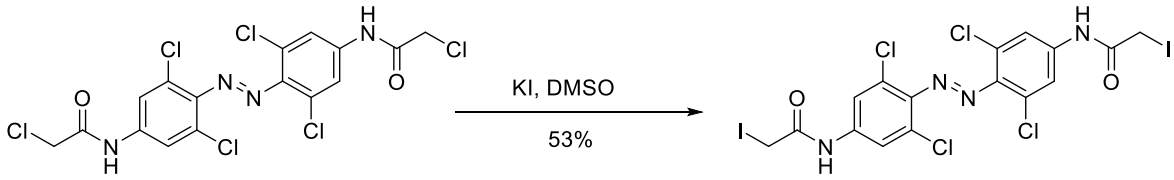

33 **49**

The reaction was carried out as described for the compound **49**. 10 mg (0.02 mmol, 1 eq) of **33** was dissolved in 1 mL of DMSO with 33 mg (0.20 mmol, 10 eq.) of KI was added to the solution and it was shaken until all precipitate was dissolved. It was processes as described and gave 5 mg of **49** (0.011 mmol, 53% yield).

^{1}H NMR (400 MHz, DMSO-d_6) δ (ppm): 10.90 (s, 1H), 7.87 (s, 2H), 3.88 (s, 2H). **^{13}C NMR** (400 MHz, DMSO-d_6) δ (ppm): 167.8, 141.5, 140.8, 127.6, 119.2, 43.3. **HR-MS** (ESI) $C_{16}H_{11}Cl_4I_2N_4O_2$ $[M+H]^+$ Calculated: 686.7696, $[M+H]^+$ found: 686.7690.

(7) Synthesis of (E)-3,3'-((((diazene-1,2-diylbis(3,5-dichloro-4,1-phenylene))bis(azanediyl))bis(2-oxoethane-2,1-diyl))bis(sulfanediyl))bis(2-aminopropanoic acid**)** (**48**)

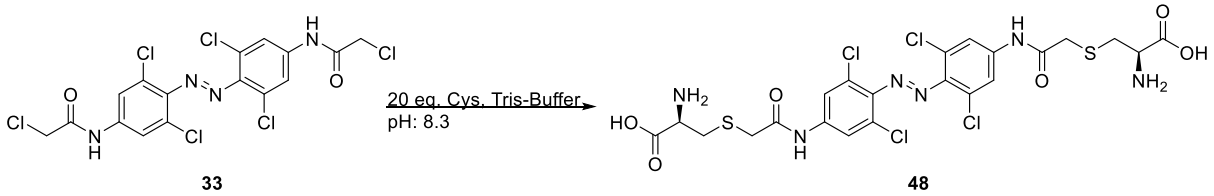

33 48

L-cysteine (48 mg, 0.4 mmol, 20 eq.) was dissolved in 1 mL Tris-buffer (pH 8.3, 50 mM) containing 0.5 mM TCEP. To this 10 mg (0.02 mmol, 1.0 eq) of **33** in 0.5 mL DMF was added and the reaction mixture left in a shaker at 45 °C for 16 h to observe the formation of precipitate. The reaction mixture was diluted in 20 mL of 0.1 M HCl and centrifuged. The obtained precipitate was insoluble in most organic solvents and subsequently only analysed using mass spectrometry.

LR-MS (ESI) $C_{22}H_{22}Cl_4N_6O_6S_2$ $[M+H]^+$ Calculated: 672.98, $[M+H]^+$ found: 672.98.

iii. Synthesis of the Dimethyl-Amine Azobenzene Derivative (**47**)

(1) Synthesis of (E)-5-chloro-6-((2,6-dichloro-4-nitrophenyl)diazenyl)-N1,N1-dimethylbenzene-1,3-diamine (**46**)

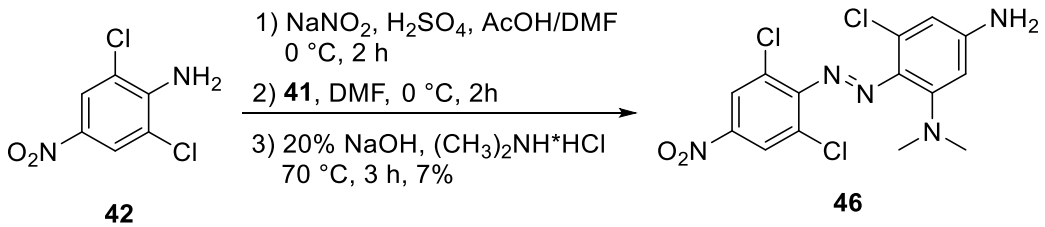

42 46

The reaction was carried out as described for the compound **44** with the exception that the isolated intermediate **43** was further basified by addition of with 20% aqueous sodium hydroxide and 510 mg (6.25 mmol, 2 eq.) of dimethylamine hydrochloride. The stirred reaction mixture was heated to 70 °C for 3 h, cooled down to room temperature and left stirring for

72 h. The crude product was purified as described for the compound **44** to give 74 mg (0.19 mmol, 7% yield) of **46** as red solid.

R_f: 0.33 (ethyl acetate/hexane) (30:70 (*v*/*v*)). **^{1}H NMR** (500 MHz, DMSO-d_6) δ (ppm): 8.34 (s, 1H), 6.78 (s, 1H), 6.48 (d, *J* = 2.3 Hz, 1H), 6.13 (d, *J* = 2.3 Hz, 1H), 2.79 (s, 3H). **^{13}C NMR** (500 MHz, DMSO-d_6) δ (ppm): 154.7, 153.8, 149.9, 144.2, 140.2, 129.0, 126.70, 124.5, 108.7, 98.1, 43.9. **LR-MS** (ESI) $C_{14}H_{13}Cl_3N_5O_2$ $[M+H]^+$ Calculated: 388.01 $[M+H]^+$ found: 388.01.

(2) Synthesis of (E)-6-((4-amino-2,6-dichlorophenyl)diazenyl)-5-chloro-N1,N1-dimethylbenzene-1,3-diamine (**47**)

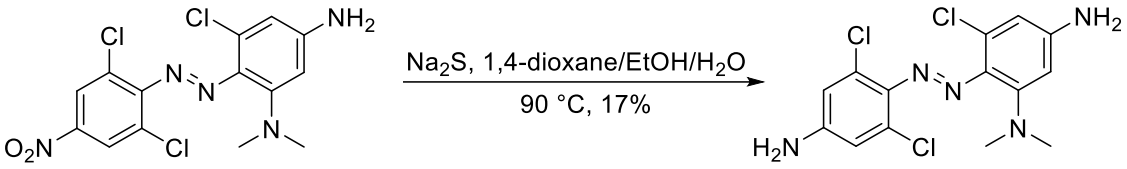

46 **47**

The reaction was carried out as described for the compound **45**. 100 mg (0.26 mmol, 1 eq.) were dissolved in a mixture of dioxane/EtOH/water (8 mL:2 mL:0.5 mL) and 60 mg (0.77 mmol, 3 eq.) of Na_2S was added. The reaction mixture was heated to 90 °C for 24 h. The reaction was cooled down to room temperature and concentrated under reduced pressure and extracted with ethyl acetate. The combined organic fractions were washed with brine, dried over magnesium sulfate and concentrated under reduced pressure. The crude product was purified using silica gel chromatography with a gradient of 0-100% EtOAc in hexane (*v*/*v*) to give **47** (16 mg, 0.04 mmol, 17% yield) as a red solid.

R_f: 0.15 (ethyl acetate/hexane) (30:70 (*v*/*v*)). **^{1}H NMR** (500 MHz, Acetone-d_6) δ (ppm):6.78 (s, 1H), 6.47 (d, *J* = 8.8 Hz, 1H), 6.32 (s, *J* = 12.5 Hz, 1H), 5.47 (s, 1H), 5.39 (s, 1H), 2.74 (s, 3H). **^{13}C NMR** (500 MHz, Acetone-d_6) δ (ppm): 151.2, 149.9, 148.6, 138.6, 133.1, 132.3, 128.6, 114.1, 108.4, 101.1, 43.9. **HR-MS** (ESI) $C_{14}H_{15}Cl_3N_5$ $[M+H]^+$ Calculated: 358.0393, $[M+H]^+$ found: 358.0408.

iv. Synthesis of the STmp-protected Fmoc-*L*-cysteine (**55**)

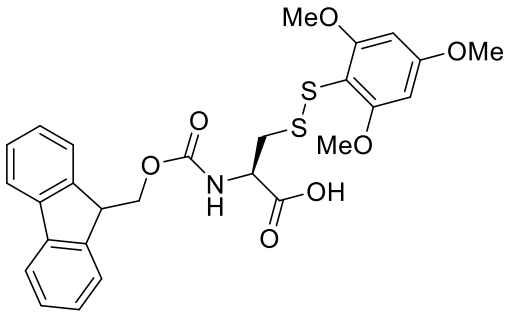

55

The synthesis of the protected cysteine **55** was carried out following the literature procedure from reference [234].

(1) Synthesis of sodium (((9H-fluoren-9-yl)methoxy)carbonyl)-L-cysteine (**52**):

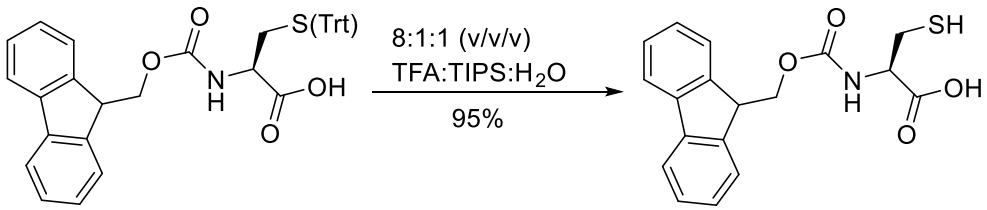

51 **52**

Fmoc-Cys(Trt)-OH (**51**) (10 g, 17.1 mmol) was suspended in 50 mL of a solution containing TFA, TIPS and water (8:1:1, *v*/*v*/*v*), 500 mL of DCM was added. The reaction mixture was stirred for 10 min at room temperature until the orange solution turned colourless. The reaction mixture was concentrated under reduced pressure. The residue was suspended in hexanes, centrifuged and the supernatant discarded, which was repeated for five times. The pellet was dried under reduced pressure to yield 5.58 g of **52** as a white solid (16.2 mmol, 95% yield).

^{1}H NMR (400 MHz, DMSO-d_6) δ (ppm): 12.90 (s, 1H), 7.91 (d, *J* = 7.5 Hz, 2H), 7.74 (d, *J* = 7.6 Hz, 2H), 7.71 (s, 1H), 7.43 (td, *J* = 7.3, 1.0 Hz, 2H), 7.34 (td, *J* = 7.4, 1.0 Hz, 2H), 4.34 – 4.30 (m, 2H), 4.25 (t, *J* = 8.0 Hz, 1H), 4.13 (td, *J* = 8.4, 4.3 Hz, 1H), 2.94 – 2.86 (m, 1H), 2.79 – 2.69 (m, 1H). **^{13}C NMR** (400 MHz, DMSO-d_6) δ (ppm): 171.9, 156.1, 143.8, 140.8, 127.7, 127.1, 125.3, 120.2, 65.7, 56.6, 46.6, 25.5. **LCMS** $C_{18}H_{18}NO_4S$ $[M+H]^+$ Calculated: 344.4, $[M+H]^+$ found: 344.4.

(2) Synthesis of sodium 2,4,6-trimethoxybenzenethiol (**54**):

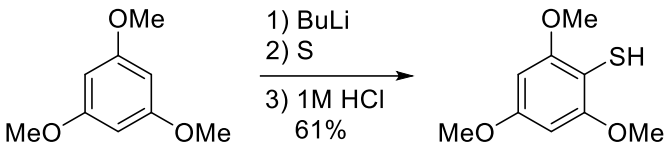

53 **54**

13.5 g (80.0 mmol, 1 eq.) of 1,3,5-trimethoxybenzene (**53**) were dissolved in 100 mL of tetrahydrofuran and 80.0 mmol (32 mL, 2.5 M, 1 eq.) of *n*-butyl lithium in hexane was added to the solution at 0 °C followed by the addition of a catalytic amount of *N,N,N',N'*-tetramethylethylenediamine (1 mL). The reaction mixture was let to warm up to room temperature and stirred for 1 h. 2.3 g (72.0 mmol, 0.9 eq.) of elemental sulphur were dissolved in 60 mL of toluene at 55 °C and added drop-wise to the reaction mixture. It was stirred for 6 h and the reaction mixture quenched by addition of 100 mL of water. The aqueous layer was acidified with 1 M aqueous hydrochloric acid (80 mL), extracted with CH_2Cl_2 (3 × 50 mL), washed with water (3 × 50 mL), brine (50 mL) dried ($MgSO_4$) and concentrated under reduced pressure. The yellow oil was crystalized at -80 °C and recrystallized from hexanes containing a few drops of CH_2Cl_2 to yield **54** as a crystalline pale yellow solid (9.6 g, 48 mmol, 61%).

^{1}H NMR (300 MHz, $CDCl_3$) δ (ppm): 6.17 (s, 1H), 3.86 (s, 3H), 3.79 (s, 1H), 3.77 (s, 1H). **^{13}C NMR** (300 MHz, $CDCl_3$) δ (ppm): 158.7 (s), 156.2 (s), 99.7 (s), 91.2 (s), 56.1 (s), 55.5 (s).

(3) Synthesis of sodium *N*-(((9H-fluoren-9-yl)methoxy)carbonyl)-S-((2,4,6-trimethoxyphenyl)thio)-L-cysteine (**55**):

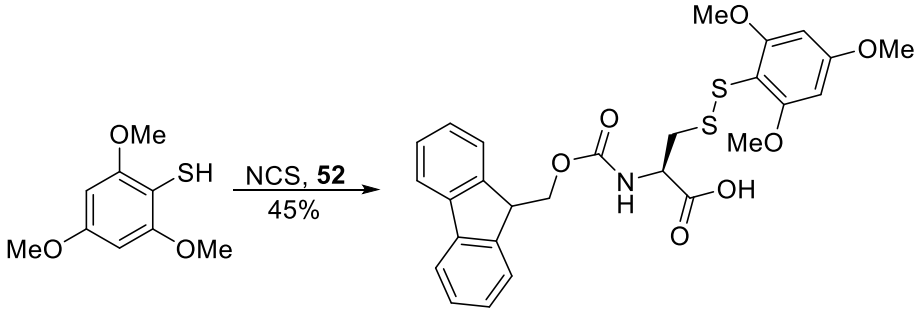

54 **55**

N-chlorosuccinimide was freshly recrystallized from hot water and 2.8 g (20.9 mmol, 1 eq.) of the dried crystals suspended in 30 mL of DCM at -78 °C under a nitrogen atmosphere. To this 4.01 g (20.0 mmol, 1 eq.) of **54** and 6.87 g (20.0 mmol, 1 eq.) of **52** in 40 mL of THF was added drop-wise under the exclusion of light. The reaction mixture was stirred at -78 °C for 2 h and allowed to warm to room temperature (3-4 h). It was diluted with DCM (200 mL), washed with 2 M HCl (3x 200 mL), water (200 mL), brine (200 mL), dried using magnesium sulphate and concentrated under reduced pressure to give a pale yellow foam. The residue was purified using a preparative HPLC system using a gradient of 0-40% MeCN in water. The fractions containing product were combined and the solvent removed under reduced pressure to yield **55** as white powder (5.1 g, 9.4 mmol, 45% yield).

^{1}H NMR (400 MHz, $CDCl_3$) δ (ppm): 7.78 (d, *J* = 7.5 Hz, 2H), 7.63 (t, *J* = 7.2 Hz, 2H), 7.41 (t, *J* = 7.5 Hz, 2H), 7.32 (t, *J* = 7.5 Hz, 2H), 6.15 (s, 1H), 6.13 (s, 2H), 4.92 – 4.81 (m, 1H), 4.43 (d, *J* = 7.1 Hz, 2H), 4.26 (t, *J* = 7.1 Hz, 1H), 3.87 (s, 6H), 3.80 (s, 3H), 3.37 (dd, *J* = 14.1, 3.4 Hz, 1H), 3.09 (dd, *J* = 14.3, 8.7 Hz, 1H). **^{13}C NMR** (400 MHz, $CDCl_3$) δ (ppm): 163.5, 162.5, 143.8, 141.4, 127.9, 127.3, 125.2, 120.1, 103.5, 91.2, 67.5, 56.3, 55.6, 54.5, 47.2, 38.0. **HR-MS** (ESI) $C_{27}H_{28}NO_7S_2$ $[M+H]^+$ Calculated: 542.1307, $[M+H]^+$ found: 542.1308.

2. Peptide Synthesis

    a. Materials

Low loading rink-amide resin (0.19 mmol/g, ProTide, CEM) was used for the solid phase peptide synthesis. Reagents were obtained from commercial suppliers without further purification. Fmoc-amino acids (PG)-COOH, *N, N, N', N'*-tetramethyl-O-(1H-benzotriazol-1-yl) uronium hexafluorophosphate (HBTU), hydroxybenzotriazole (HOBT), triisopropylsilane (TIS), 3,6-dioxa-1,8-octane-dithiol (DODT), *N,N'*-diisopropylethylamine (DIPEA), *N,N'*-diisopropylcarbodiimide (DIC) and *N,N*-dimethylformamide (DMF) were purchased from Cambridge Reagents. The spacer Fmoc-NH-(PEG)-COOH (9 atoms) was purchased from Novabiochem. Ethyl cyanohydroyiminoacetate (oxyma) was obtained from CEM. For the HPLC-purification, HPLC grade acetonitrile was obtained from Fisher Scientific and trifluoroacetic acid (TFA) from Fluorochem.

b. Solid-Phase Peptide Synthesis

A number of different peptides were synthesised using either manual or microwave assisted solid-phase peptide synthesis techniques (Table IV.1). The successful synthesis of the peptides was then confirmed by LC-MS analysis (Table IV.2).

Table IV.1 *Synthesised, purified and characterised peptides*

Peptide	**Sequence**
(5mer) GL- Bid$^{i,i+4}$-NH_2	GL-DIIRN-NH_2
Bid$^{i,i+4}$-NH_2	DIIRNIARHLACVGDCIDRSI-NH_2
GL- Bid$^{i,i+4}$-NH_2	GL-DIIRNIARHLACVGDCIDRSI-NH_2
(5)[FAM]-GL-Bid$^{i,i+4}$-NH_2	(5)[FAM]-GL-DIIRNIARHLACVGDCIDRSI-NH_2
Bid$^{i,i+7}$-NH_2 (Cys(STmp))	DIIRNIASCLASVGDCIDRSI-NH_2
Ant-NH_2	RQIKIWFQNRRMKWKK-NH_2
(5mer) Ant-NGLG-NH_2	MKWKK-NGL-G-NH_2
Ant-NGLG-NH_2	RQIKIWFQNRRMKWKK-NGL-G-NH_2
Ant-NCLG-NH_2	RQIKIWFQNRRMKWKK-NCL-G-NH_2
Ant-Bid$^{i,i+4}$-NH_2	RQIKIWFQNRRMKWKKDIIRNIARHLACVGDCIDRSI-NH_2
(5)[FAM]-Ant- Bid$^{i,i+4}$-NH_2	(5)[FAM]-RQIKIWFQNRRMKWKKDIIRNIARHLACVGDCIDRSI-NH_2
Pas-Ant-Bid$^{i,i+4}$-NH_2	FFLIPKG RQIKIWFQNRRMKWKKDIIRNIARHLACVGDCIDRSI-NH_2
(5)[FAM]-Pas-Ant- Bid$^{i,i+4}$-NH_2	(5)[FAM]- FFLIPKGRQIKIWFQNRRMKWKKDIIRNIARHLACVGDCIDRSI–NH_2
Bim$^{i,i+4}$-NH_2	IWIAQELRCIGDCFNAYYARR-NH_2
Bak$^{i,i+11}$-NH_2	GCVGRALAAIGDCINR-NH_2
$(Peg_9)_3$-Bak$^{i,i+11}$-NH_2	$(Peg_9)_3$-GCVGRALAAIGDCINR-NH_2
(5)[FAM]-$(Peg_9)_3$-Bak$^{i,i+11}$-NH_2	(5)[FAM]-$(Peg_9)_3$-GCVGRALAAIGDCINR-NH_2
E5-TAT-NH_2	GLFEAIAEFIENGWEGLIEGWYGGRKKRRQRRR-NH_2

Table IV.2 *Calculated and observed masses of the synthesised peptides*

Peptide	Mass (calc.) / Da.	Mass (obsv.) / Da.
(5mer) GL- Bid$^{i,i+4}$-NH_2	798.92	798.50
Bid$^{i,i+4}$-NH_2	2352.75	2352.53
GL- Bid$^{i,i+4}$-NH_2	2522.96	2521.03
(5)[FAM]-GL-Bid$^{i,i+4}$-NH_2	2881.28	2881.33
Bid$^{i,i+7}$-NH_2 (Cys(STmp))	2630.04	2630.80
Ant-NH_2	2245.75	2245.43
(5mer) Ant-NGLG-NH_2	1060.31	1059.55
Ant-NGLG-NH_2	2587.12	2585.17
(5)[FAM]-Ant-NGLG-NH_2	2945.44	2946.00
Ant-NCLG-NH_2	2633.51	2632.60
Ant-Bid$^{i,i+4}$-NH_2	4581.48	4581.85
(5)[FAM]-Ant- Bid$^{i,i+4}$-NH_2	4939.80	4941.23
Pas-Ant-Bid$^{i,i+4}$-NH_2	5384.50	5384.13
(5)[FAM]-Pas-Ant- Bid$^{i,i+4}$-NH_2	5742.82	5743.08
Bim$^{i,i+4}$-NH_2	2560.96	2561.35
Bak$^{i,i+11}$-NH_2	1587.87	1586.75
$[PEG]_3$-Bak$^{i,i+11}$-NH_2	2023.09	2022.95
(5)[FAM]-$[PEG]_3$-Bak$^{i,i+11}$-NH_2	2381.41	2379.4
E5-TAT-NH_2	3978.51	3978.36

i. Manual Peptide Synthesis

Fmoc-SPPS was carried out on Rink Amide resin (0.19 mmol g^{-1} loading, CEM Corporation) at 0.1 mmol scale using standard techniques. Coupling was performed using 5.0 eq. *O*-(Benzotriazol-1-yl)-*N,N,N',N'*-tetramethyluronium hexafluorophosphate (HBTU), 5.0 eq. 1-Hydroxybenzotriazole (HOBT), *N*,*N*-Diisopropylethylamine (DIPEA) and 4.0 eq. of amino acid. 2.0 eq. of the amino acid Fmoc-Cys(STmp)-OH was used during peptide synthesis but under double coupling conditions and extended reaction times. Single coupling was performed for 60 min, double coupling was carried out for 45 min per cycle for arginine and valine and their

direct successive amino acids. Fmoc-deprotection was achieved by exposing the resin to 3 mL of either a 10% (*w*/*v*) piperazine in 1-Methyl-2-pyrrolidinone (NMP)/Ethanol (9:1 (*v*/*v*)) + 0.1 M 1-Hydroxybenzotriazole (HOBt) or a 20% Piperidine in DMF (v/v)-solution for 15 min, twice.

Following the synthesis, the DMF was washed off the resin using DCM and diethyl ether and dried on air. The peptide was cleaved off the resin by stirring it in 92.5 % (*v*/*v*) TFA (Trifluoroacetic acid), 2.5 % (*v*/*v*) water, 2.5 % (*v*/*v*) DODT (2,2'-(Ethylenedioxy)diethanethiol), 2.5 % (*v*/*v*) TIS (Triisopropylsilane) for 2-3.5 h at room temperature. The TFA was then blown off under a stream of nitrogen, the crude peptide precipitated in ice-cold diethyl ether and stored at -20 °C overnight. It was then centrifuged (4000 *g*, 20 min) and the diethylether phase decanted. The precipitate was centrifuged and the supernatant carefully discarded. The crude peptide was dissolved in an appropriate mixture of water and acetonitrile before being purified by HPLC.

ii. Microwave-Assisted Solid-Phase Peptide Synthesis

Automated microwave-assisted peptide synthesis was carried out on a Liberty-Blue™ (CEM) on a 0.1 mmol scale. 5.0 eq. of Fmoc-protected amino acids (0.2 M in DMF) were used together with 10.0 eq. of DIC (1.0 M in DMF) and 5.0 eq. of Oxyma (1.0 M in DMF). Piperazine (4 mL of a 10% *w*/*v)* in NMP/EtOH (9:1 *v*/*v*) with 0.1 M HOBt as an additive were used to remove the Fmoc-protecting group. The deprotection was carried out for 1 min at 90 °C. The amino acids Val, Leu and Ile were double coupled for 4 min at 90 °C, His-residues were single coupled at 50 °C and Arg-residues were double coupled at 50 °C.

iii. HPLC Purification

The peptides were purified by reverse phase high performance liquid chromatography (RP-HPLC) either on a Dionex or on an Agilent 1260 Infinity HPLC using a Phenomex Gemini C18 column, 10 µm particle size, 110 Å pore size, 10.0 mm × 250 mm and a YMC-Triart Prep C18-S, 250 x 10 mm, 10 µm particle size, 120 Å pore size over a linear gradient of 10 % to 95 % acetonitrile-water (+0.1% trifluoroacetic acid) over 60 min. The wavelengths at 215 nm, 280 nm, 360 nm and 450 nm were monitored and the fractions containing potential product analysed by LC-MS. The product-fractions were combined and the acetonitrile removed under

reduced pressure before being lyophilized. All constructs and peptides were then stored at -20 °C and constructs sensitive to light were shielded from light using aluminium foil.

c. Peptide Stapling Protocol

The peptides (0.5 mM) were incubated in Tris-buffer (pH 8.3, 50 mM) containing 0.5 mM TCEP and 16 M guanidine hydrochloride for 1 h to ensure that the cysteine residues were reduced. The crosslinker (1.5 eq.) dissolved in DMF was added to the solution drop-wise and the reaction vessel thoroughly mixed after each addition to avoid local concentration maxima in the solution. Further DMF was added to a total volume of 50% to support solubilisation of the crosslinker and peptide-constructs. The reaction was left shaking at 45 °C for 16 h and the reaction progress monitored using LC(-MS) techniques. More TCEP and crosslinker were added when the reaction wasn't complete after this time and it was let to react for another 6 h. The reaction mixture was further diluted with water, filtered and purified by reverse phase HPLC.

For the optimised stapling conditions in solution, the peptide was incubated in the stapling buffer without any TCEP for 3 h and compressed air was bubbled through the solution to oxidise the cysteine-residues. The solution was then degassed to remove any oxygen from the solution following the addition of 1.0 eq. of TCEP. Argon was bubbled through the solution to minimise the exposure to oxygen and it was let to react until no oxidised peptide could be observed by LC(-MS). The crosslinker was added in DMF under an argon atmosphere and the reaction mixture was shaken at 45 °C for 16h and the progress monitored using LC(-MS) techniques.

Approximately one tenth of a 0.1 mmol scale of peptides that were still anchored onto the resin was taken and transferred into a separate syringe filter. It was crosslinked by selectively deprotecting the STmp-protected cysteine-side chains using 3 mL of 5% DTT in DMF (*w*/*v*) (3x5 min). The resin was washed three times with 5 mL DMF to remove any remaining DTT. 0.02 mmol of crosslinker were dissolved in 3 mL of DMF and 0.02 mmol of DIPEA was added to it. The reaction mixture was transferred to the resin and it was allowed to react overnight at room temperature. The crosslinker solution was washed off the resin using three times 5 mL of DMF and the Fmoc-group on the N-terminus of the peptide removed as described. The peptide was cleaved off the resin as described and analysed by LC-MS analysis.

37 and **33** stapled peptides that were purified by HPLC and analysed by LC-MS are listed below.

Table IV.3 *Calculated and observed masses of the stapled and purified peptides*

Construct	Mass (calc.) / Da.	Mass (obsv.) / Da.
37-GL-Bid$^{i,i+4}$-NH_2	2976.00	2974.50
33-GL-Bid$^{i,i+4}$-NH_2	2953.02	2954.04
33-(5)[FAM]-GL-Bid$^{i,i+4}$-NH_2	3311.34	3310.75
37-(5)[FAM]-GL-Bid$^{i,i+4}$-NH_2	3334.32	3333.40
36-Bid$^{i,i+7}$-NH_2 (Cys(STmp))	2525.87	2529.90
33-Ant-Bid$^{i,i+4}$-NH_2	5011.54	5011.80
33-Bim$^{i,i+4}$-NH_2	2991.02	2990.70
33-Bak$^{i,i+11}$-NH_2	2017.93	2017.75
33-(5)[FAM]-$[PEG]_3$-Bak$^{i,i+11}$-NH_2	2811.47	2812.90

d. Enzymatic Ligation Protocol

The enzymatic ligation of the peptides was carried out using the enzyme OaAEP1, which was expressed, purified and activated by Simon Tang (Cardiff University). The samples were reacted in sodium acetate buffer (pH 5.0; NaOAc: 0.205 g, NaCl: 0.146 g, EDTA: 0.015 g, TCEP: 7.17 x 10^{-6} g in 50 mL) at 37 °C with an OaAEP1 concentration of 100 nM. Peptides were added in different ratios with concentrations ranging from 100 µM to 2 mM (10 mM stock solution) and the reaction progress monitored by LC-MS at time points ranging from 1 h to 3 h. The reactions were quenched by the addition of 10 vol.% HCl at different time points to evaluate the progress of the ligation and compared to samples exposed to the same conditions without any enzyme.

e. Trypsin Digest

1 mg of the stapled peptide was dissolved in 1 mL of 50 mM Tris-HCl (pH 8.0) containing 8 M urea, 2 mM DTT. The sample was heated to 37 °C for 60 min before the solution was diluted using 9 mL of 50 mM Tris HCl (pH 7.8). 1.11 mg of $CaCl_2$ was added to obtain a final concentration of 1 mM $CaCl_2$. An aliquot of MS-grade trypsin (Trypsin Gold, Promega) was

added to the solution in a protease : peptide ratio of 1 : 20 (*w*/*w*) and the solution incubated 37 °C overnight. The digestion was quenched by addition of 5% (*v*/*v*) of formic acid to the sample and subsequently analysed by LC-MS.

f. Liquid-Chromatography-Mass-Spectrometry Analysis (LC-MS)

Liquid chromatography–mass spectrometry (LC-MS) was performed on a 1260 Infinity II from Agilent Technologies employing a C18 column; 4.6 mm × 100 mm. Mass-spectrometric data were obtained from an attached Agilent 6120 quadrupole ESI mass spectrometer at positive-ion mode (Agilent). Samples were eluted over a linear gradient of 5% to 95% acetonitrile:water (+0.1% formic acid) over 18-45 min (depending on the peptide sequences) with varying flow rates depending on the specifications of the used columns. The peptides Ant-Bid$^{i,i+4}$-NH_2 and E5-Tat-NH_2 and any of their modifications (fluorophore labeled, crosslinked, Pas-sequence added) were run with solvents containing 0.1% TFA in order to obtain a better peak shape. Over the entire time of the run, the wavelengths 210/215 nm, 280 nm, 360 nm and 450 nm were monitored. In some cases, the run was carried out using the diode-array in order to obtain the absorption spectra from 200-800 nm.

g. UV/Visible Absorption Experiments and Photoisomerisation

Ultraviolet absorbance spectra were obtained using a Shimadzu UV-2401PC UV/Vis spectrometer coupled to a temperature controlled cuvette holder. Spectra were recorded at 20 °C unless otherwise stated. Measurements of thermal relaxation rates were carried out by measuring the absorbance of the compound at specific time intervals. Dark adapted states were obtained by incubation of the constructs in the dark at 60 °C for 16 h. Light-state isomerization was achieved using 365 nm light from a UVP Benchtop 2UV transilluminator, 450 nm and 625 nm light-emitting diodes (LEDs). Samples were irradiated until a steady state was reached as determined by UV–vis spectroscopy. Crosslinker were recorded in DMSO and the peptides **33**-Ant-Bid$^{i,i+4}$-NH_2 and **33**-GL-Bid$^{i,i+4}$-NH_2in water and water/acetonitrile (2:1 *v*/*v*), respectively.

3. Biological Methods

a. Materials

All chemicals were obtained from Apollo Scientific UK (Cheshire, United Kingdom), Sigma-Aldrich UK (Poole, United Kingdom), Melford Laboratories Ltd (Suffolk, United Kingdom) or Fisher Scientific Ltd (Loughborough, United Kingdom) and were used without further purification. Restriction enzymes, Pfu polymerase and T4 ligase were purchased from New England Biolabs UK Ltd (Hitchin, United Kingdom). PrimeSTAR polymerase was purchased from Takara Bio Europe (Saint-Germain-en-Laye, France).

b. Media Preparation

i. Lysogeny Broth (LB)

10 g Tryptone,
5 g Yeast extract,
10 g NaCl,
H_2O to 1 L total volume.
Autoclaved.

ii. Terrific Broth (TB)

<u>Flask 1:</u>
12 g Tryptone,
24 g Yeast extract,
4 mL Glycerol,
H_2O to 900 mL total volume.

<u>Flask 2:</u>
2.31 g Monopotassium phosphate ,
12.54 g Dipotassium phosphate,
H_2O to 100 mL total volume.

Both solutions were autoclaved separately and combined at a sterile bench immediately before usage.

iii. M9 Minimal Media

10x M9 minimal salts

71.6 g Na_2HPO_4,

30 g KH_2PO_4,

5 g NaCl,

H_2O to 1L total volume,

Autoclaved.

100x Trace elements solution:

0.3 mM $ZnCl_2$,

0.7 mM $FeCl_3 \cdot 6\ H_2O$,

0.06 mM $CuCl_2 \cdot 2\ H_2O$,

0.05 mM $MnCl_2 \cdot 4\ H_2O$,

0.03 mM $Na_2B_4O_7 \cdot 10\ H_2O$,

0.006 mM $(NH_4)_6Mo_7O_{24} \cdot 4\ H_2O$,

H_2O to 1 L total volume.

M9 minimal media:

100 mL M9 salts,

10 mL sterile-filtered 5% NH_4Cl (or $^{15}NH_4Cl$),

20 mL sterile-filtered 15-20% D-glucose,

10 mL trace elements solution,

0.1 mL sterile-filtered 1 M $CaCl_2$,

2 mL sterile-filtered 1 M $MgSO_4$,

H_2O to 1 L total volume.

c. Antibiotic Stock Preparation

Antibiotics were freshly prepared as sterile solutions. Solid antibiotics were weighted out and dissolved in deionised water (10 mL). Solutions were then filter-sterilised at the sterile bench

and the antibiotics then diluted 1:1000 into the media to yield final concentrations of 100 μg/ml for ampicillin and 45 μg/ml for kanamycin.

d. Agar Plates Preparation

5 g Tryptone,
2.5 g Yeast extract,
10 g NaCl,
7.5 g Agar,
H_2O to 500 ml total volume,
Autoclaved, cooled to approximately 50 °C, antibiotic added, mixed thoroughly and poured onto sterile plastic Petri dishes. Plates were stored at 4 °C until required.

e. Bacterial Strains

XL1 Blue and DH5α cell lines were used for cloning and DNA amplification. Bl21 (DE3) and BL21 AI cell lines were used for protein expression.

f. (Super-)Competent Cells

Transformation buffers (TFB) were prepared, autoclaved and stored at 4 °C prior their use (Table IV.4).

Table IV.4 *Composition of the transformation buffers (TFB) that were used to produce competent cells.*

Components	TFB I / mM	TFB II / mM
Rubidium chloride	100	10
Calcium chloride	10	75
Potassium acetate	30	-
Manganese chloride	50	-
3-Morpholinopropane-1-sulfonic acid (MOPS)	-	10
pH	5.8	6.5

50 µM of a cell strain were incubated in 50 mL of LB media at 37 °C overnight. No antibiotic was used except for XL1-blue cells where the media was supplemented with tetracycline. 100 mL of fresh LB-media was inoculated with 1 mL of the overnight culture and grown at 37 °C until an optical density at 600 nm (OD_{600}) of 0.4-0.5 for XL1-Blue and DH5a or 0.9-1.2 for BL21 (DE3) cells was reached. Cells were cooled on ice for 20 min and then poured into two sterile falcon tubes. The cells were collected by centrifugation (3,400 g, 10 min) and the supernatant discarded. The cells were carefully re-suspended in 5 mL of TFB I and combined in a single falcon tube. They were incubated on ice for another 15 min and then harvested by centrifugation (3,400 g, 10 min). The supernatant was discareded and the pellets gently re-suspended in 5 mL TFB II. The cell suspension was quickly distributed into aliquots (50 µL) into pre-cooled 1.5 mL Eppendorf tubes and flash-frozen in liquid nitrogen. The cells were stored at -80 °C until required.

g. Agarose Gel

Tris-acetate-EDTA (TAE) buffer was prepared as a 1 L 50x stock solution (Table IV.5).

Table IV.5 *Recipe for 1 L of 50x stock solution of TAE-buffer.*

Components	Mass / Volume
Tris base	242 g
Acetic acid	57.1 mL
0.5 M EDTA (pH 8.0)	100

1x TAE buffer was prepared by diluting 20 mL of 50x TAE-buffer in 1 L of water. The gels were prepared by suspending 1 g of agarose in 100 mL of 1x TAE buffer and heating in a microwave until boiling. 5 µL of SYBR Safe dye was added and the solution poured into a gel casting tray (Bio-Rad Sub Cell GT Mini). It was left to set for 30 min at room temperature. The gel was submerged in a gel tank (Bio-Rad) using 1x TAE buffer and FastDigest Green buffer (x10, ThermoFisher Scientific) was added to the DNA samples. Samples were loaded into gel and it was run at 100 V for 40 min. A ChemiDoc Gel Imaging System (Bio-Rad) was used to visualise the gels afterwards.

h. Gel Extraction

Two different buffers were used to extract and purify the DNA from the agarose gel (Table IV.6).

Table IV.6 *Buffers used for the DNA purification protocol*

QG buffer	PE buffer
20 mM Tris-HCl	10 mM Tris-HCl
5.5 M Guanidine thiocyanate	80% Ethanol
pH 6.6	pH 7.5

DNA-bands of interest of the agarose gel were cut out using a scalpel and transferred onto a weighted 1.5 mL Eppendorf tube. The gel slices were dissolved in QG buffer (300 µL/100 µg gel) and incubated at 50 °C for 10 min. 100 µL/100 µg gel of PE buffer was added and thoroughly mixed. The mixture was applied to a Quagen Spin Miniprep Column and spun down at 16,000 g for 1 min in a Eppendorf benchtop microcentrifuge. The flow-through was discarded and it was washed with 750 µL of PE buffer and spun down for another 1 min. The flow-through was discarded and the column spun down again to remove any residual PE buffer. The column was placed onto a new Eppendorf tube and 50 µL of water was used loaded onto the column and spun down for another minute to elute the purified DNA. The final concentration was determined by 260 nm absorbance on a Nanodrop 1000 UV Visible spectrophotometer (ThermoFisher Scientific).

i. General PCR Recipes, Programmes and Plasmids

Polymerase chain reactions (PCR) were carried out on parental plasmids and genes. The thermophilic polyermase PrimeSTAR was purchased individually and as a 2x MasterMix. The plasmids used were taken from the plasmid library of Prof. Allemann; sense and antisense oligonucleotides required for the production of the new plasmids were acquired from Sigma-Aldrich.

Table IV.7 *PCR mixture for the polymerase PrimeSTAR*

Components	V / µL	Master Mix V / µL
DNA template (100 ng/µL)	1	1
Primer FWD[a] (10 ng/µL)	5	5
Primer REV[b] (10 ng/µL)	5	5
5x Buffer (incl. Mg^{2+})	10	-
dNTP[c]	1	-
DMSO	2	2
PrimeSTAR polymerase	0.5	-
Master mix[d]	-	25
H_2O	25.5	12

[a] FWD = forward (5' to 3'). [b] REV = reverse (3' to 5'). [c] dNTP = deoxyribose nucleotide triphosphate. [d] Master mix contains dNTP and the polymerase in the buffer.

The PCR-reactions were performed on one of the three available thermocyclers available in the laboratory interchangeably: Biometra Thermocycler T-Gradient Thermoblock, Eppendorf Mastercycler EP Gradient S thermocycler and Techne Flexigene Thermal Cycler FFG02FSD.

Table IV.8 *PCR conditions used on the thermocycler*

Step	Temperature / °C	Time / s	Number of cycles
Initial denaturation	98	10	1
Denaturation	98	10	
Annealing	55-62[a]	5	33
Extension	72	60/kbp[b]	-
Final extension	72	600	1

[a] Annealing temperature depends on the primers T_M to the selected plasmid. [b] extension time was set around 60 s per 1 kilo base pair of the desired PCR product.

Oligonucleotides used to copy the Bid$^{i,i+4}$ sequence:

FWD: GGTAGAGGGTCTCCAGTCCGATATTATCCGTAACATTGCG

REV: GGTAGAGGGTCTCCATCAAATAGAACGATCGATACAGTCG

The sequence of the plasmid containing His_6-GB1-TEV-Bid$^{i,i+4}$ was confirmed by sequencing from the T7 termination site. Sequencing data for the final acceptor-plasmid containing His_6-GB1-TEV-Bid$^{i,i+4}$ sites:

AAATAATTTTGTTTAACTTTAAGAAGGAGATATACCATGGGCAGCAGCCATCATCATCAT
CATCACACTTACAAATTAATCCTTAATGGTAAAACATTGAAAGGCGAAACAACTACTGAA
GCTGTTGATGCTGCTACTGCAGAAAAAGTCTTCAAACAATACGCTAACGACAACGGTGTT
GACGGTGAATGGACTTACGACGATGCGACTAAGACCTTTACAGTTACTGAACATATGGAA
AACCTGTATTTTCAGTCCGATATTATCCGTAACATTGCGCGCCATCTGGCCTGCGTGGGC
GACTGTATCGATCGTTCTATTTGATAACTCGAGCACCACCACCACCACCACTGAGATCCG
GCTGCTAACAAAGCCCGAAAGGAAGCTGAGTTGGCTGCTGCCACCGCTGAGCAATAACTA
GCATAACCCCTTGGGGCCTCTAAACGGGTCTTGAGGGGTTTTTTGCTGAAAGGAGGAACT
ATATCCGGATTGGCGAATGGGACGCGCCCTGTAGCGGCGCATTAAGCGCGGCGGGTGTGG
TGGTTACGCGCAGCGTGACCGCTACACTTGCCAGCGCCCTAGCGCCCGCTCCTTTCGCTT

TCTTCCCTTCCTTTCTCGCCACGTTCGCCGGCTTTCCCCGTCAAGCTCTAAATCGGGGGC
TCCCTTTAGGGTTCCGATTTAGTGCTTTACGGCACCTCGACCCCAAAAAACTTGATTAGG
GTGATGGTTCACGTAGTGGGCCATCGCCCTGATAGACGGTTTTTCGCCCTTTGACGTTGG
AGTCCACGTTCTTTAATACTGGACTCTTGTTCCAAACTGGAACAACACTCAACCCTATCT
CGGTCTATTCTTTTGATTTATAAGGGATTTTGCCGATTTCGGCCTATTGGTTAAAAAATG
AGCTGATTTAACAAAAATTTAACGCGAATTTTAACAA

Oligonucleotides used for the introduction of the BsaI-sites in the acceptor plasmid from the existing plasmid containing His_6-GB1-TEV-$Bid^{i,i+4}$-tag:

FWD: ATGCCGGATCCGGTCTCCTGATAACtcgagcaccaccacc
REV: ATGCGGATCCGGTCTCGAATAGAACGATCGATACAGTCGCCCACGC

The sequence of the acceptor plasmid containing His_6-GB1-TEV-$Bid^{i,i+4}$-BSAI-sites was confirmed by sequencing from the T7 termination site. Sequencing data for the final acceptor-plasmid containing His_6-GB1-TEV-$Bid^{i,i+4}$-BSAI-sites:

GAAATAATTTTGTTTAACTTTAAGAAGGAGATATACCATGGGCAGCAGCCATCATCATCATCAT
CACACTTACAAATTAATCCTTAATGGTAAAACATTGAAAGGCGAAACAACTACTGAAGCTGTTG
ATGCTGCTACTGCAGAAAAAGTCTTCAAACAATACGCTAACGACAACGGTGTTGACGGTGAATG
GACTTACGACGATGCGACTAAGACCTTTACAGTTACTGAACATATGGAAAACCTGTATTTTCAG
TCCGATATTATCCGTAACATTGCGCGCCATCTGGCCTGCGTGGGCGACTGTATCGATCGTTCTA
TTCGAGACCGGATCCGGTCTCCTGATAACTCGAGCACCACCACCACCACCACTGAGATCCGGCT
GCTAACAAAGCCCGAAAGGAAGCTGAGTTGGCTGCTGCCACCGCTGAGCAATAACTAGCATAAC
CCCTTGGGGCCTCTAAACGGGTCTTGAGGGGTTTTTTGCTGAAAGGAGGAACTATATCCGGATT
GGCGAATGGGACGCGCCCTGTAGCGGCGCATTAAGCGCGGCGGGTGTGGTGGTTACGCGCAGCG
TGACCGCTACACTTGCCAGC

j. Golden Gate Assembly

During the Golden-Gate assembly, the restriction enzyme *Bsa*I cuts the DNA up-stream from the recognition site leading to a 4bp sticky end. Addition of a DNA fragment containing complementary sites to this overhang, allows the T4 ligase to join the segments without any *Bsa*I recognition sites in the final sequence driving the equilibrium towards the product. The reaction mixture was incubated at 37 °C for 1h. The enzymes were deactivated for 5 min at 50 °C, followed by 80 °C before the mixture was transformed in XL1-Blue cells.

Table IV.9 *Reaction mixture for the Golden Gate ligation*

Reaction components	V / µL
DNA segment 1 (100 ng/µL)	1
DNA segment 2 (100 ng/µL)	1
*Bsa*I	0.5
*Bsa*I 10x Buffer (incl. Mg^{2+})	1
T4 ligase	0.5
BSA[a] (x100)	0.5
H_2O	Up to 10[b]

[a] *BSA = Bovine serum albumin.* [b] *Final volume was 10 µL. Volume of water to be added depended on the concentration of the DNA segments.*

k. Transformation Protocol

Competent XL1-Blue or DH5α cells were thawed on ice from -80 °C. The plasmid (1 µL for plasmids of 100 ng/µL DNA concentration) was mixed with the cells and incubated on ice for 30 min before being heat-shocked in a 42 °C water bath for 45 s before returned on ice. 1 mL of LB-media was added to the cells and the culture shaken at 37 °C for 1 h. The cell-suspension was then centrifuged at 3,300 g for 60 s and the supernatant discarded. It was re-suspended in 100 µL of fresh LB-media and the spread onto agar-plates with the appropriate antibiotic. The places were incubated at 37 °C overnight.

l. Protein Expression

Using a sterile pipette tip, a single colony was picked from the agar plate and used to inoculate 100 mL of fresh LB media containing the corresponding antibiotic. The suspension was left shaking in an incubator at 37 °C overnight and used to inoculate fresh media of choice (5 mL of culture per 500 mL of media). The culture was grown to an OD_{600} of 0.6 and gene transcription induced by the addition of isopropyl-β-D-1-thiogalactopyranoside (IPTG, 60 mg per 500 ml culture). Expression was carried out at 20 °C overnight and the cells harvested by centrifugation (3,400 g, 15 min). The supernatant was discarded and the cell pellets stored at -20 °C.

Bacterial expression was carried out in LB/TB medium for the binding studies and in M9 medium supplemented with $^{15}NH_4Cl$ as sole sources of nitrogen for NMR sample preparation.

m. Protein Purification Protocol

i. Buffers

The purification of the proteins required different buffer systems (Table IV.10). The pH of the buffers was adjusted to the appropriate value using NaOH or HCl solutions.

Table IV.10 *Different buffers used for the purification of the proteins*

Lysis buffer I	Lysis buffer II	Ni-NTA elution buffer	Dialysis buffer
100 mM Sodium phosphate	50 mM Potassium phosphate	100 mM Sodium phosphate	5 mM Sodium Phosphate
500 mM NaCl	300 mM NaCl	500 mM NaCl	-
5 mM β-mercapto-ethanol	-	5 mM β-mercapto-ethanol	5 mM β-mercapto-ethanol
-	-	Imidazole (5-500 mM)	-
pH 7.5	pH 7.0	pH 7.5	pH 7.3

ii. Cell Lysis

Following one freeze-thaw cycle, the bacterial pellet was re-suspended in lysis buffer I. The suspension was supplemented with phenylmethylsulphonyl fluoride (PMSF, 1 mM) and lysozyme (0.1 mg/mL) to prevent the degradation of the protein. The cell suspension was kept on ice and was lysed by sonication with pulses of 5 s (40% amplitude) and 10 s off for a total time of 15 min. The resulting lysate was centrifuged at 38,000 g for 45 min and the supernatant containing the protein subjected to Ni-NTA affinity chromatography.

Proteins fused to a KSI-tag are predominantly located in inclusion bodies. For them, the cells were suspended in lysis buffer II and lysed using the same programme. The supernatant was discarded and it was stirred in lysis buffer II with 1 M NaCl for 2 h. It was centrifuged (20 min, 12,000 g) and the resulting pellet dissolved in guanidine hydrochloride (6 M) and stirred over night at 4 °C. After centrifugation (30,000 g, 30 min), the supernatant was dialyzed against 5 L of H_2O twice using a 10 kDa cut off dialysis membrane.

iii. Ni-NTA Affinity Chromatography

A Ni-NTA column was equilibrated with the *lysis buffer I* before the supernatant of the centrifuged lysate was applied. The protein was eluted using a step gradient of increasing concentration of imidazole (5, 20, 50, 100, 150, 200, 500 mM) in the *Ni-NTA elution buffer*. The column was washed with 5 CV of each solution and the fractions collected separately. All fractions were analysed by SDS-PAGE and the ones containing the protein combined for dialysis. The expressed protein Bcl-x_L contained a double His_6-tag and typically eluted in the fractions of 200mM and 500 mM imidazole.

iv. Dialysis

Combined fractions containing the protein of interest were dialysed twice in 5 L of *dialysis buffer* to remove imidazole from the sample. For the protein Bcl-x_L, this was followed by a third dialysis to buffer-exchange the protein into buffers appropriate for CD- or NMR-spectroscopy. Protein samples were dialysed at 4 °C for 8-16 h using a 12-14 kDa membrane. Protein samples were then concentrated using either an Amicon® system with a 5.0 kDa cut-off membrane at 4 °C connected to a nitrogen gas cylinder or a VivaSpin centrifugal concentrator (10 kDa).

v. TEV-Cleavage

The $Bid^{i,i+4}$-peptide was expressed with a Tobacco Etch Virus (TEV) cleaving site after a His_6- and GB1-tag. Protein solutions were supplemented with 1,4-dithiothreitol (DTT, 5 mM) and TEV-protease (1 mg protease per 100 mg protein) was added to the protein sample. The reaction was carried out overnight at 4 °C. The TEV protease contained a His_6-tag itself and was removed by Ni-NTA chromatography. The cleaved peptide did not contain any His_6-tag and therefore eluted from the Ni-NTA column in the flow-through.

vi. Cyanogen Bromide Cleaving

Following the dialysis of the KSI-fusion protein against water, the content of the dialysis-membrane was centrifuged (10,000 *g*, 10 min) and the precipitate collected. It was solubilized using 50 mL of 70% formic acid and transferred into a 500 mL round bottom flask wrapped in aluminium foil. 2 g of cyanogen bromide was added and the mixture stirred for 16 h at room

temperature under nitrogen atmosphere. It was basified 0.2 M NaOH to open the lactone ring and the solvent removed under reduced pressure. The resulting residue was re-suspended in an acetonitrile/water mixture (40/60, *v*/*v*) containing 0.1% TFA. The suspension was centrifuged at 10,000 g for 10 min, the supernatant filtered and subjected to reverse phase HPLC purification using a C18 column.

n. SDS-PAGE

Protein samples were subjected to sodium dodecylsulfate-polyacrylamide gel electrophoresis (SDS-PAGE) and analysed by comparison against prestained molecular weight markers. The gels were cast run using the Mini-PROTEAN system (Bio-Rad).

i. Gel Casting

Proteins were analysed using resolving and stacking gels (Table IV.11). For the analysis of the peptide Bid$^{i,i+4}$, a 20% acrylamide/*bis*-acrylamide resolving gel was used. Apart from 10% (*w*/*v*) APS, all solutions were prepared in advance and stored at room temperature.

Table IV.11 *Compositions of the SDS-gels.*

Components	Resolving Gel (12%)	Resolving Gel (20%)	Stacking Gel (5%)
H_2O	3.4 mL	0.65 mL	2.85 mL
1.5 M Tris-HCl (pH 8.0)	2.5 mL	2.5 mL	-
0.5 M Tris-HCl (pH 6.8)	-	-	1.25 mL
Acrylamide/*bis*-acrylamide 30% (8% *w*/*v*)	4 mL	6.75 mL	0.85 mL
SDS[a] 10% (w/v)	100 µL	100 µL	50 µL
APS[b] 10% (w/v)	100 µL	100 µL	50 µL
TEMED[c]	20 µL	20 µL	10 µL

[a] SDS = sodium dodecylsulfate. [b] APS = ammonium persulfate. [c] tetramethylene ethylenediamine.

APS was added last to the gel mixtures when prepared as it initiates the gel-polymerisation process. Gels were prepared in a Sterelin tube and poured between the gel plates held together in a casting gate. Isopropanol was added on top of the resolving gel and any air-bubbles removed until it had set. The isopropanol layer was removed and the stacking gel

mixture (5%) was prepared and poured over the resolving gel. A comb was added into the still liquid stacking gel to create the sample wells. The comb was removed when the gel had set and fully polymerised (~20 min).

ii. Sample Preparation

SDS-PAGE loading dye (4x) was prepared in a Sterelin tube, divided into 1 mL aliquots and stored at -20 °C until required (Table IV.9). Protein samples were mixed with the loading dye (4x) in a 3:1 ratio to a final concentration of 40 µL. The samples were heated to 95 °C for 5 min, centrifuged when necessary on a benchtop centrifuge and allowed to cool down to room temperature before loading them into the gel wells.

Table IV.12 *Recipe for the SDS-PAGE loading dye (4x).*

Reaction components	Volume / Mass
1 M Tris-HCl (pH 6.8)	2 mL
SDS[a]	0.8 g
Glycerol	4 mL
Bromophenol blue (10% *w*/*v*)	10 µL
β-mercapto-ethanol	4 mL

[a] *SDS = sodium dodecylsulfate*

iii. Running Protocol and Visualisation

The gels were fitted in the running chambers, which were filled with 1x running buffer (Table IV.13). Samples were loaded into the well and the gels were run at 150 V for 1 h. Gels were washed and soaked in warm water three times for 3 min to remove any SDS.

Table IV.13 *Running buffer (10x) recipe dissolved in 1 L of H_2O*

Reaction components	Mass per 1 L
Tris-base	30.3 g
SDS[a]	10 g
Glycine	144 g

[a] *SDS = sodium dodecylsulfate*

SDS gel stain was used to visualise the protein-bands following the electrophoresis (TableIV.14). Coomassie Brilliant Blue R-250 was dissolved in ethanol and concentrated hydrochlorid acid before being diluted in water. Gels were stained for 15 min at room. Water was used to de-stain the gels to remove the background of blue stain until the protein-bands become clear and visible. The protein bands were imaged on a ChemiDocTM XRS+ gel imager (Bio-Rad).

Table IV.14 *SDS-gel stain in 1 L of H_2O*

Reaction components	Mass/Volume per 1 L
Coomassie Brilliant Blue R-250	60 mg
Ethanol	20 mL
Conc. HCl	2 mL

4. Bio-Physical Methods

    a. Circular Dichroism Spectroscopy

The backbone of each amino acid in a peptide- or protein-structure possesses a degree of rotational freedom. Different structural motifs lead to specific rotations of the backbone bonds resulting in the distinct absorption of elliptically polarized light. α-helical motifs show negative mean ellipticity-values at wavelengths of 208 nm and 222 nm. Circular dichroism spectra were recorded in 5 mM potassium phosphate buffer (pH 8.0) and deionised water for the construct **33**-Ant-Bid$^{i,i+4}$-NH_2 in a 1 mm path length cuvette on a Chirascan (Applied Photophysics)

spectrometer at 20 °C. The peptide concentration was typically around 100 pM. Mean residual ellipticities (in deg cm^{-2} $dmol^{-1}$) were auto-zeroed at 300 nm to remove any background noise and calculated in according to following equation.

$$[\theta]_r = \frac{\theta}{10ncl}$$

Θ = measured ellipticity [mdeg], n = number of backbone amide bonds, c = concentration in M, l = path length in cm.

The percentage of the α-helical structure was calculated using the mean residual ellipticity $[\Theta]_r$ at the wavelength of 222 nm.

$$\%helicity = \frac{-100[\theta]_{r,222}}{40{,}000(n-4)}$$

$[\Theta]_{r,222}$ = mean residual ellipticity at 222 nm, n = number of backbone amide bonds.

b. Fluorescence Polarisation Binding Assays

Fluorophores that are excited by polarised light will emit light with a retained polarisation. Tumbling or moving of the fluorophore during this process, however, causes the emitted light to be depolarised. The tumbling speed of the molecule depends on the size of the molecule with macromolecule moving slower than smaller molecules. Binding of two molecules can be monitored by the change in polarised light due to the slower tumbling of the bigger, bound complex. This technique is most sensitive when the fluorophore-labelled molecule is small compared to the binding partner. FP measures the emitted light in the horizontal and vertical plane after excitation with plane-polarized light. The intensities of the light in their respective planes are then related to the polarisation. However, anisotropy is often used instead of polarisation values and both can be used interchangeably.

$$P = \frac{I_{\parallel} - I_{\perp}}{I_{\parallel} + I_{\perp}}; \quad A = \frac{I_{\parallel} - I_{\perp}}{I_{\parallel} + 2I_{\perp}}$$

P = Polarizaiton, A = Anisotropy, $I_{\parallel}$ = Parallel light intensity, $I_{\perp}$ = Perpendicular light intensity.

The measured anisotropy is the sum of the free fluorescent ligand and the fraction of the fluorescent ligand bound to a receptor.

$$A_M = F_F A_{L^*} + F_B A_{L^*P}$$

A_M = Measured Anisotropy, F_F = Fraction of free ligand, A_{L^*} = Anisotropy fluorescent ligand, F_B = Fraction bound ligand, A_{L^*P} = Anisotropy fluorescent ligand bound to receptor.

The dissociation constant of the binding reaction is defined as the following and the equation can be used to describe the concentration of the receptor-ligand complex:

$$K_d = \frac{[P][L]^n}{[PL_n]} \rightarrow [PL_n] = \frac{[P][L]^n}{K_d}$$

$[PL_n]$ = Concentration of receptor-ligand complex, [P] = Concentration of unbound receptor, n = Number of binding sites.

The ratio of the occupied to total receptor concentration is defined in the following equation. The concentration of the receptor-ligand complex was described using the dissociation constant.

$$\theta = \frac{[PL_n]}{[P] + [PL_n]} \rightarrow \theta = \frac{[L]^n}{K_d + [L]^n}$$

Θ = Ratio of occupied to total receptor, $[PL_n]$ = Concentration of receptor-ligand complex, [P] = Concentration of unbound receptor, [L] = Concentration of ligand, K_D = Dissociation constant, n = Number of binding sites.

Assuming that the receptor was completely unbound before the binding experiment, Θ can be described using following equation:

$$[P_0] = [P] + [PL_n] \rightarrow \theta = \frac{[PL_n]}{[P_0]}$$

Θ = Ratio of occupied to total receptor, $[PL_n]$ = Concentration of receptor-ligand complex, [P] = Concentration of unbound receptor, $[P_0]$ = Concentration of receptor (total), n = Number of binding sites.

Subsequently, the Hill-Langmuir equation can be written as following equation:

$$[PL_n] = [P_0]\ \frac{[L]^n}{K_d + [L]^n}$$

$[PL_n]$ = Concentration of receptor-ligand complex, [P] = Concentration of unbound receptor, [L] = Concentration of ligand, $[P_0]$ = Concentration of receptor (total), K_D = Dissociation constant, n = Number of binding sites.

The total concentration of available receptor $[P_0]$ is equal to the maximum specific binding, which is often expressed as B_{max}. Assuming that only one binding site exists (*n* =1) to describe the receptor-ligand relationship and that non-specific binding interactions are directly proportional to the concentration of the added ligand, the observed total binding can be described using following function:

$$f(x) = B_{max}\ \frac{x}{K_d + x} + NS * x + C$$

B_{max} = Maximum specific binding, NS = Factor for non-specific (NS) binding, C = Background signal, K_D = Dissociation constant.

The fluorescence polarisation (FP) measurements were carried out in 100 mM sodium phosphate buffer (pH 7.5) containing 10 mM NaCl. Stock solutions of the peptides were prepared and the concentration of the peptides determined by their extinction coefficient of the carboxyfluorescein group in 0.1 M NaOH at 492 nm. The peptide-stock solution (typically ~100 mM) was diluted in the buffer to a total concentration of 10 nM. TCEP was added as a reducing agent to the stock solution for non-crosslinked peptides in order to avoid disulfide-formation. Stapled peptides were thermally relaxed into their thermodynamically preferred state by incubating them at 60 °C for 16 h prior the experiment. Light states of the constructs were maintained by irradiating the sample every 5 min with an appropriate light source for 2 min during the experiment. The protein Bcl-x_L was expressed in BL21 (DE3) strain of *E. coli* as described, concentrated using a spin-column and the concentration determined by its extinction coefficient at 280 nm. The measurements were carried out on a Perkin-Elmer LS-55 fluorescence spectrometer at 20 °C where the sample was excited at 495 nm and the fluorescence emitted detected at 525 nm. During the experiment, the protein was titrated to the fluorophore-labelled peptide in concentrations from 10 nM to 2 µM resulting in a total increase in volume of <2.5 vol.% and the changes in fluorescence anisotropy recorded. All measurements were recorded in triplicate unless otherwise stated. The background signal of

the measurement was removed by subtracting the anisotropy-value of the (5)FAM-labelled peptide without any protein (0 nM) from the remaining values. The results were fitted using the Hill-Langmuir equation for the specific- and total-binding model on the software GraphPad Prism 8.4.3. K_D, B_{max} and 95% CI-values were obtained from the fit of the software. The standard deviation (SD) was calculated using the sample size and t-distribution:

$$SD = \frac{\sqrt{N} * (upper\ limit - lower\ limit)}{2 * (t_v(N))}$$

N = Sample size/number of data points, upper limit – lower limit = values from the 95% CI, t_v = t-value as a function of the sample size.

c. ^{15}N-Protein NMR

The protein Bcl-x_L was expressed in M9 minimal media supplemented with $^{15}NH_4Cl$ (99 %) and purified as described. It was dialysed three times against 5 L of 5 mM NaH_2PO_4/Na_2HPO_4 buffer (pH 7.3) and concentrated by ultrafiltration to a total concentration of ~ 400 µM. Peptides were added in varying concentration depending on the obtained signal but at least to a ratio of 1:1 (protein:peptide). All NMR samples were supplemented with 5% D_2O and recorded at 298.15 K using a DPX-600MHz spectrometer (Bruker) equipped with QCI-P cryoprobe and preamplifiers using a ^{1}H-^{15}N-HSQC pulse sequence. ^{15}N-HSQC peaks for the bound protein-peptide complexes were evaluated by comparison with the unbound protein and the published assignments for the Bcl-x_L/**37**-Ac-Bak$^{i,i+11}$-NH_2 complex.[212,213]

5. Cell Culture Methods

a. Cell Culture

Human epithelial carcinoma cell line HeLa (ATCC) was used in cell culture experiments. The cells were cultured in Dubecco's Modified Eagle Medium (DMEM containing phenol red, Fisher Scientific) supplemented with 10% heat-inactivated fetal bovine serum (FBS, Fisher Scientific) at 37 °C in a 5% CO_2 atmosphere. Cells were passaged at ~80% confluency by detaching them from the flask using trypsin (0.25% EDTA, Dulbecco, Fisher Scientific). 10 µL of trypsin was applied per 1.0 cm^2 of growth area. Cells were washed with phosphate-buffered saline (PBS) buffer (10 mM sodium phosphate pH 7.4, 2 mM monopotassium phosphate, 140 mM sodium

chloride, 3 mM potassium chloride) to remove any media. It incubated for 5 min at 37 °C in a 5% CO_2 atmosphere and the cells re-suspended in fresh media. The cell suspension was centrifuged (1000 rpm, 5 min) on a table top centrifuge, the supernatant discarded and the cell pellet re-suspended in fresh media and counted using a hemocytometer. An aliquot of the cell suspension was then transferred into a new flask and mixed with fresh media before being incubated at 37 °C in a 5% CO_2 atmosphere.

b. Peptide Delivery Procedure

Cells were split into 24-well plates (250,000 cells/well) for uptake-experiments and 96-well plates (20,000 cells/well) for cell-viability experiments to reach 70-80% confluency. The cells were incubated overnight at 37 °C in 5% CO_2 atmosphere. The media was removed and the cells were washed with PBS buffer. The cells were incubated with the peptide-samples for the stated time and concentration in triplicates (in serum free DMEM) to a total volume of 200 µL per well for the 24-well plates and 50 µL per well for the 96-well plate. The media was removed and the cells were washed three times with 200 µL of a heparin sulfate solution (0.5 mg/mL). Excess heparin was washed off using 200 µL PBS buffer before being processed for FACS or cell-viability assays.

Constructs were dissolved in either DMSO or water depending on their solubility properties and diluted out into serum free DMEM to a total concentration of 1% DMSO or water, respectively. The diluted samples were applied to the cells instantly to minimize precipitation of the constructs before administration.

c. Fluorescence-Assisted Cell Sorting (FACS)

The cells were detached from their 24-well plate with 50 µL per well of trypsin for 5 min at 37 °C and suspended in 450 µL of PBS buffer. The suspension was transferred into a test tube to be analysed on a S3e Cell Sorter (Bio-Rad) equipped with a 488 nm, 526 nm and 586 nm laser. Fluorescence was collected at 586/48 nm and 526/25 nm, respectively. For each experiment, a minimum of 10,000 events were collected in triplicates. Dead cells and debris were excluded from the data using gating on a side scatter (SSC) *vs* forward scatter (FSC) graph. The data was analysed on the ProSortTM software (Bio-Rad) and the data plotted using Microsoft Excel as geometric mean of fluorescence ± SD.

d. Cell Viability Assays

Cells were incubated with 100 µL of media (DMEM supplemented with serum) lacking phenol red overnight at 37 °C in 5% CO_2 atmosphere. To measure the cell viability, cells were treated with Celltiter® Blue (Promega) for 4 h. The fluorescence was measured at 585 nm on a VICTOR X5 Multilabel Plate Reader (PerkinElmer) to determine the cell viability. Untreated cells were used as a control and considered 100% viable whereas cells that were incubated with 0.01% Trition X-100 were used as positive controls. The data was plotted using Microsoft Excel as mean of cell viability ± SD.

V. References

1 E. M. Phizicky and S. Fields, *Microbiol. Rev.*, 1995, **59**, 94–123.

2 J. J. Li, X. Fang, S. M. Schuster and W. Tan, *Angew. Chemie*, 2000, **112**, 1091–1094.

3 N. Tsomaia, *Eur. J. Med. Chem.*, 2015, **94**, 459–470.

4 A. Ali and A. Bagchi, *Curr. Chem. Biol.* , 2015, **9**, 53–65.

5 J. M. Nooren, I. M.A.; Thornton, *EMBO J.*, 2003, **22**, 3486–3492.

6 S. Jones and J. M. Thornton, *J. Mol. Biol.*, 1997, **272**, 121–132.

7 J. A. Wells and C. L. McClendon, *Nature*, 2007, **450**, 1001–1009.

8 M. R. Arkin, Y. Tang and J. a Wells, *Cell Chem. Biol.*, 2015, **21**, 1102–1114.

9 H. Hwang, T. Vreven, J. Janin and Z. Weng, *Proteins Struct. Funct. Bioinforma.*, 2010, **78**, 3111–3114.

10 L. Young, R. L. Jernigan and D. G. Covell, *Protein Sci.*, 1994, **3**, 717–729.

11 A. Dailing, A. Luchini and L. Liotta, *Expert Rev. Proteomics*, 2015, **12**, 457–467.

12 S. Fletcher and A. Hamilton, *Curr. Top. Med. Chem.*, 2007, **7**, 922–927.

13 M. R. Arkin, Y. Tang and J. A. Wells, *Chem. Biol.*, 2014, **21**, 1102–1114.

14 A. Dailing, A. Luchini and L. Liotta, *Expert Rev. Proteomics*, 2015, **12**, 457–467.

15 A. A. Ivanov, F. R. Khuri and H. Fu, *Trends Pharmacol. Sci.*, 2013, **34**, 393–400.

16 E. Valkov, T. Sharpe, M. Marsh, S. Greive and M. Hyvönen, *Top. Curr. Chem.*, 2012, **317**, 145–79.

17 L. Jin, W. Wang and G. Fang, *Annu. Rev. Pharmacol. Toxicol.*, 2014, **54**, 435–456.

18 L. Milroy, T. N. Grossmann, S. Hennig, L. Brunsveld and C. Ottmann, *Chem. Rev.*, 2014, **114**, 4695–4748.

19 J. C. Fuller, N. J. Burgoyne and R. M. Jackson, 2009, **14**, 155–161.

20 J. T. Metz and P. J. Hajduk, *Curr. Opin. Chem. Biol.*, **14**, 498–504.

21 I. S. Moreira, P. A. Fernandes and M. J. Ramos, *Proteins*, 2007, **68**, 803–12.

22 M. R. Arkin and J. A. Wells, *Nat. Rev. Drug Discov.*, 2004, **3**, 301–317.

23 J. A. DiMasi and H. G. Grabowski, *Manag. Decis. Econ.*, 2007, **28**, 469–479.

24 I. Kola and J. Landis, *Nat. Rev. Drug Discov.*, 2004, **3**, 711–716.

25 P. Vlieghe, V. Lisowski, J. Martinez and M. Khrestchatisky, *Drug Discov. Today*, 2010, **15**, 40–56.

26 A. Mullard, *Nat. Rev. Drug Discov.*, 2019, **18**, 85–89.

27 K. Fosgerau and T. Hoffmann, *Drug Discov. Today*, 2015, **20**, 122–8.

28 J. L. Lau and M. K. Dunn, *Bioorg. Med. Chem.*, 2018, **26**, 2700–2707.

29 F. Albericio and H. G. Kruger, *Future Med. Chem.*, 2012, **4**, 1527–1531.

30 E. B.-M. Daliri, B. H. Lee and D. H. Oh, *Crit. Rev. Food Sci. Nutr.*, 2018, **58**, 2273–2284.

31 D. S. Nielsen, N. E. Shepherd, W. Xu, A. J. Lucke, M. J. Stoermer and D. P. Fairlie, *Chem. Rev.*, 2017, **117**, 8094–8128.

32 C. Adessi and C. Soto, *Curr. Med. Chem.*, 2002, **9**, 963–78.

33 C. Pichereau and C. Allary, *EBR - Eur. Biopharm. Rev.*, 2005, 88–93.

34 S. Varland, C. Osberg and T. Arnesen, *Proteomics*, 2015, **15**, 2385–2401.

35 J. H. Hamman, G. M. Enslin and A. F. Kotzé, *BioDrugs*, 2005, **19**, 165–177.

36 N. Marks, F. Stern and A. J. Kastin, *Brain Res. Bull.*, 1976, **1**, 591–3.

37 S. J. Weber, T. J. Abbruscato, E. A. Brownson, A. W. Lipkowski, R. Polt, A. Misicka, R. C. Haaseth, H. Bartosz, V. J. Hruby and T. P. Davis, *J. Pharmacol. Exp. Ther.*, 1993, **266**, 1649–55.

38 C. R. Beddell, R. B. Clark, G. W. Hardy, L. A. Lowe, F. B. Ubatuba, J. R. Vane and S. Wilkinson, *Proc. R. Soc. London. Ser. B. Biol. Sci.*, 1977, **198**, 249–265.

39 A. F. B. Räder, F. Reichart, M. Weinmüller and H. Kessler, *Bioorg. Med. Chem.*, 2018, **26**, 2766–2773.

40 E. M. Taylor, D. A. Otero, W. A. Banks and J. S. O'Brien, *J. Pharmacol. Exp. Ther.*, 2000, **293**, 403–9.

41 J.-F. Yao, H. Yang, Y.-Z. Zhao and M. Xue, *Curr. Drug Metab.*, 2018, **19**, 892–901.

42 N. Qvit, S. J. S. Rubin, T. J. Urban, D. Mochly-Rosen and E. R. Gross, *Drug Discov. Today*, 2017, **22**, 454–462.

43 J. W. Bode, *Acc. Chem. Res.*, 2017, **50**, 2104–2115.

44 T. J. R. Harmand, C. E. Murar and J. W. Bode, *Curr. Opin. Chem. Biol.*, 2014, **22**, 115–121.

45 L. D. Walensky and G. H. Bird, *J. Med. Chem.*, 2014, **57**, 6275–6288.

46 C. J. White and A. K. Yudin, *Nat. Chem.*, 2011, **3**, 509–524.

47 J.-R. Deng, S.-F. Chung, A. S.-L. Leung, W.-M. Yip, B. Yang, M.-C. Choi, J.-F. Cui, K. K.-Y. Kung, Z. Zhang, K.-W. Lo, Y.-C. Leung and M.-K. Wong, *Commun. Chem.*, 2019, **2**, 93.

48 D. P. Nguyen, M. Mahesh, S. J. Elsässer, S. M. Hancock, C. Uttamapinant and J. W. Chin, *J. Am. Chem. Soc.*, 2014, **136**, 2240–2243.

49 P. Arranz-Gibert, B. Guixer, M. Malakoutikhah, M. Muttenthaler, F. Guzmán, M. Teixidó and E. Giralt, *J. Am. Chem. Soc.*, 2015, **137**, 7357–7364.

50 M. A. Karnes, S. L. Schettler, H. M. Werner, A. F. Kurz, W. S. Horne and G. A. Lengyel, *Org. Lett.*, 2016, **18**, 3902–3905.

51 J. Rai, *Chem. Biol. Drug Des.*, 2019, **93**, 724–736.

52 N. Fujii, T. Takata, N. Fujii, K. Aki and H. Sakaue, *BBA - Proteins Proteomics*, 2018, **1866**, 840–847.

53 C. Ollivaux, D. Soyez and J. Toullec, *J. Pept. Sci.*, 2014, **20**, 595–612.

54 P. Wójcik and Ł. Berlicki, *Bioorg. Med. Chem. Lett.*, 2016, **26**, 707–713.

55 P. Arranz-Gibert, S. Ciudad, J. Seco, J. García, E. Giralt and M. Teixidó, *Sci. Rep.*, 2018, **8**, 6446.

56 Y. H. Lau, P. de Andrade, Y. Wu and D. R. Spring, *Chem. Soc. Rev.*, 2015, **44**, 91–102.

57 L. Zhang and J. P. Tam, *J. Am. Chem. Soc.*, 1997, **119**, 2363–2370.

58 S. Bondalapati, M. Jbara and A. Brik, *Nat. Chem.*, 2016, **8**, 407–418.

59 J. P. Tam, J. Xu and K. D. Eom, *Biopolymers*, 2001, **60**, 194–205.

60 P. Dawson, T. Muir, I. Clark-Lewis and S. Kent, *Science (80-.).*, 1994, **266**, 776–779.

61 A. A. Aimetti, R. K. Shoemaker, C.-C. Lin and K. S. Anseth, *Chem. Commun.*, 2010, **46**, 4061.

62 Y. Tian, J. Li, H. Zhao, X. Zeng, D. Wang, Q. Liu, X. Niu, X. Huang, N. Xu and Z. Li, *Chem. Sci.*, 2016, **7**, 3325–3330.

63 J. M. Beierle, W. S. Horne, J. H. van Maarseveen, B. Waser, J. C. Reubi and M. R. Ghadiri, *Angew. Chemie Int. Ed.*, 2009, **48**, 4725–4729.

64 R. A. Turner, A. G. Oliver and R. S. Lokey, *Org. Lett.*, 2007, **9**, 5011–5014.

65 C. E. Schafmeister, J. Po and G. L. Verdine, *J. Am. Chem. Soc.*, 2000, **122**, 5891–5892.

66 S. J. Miller, H. E. Blackwell and R. H. Grubbs, *J. Am. Chem. Soc.*, 1996, **118**, 9606–9614.

67 M. Schmidt, A. Toplak, P. J. Quaedflieg and T. Nuijens, *Curr. Opin. Chem. Biol.*, 2017, **38**, 1–7.

68 G. K. T. Nguyen, S. Wang, Y. Qiu, X. Hemu, Y. Lian and J. P. Tam, *Nat. Chem. Biol.*, 2014, **10**, 732–738.

69 K. S. Harris, T. Durek, Q. Kaas, A. G. Poth, E. K. Gilding, B. F. Conlan, I. Saska, N. L. Daly, N. L. van der Weerden, D. J. Craik and M. A. Anderson, *Nat. Commun.*, 2015, **6**, 10199.

70 I. E. Valverde and T. L. Mindt, 2013, **67**, 262–266.

71 C. Proulx, D. Sabatino, R. Hopewell, J. Spiegel, Y. García Ramos and W. D. Lubell, *Future Med. Chem.*, 2011, **3**, 1139–1164.

72 J. Andrieu, F. Re, L. Russo and F. Nicotra, *J. Drug Target.*, 2019, **27**, 555–565.

73 P. W. Schiller, *Life Sci.*, 2010, **86**, 598–603.

74 G. Guidotti, L. Brambilla and D. Rossi, *Trends Pharmacol. Sci.*, 2017, **38**, 406–424.

75 D. J. Drucker, *Nat. Rev. Drug Discov.*, 2020, **19**, 277–289.

76 Y. Fuchs and H. Steller, *Cell*, 2011, **147**, 742–758.

77 G. Mariño, M. Niso-Santano, E. H. Baehrecke and G. Kroemer, *Nat. Rev. Mol. Cell Biol.*, 2014, **15**, 81–94.

78 L. Ouyang, Z. Shi, S. Zhao, F.-T. Wang, T.-T. Zhou, B. Liu and J.-K. Bao, *Cell Prolif.*, 2012, **45**, 487–498.

79 L. Galluzzi and G. Kroemer, *Cell*, 2008, **135**, 1161–1163.

80 E. Kuranaga, T. Matsunuma, H. Kanuka, K. Takemoto, A. Koto, K. -i. Kimura and M. Miura, *Development*, 2011, **138**, 1493–1499.

81 E. H. Baehrecke, *Nat. Rev. Mol. Cell Biol.*, 2002, **3**, 779–787.

82 I. Lohmann, N. McGinnis, M. Bodmer and W. McGinnis, *Cell*, 2002, **110**, 457–466.

83 E. Moreno, *Nat. Rev. Cancer*, 2008, **8**, 141–147.

84 W. Li and N. E. Baker, *Cell*, 2007, **129**, 1215–1225.

85 T. Lindsten, A. J. Ross, A. King, W.-X. Zong, J. C. Rathmell, H. A. Shiels, E. Ulrich, K. G. Waymire, P. Mahar, K. Frauwirth, Y. Chen, M. Wei, V. M. Eng, D. M. Adelman, M. C. Simon, A. Ma, J. A. Golden, G. Evan, S. J. Korsmeyer, G. R. MacGregor and C. B. Thompson, *Mol. Cell*, 2000, **6**, 1389–1399.

86 S. Elmore, *Toxicol. Pathol.*, 2007, **35**, 495–516.

87 A. Ashkenazi, *Science (80-.).*, 1998, **281**, 1305–1308.

88 J. A. Trapani and M. J. Smyth, *Nat. Rev. Immunol.*, 2002, **2**, 735–747.

89 M. Barry and R. C. Bleackley, *Nat. Rev. Immunol.*, 2002, **2**, 401–409.

90 I. M. Ghobrial, T. E. Witzig and A. A. Adjei, *CA. Cancer J. Clin.*, 2005, **55**, 178–194.

91 C. Scaffidi, S. Fulda, A. Srinivasan, C. Friesen, F. Li, K. Tomaselli, K.-M. Debatin, P. Krammer and M. Peter, *EMBO J.*, 1998, **17**, 1675–1687.

92 A. Gross, J. M. McDonnell and S. J. Korsmeyer, *Genes Dev.*, 1999, **13**, 1899–1911.

93 A. M. Petros, E. T. Olejniczak and S. W. Fesik, *Biochim. Biophys. Acta - Mol. Cell Res.*, 2004, **1644**, 83–94.

94 A. Shamas-Din, J. Kale, B. Leber and D. W. Andrews, *Cold Spring Harb. Perspect. Biol.*, 2013, **5**, a008714–a008714.

95 R. J. Youle and A. Strasser, *Nat. Rev. Mol. Cell Biol.*, 2008, **9**, 47–59.

96 A. Shamas-Din, H. Brahmbhatt, B. Leber and D. W. Andrews, *Biochim. Biophys. Acta - Mol. Cell Res.*, 2011, **1813**, 508–520.

97 A. Gross and S. G. Katz, *Cell Death Differ.*, 2017, **24**, 1348–1358.

98 P. Polcic, P. Jaka and M. Mentel, *Microb. Cell*, 2015, **2**, 74–87.

99 J. M. Bowen, R. J. Gibson, A. G. Cummins and D. M. K. Keefe, *Support. Care Cancer*, 2006, **14**, 713–731.

100 C. R. L. Oudenaarden, R. A. H. van de Ven and P. W. B. Derksen, *J. Cell Sci.*, 2018, **131**, 1–11.

101 M. Sattler, H. Liang, D. Nettesheim, R. P. Meadows, J. E. Harlan, M. Eberstadt, H. S. Yoon, S. B. Shuker, B. S. Chang, A. J. Minn, C. B. Thompson and S. W. Fesik, *Science (80-.).*, 1997, **275**, 983–986.

102 M. G. Hinds, C. Smits, R. Fredericks-Short, J. M. Risk, M. Bailey, D. C. S. Huang and C. L. Day, *Cell Death Differ.*, 2007, **14**, 128–136.

103 A. Letai, M. C. Bassik, L. D. Walensky, M. D. Sorcinelli, S. Weiler and S. J. Korsmeyer, *Cancer Cell*, 2002, **2**, 183–192.

104 L. P. Billen, C. L. Kokoski, J. F. Lovell, B. Leber and D. W. Andrews, *PLoS Biol.*, , DOI:10.1371/journal.pbio.0060147.

105 H. Kim, H.-C. Tu, D. Ren, O. Takeuchi, J. R. Jeffers, G. P. Zambetti, J. J. D. Hsieh and E. H. Y. Cheng, *Mol. Cell*, 2009, **36**, 487–499.

106 K. Raltchev, J. Pipercevic and F. Hagn, *Chem. - A Eur. J.*, 2018, **24**, 5493–5499.

107 E. H. Y. Cheng, D. G. Kirsch, R. J. Clem, R. Ravi, M. B. Kastan, A. Bedi, K. Ueno and M. J. Hardwick, *Science (80-.).*, 1997, **278**, 1966–1968.

108 P. K. Kim, M. G. Annis, P. J. Dlugosz, B. Leber and D. W. Andrews, *Mol. Cell*, 2004, **14**, 523–529.

109 D. Westphal, G. Dewson, P. E. Czabotar and R. M. Kluck, *Biochim. Biophys. Acta - Mol. Cell Res.*, 2011, **1813**, 521–531.

110 I. S. Goping, A. Gross, J. N. Lavoie, M. Nguyen, R. Jemmerson, K. Roth, S. J. Korsmeyer and G. C. Shore, *J. Cell Biol.*, 1998, **143**, 207–215.

111 E. Gavathiotis, M. Suzuki, M. L. Davis, K. Pitter, G. H. Bird, S. G. Katz, H. Tu, H. Kim, E. H.-Y. Cheng, N. Tjandra and L. D. Walensky, *Nature*, 2008, **455**, 1076–1081.

112 E. Gavathiotis, D. E. Reyna, M. L. Davis, G. H. Bird and L. D. Walensky, *Mol. Cell*, 2010, **40**, 481–492.

113 P. E. Czabotar, D. Westphal, G. Dewson, S. Ma, C. Hockings, W. D. Fairlie, E. F. Lee, S. Yao, A. Y. Robin, B. J. Smith, D. C. S. Huang, R. M. Kluck, J. M. Adams and P. M. Colman, *Cell*, 2013, **152**, 519–531.

114 G. Dewson, T. Kratina, P. Czabotar, C. L. Day, J. M. Adams and R. M. Kluck, *Mol. Cell*, 2009, **36**, 696–703.

115 G. Dewson, T. Kratina, H. W. Sim, H. Puthalakath, J. M. Adams, P. M. Colman and R. M. Kluck, *Mol. Cell*, 2008, **30**, 369–380.

116 J. Zha, H. Harada, K. Osipov, J. Jockel, G. Waksman and S. J. Korsmeyer, *J. Biol. Chem.*, 1997, **272**, 24101–24104.

117 J. M. McDonnell, D. Fushman, C. L. Milliman, S. J. Korsmeyer and D. Cowburn, *Cell*, 1999, **96**, 625–634.

118 L. P. Billen, A. Shamas-Din and D. W. Andrews, *Oncogene*, 2008, **27**, 93–104.

119 H. Kim, M. Rafiuddin-Shah, H.-C. Tu, J. R. Jeffers, G. P. Zambetti, J. J. D. Hsieh and E. H. Y. Cheng, *Nat. Cell Biol.*, 2006, **8**, 1348–1358.

120 L. Chen, S. N. Willis, A. Wei, B. J. Smith, J. I. Fletcher, M. G. Hinds, P. M. Colman, C. L. Day, J. M. Adams and D. C. S. Huang, *Mol. Cell*, 2005, **17**, 393–403.

121 T. Shimazu, K. Degenhardt, A. Nur-E-Kamal, J. Zhang, T. Yoshida, Y. Zhang, R. Mathew, E. White and M. Inouye, *Genes Dev.*, 2007, **21**, 929–941.

122 S. N. Willis, J. I. Fletcher, T. Kaufmann, M. F. van Delft, L. Chen, P. E. Czabotar, H. Ierino, E. F. Lee, W. D. Fairlie, P. Bouillet, A. Strasser, R. M. Kluck, J. M. Adams and D. C. S. Huang, *Science (80-.).*, 2007, **315**, 856–859.

123 J. Kale, E. J. Osterlund and D. W. Andrews, *Nat. Publ. Gr.*, 2017, **25**, 65–80.

124 J. F. Lovell, L. P. Billen, S. Bindner, A. Shamas-Din, C. Fradin, B. Leber and D. W. Andrews, *Cell*, 2008, **135**, 1074–1084.

125 F. Llambi, T. Moldoveanu, S. W. G. Tait, L. Bouchier-Hayes, J. Temirov, L. L. McCormick, C. P. Dillon and D. R. Green, *Mol. Cell*, 2011, **44**, 517–531.

126 N. N. Danial and S. J. Korsmeyer, *Cell*, 2004, **116**, 205–219.

127 J. C. Reed, *Cancer Cell*, 2003, **3**, 17–22.

128 A. M. Beekman and L. A. Howell, *ChemMedChem*, 2016, **11**, 802–813.

129 L. Zhang, L. Ming and J. Yu, *Drug Resist. Updat.*, 2007, **10**, 207–217.

130 V. Del Gaizo Moore, J. R. Brown, M. Certo, T. M. Love, C. D. Novina and A. Letai, *J. Clin. Invest.*, 2007, **117**, 112–121.

131 T. N. Chonghaile, J. E. Roderick, C. Glenfield, J. Ryan, S. E. Sallan, L. B. Silverman, M. L. Loh, S. P. Hunger, B. Wood, D. J. DeAngelo, R. Stone, M. Harris, A. Gutierrez, M. A. Kelliher and A. Letai, *Cancer Discov.*, 2014, **4**, 1074–1087.

132 J. Montero and A. Letai, *Cell Death Differ.*, 2018, **25**, 56–64.

133 M. R. Arkin, Y. Tang and J. A. Wells, *Chem. Biol.*, 2014, **21**, 1102–1114.

134 E. Milanesi, P. Costantini, A. Gambalunga, R. Colonna, V. Petronilli, A. Cabrelle, G. Semenzato, A. M. Cesura, E. Pinard and P. Bernardi, *J. Biol. Chem.*, 2006, **281**, 10066–10072.

135 M. F. van Delft, A. H. Wei, K. D. Mason, C. J. Vandenberg, L. Chen, P. E. Czabotar, S. N. Willis, C. L. Scott, C. L. Day, S. Cory, J. M. Adams, A. W. Roberts and D. C. S. Huang, *Cancer Cell*, 2006, **10**, 389–399.

136 T. Oltersdorf, S. W. Elmore, A. R. Shoemaker, R. C. Armstrong, D. J. Augeri, B. A. Belli, M. Bruncko, T. L. Deckwerth, J. Dinges, P. J. Hajduk, M. K. Joseph, S. Kitada, S. J. Korsmeyer, A. R. Kunzer, A. Letai, C. Li, M. J. Mitten, D. G. Nettesheim, S. Ng, P. M. Nimmer, J. M. O'Connor, A. Oleksijew, A. M. Petros, J. C. Reed, W. Shen, S. K. Tahir, C. B. Thompson, K.

J. Tomaselli, B. Wang, M. D. Wendt, H. Zhang, S. W. Fesik and S. H. Rosenberg, *Nature*, 2005, **435**, 677–681.

137 C. Tse, A. R. Shoemaker, J. Adickes, M. G. Anderson, J. Chen, S. Jin, E. F. Johnson, K. C. Marsh, M. J. Mitten, P. Nimmer, L. Roberts, S. K. Tahir, Y. Xiao, X. Yang, H. Zhang, S. Fesik, S. H. Rosenberg and S. W. Elmore, *Cancer Res.*, 2008, **68**, 3421–3428.

138 B. S. X. Lian, A. E. H. Yek, H. Shuvas, S. F. Abdul Rahman, K. Muniandy and N. Mohana-Kumaran, *BMC Res. Notes*, 2018, **11**, 197.

139 ClinicalTrials.gov Date accessed: 15.04.2020, (https://clinicaltrials.gov/ct2/results?cond=&term=ABT-263&cntry=&state=&city=&dist=).

140 D. Yecies, N. E. Carlson, J. Deng and A. Letai, *Blood*, 2010, **115**, 3304–3313.

141 J. Mueller, I. Kretzschmar, R. Volkmer and P. Boisguerin, *Bioconjugate Chem.*, 2008, **19**, 2363–2374.

142 C. Bechara and S. Sagan, *FEBS Lett.*, 2013, **587**, 1693–1702.

143 E. P. Holinger, T. Chittenden and R. J. Lutz, *J. Biol. Chem.*, 1999, **274**, 13298–13304.

144 R. Li, A. L. Boehm, M. B. Miranda, S. Shangary, J. R. Grandis and D. E. Johnson, *Neoplasia*, 2007, **9**, 801–811.

145 J. D. Sadowsky, M. A. Schmitt, H. Lee, N. Umezawa, S. Wang, Y. Tomita and S. H. Gellman, 2005, 11966–11968.

146 E. F. Lee, J. D. Sadowsky, B. J. Smith, P. E. Czabotar, K. J. Peterson-Kaufman, P. M. Colman, S. H. Gellman and W. D. Fairlie, *Angew. Chemie Int. Ed.*, 2009, **48**, 4318–4322.

147 L. D. Walensky, K. Pitter, J. Morash, K. J. Oh, S. Barbuto, J. Fisher, E. Smith, G. L. Verdine and S. J. Korsmeyer, *Mol. Cell*, 2006, **24**, 199–210.

148 L. D. Walensky, A. L. Kung, I. Escher, T. J. Malia, S. Barbuto, R. D. Wright, G. Wagner, G. L. Verdine and S. J. Korsmeyer, *Science (80-.).*, 2004, **305**, 1466–1470.

149 J. Berg, J. Tymoczko and L. Stryer, *Biochemistry*, W H Freeman, New York, 5th edn., 2002.

150 S. Baek, P. S. Kutchukian, G. L. Verdine, R. Huber, T. A. Holak, K. W. Lee and G. M. Popowicz, *J. Am. Chem. Soc.*, 2012, **134**, 103–106.

151 M. L. Stewart, E. Fire, A. E. Keating and L. D. Walensky, *Nat. Chem. Biol.*, 2010, **6**, 595–601.

152 Clinical Programs Aileron, 16.04.2020, https://www.aileronrx.com/clinical-programs/, https://www.aileronrx.com/clinical-programs/, (accessed 16 April 2020).

153 N. Robertson and D. Spring, *Molecules*, 2018, **23**, 959.

154 A. M. Felix, E. P. Heimer, C. T. Wang, T. J. Lambros, A. Fournier, T. F. Mowles, S. Maines, R. M. Campbell, B. B. Wegrzynski and V. Toome, *Int. J. Pept. Protein Res.*, 1988, **32**, 441–54.

155 J. C. Phelan, N. J. Skelton, A. C. Braisted and R. S. McDowell, *J. Am. Chem. Soc.*, 1997,

119, 455–460.

156 M. Moiola, M. G. Memeo and P. Quadrelli, *Molecules*, 2019, **24**, 3654.

157 Y. H. Lau, P. de Andrade, N. Sköld, G. J. McKenzie, A. R. Venkitaraman, C. Verma, D. P. Lane and D. R. Spring, *Org. Biomol. Chem.*, 2014, **12**, 4074–4077.

158 M. Scrima, A. Le Chevalier-Isaad, P. Rovero, A. M. Papini, M. Chorev and A. M. D'Ursi, *European J. Org. Chem.*, 2010, **2010**, 446–457.

159 C. K. Wang and D. J. Craik, *Nat. Chem. Biol.*, 2018, **14**, 417–427.

160 F. M. Brunel and P. E. Dawson, *Chem. Commun.*, 2005, 2552–2554.

161 G. T. Perell, R. L. Staebell, M. Hairani, A. Cembran and W. C. K. Pomerantz, *ChemBioChem*, 2017, **18**, 1836–1844.

162 Y. Wang and D. H.-C. Chou, *Angew. Chemie Int. Ed.*, 2015, **54**, 10931–10934.

163 Y. Wang, B. J. Bruno, S. Cornillie, J. M. Nogieira, D. Chen, T. E. Cheatham, C. S. Lim and D. H.-C. Chou, *Chem. - A Eur. J.*, 2017, **23**, 7087–7092.

164 A. M. Spokoyny, Y. Zou, J. J. Ling, H. Yu, Y.-S. Lin and B. L. Pentelute, *J. Am. Chem. Soc.*, 2013, **135**, 5946–5949.

165 H. Jo, N. Meinhardt, Y. Wu, S. Kulkarni, X. Hu, K. E. Low, P. L. Davies, W. F. DeGrado and D. C. Greenbaum, *J. Am. Chem. Soc.*, 2012, **134**, 17704–17713.

166 X. Qin, X. Shi, L. Tu, Y. Ma, Z. Zhou, R. Zhao, M. Zhan, F. Yin and Z. Li, *Chem. Commun.*, 2019, **55**, 4198–4201.

167 E. Y. L. Hui, B. Rout, Y. S. Tan, C. S. Verma, K.-P. Chan and C. W. Johannes, *Org. Biomol. Chem.*, 2018, **16**, 389–392.

168 G. H. Bird, E. Mazzola, K. Opoku-Nsiah, M. A. Lammert, M. Godes, D. S. Neuberg and L. D. Walensky, *Nat. Chem. Biol.*, 2016, **12**, 845–852.

169 G. H. Bird, E. Gavathiotis, J. L. LaBelle, S. G. Katz and L. D. Walensky, *ACS Chem. Biol.*, 2014, **9**, 831–837.

170 A. J. Huhn, R. M. Guerra, E. P. Harvey, G. H. Bird and L. D. Walensky, *Cell Chem. Biol.*, 2016, **23**, 1123–1134.

171 E. P. Harvey, H.-S. Seo, R. M. Guerra, G. H. Bird, S. Dhe-Paganon and L. D. Walensky, *Structure*, 2018, **26**, 153–160.

172 J. Iegre, N. S. Ahmed, J. S. Gaynord, Y. Wu, K. M. Herlihy, Y. S. Tan, M. E. Lopes-Pires, R. Jha, Y. H. Lau, H. F. Sore, C. Verma, D. H. O' Donovan, N. Pugh and D. R. Spring, *Chem. Sci.*, 2018, **9**, 4638–4643.

173 C. M. Fadzen, J. M. Wolfe, C.-F. Cho, E. A. Chiocca, S. E. Lawler and B. L. Pentelute, *J. Am. Chem. Soc.*, 2017, **139**, 15628–15631.

174 C. M. Grison, G. M. Burslem, J. A. Miles, L. K. A. Pilsl, D. J. Yeo, Z. Imani, S. L. Warriner, M. E. Webb and A. J. Wilson, *Chem. Sci.*, 2017, **8**, 5166–5171.

175 A. Muppidi, K. Doi, C. P. Ramil, H.-G. Wang and Q. Lin, *Tetrahedron*, 2014, **70**, 7740–

7745.

176 D. Bléger and S. Hecht, *Angew. Chemie Int. Ed.*, 2015, **54**, 11338–11349.

177 M. Hammerich, C. Schütt, C. Stähler, P. Lentes, F. Röhricht, R. Höppner and R. Herges, *J. Am. Chem. Soc.*, 2016, **138**, 13111–13114.

178 A. A. Beharry and G. A. Woolley, *Chem. Soc. Rev.*, 2011, **40**, 4422.

179 M. N. Roberts, J. K. Nagle, M. B. Majewski, J. G. Finden, N. R. Branda and M. O. Wolf, *Inorg. Chem.*, 2011, **50**, 4956–4966.

180 C. Carling, J. Boyer and N. R. Branda, *J. Am. Chem. Soc.*, 2009, **131**, 10838–10839.

181 J. Croissant, M. Maynadier, A. Gallud, H. Peindy N'Dongo, J. L. Nyalosaso, G. Derrien, C. Charnay, J.-O. Durand, L. Raehm, F. Serein-Spirau, N. Cheminet, T. Jarrosson, O. Mongin, M. Blanchard-Desce, M. Gary-Bobo, M. Garcia, J. Lu, F. Tamanoi, D. Tarn, T. M. Guardado-Alvarez and J. I. Zink, *Angew. Chemie Int. Ed.*, 2013, **52**, 13813–13817.

182 W. Szymański, J. M. Beierle, H. A. V. Kistemaker, W. A. Velema and B. L. Feringa, *Chem. Rev.*, 2013, **113**, 6114–6178.

183 G. Hartley, *Nature*, 1937, **14**, 281.

184 H. Fliegl, A. Köhn, C. Hättig and R. Ahlrichs, *J. Am. Chem. Soc.*, 2003, **125**, 9821–9827.

185 J. M. Robertson, *J. Chem. Soc.*, 1939, 232–236.

186 H. M. D. Bandara and S. C. Burdette, *Chem. Soc. Rev.*, 2012, **41**, 1809–1825.

187 G. Angelini, N. Canilho, M. Emo, M. Kingsley and C. Gasbarri, *J. Org. Chem.*, 2015, **80**, 7430–7434.

188 M. Zhu and H. Zhou, *Org. Biomol. Chem.*, 2018, **16**, 8434–8445.

189 D. Bléger, J. Schwarz, A. M. Brouwer and S. Hecht, *J. Am. Chem. Soc.*, 2012, **134**, 20597–20600.

190 U. Kusebauch, S. A. Cadamuro, H.-J. Musiol, M. O. Lenz, J. Wachtveitl, L. Moroder and C. Renner, *Angew. Chemie Int. Ed.*, 2006, **45**, 7015–7018.

191 J. Kuil, L. T. M. van Wandelen, N. J. de Mol and R. M. J. Liskamp, *J. Pept. Sci.*, 2009, **15**, 685–691.

192 F. Zhang, O. Sadovski and G. A. Woolley, *ChemBioChem*, 2008, **9**, 2147–2154.

193 N. Pozhidaeva, M.-E. Cormier, A. Chaudhari and G. A. Woolley, *Bioconjug. Chem.*, 2004, **15**, 1297–1303.

194 L. Chi, O. Sadovski and G. A. Woolley, *Bioconjug. Chem.*, 2006, **17**, 670–676.

195 A. A. Beharry, O. Sadovski and G. A. Woolley, *Org. Biomol. Chem.*, 2008, **6**, 4323.

196 N. Nishimura, T. Sueyoshi, H. Yamanaka, E. Imai, S. Yamamoto and S. Hasegawa, *Bull. Chem. Soc. Jpn.*, 1976, **49**, 1381–1387.

197 M. Han, D. Ishikawa, T. Honda, E. Ito and M. Hara, *Chem. Commun.*, 2010, **46**, 3598–3600.

198 C. L. Forber, E. C. Kelusky, N. J. Bunce and M. C. Zerner, *J. Am. Chem. Soc.*, 1985, **107**, 5884–5890.

199 O. Sadovski, A. A. Beharry, F. Zhang and G. A. Woolley, *Angew. Chemie Int. Ed.*, 2009, **48**, 1484–1486.

200 A. A. Beharry, O. Sadovski and G. A. Woolley, *J. Am. Chem. Soc.*, 2011, **133**, 19684–19687.

201 S. Samanta, T. M. McCormick, S. K. Schmidt, D. S. Seferos and G. A. Woolley, *Chem. Commun.*, 2013, **49**, 10314.

202 C. Boulègue, M. Löweneck, C. Renner and L. Moroder, *ChemBioChem*, 2007, **8**, 591–594.

203 S. Samanta, A. Babalhavaeji, M. Dong and G. A. Woolley, *Angew. Chemie Int. Ed.*, 2013, **52**, 14127–14130.

204 M. Dong, A. Babalhavaeji, C. V Collins, K. Jarrah, O. Sadovski, Q. Dai and G. A. Woolley, *J. Am. Chem. Soc.*, 2017, **139**, 13483–13486.

205 C. Knie, M. Utecht, F. Zhao, H. Kulla, S. Kovalenko, A. M. Brouwer, P. Saalfrank, S. Hecht and D. Bléger, *Chem. - A Eur. J.*, 2014, **20**, 16492–16501.

206 S. Samanta, A. A. Beharry, O. Sadovski, T. M. McCormick, A. Babalhavaeji, V. Tropepe and G. A. Woolley, *J. Am. Chem. Soc.*, 2013, **135**, 9777–9784.

207 R. Siewertsen, H. Neumann, B. Buchheim-Stehn, R. Herges, C. Näther, F. Renth and F. Temps, *J. Am. Chem. Soc.*, 2009, **131**, 15594–15595.

208 S. Samanta, C. Qin, A. J. Lough and G. A. Woolley, *Angew. Chemie Int. Ed.*, 2012, **51**, 6452–6455.

209 J. R. Kumita, O. S. Smart and G. A. Woolley, *Proc. Natl. Acad. Sci.*, 2000, **97**, 3803–3808.

210 Z. Zhang, D. C. Burns, J. R. Kumita, O. S. Smart and G. A. Woolley, *Bioconjug. Chem.*, 2003, **14**, 824–829.

211 S. Kneissl, E. J. Loveridge, C. Williams, M. P. Crump and R. K. Allemann, *ChemBioChem*, 2008, **9**, 3046–3054.

212 P. Wysoczanski, R. J. Mart, E. J. Loveridge, C. Williams, S. B. M. Whittaker, M. P. Crump and R. K. Allemann, *Biomol. NMR Assign.*, 2013, **7**, 187–191.

213 P. Wysoczanski, R. J. Mart, E. J. Loveridge, C. Williams, S. B. M. Whittaker, M. P. Crump and R. K. Allemann, *J. Am. Chem. Soc.*, 2012, **134**, 7644–7647.

214 R. J. Mart, R. J. Errington, C. L. Watkins, S. C. Chappell, M. Wiltshire, A. T. Jones, P. J. Smith and R. K. Allemann, *Mol. Biosyst.*, 2013, **9**, 2597.

215 B. Scrosati and C. A. Vincent, *Int. Union Pure Appl. Chem.*

216 L. He, E. J. Sayers, P. Watson and A. T. Jones, *Sci. Rep.*, 2018, **8**, 7318.

217 T. Fricke, R. J. Mart, C. L. Watkins, M. Wiltshire, R. J. Errington, P. J. Smith, A. T. Jones and R. K. Allemann, *Bioconjug. Chem.*, 2011, **22**, 1763–1767.

218 X. Ma, Q. Zhang, Q. Zhu, W. Liu, Y. Chen, R. Qiu, B. Wang, Z. Yang, H. Li, Y. Lin, Y. Xie, R. Shen, S. Chen, Z. Wang, Y. Chen, J. Guo, L. Chen, X. Zhao, Z. Dong and Y. G. Liu, *Mol. Plant.*, 2015, **8**, 1274–1284.

219 T. M. S. Tang, D. Cardella, A. J. Lander, X. Li, J. S. Escudero, Y.-H. Tsai and L. Y. P. Luk, *Chem. Sci.*, , DOI:10.1039/D0SC02023K.

220 L. Włodek and J. Czubak, *Acta Biochim. Pol.*, 1984, **31**, 279–88.

221 Y. Amino, Y. Takino, M. Kaneko, F. Ookura, M. Yamamoto, T. Kashiwagi and K. Iwasaki, *Chem. Pharm. Bull. (Tokyo).*, 2016, **64**, 1681–1691.

222 C. A. Lewis and R. Wolfenden, *Biochemistry*, 2011, **50**, 7259–7264.

223 T. v. Brennan and S. Clarke, *Int. J. Pept. Protein Res.*, 2009, **45**, 547–553.

224 S. Tsuda, H. Nishio and T. Yoshiya, *Chem. Commun.*, 2018, **54**, 8861–8864.

225 Y. Shao and S. B. H. Kent, *Chem. Biol.*, 1997, **4**, 187–194.

226 J. Dolan, *ACE HPLC columns*, 2009, **6628**, 1–20.

227 A. L. Edwards, F. Wachter, M. Lammert, A. J. Huhn, J. Luccarelli, G. H. Bird and L. D. Walensky, *ACS Chem. Biol.*, 2015, **10**, 2149–2157.

228 S. Shangary, C. L. Oliver, T. S. Tillman, M. Cascio and D. E. Johnson, *Mol. Cancer Ther.*, 2004, **3**, 1343–54.

229 X. Shi, R. Zhao, Y. Jiang, H. Zhao, Y. Tian, Y. Jiang, J. Li, W. Qin, F. Yin and Z. Li, *Chem. Sci.*, 2018, **9**, 3227–3232.

230 G. Zhang, F. Barragan, K. Wilson, N. Levy, A. Herskovits, M. Sapozhnikov, Y. Rodríguez, L. Kelmendi, H. Alkasimi, H. Korsmo, M. Chowdhury and G. Gerona-Navarro, *Angew. Chemie Int. Ed.*, 2018, **57**, 17073–17078.

231 J. E. Swedberg, L. V Nigon, J. C. Reid, S. J. de Veer, C. M. Walpole, C. R. Stephens, T. P. Walsh, T. K. Takayama, J. D. Hooper, J. A. Clements, A. M. Buckle and J. M. Harris, *Chem. Biol.*, 2009, **16**, 633–643.

232 M. Góngora-Benítez, J. Tulla-Puche, M. Paradís-Bas, O. Werbitzky, M. Giraud and F. Albericio, *Biopolymers*, 2011, **96**, 69–80.

233 Y. Lee, A. Erazo-Oliveras and J. Pellois, *ChemBioChem*, 2010, **11**, 325–330.

234 T. M. Postma, M. Giraud and F. Albericio, *Org. Lett.*, 2012, **14**, 5468–5471.

235 S. Kneissl, E. J. Loveridge, C. Williams, M. P. Crump and R. K. Allemann, 2008, 3046–3054.

236 S. Kneissl, *PhD Diss.*, 2009, 231.

237 L. Guerrero, O. S. Smart, C. J. Weston, D. C. Burns, G. A. Woolley and R. K. Allemann, *Angew. Chemie Int. Ed.*, 2005, **44**, 7778–7782.

238 T. B. Acton, R. Xiao, S. Anderson, J. Aramini, W. A. Buchwald, C. Ciccosanti, K. Conover, J. Everett, K. Hamilton, Y. J. Huang, H. Janjua, G. Kornhaber, J. Lau, D. Y. Lee, G. Liu, M. Maglaqui, L. Ma, L. Mao, D. Patel, P. Rossi, S. Sahdev, R. Shastry, G. V. T. Swapna, Y.

Tang, S. Tong, D. Wang, H. Wang, L. Zhao and G. T. Montelione, in *Methods in enzymology*, Elsevier Inc., 1st edn., 2011, vol. 493, pp. 21–60.

239 M. P. Williamson, in *Modern Magnetic Resonance*, Springer International Publishing, Cham, 2018, pp. 995–1012.

240 D. P. Frueh, *Prog. Nucl. Magn. Reson. Spectrosc.*, 2014, **78**, 47–75.

241 M. P. Foster, C. A. McElroy and C. D. Amero, *Biochemistry*, 2007, **46**, 331–340.

242 S. Pescina, C. Ostacolo, I. M. Gomez-Monterrey, M. Sala, A. Bertamino, F. Sonvico, C. Padula, P. Santi, A. Bianchera and S. Nicoli, *J. Control. Release*, 2018, **284**, 84–102.

243 K. Takayama, I. Nakase, H. Michiue, T. Takeuchi, K. Tomizawa, H. Matsui and S. Futaki, *J. Control. Release*, 2009, **138**, 128–133.

244 R. Rezgui, K. Blumer, G. Yeoh-Tan, A. J. Trexler and M. Magzoub, *Biochim. Biophys. Acta - Biomembr.*, 2016, **1858**, 1499–1506.

245 L. K. Tamm and X. Han, *Biosci. Rep.*, 2000, **20**, 501–518.

246 D. V. Zhelev, N. Stoicheva, P. Scherrer and D. Needham, *Biophys. J.*, 2001, **81**, 285–304.

247 J. S. Wadia, R. V. Stan and S. F. Dowdy, *Nat. Med.*, 2004, **10**, 310–315.

248 Y. Lee, G. Johnson, G. C. Peltier and J. Pellois, *Biochim. Biophys. Acta - Gen. Subj.*, 2011, **1810**, 752–758.

249 J. L. LaBelle, S. G. Katz, G. H. Bird, E. Gavathiotis, M. L. Stewart, C. Lawrence, J. K. Fisher, M. Godes, K. Pitter, A. L. Kung and L. D. Walensky, *J. Clin. Invest.*, 2012, **122**, 2018–2031.

250 E. J. Sayers, K. Cleal, N. G. Eissa, P. Watson and A. T. Jones, *J. Control. Release*, 2014, **195**, 55–62.

VI. **Appendix**

1. Analysis of Cysteine-Crosslinker by Mass Spectrometry

48:

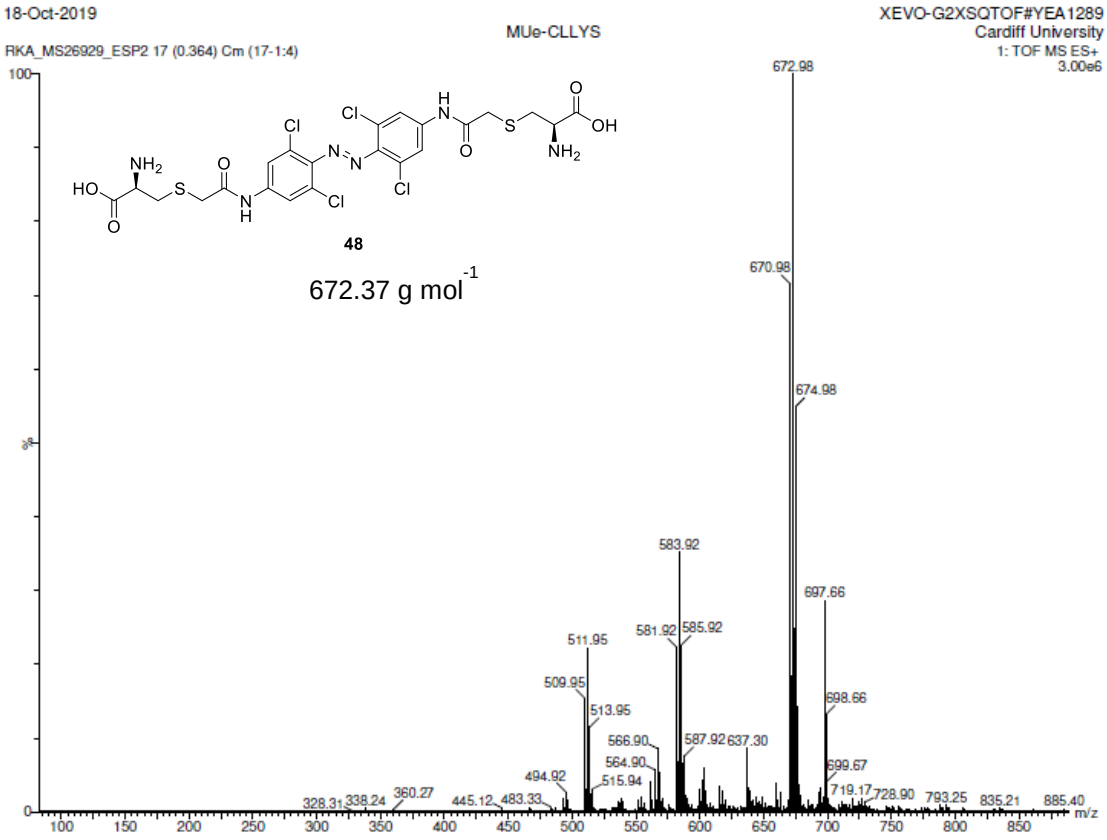

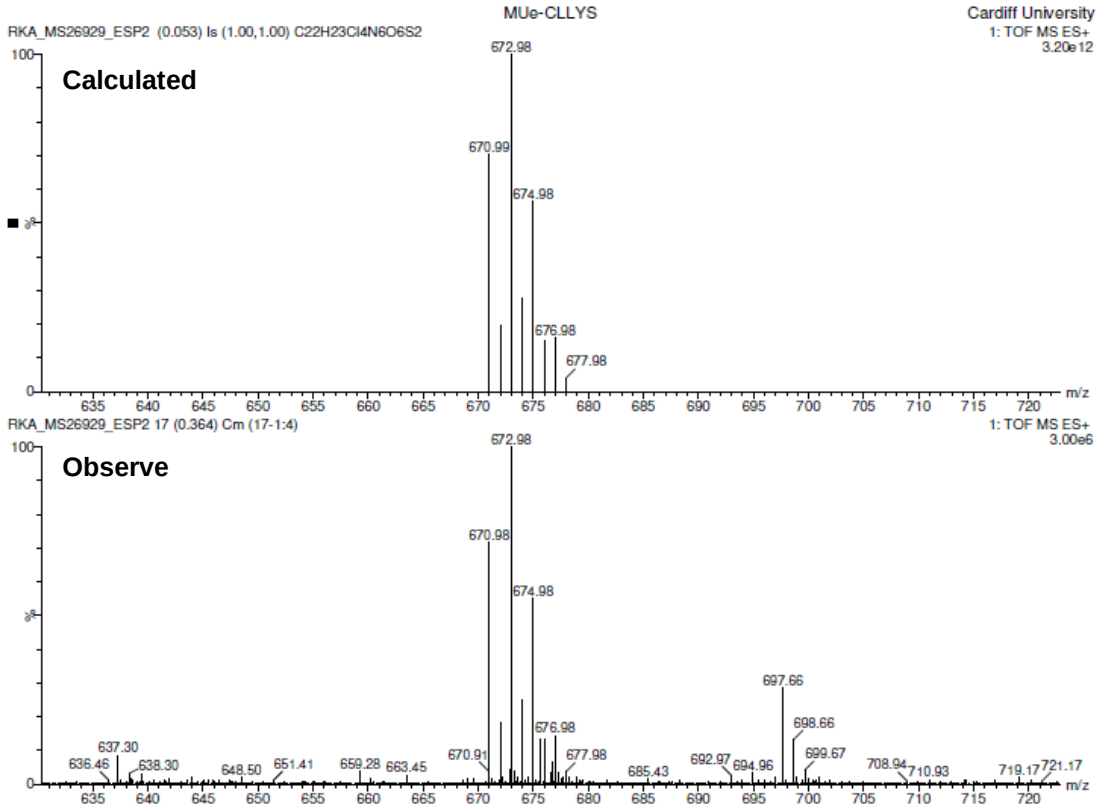

2. Proton-NMR Comparison of the Linkers after the Halide Exchange

36 vs. **38**

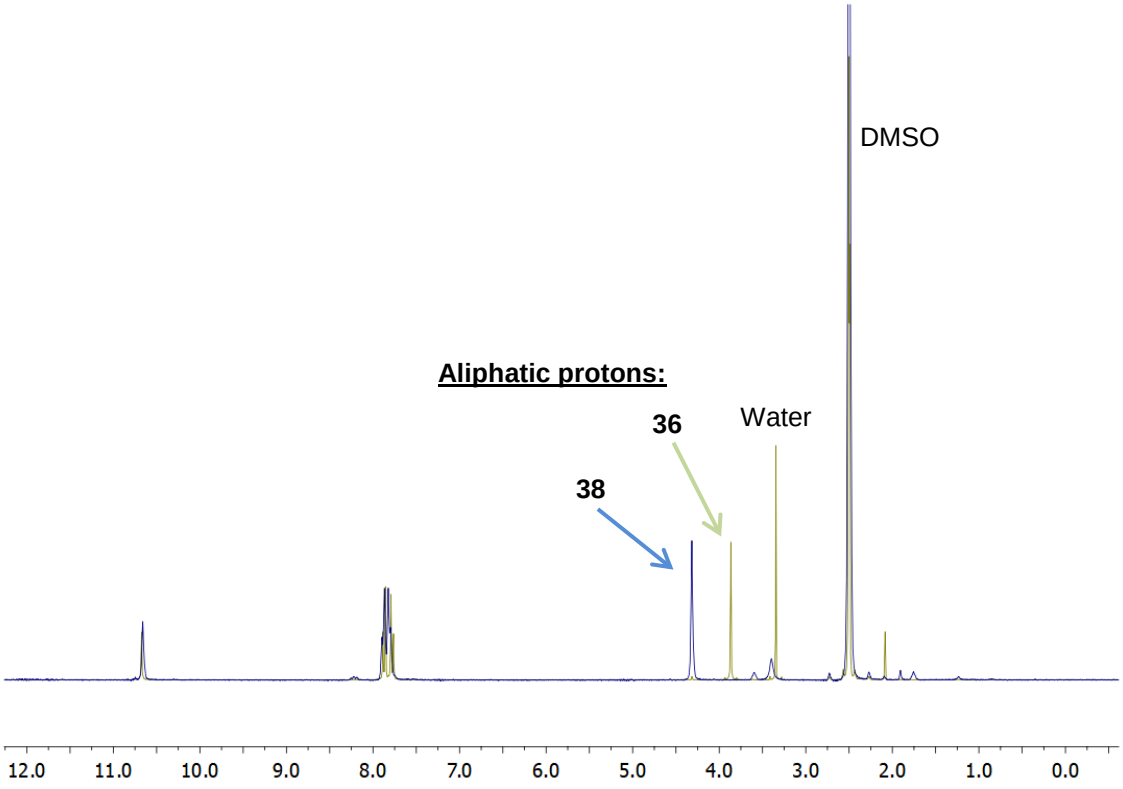

33 vs. **49**

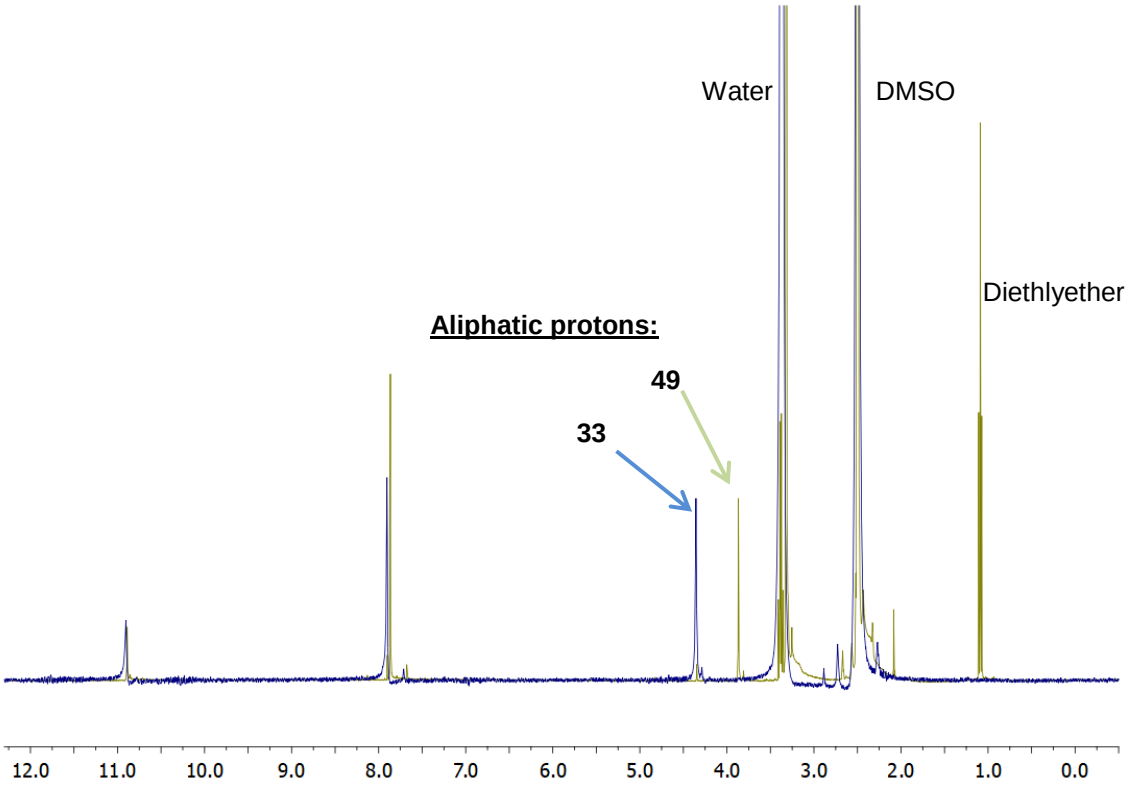

3. Analysis of the Produced Peptide by Recombinant Expression

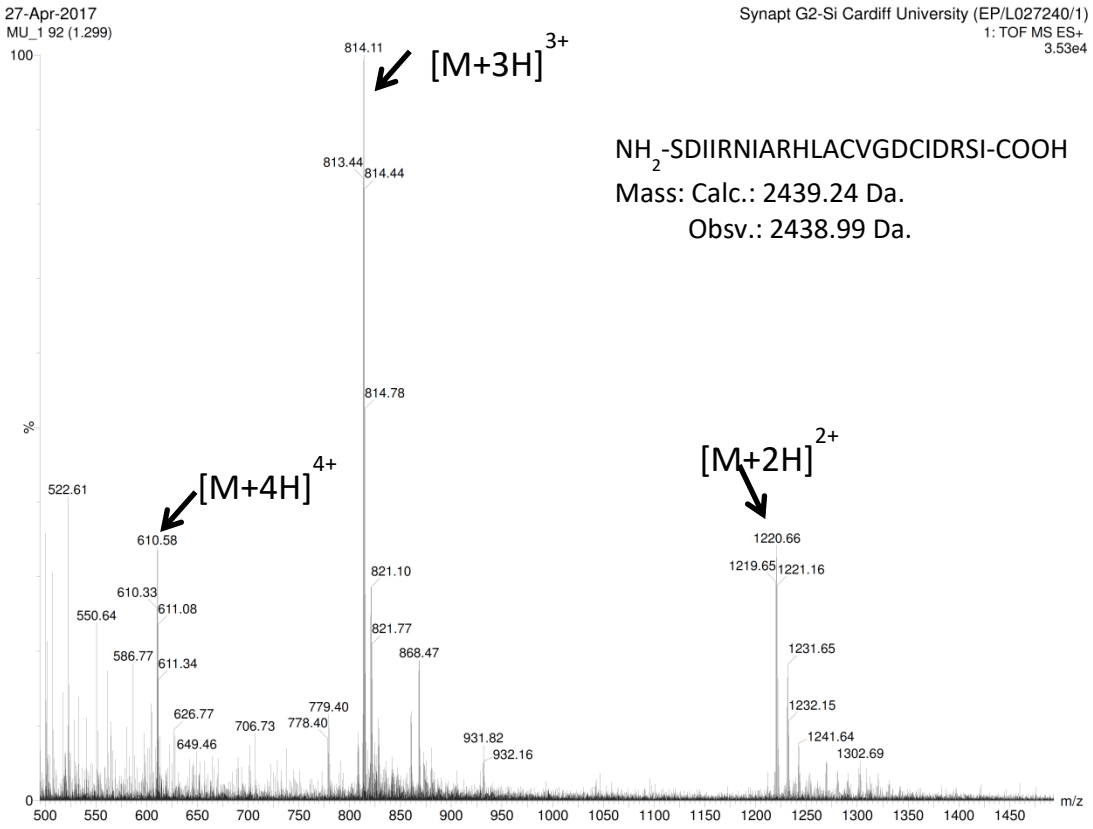

NH_2-SDIIRNIARHLACVGDCIDRSI-COOH

Mass: Calc.: 2439.24 Da.

Obsv.: 2438.99 Da.

4. Stapling Screening Reaction using the 12-mer Peptide

Peptide (eq.)	Peptide (mL)	Linker **38** (eq.)	Linker **38** ((µL)	Buffer (mL)
1	0.25	1	5	0.745
1	0.25	2	10	0.740
1	0.25	3	15	0.735
1	0.25	4	20	0.730

Precipitate-sample: Peptide:Crosslinker (1:1)

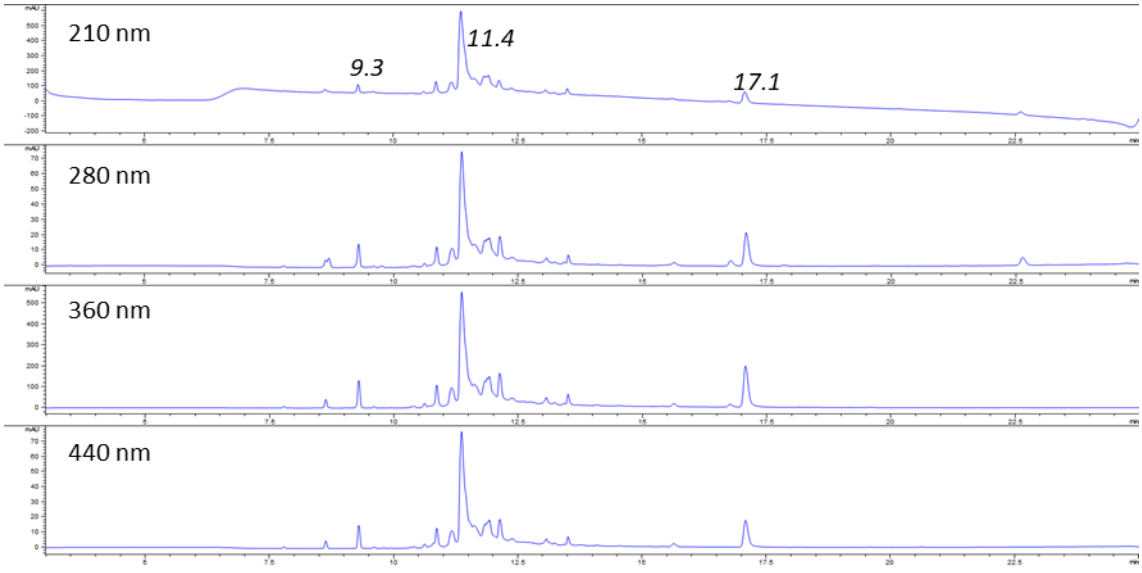

Filtrate-sample: Peptide:Crosslinker (1:1)

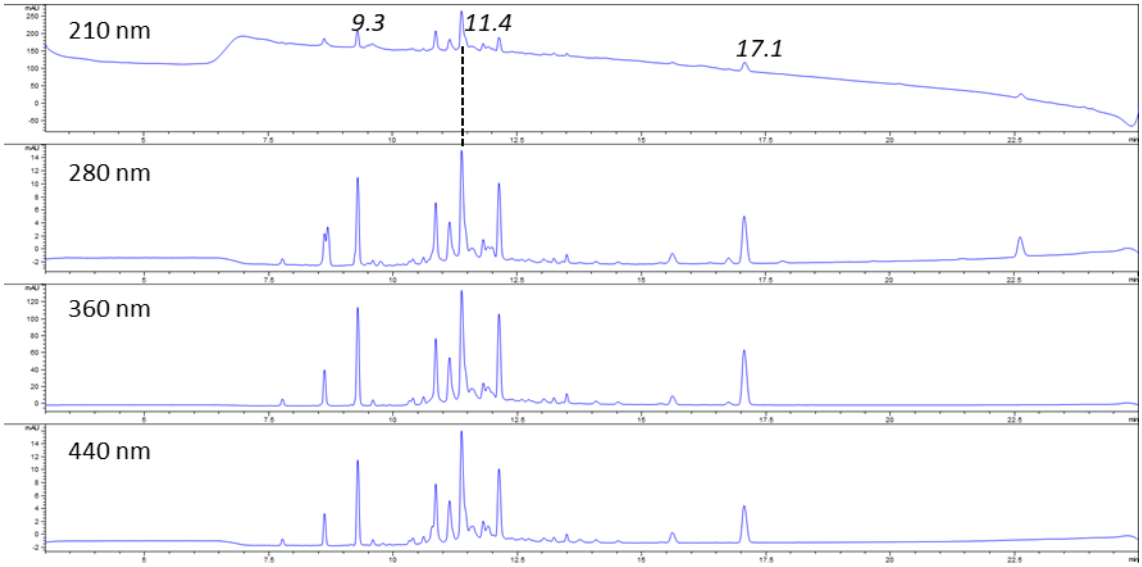

Precipitate-sample: Peptide:Crosslinker (1:2)

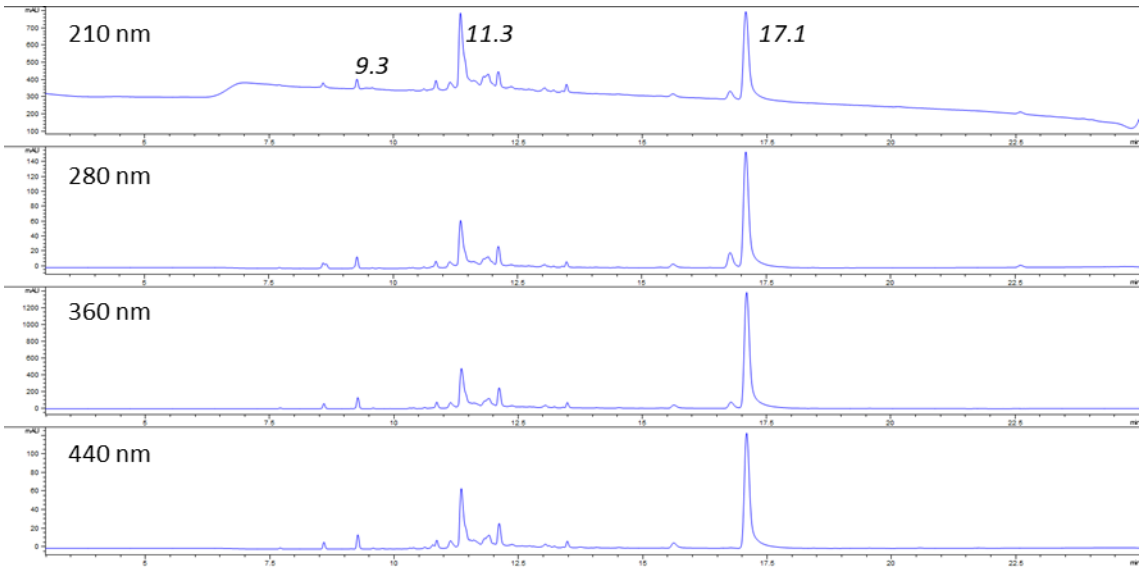

Filtrate-sample: Peptide:Crosslinker (1:2)

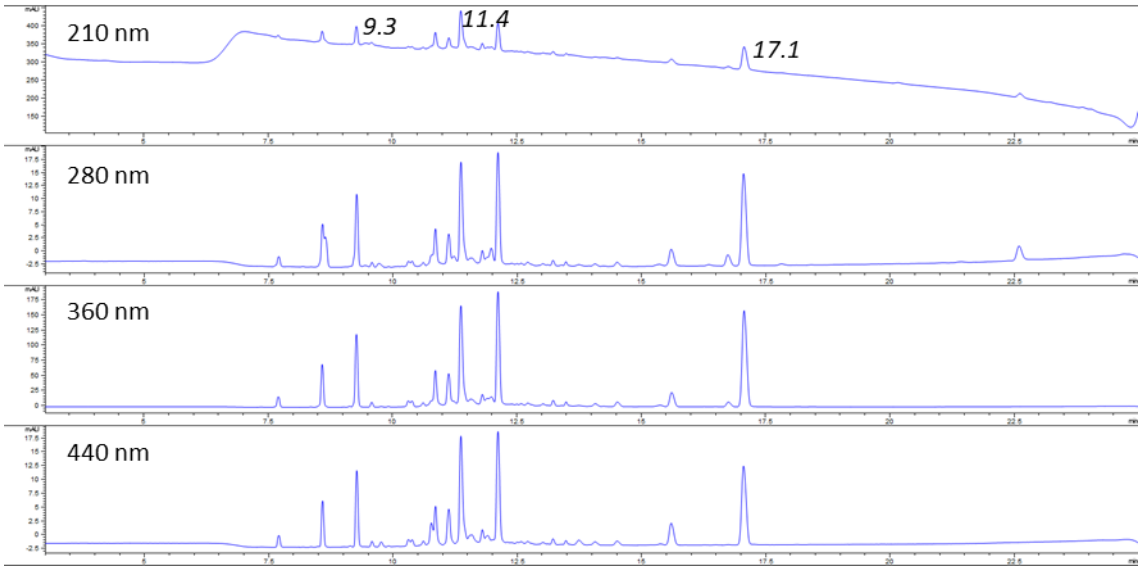

Precipitate-sample: Peptide:Crosslinker (1:3)

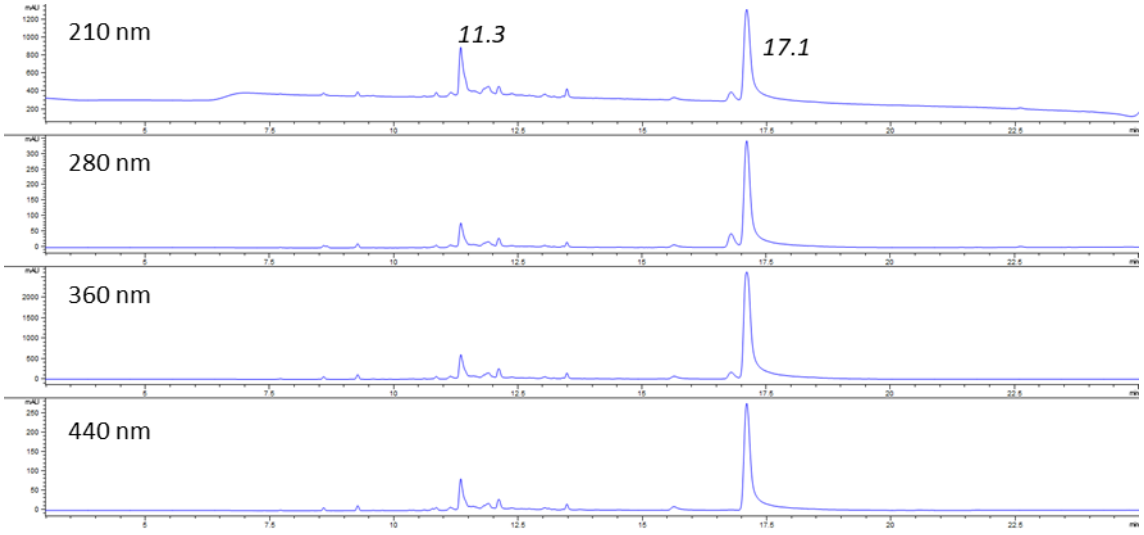

Filtrate-sample: Peptide:Crosslinker (1:3)

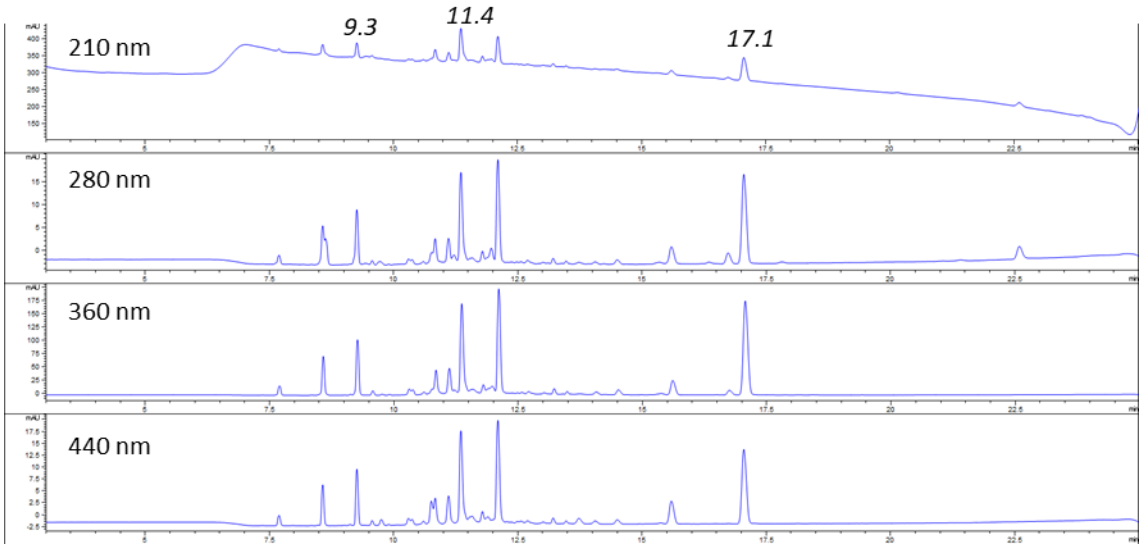

Precipitate-sample: Peptide:Crosslinker (1:4)

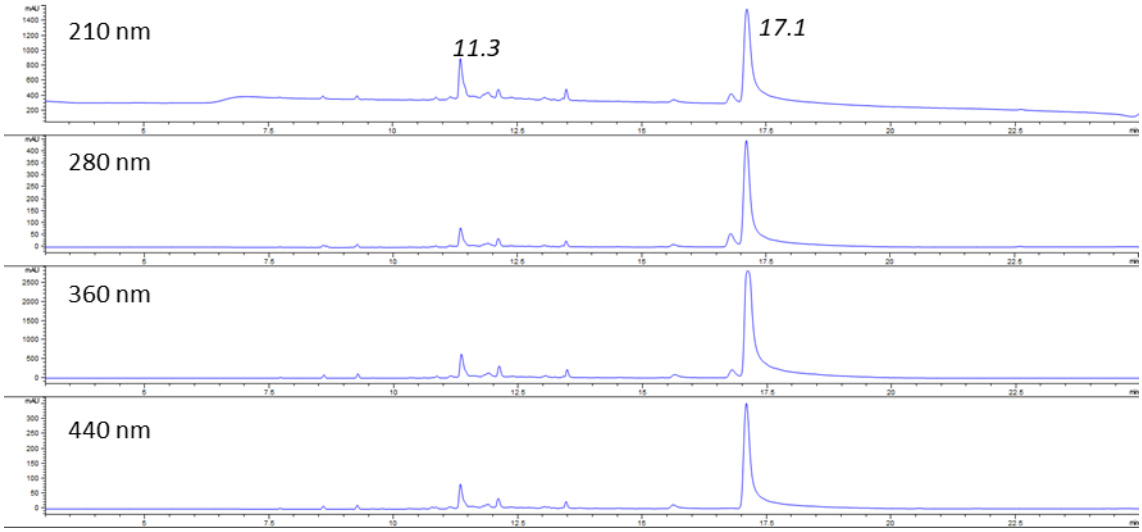

Filtrate-sample: Peptide:Crosslinker (1:4)

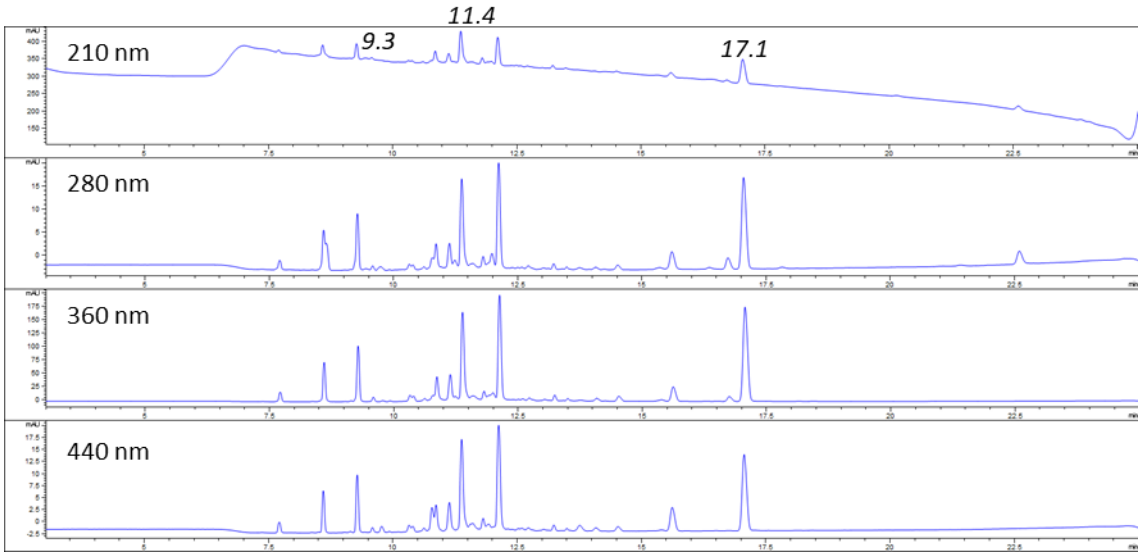

5. Analysis of the Stapled Bid-Peptide

37-stapled GL-Bid$^{i,i+4}$-NH_2:

Calculated mass: 2976.00 Da. Run carried out without any wavelength detection.

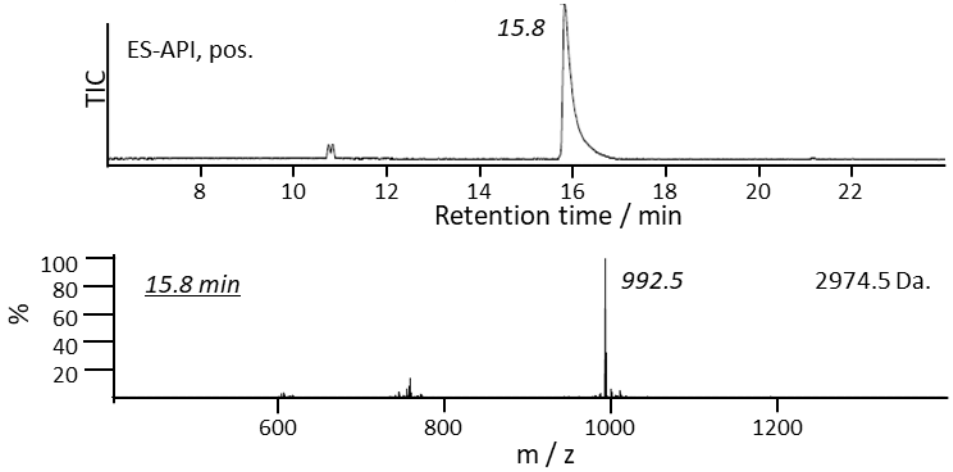

6. Analysis of the Stapled and Fluorescein-Labelled Bid-Peptides

33- and **37**-stapled (5)[FAM]-GL-Bid$^{i,i+4}$-NH_2

37-stapled peptide: Calculated mass: 3334.32 Da.

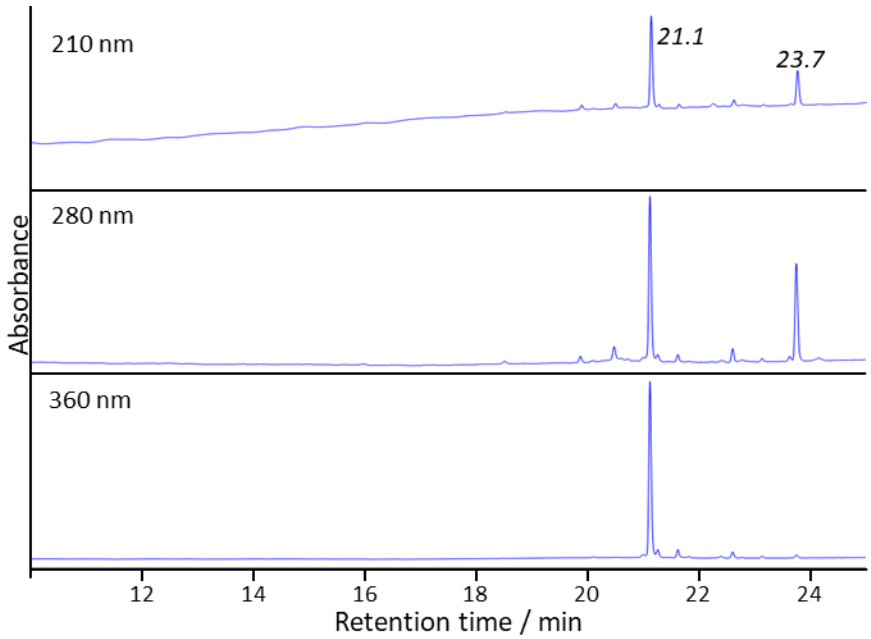

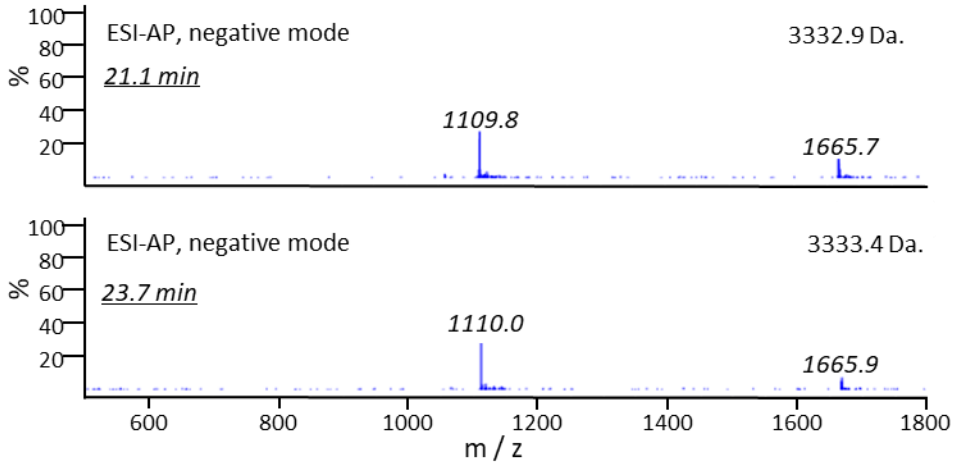

33-stapled peptide: Calculated mass: 3311.34 Da.

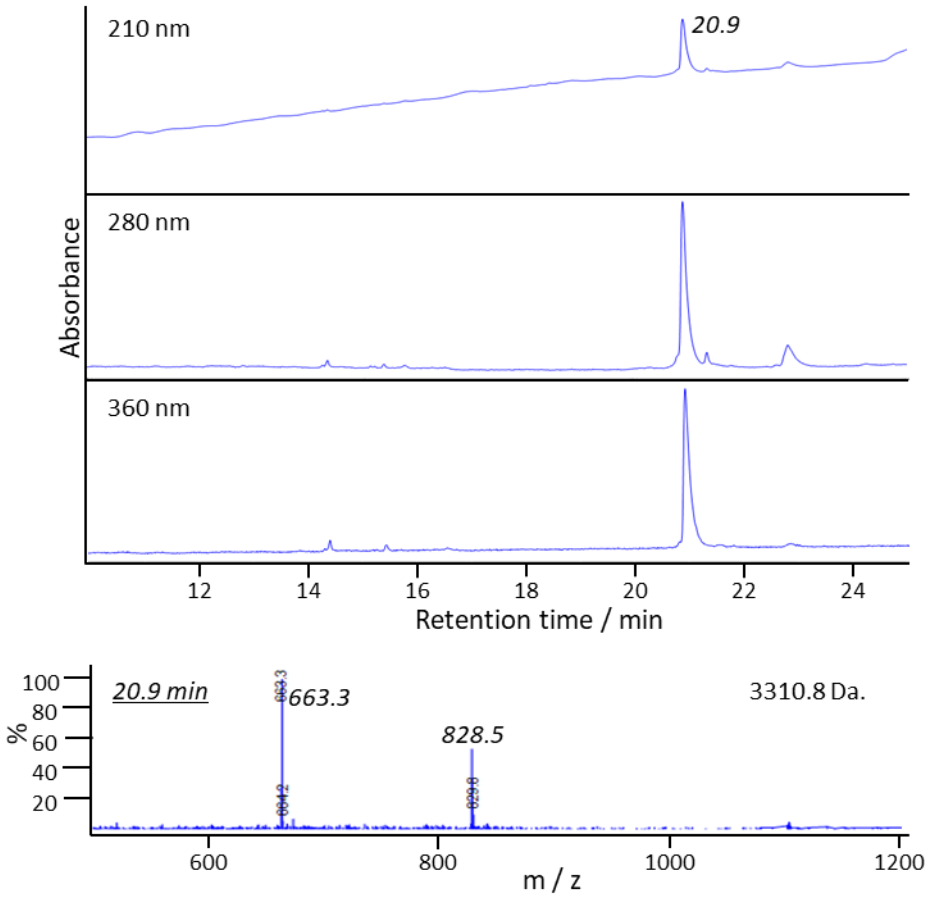

7. Analysis of the Stapled Bim-Peptide

33-stapled Bim$^{i,i+4}$-NH:

Calculated mass: 2991.02 Da.

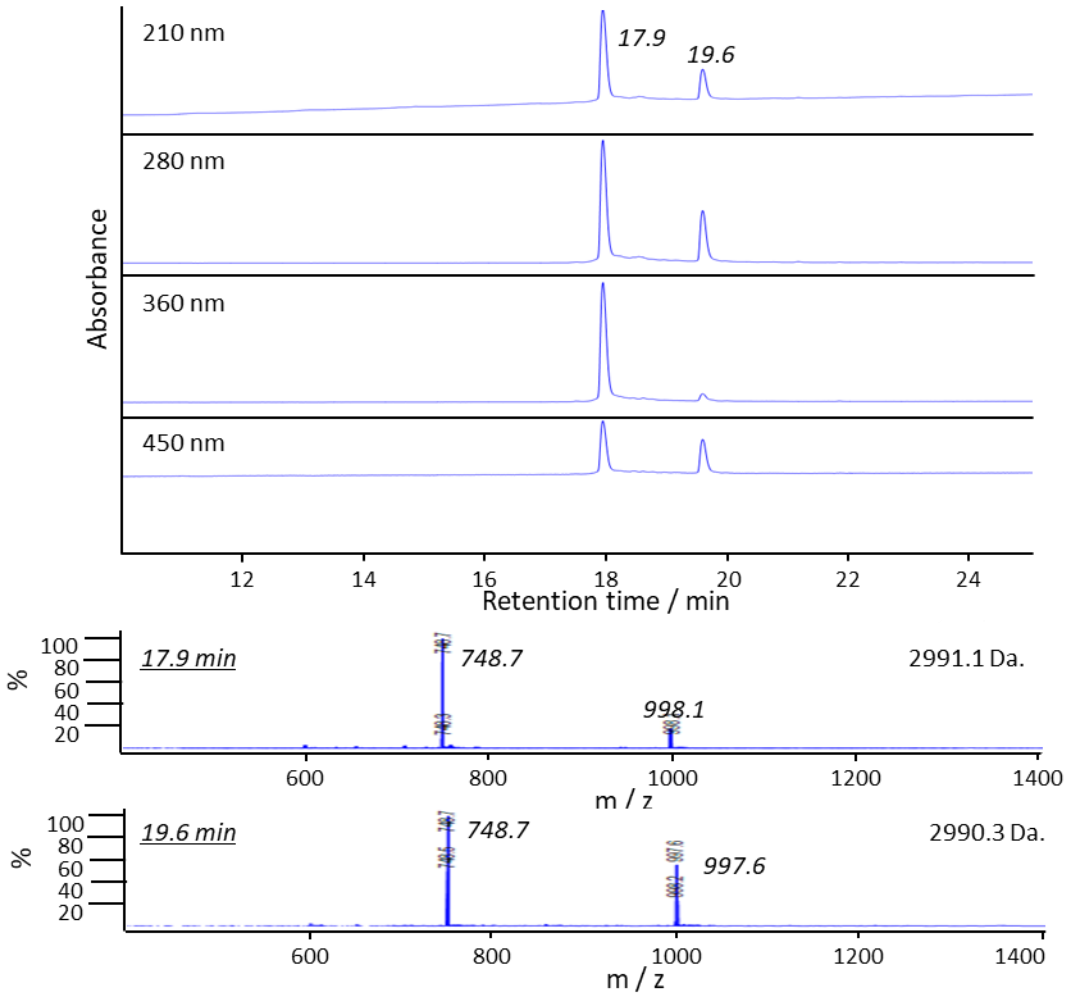

8. Analysis of the Stapled and Fluorescein-Labelled [PEG]-Bak-Peptide

33-stapled (5)[FAM]-$[PEG]_3$-$Bak^{i,i+11}$-NH_2:

Calculated mass: 2811.47 Da.

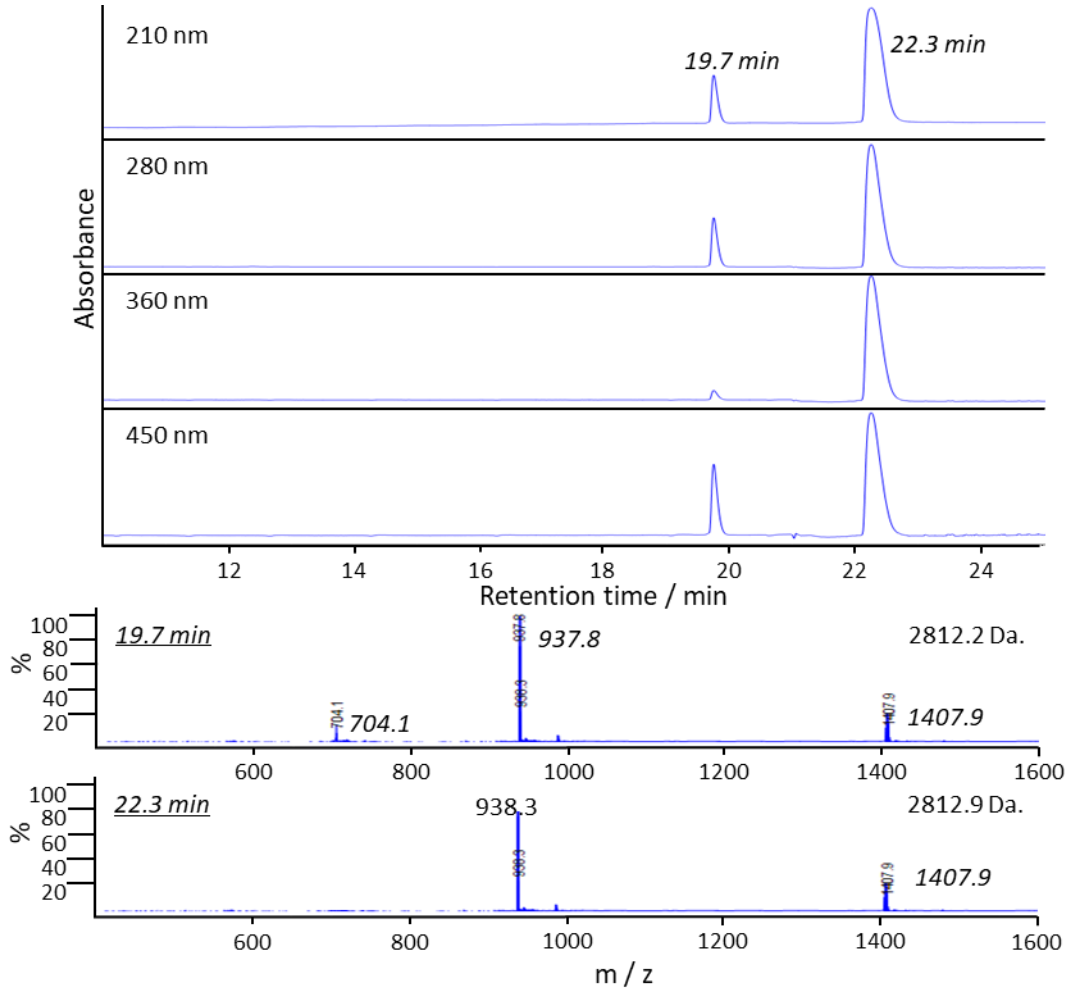

9. Analysis of Fmoc-Cys(STmp)-OH by LC-MS

Calculated mass: 541.6, Observed mass: 541.2. Sample was eluted over a linear gradient of 5% to 95% acetonitrile:water (+0.1% formic acid) over 30 min. Signal at 28 min results from contamination of the LC-MS system.

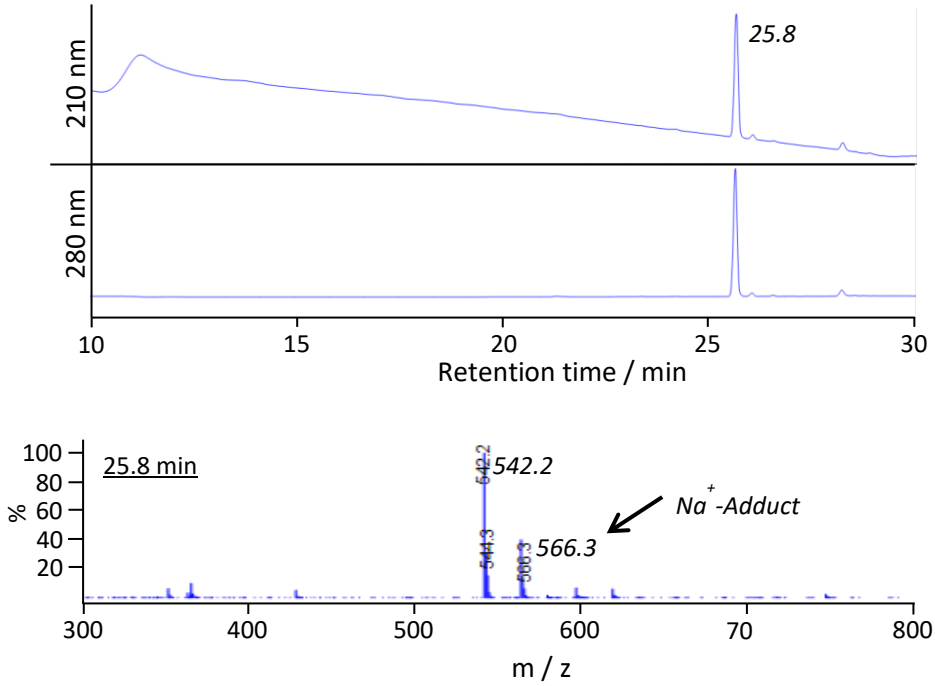

10. Protein-NMR Experiments

[PEG]$_3$-Bak$^{i,i+11}$-NH$_2$ and Bcl-x$_L$

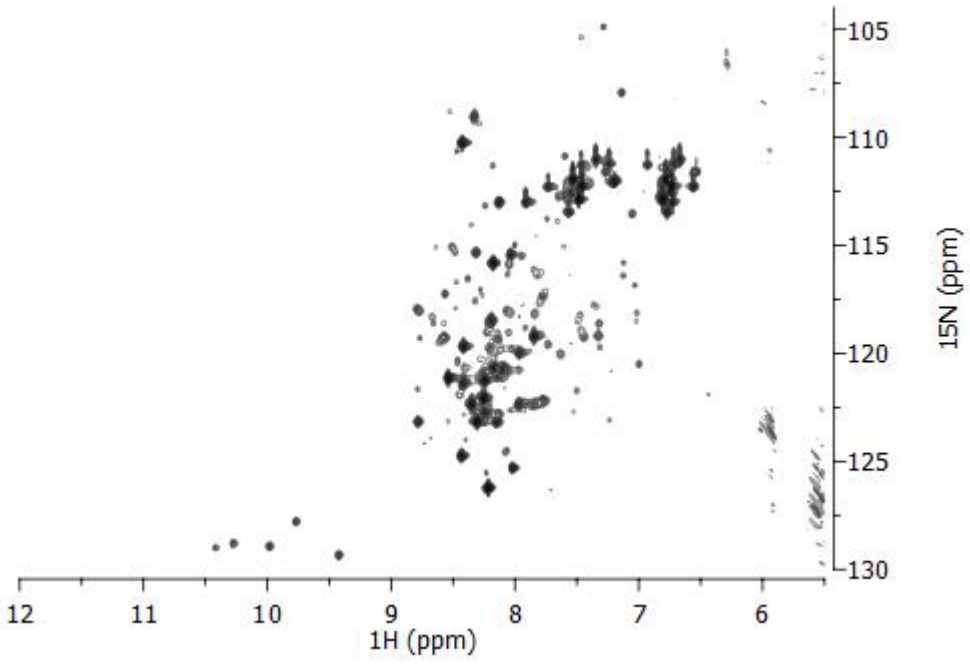

GL-Bid$^{i,i+4}$-NH_2 and Bcl-x_L

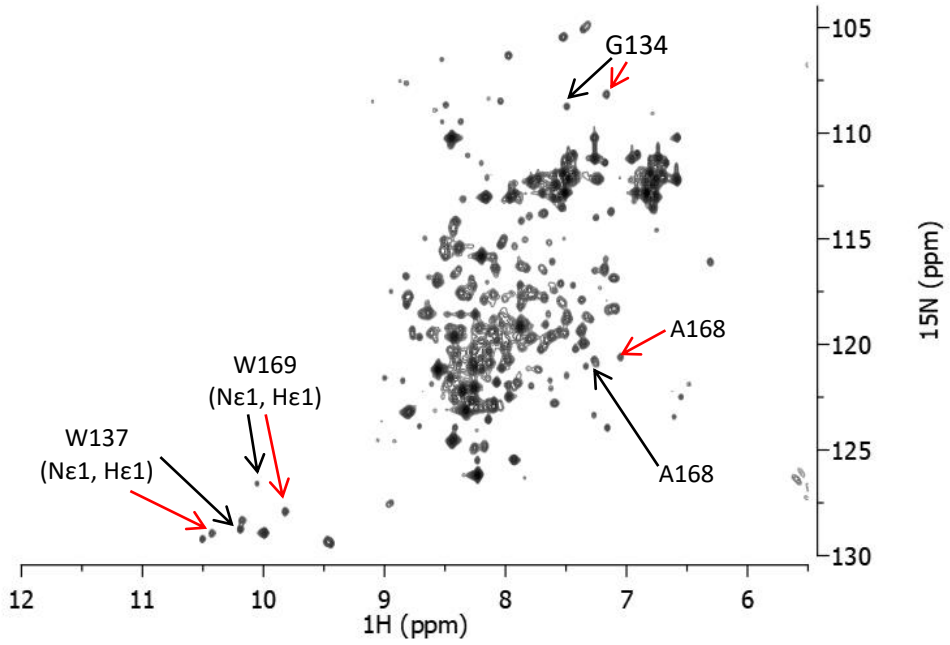

11. Cytotoxicity Assay with non-Stapled Bim-Peptide

Bim$^{i,i+4}$-NH_2:

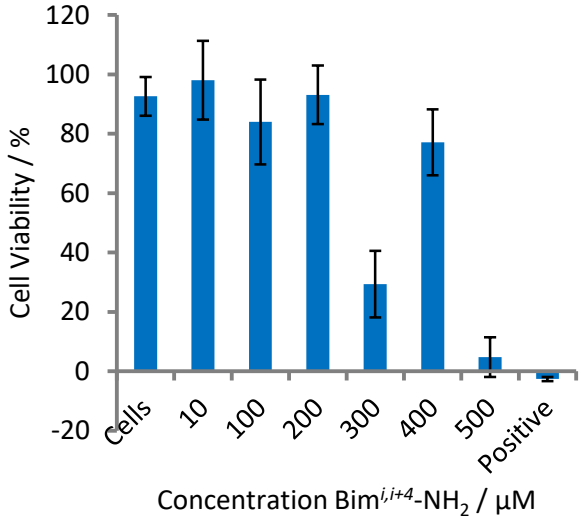

12. Cytotoxicity Assay with the CPP

Ant-NGLG-NH_2:

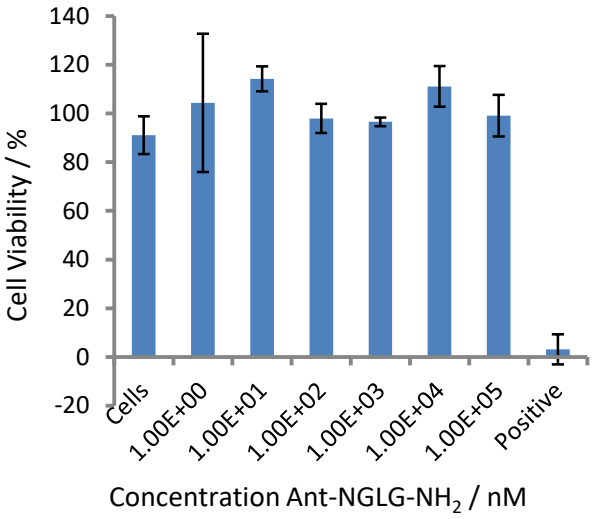

13. Cytotoxicity Assay with Precipitated and Stapled Peptide

33-Ant-Bid$^{i,i+4}$-NH_2: